OLENA LENCHUK

DENSITY-FUNCTIONAL THEORY CALCULATIONS OF SOLUTES IN MOLYBDENUM GRAIN BOUNDARIES

DICHTEFUNKTIONALTHEORIE RECHNUNGEN VON LEGIERUNGSZUSÄTZEN IN MOLYBDÄN KORNGRENZEN

Zur Erlangung des akademischen Grades des Doktors der Ingenieurwissenschaften (Dr.-Ing.) genehmigte Dissertation von M.Sc. Olena Lenchuk aus Kiew (Ukraine)

Fachgebiet Materialmodellierung
Fachbereich Material- und Geowissenschaften
Technische Universität Darmstadt

1. Gutachten: Prof. Dr. rer. nat. Karsten Albe
2. Gutachten: Prof. Dr.-Ing. Martin Heilmaier

Tag der Einreichung: 13. März 2017
Tag der Prüfung: 06. Juni 2017

Darmstadt 2017
D17

DENSITY-FUNCTIONAL THEORY CALCULATIONS OF SOLUTES IN MOLYBDENUM GRAIN BOUNDARIES

OLENA LENCHUK

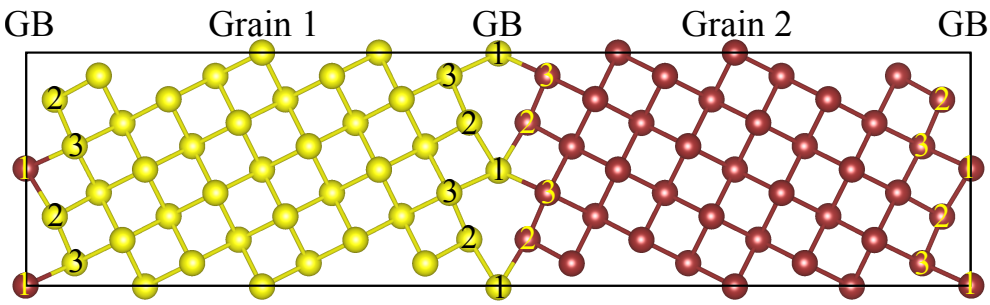

Dissertation

March 2017

On the cover: Tilt Σ5(301)[001] grain boundary in molybdenum. The visualization has been done using the free software package VESTA.

CONTENTS

LIST OF FIGURES

LIST OF TABLES

ABSTRACT

Grain boundaries (GBs) and heterophase interfaces significantly affect the mechanical properties of polycrystalline materials. The ductility and fracture toughness of materials are limited by GB decohesion, which can be manipulated by solute segregation. For example, in Mo-based materials, which are potential candidate materials for high-temperature structural applications, silicon crucially reduces the room-temperature (RT) ductility and fracture toughness [1]. However, addition of silicon is essential for improving the oxidation resistance of these materials. In contrast to silicon, addition of zirconium is an efficient way to increase the room-temperature fracture toughness, strength and ductility of Mo and Mo-based materials [2–4]. In this thesis, we address the physical origin of this experimentally observed behaviour, which remains a matter of debate and speculations. For this investigation, electronic-structure calculations based on density functional theory (DFT) are carried out. In order to determine whether the experimentally observed improvements are attributed to grain boundary or bulk effects, the solid solubility of zirconium and silicon in molybdenum is evaluated using a supercell approach. Finite-size effects are corrected by extrapolation to the dilute limit. The results reveal that the solubility of zirconium in molybdenum at elevated temperature is quite high, whereas the solubility of silicon in molybdenum is rather small. Different solubility limits of zirconium and silicon are explained based on an analysis of lattice distortion and strength of chemical bonds of solutes.

For better understanding the influence of solutes (Zr, Si) and of oxygen on the cohesive strength of grain boundaries in molybdenum, twist $\Sigma5[001]$ and tilt $\Sigma5(310)[001]$ GBs in bicrystal geometry are chosen as structural models. These GBs have a well-defined periodic atomic structure suitable for atomistic modelling. DFT calculations allow to investigate in detail all changes in the atomic and electronic structure of GBs induced by solutes. First, the site preferences for zirconium and silicon solutes at GBs are determined. Although in the dilute limit the low-energy segregation sites at the GB are different for zirconium and silicon, a site competition between solutes might occur upon increasing silicon concentration. Second, the tendency of solutes to segregate from the bulk to GBs is evaluated. The results reveal that zirconium segregated at the GB decreases the thermodynamic barrier for silicon segregation to the GB when silicon is located close to the GB and *vice versa*. Afterwards, the effect of solutes on the stability of the GBs against brittle fracture is quantified by means of energy-based (work of separation) and stress-based (theoretical strength) criteria. The results reveal that zirconium and silicon act as weak embrittlers of molybdenum GBs.

Oxygen embrittles molybdenum GBs considerably stronger. As before, contributions of strain and chemical energy are analysed in order to explain our findings.

After showing, that the experimentally observed improvement of fracture toughness and ductility in molybdenum cannot be simply explained by grain boundary strengthening due to solute segregation, the role of ZrO_2 (zirconia) on the cohesive strength of GBs in molybdenum is investigated. It is energetically preferable for zirconium to capture oxygen and form ZrO_2 at the GB. The influence of the interface to ZrO_2 precipitates and also ultrathin ZrO_2 films embedded between molybdenum grains is investigated in the last part of this thesis. Based on a minimal mismatch between lattice parameters of molybdenum and tetragonal zirconia and on a maximum planar atomic density at the interface, a Mo(001)/t-ZrO_2(001) system is chosen as a structural model. The thermodynamic stability and the mechanical properties of the zirconia/molybdenum interfaces are analysed. The results show that the stability of the interface against brittle fracture strongly depends on a cleavage plane and therefore different cuts have to be carefully investigated. The strength of zirconia/molybdenum interfaces is discussed and compared to those for pure and solute containing twist $\Sigma 5$[001] GBs in molybdenum.

In summary, our work shows that the experimentally observed strengthening of molybdenum upon addition of zirconia cannot be explained by a direct solute effect leading to an increase of the cohesive strength of molybdenum grain boundaries. Furthermore, our results reveal that addition of zirconium to Mo-based alloys can strengthen the molybdenum grain boundaries that contain oxygen by forming an ultrathin zirconia film between molybdenum grains. Choosing oxidised molybdenum GB systems as references (molybdenum with segregated oxygen), a pronounced increase of the theoretical strength can be inferred upon the formation of ultrathin t-ZrO_2 film between molybdenum grains. The stress required to cleave the ultrathin zirconia film is equal to that for the pure molybdenum grain boundary.

GERMAN SUMMARY

Korngrenzen und heterophasige Grenzflächen beeinflussen die mechanischen Eigenschaften von polykristallinen Materialien. Sowohl Duktilität als auch Bruchzähigkeit eines Materials ist von der Kohäsion der Korngrenzen begrenzt. Die Kohäsion kann durch Segregation von Legierungszusätzen manipuliert werden. In Mo-basierten Materialien, die aktuell sehr attraktiv für Hochtemperaturanwendungen sind, ist die starke Abnahme von Duktilität und Bruchzähigkeit bei Raumtemperatur durch Zugabe von Silizium experimentell nachgewiesen werden [1]. Allerdings ist Silizium für die Verbesserung der Oxidationsbeständigkeit dieser Materialien verantwortlich. Im Gegensatz zu Silizium sorgt die Zugabe von Zirkonium für eine Verbesserung der Bruchzähigkeit, Festigkeit und Duktilität bei Raumtemperatur [2–4]. Die vorliegende Dissertation beschäftigt sich mit dem physikalischen Ursprung dieser Verbesserung. Die Steigerung von Duktilität und Bruchzähigkeit steht bis jetzt zur Diskussion. In dieser Arbeit werden für die Berechnung der Materialeigenschaften Methoden der Dichtefunktionaltheorie (DFT) angewendet. Die Löslichkeit von Zirkonium und Silizium in Molybdän wird mit Hilfe der Superzellen-Methode berechnet. Diese Methode ermöglicht es, Zr-bedingte Materialverbesserungen Korngrenz- oder Bulkeffekten zuzuordnen. Um Größeneffekte zu korrigieren, werden die berechneten Daten zum Fall idealer Verdünnung hin extrapoliert. Die Ergebnisse zeigen, dass bei hohen Temperaturen die Löslichkeit von Zirkonium in Molybdän sehr gut, aber die Löslichkeit von Silizium in Molybdän relativ klein ist. Die unterschiedliche Löslichkeitsgrenze von Zirkonium und Silizium basiert auf der Analyse der Kristallzellenverzerrung und auf der Stärke der chemischen Bindungen der Legierungszusätze.

Desweiteren wird der Einfluss der Legierungszusätze (Zr, Si) und des Sauerstoffs (O) auf die kohäsive Festigkeit der Korngrenzen in Molybdän mit Hilfe der $\Sigma5[001]$ Drehkorngrenze und $\Sigma5(310)[001]$ Kippkorngrenze in der Bikristallgeometrie untersucht. Diese Korngrenzen haben eine klar definierte periodische atomare Struktur, die für atomistische Computersimulation besonders gut geeignet ist. DFT-Rechnungen sind in der Lage, alle Änderungen der atomaren und elektronischen Struktur der Korngrenzen, die von Legierungszusätzen herbeigeführt wurden, detailliert zu untersuchen. Zuerst wird die Stellenpriorität von Zirkonium und Silizium an den Korngrenzen identifiziert. Im Fall idealer Verdünnung lagern sich Zirkonium und Silizium an unterschiedlichen Positionen in der Korngrenze an, und zwar an denen mit der jeweils niedrigsten Segregationsenergie. Allerdings kann zwischen beiden Legierungszusätzen eine Konkurrenz um Gitterplätze stattfinden, wenn die Konzentration von Silizium ansteigt. Weiterhin wird die Segregationstendenz der

Legierungszusätze vom Bulk zu den Korngrenzen eingeschätzt. Die Ergebnisse zeigen, dass die Anwesenheit von Zirkonium an den Korngrenzen die thermodynamische Barriere der Si-Segregation reduziert und *vice versa*. Dies gilt für den Fall, wenn sich Silizium in der Nähe der Korngrenze befindet. Anschließend wird der Effekt der Legierungszusätze auf die Stabilität der Korngrenzen gegen Sprödbruch mit Hilfe energiebasierter (work of separation) und spannungsbasierter (theoretische Festigkeit) Methoden bestimmt. Die Ergebnisse zeigen, dass Zirkonium und Silizium die Korngrenzen von Molybdän schwach verspröden. Im Gegensatz dazu versprödet Sauerstoff die Korngrenzen von Molybdän sehr stark. Wie zuvor erwähnt, werden die Beiträge der Kristallzellenverzerrung und der Stärke der chemischen Bindung der Legierungszusätze analysiert, um die berechneten Ergebnisse erklären zu können.

Es wird gezeigt, dass der experimentell nachgewiesene Anstieg von Duktilität und Bruchzähigkeit in Molybdän nicht als Konsequenz der Korngrenzenfestigung durch die Legierungszusätze erklärt werden kann. Aus diesem Grund wird der Einfluss von ZrO_2 (Zirkonia) auf die Kohäsionsfestigkeit der Korngrenzen in Molybdän untersucht. Für Zirkonium ist es energetisch günstiger, Sauerstoff festzuhalten und ZrO_2 an den Korngrenzen zu bilden. Im letzten Kapitel wird der Einfluss der Heterogrenzflächen zwischen ZrO_2-Präzipitat und Molybdän und den ultradünnen ZrO_2-Schichten, die zwischen Mo-Körnern eingebettet sind, erforscht. Bei der Auswahl der Heterogrenzflächen wird die Gitterfehlanpassung der Kristallzellen von Molybdän und tetragonalem Zirkonia minimiert, und die planare Atomdichte an den Heterogrenzflächen maximiert. In der vorliegenden Dissertation wird als Strukturmodell ein Mo(001)/t-ZrO_2(001) System verwendet. Die thermodynamische Stabilität und die mechanischen Eigenschaften der Heterogrenzfläche zwischen Zirkonia und Molybdän werden analysiert. Die Resultate zeigen, dass die Stabilität der Heterogrenzflächen gegen Sprödbruch stark von der Spaltebene abhängig ist. Deswegen ist es von Bedeutung, verschiedene Ebenen zu untersuchen. Die Festigkeit der Heterogrenzflächen zwischen Zirkonia und Molybdän wird erörtert und wird mit der Festigkeit der $\Sigma 5[001]$ Drehkorngrenzen für reines und für legiertes Molybdän verglichen.

Zusammenfassend verdeutlicht diese Arbeit, dass die experimentell nachgewiesene Festigkeits-Steigerung von Molybdän durch Zugabe von Zirkonium kein direkter Effekt der Korngrenzenfestigung durch die Legierungszusätze ist. Außerdem zeigen unsere Ergebnisse, dass die Zugabe von Zirkonium zu Mo-basierter Materialien nur die Korngrenzen in Molybdän verstärken, die Sauerstoff enthalten. In diesem Fall bildet sich zwischen den Molybdän-Körnern eine ultradünne Zirkonia Schicht. Wenn man die Sauerstoff enthaltenden Mo-Korngrenzen als Referenzsystem auswählt, lässt sich die deutliche Zunahme der theoretischen Festigkeit der Bindung der ultradünnen Zirkonia-Schicht zwischen den Molybdän-Körnern zuordnen. Die Spannung, die man benötigt, um die ultradünne t-Zirkonia Schicht zu spalten, entspricht der Spannung, die benötigt wird, um eine reine Mo-Korngrenze zu spalten.

1

MATERIALS BACKGROUND AND APPLICATIONS

The majority of engineering materials are polycrystalline and consist of grains, represented by regions of the same phase but with different crystallographic orientations, which are connected by grain boundaries (GBs). GBs are important microstructural elements in polycrystalline solids. The presence of GBs in single phase materials, as well as heterointerfaces in multiphase materials, has a significant impact on the mechanical properties (e.g. strength and fracture toughness), thermal stability and performance of materials [5–7]. In particular, the resistance of the material to crack propagation (fracture toughness) is often limited by GB decohesion. Due to the reduced atomic stacking at the GBs compared to the bulk grain interiors, a crack preferentially propagates along GBs (intergranular fracture), rather than through the grain interior (transgranular fracture) [8].

Advances in automotive, aerospace etc. industries require materials that are stronger, ductile and more resistant to fracture. However, a material with an increased strength tends to become more brittle and breaks more easily due to intergranular fracture, resulting in the loss of ductility and fracture toughness [9]. The atomic structure of GBs defines their energy, thermodynamic stability, fracture stress and sliding resistance etc., and thus affects the overall mechanical behaviour of materials in service [6]. In order to design polycrystalline materials with improved mechanical properties, basic knowledge of GBs structure-properties relation is required.

In general, the GB properties can be manipulated by solute segregation (decoration by solute atoms). Grain boundaries are chemically more reactive compared to the grains themselves and therefore solute segregation and precipitation (the presence of secondary phases) are often thermodynamically preferred processes at the GBs [10–12]. Grain boundary segregation induces changes in the atomic structure and chemical bonding within the decorated GB affecting the GB energy and cohesive strength. The presence of solutes at GBs can enhance the cohesive strength of grain boundaries (strengthen the GBs) and reduce it (embrittle the GBs). The improved cohesive strength of GBs leads to the improved ductility and fracture toughness [13, 14]. Therefore, a detailed understanding of GB properties and changes induced by solute segregation are of significant importance for materials design.

In the present thesis the influence of solute segregation and of oxygen contamination at the GBs, including the formation of the ultrathin film of oxidised solute, on the mechanical properties of GBs in molybdenum are investigated. Mo-based alloys are potential candidate materials for high-temperature applications, for example, in a gas

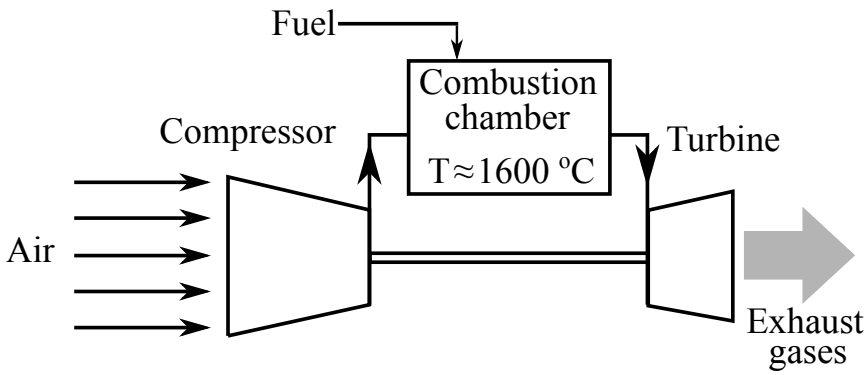

Figure 1: Principle of a gas turbine engine.

turbine engine. In the present chapter a brief overview of a gas turbine engine is given and possibilities for the optimisation of its performance are discussed. The role of constituent phases, ideal microstructure and zirconium microalloying in Mo-based alloys for obtaining the balance between oxidation resistance and fracture toughness is discussed. The effect of solutes on the cohesive strength of grain boundaries in molybdenum is also depicted.

1.1 OVERVIEW OF A GAS TURBINE ENGINE

A gas turbine engine converts chemical energy from fuel combustion into mechanical energy, which is used, for example, to create thrust for aircraft propulsion (jet engines) or to drive different facilities attached to the turbine shaft, such as an electric power generator, a compressor for pumping natural gas, a propeller for marine propulsion etc. [15, 16]. The market for gas turbine engines significantly increased over the last years. For example, in 2015 the worldwide aircraft fleet increased to over 26000 airplanes and the number of flights operated worldwide exceed 33 millions [17]. In fact, in 2014/2015 the annual fuel consumption approached 25–30% of the total operating costs of the airline industry [17]. In the context of global warming these numbers show the urgent need to increase the efficiency of gas turbine engines.

Figure 1 shows the principle of a gas-turbine engine system. A compressor squeezes the incoming air, increasing its temperature and pressure. In a combustion chamber fuel is injected into the intaken air and burnt. The high-energy gas stream leaves the combustion chamber and passes through the turbine forcing the turbine blades to turn. The pressure and the temperature of the gas stream decrease as the gas passes through the turbine. The turbine converts the energy of the bypassing hot gases into kinetic energy that is used to drive the compressor. The high velocity jet of the exhaust gases

creates the thrust force for aircraft propulsion. In the case of industrial turbines, the energy is used to drive different facilities attached to the turbine shaft [16].

The efficiency of a gas turbine engine can be mainly improved by optimising the efficiency of the turbine, which works in the hottest part of the gas turbine engine [18]. The maximum thermal efficiency of a turbine thermodynamic cycle is defined by the Carnot efficiency as [19]

$$\eta_{\mathrm{t}} = 1 - \frac{T_{\mathrm{exh}}}{T_{\mathrm{inlet}}}, \tag{1.1}$$

where T_{exh} is the turbine exhaust temperature and T_{inlet} is the turbine inlet temperature. The improvement of the gas turbine performance (thrust) with respect to the fuel consumption requires to operate the turbine with an increased inlet temperature. Over the years, the increase of the turbine inlet temperature was achieved by utilisation of different cooling techniques and thermal barrier coatings. This allowed to reduce the temperature of the turbine blades (metal) below the temperature of the hot gases that leave the combustion chamber [20]. In modern engines, single-crystalline nickel-based superalloys used for turbine blades operate above 0.8 of their melting point, approaching 1150 °C, while the turbine inlet temperature (the temperature of hot gases) can approach 1500 °C [21–24].

Improving the efficiency, performance and cost-effectiveness of energy production will depend critically on our capability to develop substantially improved materials and material systems, which are able to withstand a combination of high temperatures (beyond the operating temperature of Ni-based superalloys), high rotational speeds, high thermal stresses and oxidation [16, 25].

1.2 MOLYBDENUM-BASED ALLOYS

Applying materials with high melting temperature in gas turbines would allow to operate these components with increased gas inlet temperatures and to optimise the thermodynamic behaviour leading to a reduction of fuel consumption, emissions and costs. Hence, molybdenum has attracted attention due to its high melting temperature and high strength at elevated temperatures [26]. Moreover, molybdenum exhibits a high thermal conductivity and a low coefficient of thermal expansion, which provides advantages in controlling thermal stresses and reduces the necessary cooling power [21].

Structural materials for high-temperature applications should show an excellent oxidation- and creep resistance at elevated temperatures and, at the same time, adequate mechanical properties (strength, ductility and fracture toughness) at room temperature (RT) [3, 27, 28]. Simultaneously meeting all these requirements with a single-phase material is problematic, but can be realised in multiphase materials.

Since the early 1990s a lot of research has focused on the development of multiphase silicide alloys with Mo as a base metal (Mo-Si-B). Operation of single phase Mo alloys for high-temperature applications is limited. Beyond 700 °C pure Mo undergoes a catastrophic oxidation in air and intensive mass loss due to the formation of a volatile MoO_3 [26, 29]. The oxidation protection of Mo alloys can be achieved by addition of Si and further improved by addition of B. Silicon and boron are necessary for the formation of a protective borosilicate (SiO_2-B_2O_3) layer on the surface of the material [21, 24]. Addition of B decreases the viscosity of silica (SiO_2) enhancing the growth kinetics of the passivating borosilicate layer [30, 31]. The sources of oxidation protection in multiphase Mo-Si-B are the intermetallic phases Mo_3Si and Mo_5SiB_2 (T2), which supply Si and B [25]. The oxidation resistance of Mo-Si-B alloys depends on the amount of silicon and boron and their ratio [24]. The quality of a passivating borosilicate layer can be controlled by varying the Si/B ratio, which is also helpful in optimising the oxidation resistance of Mo-Si-B alloys, especially in the intermediate temperature range of 700–900 °C [25, 32].

The main drawback of intermetallic phases is their inherent brittleness. For example, the RT fracture toughness (resistance to crack propagation) of Mo_3Si, Mo_5Si_3 and Mo_5SiB_2 is on the order of 2–4 MPa$\sqrt{\text{m}}$ [33–37]. In order to improve the ductility and fracture toughness of Mo-Si-B, a molybdenum matrix has been introduced in the alloy. Berczik [38, 39] pioneered and patented a family of Mo-rich Mo-Si-B alloys, which consist of a Mo solid solution with substitutional silicon and interstitial boron (Mo_{ss}) and intermetallic Mo_5SiB_2 and Mo_3Si phases. These alloy systems can potentially take advantage of the beneficial oxidation and creep resistance of intermetallic phases and attractive mechanical properties of molybdenum.

1.2.1 *Fracture toughness and ductility*

The properties (oxidation resistance, fracture toughness, ductility and creep resistance) of Mo-Si-B alloys depend on the volume fraction and arrangement of each phase (Mo_{ss}, Mo_3Si, Mo_5SiB_2), the microstructure scale (coarse- or fine-grained microstructure), as well as on the homogeneity of phase distribution [27, 40]. This is schematically illustrated in Figure 2. The challenge for Mo-Si-B alloy design is that the microstructural requirements for maximising the oxidation resistance and the fracture toughness are mutually exclusive. Indeed, an intermetallic matrix with embedded discontinuous molybdenum particles (Figure 2(a)) is desirable for improved oxidation resistance. Furthermore, refining the microstructure size scale has a positive impact on the oxidation protection of Mo-Si-B alloys [30]. In contrast, a large volume fraction of a continuous, coarse molybdenum matrix with dispersed intermetallic particles (Figure 2(b)) is preferable for enhanced fracture toughness [3].

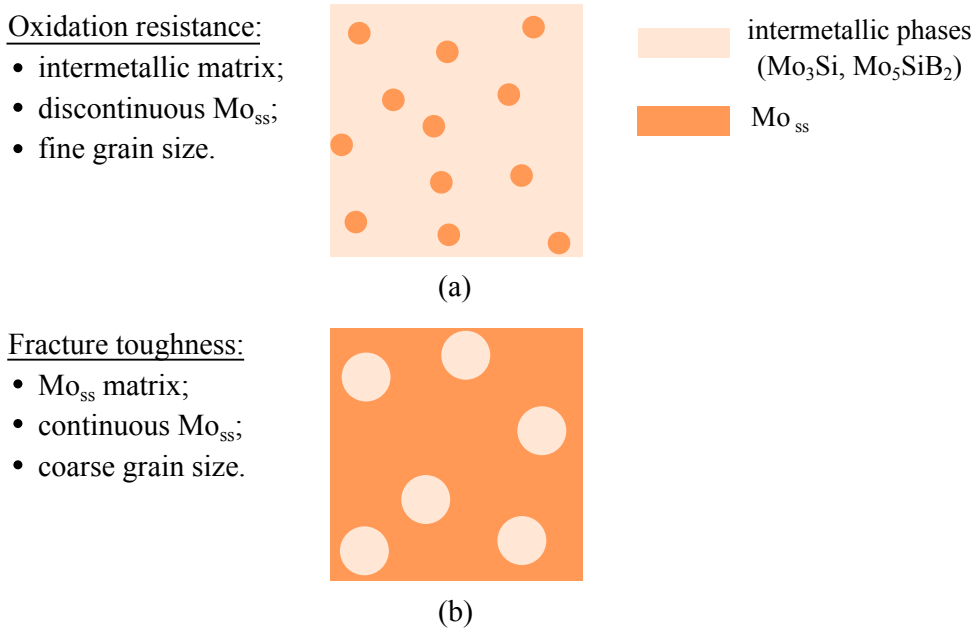

Figure 2: Schematics of the microstructure, which is required for the optimal (a) oxidation resistance and (b) fracture toughness in Mo-Si-B alloys. The microstructural requirements for maximising each property are mutually exclusive. The figure is schematically depicted from [23].

The volume fraction of the molybdenum phase as the only phase providing a toughening of Mo-Si-B alloys is of key importance [3]. The dependence of the RT fracture toughness on the volume fraction, arrangement and grain size of Mo_{ss} is summarised in Table 1. The table shows that a higher RT fracture toughness is, in general, obtained for alloys, which utilise a larger volume fraction of a continuous Mo_{ss} and a coarser microstructure. The main trends in the RT fracture toughness behaviour are visualised on Figure 3. Indeed, increasing the volume fraction of Mo_{ss} from 21% to 70% in the fine-grained Mo-Si-B alloys, the RT fracture toughness is improved from 4.1 MPa$\sqrt{\text{m}}$ [47] to 13.0–13.6 MPa$\sqrt{\text{m}}$ [41]. Similarly, the fracture toughness of Mo-12Si-8.5B (at.%) with 38% volume fraction of Mo_{ss}, investigated in a number of studies [42–44, 46, 47], is improved from 8.6–8.8 MPa$\sqrt{\text{m}}$ to 14.0–15.6 MPa$\sqrt{\text{m}}$ when the grain size of molybdenum phase increases from 1.2–2.5 μm (fine-grained microstructure) to $<$150 μm (coarse-grained microstructure). The fracture toughness of alloys possessing a continuous Mo_{ss} matrix is always higher compared to those with an intermetallic matrix.

The improvement of fracture toughness with increasing volume fraction of the molybdenum phase and microstructure coarsening is attributed to a combination of intrinsic (crack trapping) and extrinsic (crack bridging) toughening mechanisms,

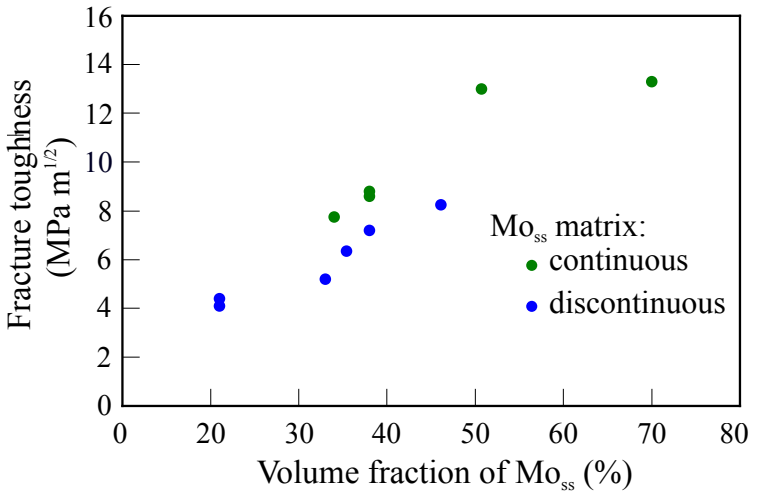

(a)

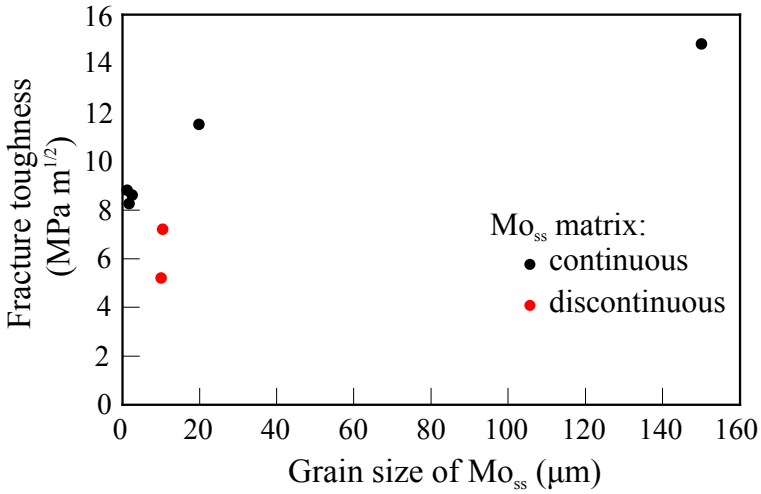

(b)

Figure 3: The RT fracture toughness of Mo-Si-B alloys as a function of (a) volume fraction and (b) grain size of Mo_{ss}. The corresponding data points measured for (a) fine-grained Mo-Si-B alloys and (b) Mo-Si-B alloys with 38 vol.% of molybdenum solid solution are given in Table 1.

Table 1: The RT fracture toughness of Mo-Si-B alloys consisting of differently arranged Mo_{ss}, Mo_3Si and Mo_5SiB_2 phases, volume fraction of Mo_{ss} and its grain size. Test methods: Vickers indentation (VI), three-point bending using chevron-notched specimens (3PB), compact-tension tests on disc-shaped specimens (CT). Continuity of Mo_{ss}: continuous (cont) or discontinuous (discont).

Composition (at.%)	Volume fraction of Mo_{ss}	Scale	Grain size of Mo_{ss} (μm)	Fracture toughness, (MPa$\sqrt{\text{m}}$)	Test method	Ref.
Mo-6Si-5B	70%	cont	1.6	13.0–13.6	VI	[41]
Mo-9Si-8B	51%	cont	1.5	12.7–13.3	VI	[41]
Mo-10Si-10B	46%	discont	1.7	8.1–8.4	VI	[41]
Mo-13Si-12B	35%	discont	2.0	6.0–6.7	VI	[41]
Mo-12Si-8.5B	38%	cont	1.2	8.8	3PB	[42]
Mo-12Si-8.5B	38%	cont	2.5	8.6	3PB	[42]
Mo-12Si-8.5B	38%	cont	19.8	11.5	3PB	[43]
Mo-12Si-8.5B	38%	cont	<150	14.0–15.6	3PB	[44]
Mo-9Si-8B	55%	cont	5–20	7.1	CT	[45]
Mo-20Si-10B	49%	cont	>100	11.8	CT	[40]
Mo-12Si-8.5B	38%	discont	10.4	7.2	CT	[46, 47]
Mo-16.8Si-8.4B	21%	discont	2.1	4.1	CT	[47]
Mo-16.8Si-8.4B	21%	discont	4.4	5.7	CT	[47]
Mo-14Si-10B	33%	discont	5–15	5.2	VI	[48]
Mo-20Si-10B	34%	cont	fine and medium	7.5–8.0	CT	[27]
Mo-20Si-10B	49%	cont	coarse	12.0	CT	[27]

which are predominantly found in the Mo_{ss} matrix [27, 40]. Figure 4 illustrates the crack trapping and the crack bridging toughening mechanisms at the Mo_{ss} phase, observed in Mo-20Si-10B (at.%) by Kruzic *et al.* [27]. Crack trapping describes local capturing of a growing crack in a particular microstructural region, for example, in a more ductile molybdenum. Thus, a higher force has to be applied to the system to overcome this trap, resulting in a higher fracture toughness of the system [49]. Crack bridging is a toughening mechanism acting on the already existing crack. When the crack surfaces interact during crack propagation, the crack tip can be partially relieved [50]. In this case, a microstructural feature, for example, a more ductile molybdenum phase, spans the crack as it opens thereby lowering the effective crack-

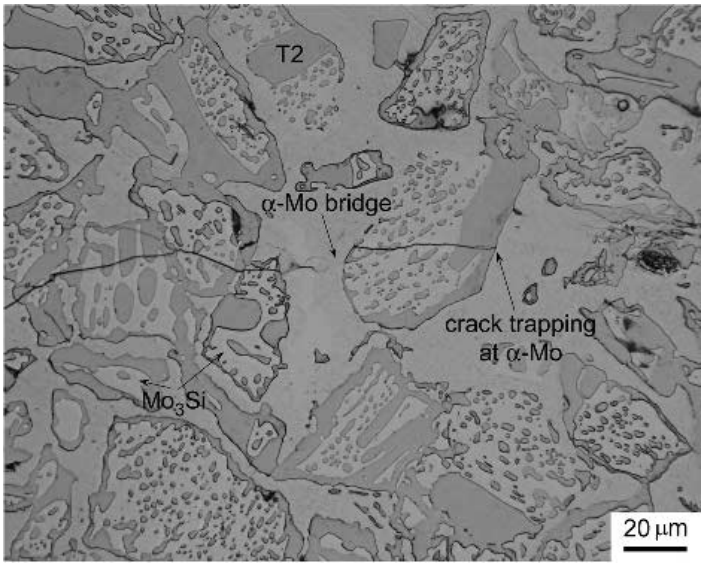

Figure 4: Optical micrograph of Mo-20Si-10B (at.%) illustrating the crack trapping and the crack bridging toughening mechanisms at the Mo_{ss} phase. The volume fraction of Mo_{ss} in the alloy is 34 vol.%. The crack is locally arrested at the Mo_{ss}, leaving Mo_{ss} bridges in the crack wake. ©(2017) reprinted with permission from Springer.

driving force that would be otherwise used to extend the crack [49]. This results in rising fracture resistance.

A continuous molybdenum matrix and its higher volume fraction are beneficial for both toughening mechanisms, since a crack will not be able to avoid the molybdenum phase. As a consequence, the fracture toughness is progressively improved (see Figure 3). On the other hand, the enhanced fracture toughness is accompanied by a catastrophic reduction of the oxidation resistance of Mo-Si-B leading to considerably higher mass losses due to the presence of a higher volume fraction of the non-protective molybdenum phase [3, 41].

Kruzic *et al.* [27] demonstrated that at 1300 °C the fracture toughness of Mo-Si-B alloys (12.6 MPa$\sqrt{\text{m}}$) with lower volume fraction of the molybdenum phase (34 vol.%) exceeded the RT fracture toughness (12.0 MPa$\sqrt{\text{m}}$) of an alloy with higher Mo volume fraction (49 vol.%). At elevated temperatures the ductility of Mo is improved resulting in the enhanced fracture toughness of Mo-Si-B alloys. This finding suggests that if the RT ductility of molybdenum could be improved, the reduced volume fraction of Mo_{ss} would be sufficient to achieve the required level of fracture toughness in Mo-Si-B alloys. As a consequence of the lower volume fraction of molybdenum, the oxidation resistance of Mo-Si-B alloys will be improved [3].

1.2.2 *Improving the ductility of molybdenum*

Molybdenum is characterised by a brittle-to-ductile transition when the temperature is increased. This is common for metals with a body-centred cubic (bcc) crystal structure. The narrow temperature range, within which a change in the fracture mode takes place, is called the brittle-to-ductile transition temperature (BDTT) [51]. Below the BDTT molybdenum fails by brittle fracture, while above the BDTT ductile fracture is mainly observed. Commercial pure, fine-grained, wrought molybdenum exhibits a BDTT temperature in the range between -10 °C and 30 °C [24]. However, the incorporation of Si and B into the Mo lattice results in an increased resistance of the Mo lattice to dislocation motion [24]. As a consequence, not only the strength of the Mo(Si, B) alloy is significantly improved, but also the ductility is reduced and the BDTT is dramatically increased. For example, in Mo-8.9Si-7.7B (at.%), processed by a power metallurgical (PM) route and possessing a nearly continuous Mo_{ss} matrix with dispersed intermetallic particles, the BDTT is around 1500 °C [24]. The BDTT is sensitive to the composition and the concentration of impurities, processing and test conditions [52].

The brittle-to-ductile transition in the fracture mode of Mo also depends on grain size [53]. Cleavage fracture, being a dominant failure mechanism in pure molybdenum [54], can be suppressed when grains are smaller than the length of dislocation pile-ups required to nucleate a cleavage crack [3]. Thereby, a stress required for yielding can be reached and the material will deform plastically. However, the microstructure scale is a key issue in determining the creep resistance of Mo-Si-B alloys and grain refinement will be harmful for creep performance of these alloys [23].

Another approach to improve the ductility of molybdenum is to strengthen its grain boundaries (GBs). The GB cohesion plays a central role in the plastic deformation of this material. Strong GBs can sustain stresses required for activation of dislocation glide in the grain interior before failing intergranularly [2]. Polycrystalline molybdenum is considered as an "intrinsically brittle" material, the brittleness of which originates from the weak bonding strength in the grain interior and at the grain boundary [55, 56]. Depending on the purity of molybdenum, the brittle fracture can occur intergranularly (along GBs) or transgranularly (across grains as cleavage). Interstitial impurities such as oxygen as well as substitutional alloying additives have a pronounced effect on the fracture behaviour. For example, Kumar and Eyre [57] have found that oxygen segregates preferable to GBs in molybdenum and has a detrimental effect on the GBs cohesion promoting the brittle intergranular fracture. The study of Sturm *et al.* [1, 22] revealed the transition from transgranular to intergranular brittle fracture in the Mo(Si) solid solution with a fraction of intergranular fracture up to 90% even for small Si concentrations ($\sim$0.3 at.%).

Table 2: The RT fracture toughness of the pure Mo and binary Mo-Si alloys, with addition of Zr in small concentrations. Test methods: three-point bending using chevron-notched specimens (3PB), centre through-thickness notched tension (CNT), compact-tension tests on disc-shaped specimens (CT).

Composition (at.%)	Processing	Grain size (μm)	Fracture toughness, (MPa$\sqrt{\text{m}}$)	Test method	Ref.
Mo-1Zr (wt.%)	annealed	300–400	17[a]	Electrospark crack	[59]
Mo-2.5Si-0.1Zr	cast and annealed	-	22.8–23.3	3PB	[60]
Mo-2.5Si-0.5Zr	cast and annealed	-	22.6–24.0	3PB	[60]
Mo	PM	-	9.5	CNT	[61]
Mo	PM	-	5[a]–12	CT	[61]
Mo	PM	97(8)	24.2 ± 2.3	3PB	[1]
Mo-0.34Si	PM	54(4)	7.8 ± 1.2	3PB	[1]
Mo-1.69Si	PM	35(5)	4.9 ± 1.4	3PB	[1]
Mo-3.34Si	PM	82(5)	3.9 ± 0.6	3PB	[1]

a Recrystallised

In general, the widely accepted view is that solute segregation is improving the cohesive strength of grain boundaries (GBs) and thus the ductility and fracture toughness [13, 14]. An alternative mechanism is that solutes with a high affinity to oxygen will getter oxygen and will form oxides. The presence of oxide phases could be less detrimental to the mechanical properties compared to oxygen itself [2, 58]. This is why microalloying of pure Mo, binary Mo-Si and ternary Mo-Si-B alloys with reactive element such as zirconium has been investigated.

1.2.3 *Zirconium microalloying*

Zirconium microalloying has improved the fracture toughness, strength and ductility in pure Mo [4, 59, 62–65], binary (Mo-Si) [2, 60] and ternary (Mo-Si-B) [3, 23, 66–68] alloys. Table 2 lists the RT fracture toughness of pure Mo and binary Mo-Si alloys with and without addition of Zr. As it is seen from the table, the RT fracture toughness of Mo varies in the range from 5 MPa$\sqrt{\text{m}}$ to 24 MPa$\sqrt{\text{m}}$ depending on the alloy microstructure and purity. For example, increasing the degree of recrystallisation results in a decrease of the fracture toughness of Mo [69]. Koval *et al.* have found

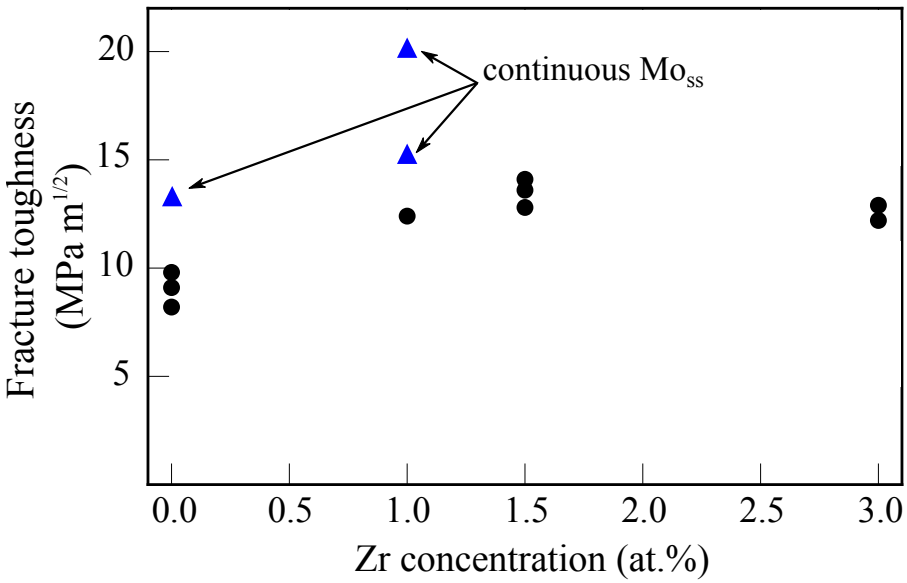

Figure 5: The RT fracture toughness of Mo-Si-B alloyed with 1 to 3 at.% Zr. Black circles correspond to arc-cast and annealed Mo-12Si-8.5B alloy, investigated by Schneibel *et al.* [3]. These alloys are composed of an intermetallic matrix with Mo_{ss} distributed in the form of islands. Blue triangles correspond to mechanically alloyed Mo-9Si-8B (at.%), investigated by Becker *et al.* [67] and Krüger *et al.* [41]. These alloys are composed of a Mo_{ss} matrix with intermetallic particles.

an improvement of the RT fracture toughness of the recrystallised Mo-1wt.% Zr alloy to 17 MPa$\sqrt{\text{m}}$. A significant improvement of the RT fracture toughness is observed in Mo-2.5Si (at.%) alloys with addition of Zr. Indeed, Sturm *et al.* [1] have shown that Mo-Si alloys exhibited a pronounced reduction in the RT fracture toughness with increasing Si concentration. Meanwhile, both 0.1 at.% and 0.5 at.% Zr-containing Mo-2.5Si alloys, investigated by Schneibel *et al.* [60], possess a fracture toughness comparable to Si-free molybdenum. Moreover, Si microalloying promotes brittle intergranular fracture. The Mo-2.5Si alloy, containing 0.1 at.% Zr fractured transgranularly, whereas the alloy with 0.5 at.% Zr exhibited partial intergranular failure [60].

The fracture toughness of different Mo-Si-B alloys is improved with addition of Zr. Figure 5 shows the fracture toughness of arc-cast and annealed Mo-12Si-8.5B (at.%) [3] and of mechanically alloyed Mo-9Si-8B (at.%) [67] with addition of 1 to 3 at.% Zr. The increase from 9.0 ± 0.8 MPa$\sqrt{\text{m}}$ to 13.5 ± 0.7 MPa$\sqrt{\text{m}}$ is observed for Mo-12Si-8.5B, reaching its maximum at around 2 at.% Zr. In the Mo-9Si-8B alloys the fracture toughness has been risen from 13.0 ± 0.3 MPa$\sqrt{\text{m}}$ [41] to 15.3–20.1 MPa$\sqrt{\text{m}}$ with addition of 1 at.% Zr [67]. The Mo-9Si-8B alloys consist of a continuous Mo_{ss}

(57–59 vol.%) and embedded intermetallic particles, whereas the Mo-12Si-8.5B alloys possess the intermetallic matrix with distributed Mo_{ss} islands of various size. Consistent with results obtained for unalloyed Mo-Si-B alloys (see Figure 3), a larger volume fraction of Mo_{ss} and its continuous distribution are required for enhanced fracture toughness. The crack growth can be suppressed by the comparably ductile molybdenum phase, whereas the effectiveness of the suppression depends on the distribution of the molybdenum phase. The crack propagates dominantly through the intermetallic phases and is stopped in the Mo regions [67].

The enhanced fracture strength and improved ductility were determined by Hiraoka *et al.* [64, 70] in electron-beam-welded molybdenum containing 0.05 at.% Zr. Although at -70 °C the total elongation of Mo-0.05Zr (at.%) is slightly improved and is around 2.5–3%, at 20 °C the total elongation for weld joints of Mo-Zr alloy exceeded 20% compared to ∼10% for pure molybdenum. Precipitates of different size have been found at GBs in the weld and base metal. The effect of small amounts of Zr (0.16 at.%), in combination with C (96 appm) and B (53 appm), on the RT ductility in molybdenum welds has been investigated by Miller *et al.* [62, 63]. The results show an improvement of ductility from ∼3 to ∼20% and a transition from intergranular to transgranular (cleavage) fracture mode. An atom map of a region of a base metal specimen containing a grain boundary has shown the enrichment of GBs with zirconium, carbon and boron, as well as the depletion of oxygen, nitrogen and silicon levels at the GB compared to the matrix levels. The presence of Zr, B and C supposedly inhibited the segregation of oxygen to the GBs in molybdenum, which in turn prevented the intergranular failure of molybdenum. In another study, Cockeram *et al.* [65] have investigated series of arc melted molybdenum alloys with a composition similar to that used in the study of Miller *et al.* [62, 63], containing Zr in the range from 1250 to 1700 ppm, C from 8 to 81 ppm and B from 8 to 160 ppm. The authors reported that all alloys exhibited improved strength compared to the pure molybdenum which is attributed to the presence of second phase particles and segregation of Zr, C and B to grain boundaries. In contrast to results obtained by Miller *et al.*, the ductility of Mo-Zr-C-B alloys is tended to decrease. The authors speculated that the presence of elevated levels of zirconium and boron has led to the formation of brittle second phase particles and as a consequence to the reduced ductility and reduced resistance to brittle fracture. Moreover, it is suggested that segregation of Zr to GBs in the Mo-Zr-C-B alloys results in a decreased fracture resistance.

Addition of 1 at.% Zr has resulted in an extremely high bend strength (∼2 GPa) of binary Mo-Si alloys and also in some bend ductility (plastic strain of 0.1%) already at room temperature [2]. Moreover, at 538 °C a plastic strain of 1.4% was observed, whereas the reference Zr-free Mo-1.5Si alloy did not show any ductility up to 816 °C. The improved strength in the low-temperature deformation mode is attributed to

Table 3: Embrittling potential ΔE_{EP} in kJ/mol of solutes segregated at Mo GBs.

Solute	GB	ΔE_{EP}, kJ/mol	Type	Reference
B	$\Sigma5(310)[001]$	-104	Enhancer	[71]
N	$\Sigma5(310)[001]$	78	Embrittler	[71]
O	$\Sigma5(310)[001]$	141	Embrittler	[71]
C	$\Sigma5(310)[001]$	-30	Enhancer	[71]
B	$\Sigma3(110)[\bar{1}11]$	-77	Enhancer	[72]
N	$\Sigma3(110)[\bar{1}11]$	-16	Enhancer	[72]
O	$\Sigma3(110)[\bar{1}11]$	105	Embrittler	[72]
C	$\Sigma3(110)[\bar{1}11]$	-95	Enhancer	[72]
Si	$\Sigma3(110)[\bar{1}11]$	$\sim$35	Embrittler	[72]
Zr	not specified	25	Embrittler	[73]
Zr	$\Sigma5(310)[001]$	$\sim$68	Embrittler	[74]
Zr	$\Sigma3(110)[\bar{1}11]$	$\sim$48	Embrittler	[75]

the significant microstructural refinement caused by addition of Zr according to the Hall-Petch relationship [10] and pinning of GBs by ZrO_2 particles. The physical origin of the ductility improvement with addition of Zr is, however, unclear. Saage *et al.* [2] suggest that the reduction of silicon and oxygen segregation to GBs in the presence of Zr due to site competition and formation of ZrO_2, respectively, might contribute to the strengthening of GBs. Moreover, the presence of Zr at GBs could potentially enhance the cohesive strength of GBs and, therefore, improve ductility.

Consistent with results for pure Mo and binary Mo-Si alloys, Zr-containing Mo-Si-B alloys also show increased strength and hardness [66]. This improvement is associated with grain size reduction, precipitation strengthening by fine ZrO_2 particles, distributed both at the GBs and inside the grains, and enhanced grain and phase boundaries cohesion due to depletion of oxygen at these boundaries. The oxygen depletion is caused by formation of ZrO_2 particles. Moreover, Zr addition leads to the reduction of the BDTT value by 100 °C.

1.3 THEORETICAL INVESTIGATIONS OF SOLUTES IN MOLYBDENUM

The number of theoretical studies on solute segregation at grain boundaries in molybdenum is rather scarce. The segregation of light elements (B, O, C, N) in Mo bicrystals has been investigated in a study of Janisch *et al.* [71] and more recently by Scheiber *et al.* [72] by means of electronic structure calculations. Oxygen and nitrogen are always present in Mo-based alloys, although their amount depends on the fabrication route.

In contrast, B and C have been added to the Mo-based alloys in order to improve their properties as, for example, in the experimental study of Miller *et al.* [62, 63]. Janisch *et al.* [71] have shown that oxygen and nitrogen embrittle Mo GBs, whereas C and B strengthen the GBs. Similar trend is found in a study of Scheiber *et al.* [72], although nitrogen is found to slightly increase GB cohesion. The embrittling potential of light elements is defined based on the Rice-Wang criterion [76] and is summarised in Table 3. The Rice-Wang criterion classifies a solute as a GB enhancer if its tendency to segregate from the bulk to the GB is stronger than that from the bulk to the surface. The investigated light elements are inserted interstitially at the GB and produce similar elastic strain. The differences in the behaviour of B, O, C, N (embrittling or enhancing) are therefore caused by the differences in the chemical bonding. Oxygen and nitrogen create polar bonds and weaken metal-metal bonds across the GB, whereas boron and carbon strengthen metal-metal bond at the GB forming covalent bonds. The charge transfer is the highest for oxygen and, therefore, the presence of oxygen at the GBs is the most detrimental for the GBs properties.

Zirconium has been chosen as a ductilizing element for Mo-based alloys in a number of studies (see Section 1.2.3). Recently, the influence of Zr on the cohesive strength Mo GBs has been investigated in tilt $\Sigma3(110)[\bar{1}11]$ [75] and in tilt $\Sigma5(310)[001]$ GBs [74]. The results obtained in these theoretical studies substantiate the findings concerning site preference and the embrittling potential of Zr, found in the present thesis. Scheiber *et al.* [75] have shown that Zr prefers to occupy sites at the GBs that offer more excess volume. Furthermore, based on the Rice-Wang criterion, Zr is found to act as a weak embrittler of Mo GBs. The embrittling potential of Zr is listed in Table 3. The presence of Zr at the GB in Mo decreases its cohesive strength, although the embrittling potential of Zr is smaller compared to that for oxygen. The type of GB has a minor effect on the observed trend. The authors also emphasise that both chemical and the elastic origins of the solute driving force for GB segregation have to be considered. The theoretical models for solute segregation based only on one of the contributions do not represent qualitatively the physical picture.

1.4 OPEN QUESTIONS

Regarding the modelling of solutes at grain boundaries, solid-solid heterophase interfaces and evaluation of their mechanical properties, several open questions can be formulated. These questions will be addressed in the following.

- **What is the solubility of zirconium and silicon in bulk molybdenum?**
  A theoretical assessment of the formation energy of Zr and Si in bulk Mo would provide helpful insights for designing of Mo and Mo-based alloys. Moreover,

knowledge of solubility of Zr and Si helps to estimate the enrichment of GBs by these elements. A number of experimental studies revealed that microalloying with Zr is an efficient way to increase the room-temperature (RT) fracture toughness, strength and ductility in pure Mo and Mo-based alloys [2–4, 23, 59, 60, 62–68]. Since the solubility limit for Zr in Mo is still a matter of debate, it is unclear, if the experimentally observed results can be attributed to grain boundary (GB) or bulk effects. In contrast to Zr, Si is known to significantly increase the RT strength (and thus reduce the ductility). Si also crucially reduces the fracture toughness of Mo [1]. However, addition of Si is essential for improving the oxidation resistance of Mo-based materials. When the system is supersaturated with silicon, SiO_2 particles are formed and passivate the system [29, 32].

- **How does solute segregation at GBs influence the materials properties?**
  Ductility and fracture toughness of materials are limited by GB decohesion, which can be manipulated by solute segregation. Grain boundaries are chemically more reactive compared to the grains themselves and therefore solute segregation is often thermodynamically preferable at the GBs. Grain boundary segregation induces changes in the atomic structure and chemical bonding within the decorated GB and affects the GB energy, stability and cohesive strength. The study of Zr, Si and O segregation at GBs in molybdenum helps, in particular, to shed some light on their tendency to enhance or reduce the cohesive strength of GBs. One working hypothesis concerning the physical origin of the improved mechanical properties of the Mo-based alloys includes strengthening of the GBs due to Zr segregation at the GBs [2]. Another working hypothesis, suggested by the same authors, concerns the reduction of oxygen concentration at the GBs due to the formation of ZrO_2 (zirconia) precipitates.

- **Can zirconia improve the cohesive strength of grain boundaries in molybdenum?**
  In general, oxides and metals often form interfaces with enhanced strength compared to the individual constituent phases. The strong adhesion is also found for interfaces between Al_2O_3, ZrO_2, HfO_2 oxides and other transition metals [77–79]. Although the interface adhesive strength strongly depends on its atomic structure, an oxide/metal interface can stabilise pure metal GBs. Also, zirconium tends to capture oxygen and form ZrO_2. Zirconia precipitates of nanometre size have been found experimentally at the GBs and in the grain interior in Mo-based alloys containing Zr [2–4, 68, 80]. However, there is no data available on the structure, strength and stability of zirconia/molybdenum interfaces.

2

COMPUTATIONAL METHODS AND THERMODYNAMIC CONCEPTS

Computer modelling provides a basis for understanding the structure and properties of materials. Density functional theory (DFT) has become the most popular method for electronic-structure calculations and has found wide applications in physics, chemistry and materials science. DFT calculations allow to describe the electronic origins of bonding in solids and to predict fundamental physical properties of solids and molecules, such as cohesive energies, equilibrium crystal structures, elastic constants etc. Moreover, the increase in computational power made it possible also to provide insights into the structure and properties of solids containing point defects, thin films or grain boundaries (GBs).

In the following chapter a brief introduction of the underlying idea and basic assumptions of density functional theory and its implementation to periodic solids are given. The overview and computational setups used in this work for investigating bulk materials, surfaces, grain boundaries and interfaces are discussed. The methods for accurate evaluation of the equilibrium crystal structure are presented. A brief introduction to solute solubility in the bulk and to solute segregation at the GBs is outlined. The basic aspects of thermodynamics of planar interfaces and solute segregation are provided.

2.1 DENSITY FUNCTIONAL THEORY (DFT)

2.1.1 *Many-body problem*

Solids can be represented as a system consisting of interacting electrons and nuclei. The corresponding Hamiltonian is [81]

$$\begin{aligned}\hat{H} = -\frac{1}{2}\sum_I \frac{\nabla_I^2}{M_I} + \frac{1}{2}\sum_{I\neq J}\frac{Z_I Z_J}{|\boldsymbol{R}_I - \boldsymbol{R}_J|} - \frac{1}{2}\sum_i \nabla_i^2 \\ + \frac{1}{2}\sum_{i\neq j}\frac{1}{|\boldsymbol{r}_i - \boldsymbol{r}_j|} - \sum_{i,I}\frac{Z_I}{|\boldsymbol{r}_i - \boldsymbol{R}_I|},\end{aligned} \tag{2.1}$$

which consists of the kinetic energy of nuclei (first term), the interaction between nuclei (second term), the kinetic energy of electrons (third term), the interaction of electrons with each other (fourth term) and the interaction between electrons and nuclei (last term). Here, Eq.(2.1) is written in the atomic units and $\hbar = m_\mathrm{e} = e = \frac{1}{4\pi\varepsilon_0}$

= 1. The indices i, j are used for electrons and I, J are used for atomic nuclei. The atomic nuclei are characterised by mass M_I and the atomic number Z_I. The charge of the electrons is denoted as e. The coordinates of the atomic nuclei and electrons are given by $\boldsymbol{R}_I$ and $\boldsymbol{r}_i$, respectively.

The description of the wavefunction for larger systems becomes an infeasible problem. The Born-Oppenheimer approximation allows to reduce the complexity of the many-body Hamiltonian by separating the electronic and nuclear subsystems. Due to the large difference in mass between nuclei and electrons, the nuclei can be considered almost stationary on the time-scale of the motion of the electron [82]. The Coulomb interaction between nuclei and electrons is described as the external potential acting on electrons.

Within the Born-Oppenheimer approximation, the many-body Hamiltonian can be compactly written as

$$\hat{H} = \hat{T} + \hat{V}_{\text{ext}} + \hat{V}_{\text{int}} + E_{\text{II}}, \tag{2.2}$$

where

$$\hat{T} = -\frac{1}{2}\sum_i \nabla_i^2, \tag{2.3}$$

$$\hat{V}_{\text{ext}} = \sum_{i,I} V_{\text{ext}}(\boldsymbol{r}), \tag{2.4}$$

$$\hat{V}_{\text{int}} = \frac{1}{2}\sum_{i\neq j} \frac{1}{|\boldsymbol{r}_i - \boldsymbol{r}_j|}. \tag{2.5}$$

Here, $\hat{T}$ is the kinetic energy operator of the electrons, $V_{\text{ext}}(\boldsymbol{r})$ is the external potential, i.e., the Coulomb potential from the interactions between electrons and atomic nuclei. $\hat{V}_{\text{int}}$ is the operator of the Coulomb potential from the electron-electron interaction. The last term, E_{II}, is the interaction of nuclei with one another. E_{II} is irrelevant for the problem of describing the electrons (for electronic subsystem).

2.1.2 *Hohenberg-Kohn theory*

The theorems formulated and proved by P. Hohenberg and W. Kohn establish the theoretical basis of density functional theory. The Hohenberg-Kohn theorems can be formulated as follows [83]:

- **Theorem I:** For any system of interacting electrons in an external potential $V_{\text{ext}}(\boldsymbol{r})$, the potential $V_{\text{ext}}(\boldsymbol{r})$ is determined uniquely (up to a constant) by the ground-state electron density $n_0(\boldsymbol{r})$.
- **Theorem II:** A universal functional for the energy $E[n]$ in terms of the density $n(\boldsymbol{r})$ can be defined such that the exact ground-state energy of the system is the

global minimum value of this functional and the density $n(\boldsymbol{r})$ that minimises the functional is the exact ground-state density $n_0(\boldsymbol{r})$.

From the first Hohenberg-Kohn theorem it follows that the many-body wavefunctions for all states are determined, since the Hamiltonian $\hat{H}$ (Eq. 2.2) is fully determined [81]. From the second Hohenberg-Kohn theorem it follows that the total energy functional $E[n]$ is sufficient to define the exact ground-state density and energy. The total energy functional $E_{\mathrm{HK}}[n]$ can be written as [84]

$$E_{\mathrm{HK}}[n] = F_{\mathrm{HK}}[n] + \int d^3r V_{\mathrm{ext}}(\boldsymbol{r}) n(\boldsymbol{r}) + E_{\mathrm{II}}, \tag{2.6}$$

where

$$F_{\mathrm{HK}}[n] = T[n] + E_{\mathrm{int}}[n]. \tag{2.7}$$

Here, E_{II} is the interaction energy of the nuclei. The functional $F_{\mathrm{HK}}[n]$ is universal by construction since the electron kinetic energy $T[n]$ and the interaction energy of the electrons with each other $E_{\mathrm{int}}[n]$ are functionals only of the density and do not depend on the external potential $V_{\mathrm{ext}}(\boldsymbol{r})$ [84].

The second Hohenberg-Kohn theorem also shows that a possible solution to find the ground-state electron density is to minimise the total energy functional $E_{\mathrm{HK}}[n]$ of the system with respect to variations in the electron density $n(\boldsymbol{r})$. In order to use this variational procedure, one has to know the exact expression for the total energy functional or to provide a sufficiently accurate approximation.

2.1.3 *The Kohn-Sham equation*

W. Kohn and L.J. Sham proposed to replace the original many-body problem by an auxiliary independent-particle problem [81]. The Kohn-Sham approach reduces a complicated problem of interacting electrons in the external field to that of non-interacting electrons moving in an effective potential [84]. The basic idea of the Kohn-Sham approach is to replace the functional of the kinetic energy by the functional of a non-interacting electron system with the auxiliary wavefunctions ψ.

For the construction of the auxiliary system, Kohn and Sham assumed that the exact ground-state density can be represented by the ground-state density of an auxiliary system of non-interacting electrons [84],

$$n(\boldsymbol{r}) = \sum_i n_i(\boldsymbol{r}) = \sum_i |\psi_i(\boldsymbol{r})|^2, \tag{2.8}$$

where ψ_i are the commonly called the Kohn-Sham wavefunctions or the Kohn-Sham orbitals.

According to the Kohn-Sham approach the ground-state energy functional E_{KS} can be written as [84]

$$E_{\mathrm{KS}} = T_{\mathrm{S}}[n] + \int d^3\boldsymbol{r} V_{\mathrm{ext}}(\boldsymbol{r}) n(\boldsymbol{r}) + E_{\mathrm{Hartree}}[n] + E_{\mathrm{II}} + E_{\mathrm{xc}}[n], \tag{2.9}$$

where

$$E_{\mathrm{Hartree}}[n] = \frac{1}{2} \int d^3\boldsymbol{r} d^3\boldsymbol{r}' \frac{n(\boldsymbol{r}) n(\boldsymbol{r}')}{|\boldsymbol{r} - \boldsymbol{r}'|}, \tag{2.10}$$

and

$$T_{\mathrm{S}} = -\sum_i \int d^3\boldsymbol{r} \psi_i^*(\boldsymbol{r}) \frac{\nabla^2}{2} \psi_i(\boldsymbol{r}). \tag{2.11}$$

Here, $T[n]$ is the kinetic energy, V_{ext} is the external potential due to the nuclei or any other external field, $E_{\mathrm{Hartree}}[n]$ is the Hartree energy and it corresponds to the Coulomb energy of a charge density interacting with itself, E_{II} is the interaction energy of the nuclei and $E_{\mathrm{xc}}[n]$ is the exchange and correlation energy.

The Kohn-Sham equations are obtained by minimising the Kohn-Sham ground-state energy functional E_{KS} (Eq.2.9) with respect to individual orbitals under the constraint of mutual orthonormality of the orbitals

$$\hat{H}_{\mathrm{eff}}(\boldsymbol{r}) \psi_i(\boldsymbol{r}) = \left[-\frac{\nabla^2}{2} + V_{\mathrm{eff}}(\boldsymbol{r}) \right] \psi_i(\boldsymbol{r}) = \epsilon_i \psi_i(\boldsymbol{r}), \tag{2.12}$$

where

$$V_{\mathrm{eff}}(\boldsymbol{r}) = V_{\mathrm{ext}}(\boldsymbol{r}) + V_{\mathrm{Hartree}}(\boldsymbol{r}) + V_{\mathrm{xc}}(\boldsymbol{r}). \tag{2.13}$$

The solution ϵ_i to the Kohn-Sham equations are called Kohn-Sham eigenvalues.

The sum of the Hartree energy E_{Hartree}, interaction energy of the atomic nuclei E_{II} and the term involving the external potential V_{ext} is well defined and can be written in analytical form [81]. The kinetic energy of the Kohn-Sham particle is a functional of the Kohn-Sham orbitals and can be calculated exactly. All many-body effects, such as a spurious self-interaction of electrons, correlation of electron motion due to a depletion in the charge density around each electron and the effects due to Pauli exclusion principle are grouped into the exchange-correlation energy E_{xc} [82]. It turns out that the contribution of the exchange-correlation functional to the to total energy is rather small. Therefore relatively simple approximations such as the local density approximation (LDA), discussed in the following section, have proved tremendously powerful [85].

2.1.4 *Exchange-correlation functionals*

The idea of a local density approximation (LDA) is to replace the exchange-correlation energy $E_{\rm xc}[n]$ by the LDA functional [82]

$$E_{\rm xc}^{\rm LDA}[n] = \int d^3r\, n(\boldsymbol{r})\epsilon_{\rm xc}^{\rm hom}(n) = \int d^3r\, n(\boldsymbol{r})[\epsilon_{\rm x}^{\rm hom}(n) + \epsilon_{\rm c}^{\rm hom}(n)], \qquad (2.14)$$

where $\epsilon_{\rm xc}^{\rm hom}(n)$ is the exchange and correlation energy per particle of a homogeneous electron gas with density $n(\boldsymbol{r})$. The exchange contribution depends on the electron density as [81]

$$\epsilon_{\rm x}^{\rm hom}(n) \sim n(\boldsymbol{r})^{\frac{4}{3}}. \qquad (2.15)$$

It describes the energy gain due to the requirement of antisymmetric wave functions for fermions. The correlation energy for the homogeneous electron gas was accurately calculated by quantum Monte Carlo [86].

The exchange-correlation functional depending on n for the homogeneous electron gas is known to a high precision [84]. Despite the expectations that LDA should work well only for systems, in which the electron density varies slowly, the DFT-LDA approach has been successfully applied for electronic structure calculations even for systems considered as very inhomogeneous [82]. The LDA satisfies the charge conservation sum role and, therefore, systematic error cancellations take place. As a result, the quantities related to the differences in energies (bond length, formation energies, cohesive energies) ar e well reproduced.

The well-known drawback of LDA is the overestimation of cohesive energies [82]. This leads to shorter bond lengths, smaller lattice parameters and larger bulk moduli in solids. For further improvement on LDA the exchange-correlation functional at the point $\boldsymbol{r}$ is represented not only as the function of the electron density at the point $\boldsymbol{r}$, but also depends on the variations (gradients) of electron density close to $\boldsymbol{r}$,

$$E_{\rm xc}^{\rm GGA}[n] = \int d^3r\, n(\boldsymbol{r})\epsilon_{\rm xc}(n, \nabla n). \qquad (2.16)$$

This approximation is called the generalised gradient approximation (GGA). Among the widely used nonempirical exchange-correlation functionals are Perdew and Wang (PW91) [87] and Perdew, Burke and Enzerhof (PBE) [88]. Often GGA represents the cohesive energies more accurately and describes elastic properties of solids better compared to LDA. However, in order to perform accurate electronic structure calculations a detailed study of how different functionals reproduce the well-known properties of the system of interest is required.

2.2 DFT APPLICATION TO CRYSTALS

2.2.1 *Solving the Kohn-Sham equations*

Numerically, the Kohn-Sham equations (Eq.(2.12)–Eq.(2.13)) are solved in an iterative way until a self-consistent solution is found. At first, an initial, trial electron density $n(\boldsymbol{r})$ is defined for a given system. Next, based on the trial electron density the effective potential $V_{\text{eff}}(\boldsymbol{r})$ that includes the Hartree potential, external potential and exchange-correlation potential is computed. Afterwards, solving the Kohn-Sham equations for a given effective potential the single-particle wavefunctions $\psi_{\text{i}}(\mathbf{k})$ are obtained. The electron density is constructed based on these wavefunctions. If the initial electron density used to solve the Kohn-Sham equations is the same as the electron density constructed from wavefunctions $\psi_{\text{i}}(\mathbf{k})$, a solution is self-consistent. Thus, the ground-state electron density has been found and can be used to compute total energy. If two electron densities differ, the computational procedure has to be repeated starting from the construction of the effective potential from the new electron densities.

2.2.2 *Plane wave expansion and Brillouin zone integration*

In order to solve the independent particle Kohn-Sham equation (Eq.(2.12)–Eq.(2.13)) in periodic solids like crystals, the plane wave (PW) method is used. The Kohn-Sham orbitals $\psi_{\text{i}}(\boldsymbol{r})$ are represented by a set of basis functions (plane waves) [84]

$$\psi_{\text{i}}(\boldsymbol{r}) = \sum_{\boldsymbol{G}} c_{\text{i},\boldsymbol{G}} \exp(i[(\boldsymbol{k}+\boldsymbol{G})\cdot\boldsymbol{r}]), \tag{2.17}$$

where the $\boldsymbol{G}$ vectors are reciprocal lattice vectors.

In practice, the infinite sum is truncated to include only plane waves with wavevector length smaller than a particular G_{max}

$$E_{\text{cutoff}} = \frac{\hbar^2}{2m_{\text{e}}} G_{\text{max}}^2, \tag{2.18}$$

and

$$|\mathbf{k}+\mathbf{G}|^2 \leq G_{\text{max}}^2. \tag{2.19}$$

Here, E_{cutoff} is called the kinetic energy cutoff and it defines the accuracy of the calculations.

The expansion coefficients of the corresponding wavefunctions are determined by solving the Kohn-Sham equation, the matrix form of which can be written as

$$\begin{pmatrix} \frac{(k+G_0)^2}{2} + V_{\text{eff}}(0) & V_{\text{eff}}(G_0 - G_1) & \cdots & V_{\text{eff}}(G_0 - G_N) \\ V_{\text{eff}}(G_1 - G_0) & \frac{(k+G_1)^2}{2} + V_{\text{eff}}(0) & \cdots & V_{\text{eff}}(G_1 - G_N) \\ \cdots & \cdots & \cdots & \cdots \\ V_{\text{eff}}(G_N - G_0) & V_{\text{eff}}(G_N - G_1) & \cdots & \frac{(k+G_N)^2}{2} + V_{\text{eff}}(0) \end{pmatrix} \begin{pmatrix} c_0 \\ c_1 \\ \vdots \\ c_N \end{pmatrix} = \epsilon \begin{pmatrix} c_0 \\ c_1 \\ \vdots \\ c_N \end{pmatrix}. \tag{2.20}$$

Plane waves are one of the possible basis functions, most suitable for structures with periodic boundary conditions like crystals. In practice, the calculations are performed on a grid of points in the first Brillouin zone (BZ) called k-points. For example, a commonly used k-point mesh in VASP is a Monkhorst-Pack grid [89]. Since the Kohn-Sham equations are solved for a given number of k-points in the BZ, the intrinsic properties of a solid, such as the total energy, the electron density, etc., are computed by a summation of all k-points over the first BZ. For example, the electron density $n(\boldsymbol{r})$ is thus obtained as

$$n(\boldsymbol{r}) \sim \sum_{\boldsymbol{k}} n_{\boldsymbol{k}}(\boldsymbol{r}). \tag{2.21}$$

2.2.3 *Pseudopotentials*

Computational difficulties in solving the Kohn-Sham equations arise near the atomic nucleus. In this region, the divergence of the Coulomb potential for electron-ion interaction results in an oscillatory behaviour of the wavefunctions. For an accurate numerical representation of the electron density in this region, an enormous number of plane waves would be required resulting in a high numerical load of the DFT calculation. This is why the pseudopotential approach has been introduced. The concept of pseudopotentials is to replace valence electrons and ion cores with pseudo valence electrons and pseudo ion cores [84]. The pseudopotential describing their interaction is designed such that outside the selected core radius it exactly reproduces the original Coulomb potential, while inside a core region the pseudopotential is quite weak. The implementation of pseudopotentials results in a smooth electron wavefunction close to the atomic nucleus, avoiding rapid oscillations, whereas the wavefunctions outside the selected core radius are reproduced exactly. The pseudopotential approach does not give information about the charge density near the nucleus. However, in most cases, core electrons are not important in defining chemical bonding and other physical properties of materials [81].

Current DFT codes provide a library with different preudopotentials for most of the elements in the periodic table. In the present study the projector-augmented waves

(PAW) [90] method is used. The PAW approach transforms the rapidly oscillating wavefunctions into smooth wavefunctions and provides a way to reconstruct the full electron density from these smooth wavefunctions.

2.2.4 *Description of forces*

A description of forces within the DFT framework is required for finding the equilibrium atomic positions and lattice geometries. Forces acting on the nuclei can be determined as derivatives of the energy with respect to the position of a nucleus $\boldsymbol{F}_I$ [81],

$$\boldsymbol{F}_I = -\frac{\partial E}{\partial \boldsymbol{R}_I}. \tag{2.22}$$

The Hellmann-Feynman theorem [91] allows to calculate the forces directly from the ground-state wavefunctions,

$$\boldsymbol{F}_I = -\frac{\partial E}{\partial \boldsymbol{R}_I} = - < \psi | \frac{\partial \hat{H}}{\partial \boldsymbol{R}_I} | \psi > . \tag{2.23}$$

For structure optimization within DFT an initial atomic structure has to be provided. For a given structure, as discussed in Section 2.2.1, the effective potential $V_{\text{eff}}(\boldsymbol{r})$ is constructed. Afterwards, the Kohn-Sham equations are solved in a self-consistent way until the electronic convergence is reached. The forces are computed using the Hellmann-Feynman theorem and the atomic positions are modified. This ionic relaxation loop is repeated until the forces are converged within a given accuracy. The VASP code allows to optimise atomic positions, cell volume and cell shape independently.

2.3 ELASTIC PROPERTIES

2.3.1 *Birch-Murnaghan equation of state*

The bulk modulus is a property of the material that determines the relative volume change, $\Delta V/V$, for a given hydrostatic pressure [7]. As discussed in Section 2.1.4, the exchange-correlation functional is not exact and includes a number of approximations. This is why, it is necessary to evaluate the well-known properties of the material such as the equilibrium lattice parameters, cell volume and the bulk modulus B_0 for a chosen exchange-correlation functional.

In order to obtain the equilibrium bulk structure, the total energy is minimised with respect to the unit cell volume. First, the unit cell of the solid has to be uniformly deformed (compressed and expanded). Second, the obtained variation of the total energy for a given unit cell volume $E(V)$ is fitted to the third order Birch-Murnaghan equation of state [92–94]

$$E(V) = E_0 + \frac{9V_0B_0}{16}\left(\left[\left(\frac{V_0}{V}\right)^{\frac{2}{3}} - 1\right]^3 B_0' + \left[\left(\frac{V_0}{V}\right)^{\frac{2}{3}} - 1\right]^2 \left[6 - 4\left(\frac{V_0}{V}\right)^{\frac{2}{3}}\right]\right), \tag{2.24}$$

where V_0 is the equilibrium volume of the unit cell and E_0 is the ground-state energy.

The equilibrium bulk modulus B_0 of a crystal is defined as

$$B_0 = -V\left(\frac{\partial P}{\partial V}\right)_{\mathrm{T}}, \tag{2.25}$$

and its pressure derivative at constant temperature

$$B_0' = \left(\frac{\partial B_0}{\partial P}\right)_{\mathrm{T}}. \tag{2.26}$$

In the following sections the equilibrium lattice parameters and bulk modulus are evaluated for all bulk phases used in the present study, namely bcc Mo, Mo_2Zr, Mo_3Si and tetragonal ZrO_2. The Mo_2Zr and Mo_3Si phases are used as reservoirs for Zr and Si, respectively (details are given in Section 3.1). The formation of ZrO_2 at molybdenum grains is discussed in Chapter 6.

2.3.1.1 *Molybdenum*

Molybdenum is a refractory metal possessing a body-centred cubic (bcc) crystal structure with two atoms located at (0,0,0) and $(\frac{1}{2},\frac{1}{2},\frac{1}{2})$ positions in the unit cell. Figure 6 shows the variation of the total energy (E_{tot}) of Mo as a function of the cell

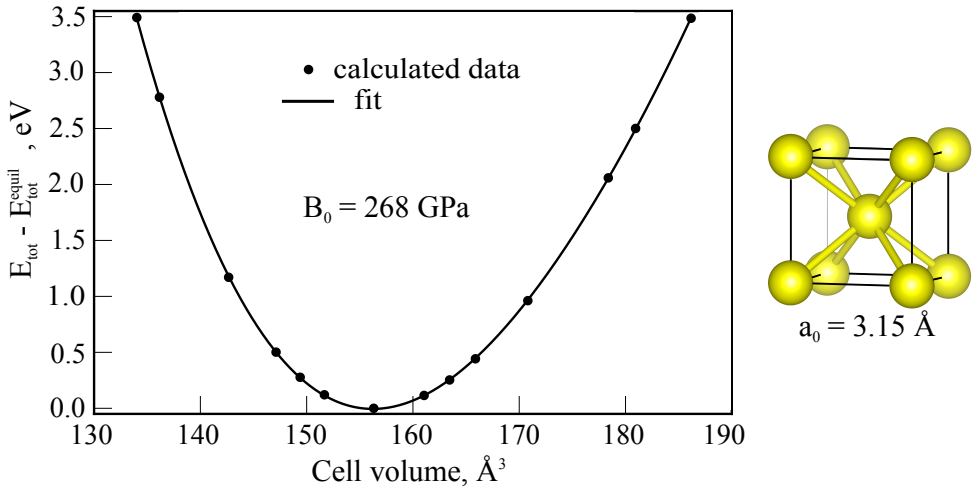

Figure 6: Variation of the total energy of bulk molybdenum with respect to the unit cell volume. Calculated data points are fitted to the Birch-Murnaghan equation of state (Eq.(2.24)). The computed bulk modulus, B_0, of Mo is equal to 268 GPa. The atomic structure of molybdenum is shown on the right-hand side.

volume. It is obtained by stepwise increasing the volume of Mo cell up to ± 5 % with a step of ± 0.5 % and fitting the corresponding energy variation to the Birch-Murnaghan equation of state (Eq.(2.24)) [92–94]. The minimum total energy of Mo ($E_{\text{tot}}^{\text{equil}}$) is computed at the lattice constant, a_0, of 3.15 Å. The bulk modulus, B_0, extracted as the second derivative of the energy-variation curve [100],

$$B(V_0) = V\left(\frac{\partial^2 E_{\text{tot}}}{\partial V^2}\right)\Bigg|_{V=V_0}, \tag{2.27}$$

Table 4: Comparison of the calculated lattice constants, a_0, and the bulk modulus, B_0, of molybdenum with other computational and experimental studies.

	Method	a_0, Å	B_0, GPa
Featherston [95]	Experiment	3.147	265
Bolef [96]	Experiment	3.147	269
Che [97]	LDA	3.160	280
Zhang [98]	2NN MEAM	3.147	265
Tahir [99]	GGA	3.153	258
Present study	GGA-PBE	3.150	268

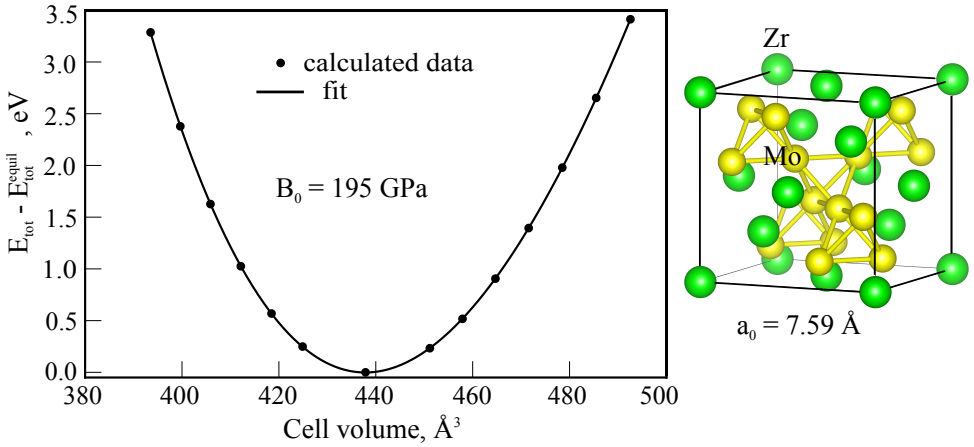

Figure 7: Variation of the total energy of Mo_2Zr for series of fixed volumes. Calculated data points are fitted to the Birch-Murnaghan equation of state (Eq.(2.24)). The computed bulk modulus, B_0, of Mo_2Zr is equal to 195 GPa. The atomic structure of Mo_2Zr is shown on the right-hand side. Yellow spheres represent molybdenum atoms and green spheres represent zirconium atoms.

is equal to 268 GPa.

Table 4 compares the calculated a_0 and B_0 with other experimental and theoretical studies and shows that both parameters are in very good agreement with values available in literature.

2.3.1.2 *Mo_2Zr*

The atomic structure of the Mo_2Zr compound is shown on the right-hand side of Figure 7. The binary intermetallic phase Mo_2Zr has a cubic crystal structure called the Laves C15 structure (space group $Fd\bar{3}m$). The conventional unit cell of Mo_2Zr contains sixteen Mo atoms and eight Zr atoms forming eight formula units of Mo_2Zr per unit cell. The crystal structure of this compound can be represented as two interpenetrating sublattices, created by Mo atoms and by Zr atoms. Zirconium atoms create sublattice of the diamond type and molybdenum atoms form tetrahedra which share one Mo atom with a neighbouring tetrahedron [101]. Each Mo atom is surrounded by six Mo atoms separated by 2.68 Å and by six Zr atoms separated by 3.15 Å. Each Zr atom has twelve Mo neighbours on a distance of 3.15 Å and four Zr neighbours on a distance of 3.29 Å.

Figure 7 shows the change in the total energy (E_{tot}) of Mo_2Zr for different unit cell volumes. Calculated total-energy variation is fitted to the Birch-Murnaghan equation of state (Eq.(2.24)) [92–94]. The equilibrium lattice constant of Mo_2Zr that corresponds to a minimum of the energy variation curve is 7.59 Å, which is in good

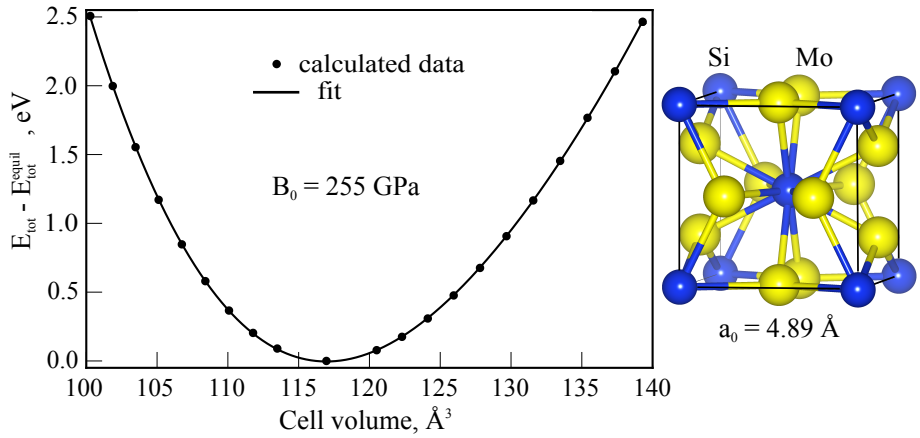

Figure 8: Variation of the total energy of Mo_3Si for series of fixed volumes. Calculated total energy variation is fitted to the Birch-Murnaghan equation of state (Eq.(2.24)). The computed bulk modulus, B_0, of Mo_3Si is equal to 255 GPa. The atomic structure of Mo_3Si is shown on the right-hand side. Yellow spheres represent molybdenum atoms and blue spheres represent silicon atoms.

agreement with experimentally found values of 7.588 Å [102] and 7.596 Å [103]. The bulk modulus of Mo_2Zr is equal to 195 GPa. Experimental or other theoretical values of B_0 are not reported.

2.3.1.3 *Mo_3Si*

The atomic structure of the intermetallic Mo_3Si phase is shown on the right-hand side of Figure 8. It is the cubic A15 structure ($Pm3n$ space group) with Si atoms occupying the bcc positions ((0,0,0) and $(\frac{1}{2},\frac{1}{2},\frac{1}{2})$) and the Mo atoms located on the faces of the unit cell and forming three mutually perpendicular chains in the <100>, <010> and <001> directions [104]. The conventional unit cell of Mo_3Si contains six molybdenum atoms and two silicon atoms, forming three formula units of Mo_3Si per cell. The bond length between two adjacent molybdenum atoms is 2.45 Å and 2.99 Å, whereas the bond length between molybdenum and silicon atoms is 2.73 Å.

Figure 8 illustrates the variation of the total energy (E_{tot}) of Mo_3Si for different volumes of Mo_3Si unit cell. Calculated total-energy variation is fitted to the Birch-Murnaghan equation of state (Eq.(2.24)) [92–94]. The equilibrium lattice constant of Mo_3Si is 4.89 Å and the calculated bulk modulus is 255 GPa. The lattice constant of Mo_3Si found in other experimental and theoretical studies almost does not deviate and is equal to 4.890–4.897 [104–106]. The values of the bulk modulus B_0 found in the literature varies in the range from 239 GPa till 256 GPa [105–108].

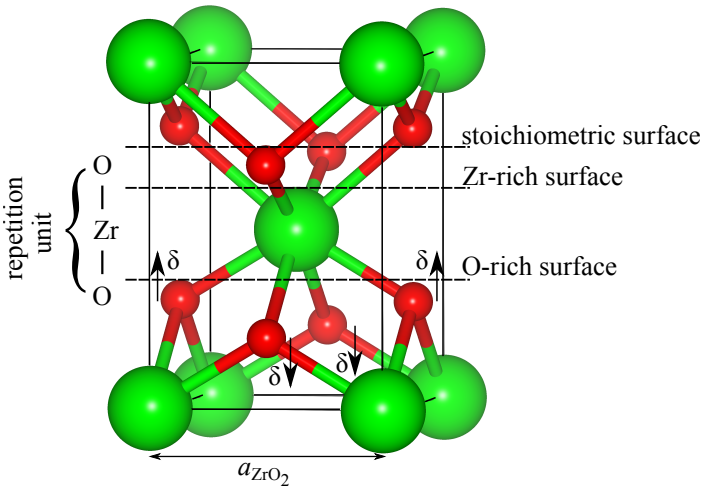

Figure 9: The atomic structure of tetragonal zirconia (t-ZrO_2). The arrows indicate the displacement of the oxygen pairs along the [001] axis from the plane located in between two Zr planes by an amount δ. Red spheres represent oxygen atoms and green spheres represent zirconium atoms. Black dashed lines correspond to the cleavage planes required to create a stoichiometric, Zr-rich and O-rich (001) zirconia surfaces.

2.3.1.4 *Tetragonal zirconia*

Zirconia (ZrO_2) exhibits three structural polymorphs depending on temperature and pressure. At ambient pressure, the low-temperature phase, m-ZrO_2, has monoclinic crystal structure. At around 1170 °C m-ZrO_2 undergoes a crystallographic transformation to a tetragonal phase ($P4_2/nmc$), t-ZrO_2, and at around 2370 °C tetragonal zirconia transforms into the cubic fluorite structure, c-ZrO_2, which is stable up to the melting temperature of zirconia [109, 110].

Mo-based alloys with addition of Zr are fabricated via a powder metallurgy (PM) process [2, 4]. The most stable ZrO_2 polymorph at the characteristic synthesis conditions (T = 1500 °C–1980 °C, 1 atm) is tetragonal [110]. Atomic structure of tetragonal zirconia is shown on Figure 9. It is described by three structural parameters: the size of the unit cell in x and z directions (a and c, respectively) and an internal parameter δ. Here, δ describes the displacement of oxygen pairs along the [001] direction from the plane located in between two Zr planes. In tetragonal zirconia each zirconium atom is surrounded by eight oxygen atoms, four at a distance of 2.11 Å in a flattened tetrahedron and four at 2.38 Å in an elongated tetrahedron which is rotated 90° relative to the former one [110]. Each oxygen atom has two oxygen neighbours

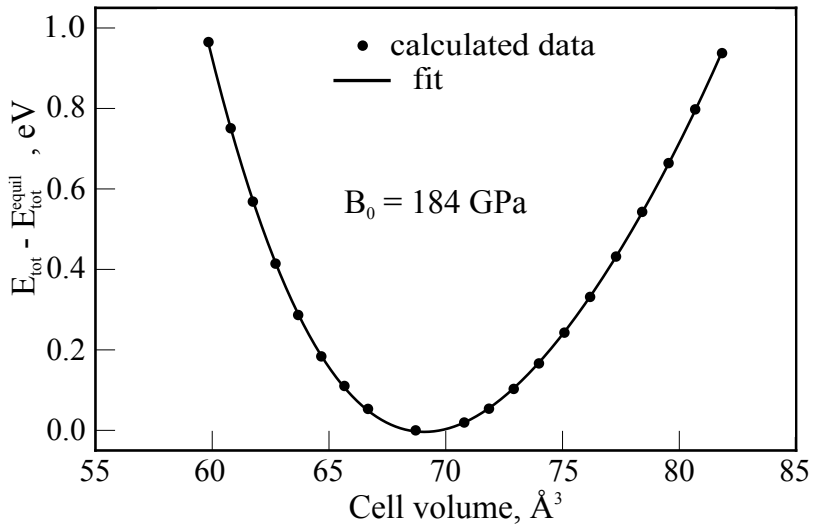

Figure 10: Variation of the total energy of tetragonal zirconia for series of fixed volumes (keeping the *a*/*c* ratio fixed). The calculated total-energy variation is fitted to the Birch-Murnaghan equation of state (Eq.(2.24)). The computed bulk modulus, B_0, of ZrO_2 is equal to 184 GPa. The atomic structure of tetragonal zirconia is shown on Figure 9.

at 2.61 Å and four at 2.60 Å, and is bonded to two zirconium atoms at 2.11 Å and two more Zr at 2.38 Å distance.

The equilibrium lattice constants of t-ZrO_2 are obtained by fitting the calculated total energies (E_{tot}) to the Birch-Murnaghan equation of state (Eq.(2.24)) [92–94]. Figure 10 illustrates the total-energy variation as a function of the volume of the zirconia cell keeping the *a*/*c* ratio fixed. The minimum total energy of zirconia is obtained at the lattice parameters equal to a = 3.626 Å, c = 5.225 Å and the relative displacement of oxygen pairs δ = 0.045.

Table 5 lists the lattice parameters of tetragonal zirconia and the displacement of the opposite pairs of oxygen atoms, δ, that have been found in other experimental and computational studies. Lattice constants obtained in a present study using GGA-PBE potential are reproduced in a good agreement with other studies.

The bulk modulus, B_0, calculated using the Birch-Murnaghan equation of state (Eq.(2.24)), with a fixed *c*/*a* ratio is also given in Table 5. However, for tetragonal systems the *c*/*a* ratio generally changes with volume, which is related to differences in compressibility along the *a* and *c* directions. A more accurate description of the bulk modulus of tetragonal zirconia is based on defining the elastic constants of the system.

Table 5: Comparison of the calculated lattice parameters (a, c and δ) and bulk modulus B_0 of tetragonal zirconia with other computational and experimental studies.

	Method	a, Å	c, Å	δ	B_0
Aldebert [111]	Experiment	3.57	5.18	0.057	190
Terki [112]	FP-LAPW	3.61	5.25	0.047	226
Fabris [113]	SC-TB	3.55	5.12	0.047	190
Cohen [114]	PIB model	3.64	5.27	0.065	173
Stapper [115]	LDA	3.59	5.15	0.042	197
Milman [116]	LDA	3.57	5.13	0.044	212
Jaffe [117]	GGA	3.63	5.21	0.040	199
Natanzon [118]	GGA	3.61	5.20	-	210
Present study	GGA-PBE	3.63	5.23	0.045	184

2.3.2 *Elastic constants*

The elastic constants, C_{ijkl}, describe the anisotropic response of a crystal to a mechanical stress. They are computed based on variation of the total energies under small strains that are applied to the equilibrium cells. The strain tensor applied to the crystal is of the form

$$\varepsilon = \begin{pmatrix} 1+e_{11} & \frac{1}{2}e_{12} & \frac{1}{2}e_{13} \\ \frac{1}{2}e_{21} & 1+e_{22} & \frac{1}{2}e_{23} \\ \frac{1}{2}e_{31} & \frac{1}{2}e_{32} & 1+e_{33} \end{pmatrix}. \tag{2.28}$$

The Taylor expansion of the total energy of the crystal is

$$E(\varepsilon) = E(0) + \sum_{ij} \left.\frac{\partial E}{\partial \varepsilon_{ij}}\right|_0 \varepsilon_{ij} + \frac{1}{2}\sum_{ijkl} \left.\frac{\partial^2 E}{\partial \varepsilon_{ij}\partial \varepsilon_{kl}}\right|_0 \varepsilon_{ij}\varepsilon_{kl} + O(\varepsilon^3). \tag{2.29}$$

In equilibrium, the first derivative of energy in Eq.(2.29) is zero and the elastic constants are [100]

$$C_{ijkl} = \frac{1}{V}\frac{\partial^2 E}{\partial \varepsilon_{ij}\partial \varepsilon_{kl}}. \tag{2.30}$$

The bulk modulus for polycrystalline material can be estimated in terms of single-crystal elastic stiffness constants [119]. The most reasonable value of B_0 is evaluated as

$$B_0^{VR} = \frac{1}{2}(B_0^{Voigt} + B_0^{Reuss}), \tag{2.31}$$

Table 6: Comparison of the elastic constants and the bulk modulus of tetragonal zirconia with other studies.

	Method	C_{11}	C_{12}	C_{13}	C_{33}	C_{44}	C_{66}	B_0^{VR}
Kisi [121]	Experiment	327	100	62	264	59	64	151
Cohen [114]	PIB model	465	83	49	326	101	156	176
Milman [116]	LDA	401	245	90	345	49	174	212
Natanzon [118]	GGA	293	248	111	385	51	187	212
Present study	GGA-PBE	368	227	65	296	27	167	187

where the Voigt average of the bulk modulus for tetragonal system is defined as

$$B_0^{\text{Voigt}} = \frac{1}{9}[2(C_{11} + C_{12}) + C_{33} + 4C_{13}], \tag{2.32}$$

and the Reuss average of the bulk modulus for tetragonal system is [120]

$$B_0^{\text{Reuss}} = \frac{C_{33}(C_{11} + C_{12}) - 2C_{13}^2}{C_{11} + C_{12} + 2C_{33} - 4C_{13}}. \tag{2.33}$$

In a tetragonal lattice symmetry, there are six independent elastic constants (C_{11}, C_{12}, C_{13}, C_{33}, C_{44} and C_{66}). Table 6 lists the calculated elastic constants and the bulk modulus B_0^{VR} of tetragonal ZrO_2. The bulk modulus calculated using Eq.(2.31) and the one computed using the Birch-Murnaghan equation of state are very similar and exhibit 184 GPa and 187 GPa, respectively. The values of the C_{ij} constants found in the literature vary significantly and the best agreement is found with study of Milman *et al.* [116], although the values of all elastic constants are smaller in the present work. The value of the bulk modulus of t-ZrO_2, available in the literature, varies in the range from 151 GPa till 226 GPa [112, 121] (see Table 5 and Table 6). The B_0^{VR} computed in this work lies in the middle of this range.

2.4 COMPUTATIONAL SETUP

In this work the solute (Zr, Si) solubility in the bulk molybdenum and the segregation of Zr, Si and oxygen at the Mo grain boundaries (GBs) is investigated. Because of the periodic boundary conditions and computational demands of electronic-structure calculations, GBs constructed from a coincidence site lattice (CSL) with small Σ value are considered. Namely, a tilt $\Sigma5(310)[001]$ and a twist $\Sigma5[001]$ GBs in bicrystal geometries are chosen as structural models and represented in a 3D periodic and a slab supercell, respectively (for details, see Section 4.1.1). Oxidation of Zr and formation of ZrO_2/Mo interfaces is considered in Chapter 6. In order to evaluate the stability of Mo grain boundaries and zirconia/molybdenum interfaces against brittle fracture, the work required to separate the interfaces into two surfaces is evaluated. For this purpose, Mo(001), Mo(310) and t-ZrO_2(001) surfaces are constructed in slab supercells.

In the present section the computational parameters are summarised. The methods for accurate evaluation of the charge distribution between atoms in crystals are presented.

2.4.1 *Computational parameters*

All calculations in this thesis are performed using the plane-wave projector-augmented wave [90] density functional theory [83, 122] code VASP [123, 124].

The generalised gradient approximation (GGA) in the parametrisation by Perdew, Burke and Ernzerhof (PBE) [88] is chosen to mimic exchange-correlation interactions. Molybdenum and oxygen are represented by six valence electrons, zirconium and silicon by four valence electrons. We have carefully converged our results with respect to the energy cutoff and k-point mesh. For all investigated models an energy cutoff of 450 eV is used. The k-point mesh is generated using Monkhorst-Pack scheme [89]. Table 7 lists the k-points grid used for all investigated models. The convergence of different parameters of interest with a given accuracy is considered for each model. For example, a convergence of the surface energy of Mo(001), $\sigma_{\mathrm{Mo(001)}}$, to ±0.02 J/m^2 is achieved for a $14\times14\times1$ Monkhorst-Pack scheme (see Table 20).

For the non-stoichiometric surfaces of t-ZrO_2 spin-polarised calculations are performed. Structure optimisations are performed keeping the cell parameters fixed until the maximum force acting on individual atoms is less than 10–50 meV Å^{-2}. For bulk references, the same k-point sampling density is used, corresponding to a reciprocal space sampling of the Mo GB or of the t-ZrO_2/Mo interface.

Table 7: The k-point mesh generated using Monkhorst-Pack scheme [89] for all investigated models. The grid ensures a convergence of different parameters with provided accuracy level, namely the surface energy (σ), the solute formation energy (E_f) and the interface energy ($\gamma_{A/B}$).

Model	Supercell	k-points mesh	Convergence parameter	Accuracy
(1×1) Mo(001)	Slab	14×14×1	$\sigma_{Mo(001)}$	±0.02 J/m^2
(1×1) t-ZrO_2(001)	Slab	12×12×1	$\sigma_{t\text{-}ZrO_2(001)}$	±0.02 J/m^2
Twist Σ5[001] GB	3D periodic	7×7×1	E_f	±0.02 eV
Tilt Σ5(310)[001] GB	Slab	2×6×8	E_f	±0.02 eV
t-ZrO_2(001)/Mo(001)	Slab	7×7×1	$\gamma_{ZrO_2/Mo}$	±0.02 J/m^2

2.4.2 *Bader charge analysis*

The Bader analysis [125] is a computational tool that allows to quantify the charge distribution between atoms in crystals or molecules. A Bader volume is associated with each atom and represents a volume which is surrounded by a surface on which the charge density reaches a minimum in the direction perpendicular to the surface [125]. The charge located within the Bader volume is associated with a particular atom and corresponds to a total electronic charge of this atom. In the present study the Bader charge analysis algorithm developed by Henkelman *et al.* [126–128] is used. The analysis is based on the core and valence electron densities computed using VASP. The Bader charges are extremely sensitive to a charge density grid. Therefore, it is necessary to choose the charge density grid which accurately represents the total number of core and valence electrons in the system. This convergence study has to be done for every investigated system separately.

2.4.3 *Supercell method*

The atomic arrangement in perfect crystals is periodic and can be described by a unit cell repeated periodically. The electronic structure of crystalline solids are computed using the 3D periodic simulation cells. In order to investigate properties of more complicated structures like surfaces, which are periodic only in two dimensions, a vacuum region is introduced into the simulation cell. A supercell for surface modelling is schematically illustrated on Figure 11. The supercell contains a region of bulk material called a slab, which is separated by vacuum region. Each slab in the supercell is terminated by two surfaces of the desired stoichiometry. The slab has to be thick

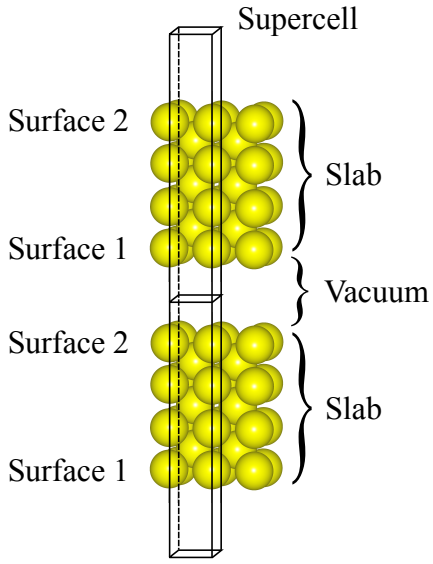

Figure 11: Illustration of the supercell approach for surface modelling.

enough to ensure the bulk behaviour of atoms at the center of the slab. The vacuum layer also has to be thick enough (10–20 Å on each side) to prevent any interactions between adjacent periodic images of the surfaces. The form and the size of the supercell depend on the physical system being studied.

2.4.4 *Long-range electron density oscillations*

Similar to surface modelling discussed in Section 2.4.3, grain boundary and interface models are also represented in supercells, although the addition of vacuum in the supercell is optional. If the vacuum is introduced, the slab supercell, in addition to two surfaces terminating the slab, also contains one GB or one interface. If the vacuum is not added in a computational cell, the supercell is periodic in three dimensions and, therefore, contains two GBs or interfaces separated by a bulk region. The optimisation of the cell volume only in one direction is not implemented in VASP and, this is why, for periodic supercell the cell length perpendicular to the GB or interface plane has to be adjusted manually following the procedure described in Section 2.3.1. This requires much higher computational load. This problem vanishes for the slab supercell. Because of the vacuum, the GB or interface separation can contract or expand without influencing the cell size in total. However, for the slab supercell the oscillations of the charge density introduced by a surface have to be considered.

In Section 4.2 the driving force for Zr and Si segregation from Mo bulk to grain boundaries is quantified. The formation energies show an oscillatory behaviour, which

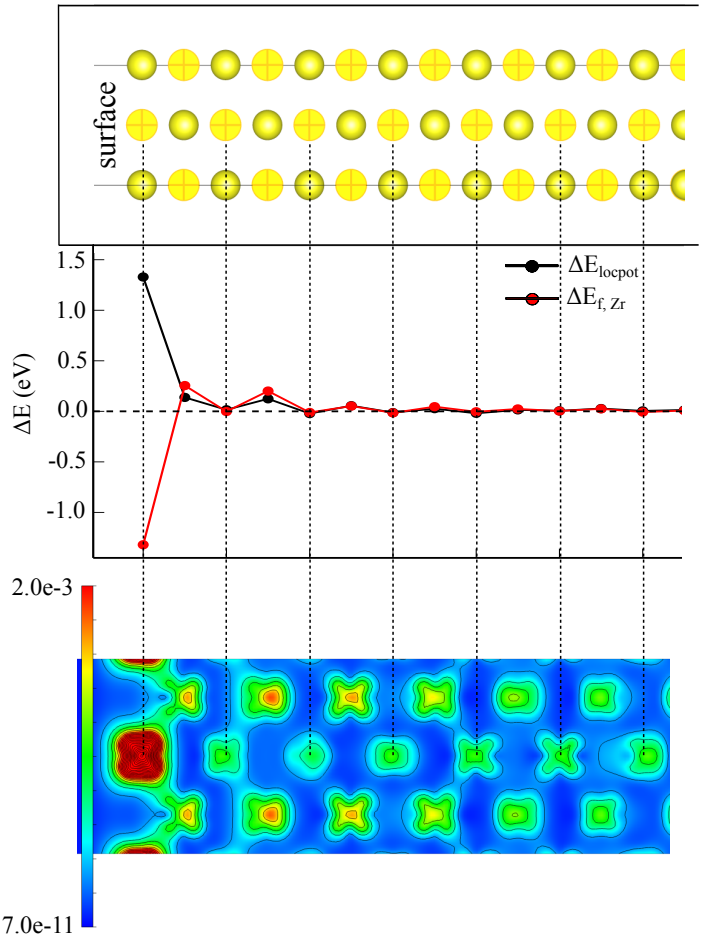

Figure 12: (Top) Atomic structure of the bulk-truncated molybdenum surface having the same geometry as one of the twist Σ5[001] grains. Yellow spheres represent molybdenum atoms, while highlighted atoms represent atoms that have been substituted by Zr while moving from the surface to the bulk. (Middle) Changes in the formation energy of Zr in the bulk-truncated Mo surface slab and in the local electrostatic potential of the corresponding pure surface relative to the bulk values. (Bottom) Oscillations in the electron density penetrating into bulk and having an enhancement on certain atomic positions (surface resonance).

is particularly pronounced for the slab supercells (see Figure 30(a)). The presence of the surfaces significantly affects the local electronic configuration. In the vicinity of a defect, e.g. surface, the electrons in the metal will be rearranged in order to minimise the disturbance caused by this defect. At a metal surface, the screening of the surface results in oscillations in the charge density propagating into the bulk perpendicular to the surface [129, 130]. These oscillations are called Friedel oscillations and show a low-range character [131, 132]. Using first-principles calculations, the Friedel oscillations normal to the low Miller-index surfaces of bcc Na [133] and fcc Al [134] were investigated. This investigation reveals that the surface orientation and the local atomic structure at the surface have considerable influence on the Friedel oscillations.

The oscillatory behaviour of the formation energy of Zr in the surface slab is correlated with the Friedel oscillations caused by the presence of the surface. In particular, the difference in the local electrostatic potential of a bulk-truncated surface and in the bulk for a pure molybdenum system is computed,

$$\Delta E_{\text{locpot}} = E^{\text{surf}}_{\text{locpot}} - E^{\text{bulk}}_{\text{locpot}}, \tag{2.34}$$

and compared with the variation of the formation energy,

$$\Delta E_{\text{f}}(\text{Zr}) = E^{\text{surf}}_{\text{f}}(\text{Zr}) - E^{\text{bulk}}_{\text{f}}(\text{Zr}). \tag{2.35}$$

In Eq.(2.34), the value of the electrostatic potential in the centre of the bulk-truncated surface slab is taken as the bulk value.

Figure 12 (middle) shows the change in the local electrostatic potential in the bulk-truncated Mo(001) surface calculated using Eq.(2.34). The E_{locpot} corresponds to the value of the local electrostatic potential at the same atomic position for which the value of formation energy E_{f} was calculated. Here, E_{locpot} is a line profile, not averaged within the plane. The change in the electrostatic potential shows the same behaviour as the change in the formation energy of Zr, showing oscillatory character and approaching a bulk value approximately in the middle of the slab. In other words, changes in the local electrostatic potential due to the presence of the surface causes the oscillatory behaviour of the Zr formation energy. Figure 12 (top) shows the atomic structure of the pure bulk-truncated Mo(001) surface having the same geometry as one of the grains in twist $\Sigma 5$ GBs. Highlighted atoms represent sites where Zr has been inserted. Figure 12 (bottom) shows a partial electron density that corresponds to a surface state penetrating into a bulk and showing enhancement only on the certain atomic positions. These positions are identical to the sites, where the peaks in formation energy appear. The surface plane goes through highlighted positions of Mo atoms. The red regions correspond to the accumulation of electron density, while the blue regions represent the electron density depletion.

The choice of the slab or periodic supercell depends on the system that is studied. In the case of the slab supercell, the slab has to be thick enough to ensure the decay

of the Friedel oscillations from both surfaces approximately in the middle of the corresponding slab. In the case of periodic supercell, the Friedel oscillations are less pronounced and, therefore, smaller slabs can be constructed. Periodic supercell, however, require an additional computational load due to the optimisation procedure.

2.5 SOLUTES IN THE BULK

Solid solutions form, when solute atoms are incorporated into a lattice of a crystalline material in a particular concentration range [7]. The maximum amount of solute that can be dissolved in the host lattice is called the solid solubility. Beyond this amount, a supersaturation of the solid solution occurs resulting in the formation of the secondary phase particles called precipitates [14]. Depending on the site that solutes occupy in the host lattice, interstitial and substitutional solid solutions can be distinguished.

In the dilute limit, the solid solubility c at a given temperature T can be calculated according to [7]

$$c = c_0 \exp\left(- \frac{\Delta G_\mathrm{f}}{k_\mathrm{B} T} \right) = \exp\left(- \frac{\Delta E_\mathrm{f} + p\Delta V_\mathrm{f} - T\Delta S_\mathrm{f}}{k_\mathrm{B} T} \right), \tag{2.36}$$

where c_0 is the concentration of available positions for the solute in the lattice, ΔG_f is the Gibbs free energy of solute formation, ΔE_f is the formation energy and ΔS_f is the formation entropy of a solute. Here, k_B is the Boltzmann constant. The solute concentration in thermodynamic equilibrium is mainly determined by the solute formation enthalpy ΔH_f and the entropy term can be typically neglected [7]. The solute formation enthalpy is defined as

$$\Delta H_\mathrm{f} = \Delta E_\mathrm{f} + p\Delta V_\mathrm{f}, \tag{2.37}$$

where ΔV_f is the formation volume of a solute and p is pressure.

Furthermore, for low pressure the formation enthalpy ΔH_f and the formation energy ΔE_f are virtually equal [135] and thus Eq.(2.36) is further reduced to

$$c = c_0 \exp\left(- \frac{\Delta E_\mathrm{f}}{k_\mathrm{B} T} \right). \tag{2.38}$$

DFT calculations are limited to relatively small systems containing up to 250–300 atoms, which leads of finite-size effects caused by image interactions. In order to correct for finite-size effects, the solute formation energy is calculated for various supercells containing different number of atoms and extrapolated to energies relating to an infinite crystal [136]. In detail, this procedure is described in Chapter 3.

The tendency of two metals to form a substitutional solid solution depends on the variety of physical and chemical properties, summarised in a set of empirical rules known as the Hume-Rothery solubility rules [137]. Two metals are likely to have a high solubility if both metals have

1. an identical crystal structure and differ in atomic sizes not more than 15%;
2. similar electronegativity and the same number of valence electrons.

Similarity in atomic size between solute and solvent atoms is associated with the elastic distortion produced in a host lattice. The elastic energy increases the free energy of the solid solution decreasing its stability relative to other phases [7]. With increasing difference in electronegativity, the polarity of the bond increases resulting in an enhanced tendency to form of an intermetallic compound [11]. The presence of the intermetallic compound limits the solubility.

A theoretical assessment of solid solubility is useful for understanding grain boundary segregation in polycrystalline materials. Qualitatively, the GB segregation tendency is inverse to the solid solubility. Enrichment of solutes at the GB may differ considerably relative to the bulk concentrations. For example, few layers of solute atoms can be formed at the GB without formation of secondary phase particles [14]. Using bulk solid solubility it is possible to predict the value of segregation enthalpy for the corresponding element at the GB [138].

The formation energy of a solute in the bulk, ΔE_{f}, can be divided into elastic strain (misfit) and electronic (chemical bonding) contributions [11]. For a solute occupying a substitutional site, a strain energy is stored in the form of broken and stretched/compressed host-host bonds due to the atomic relaxations [139]. The chemical bonding contribution to the formation energy describes the bonding strength between the solute and the host atoms. By means of the DFT calculations strain and chemical bonding contributions to the solute formation energy can be evaluated. The procedure has been proposed by Finnis *et al.* [139] and is used later in the present work for Zr and Si segregation in the Mo bulk as well as at the GBs. The analysis provides information required to explain the origin of different solubility limits of various solutes.

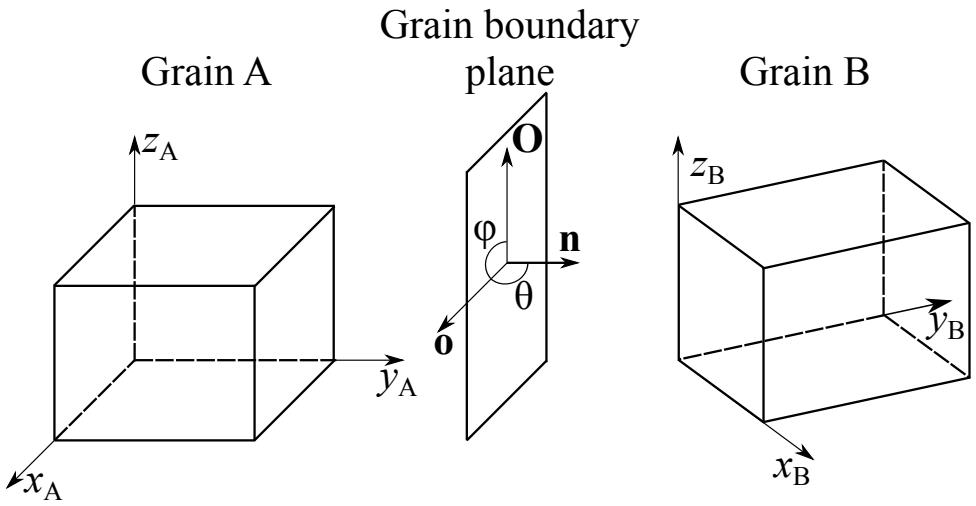

Figure 13: Macroscopic characterisation of a grain boundary. The coordinate axes in grain A (x_A, y_A and z_A) and in grain B (x_B, y_B and z_B) are parallel to the main crystallographic directions ([100], [010] and [001]) in the grains. The normal of the grain boundary plane is marked as **n**. The grain boundary plane can be changed by rotation either about the **O** axis by angle θ or about the **o** axis by angle φ.

2.6 FUNDAMENTALS OF GRAIN BOUNDARIES AND SOLUTE SEGREGATION

2.6.1 *Grain boundary geometries*

A grain boundary (GB) is characterised by five macroscopic degrees of freedom (DOFs) [5, 6, 11, 140]. Three DOFs describe the misorientation between two grains and the other two DOFs define the orientation of the grain boundary plane with respect to one of the grains [140, 141]. Figure 13 details geometric variables that characterise a planar grain boundary. The coordinate axes in grain A (x_A, y_A and z_A) and in grain B (x_B, y_B and z_B) are chosen parallel to the main crystallographic directions ([100], [010] and [001]) in the grains.

In order to transform grain B in the position identical to the position of grain A, rotations about x, y and z axis (three Euler angles) are required. The grain boundary plane with a normal **n** pointing towards one of the crystallographic axis (in Figure 13, **n** is parallel to y_A), could be changed by rotation either about the **O** axis by angle θ or about the **o** axis by angle φ. Hence, to specify the orientation of the GB plane two angles are required. In addition to the macroscopic parameters, there are three microscopic parameters. These parameters describe translations of the grains parallel and perpendicular to the GB plane [11, 12, 142].

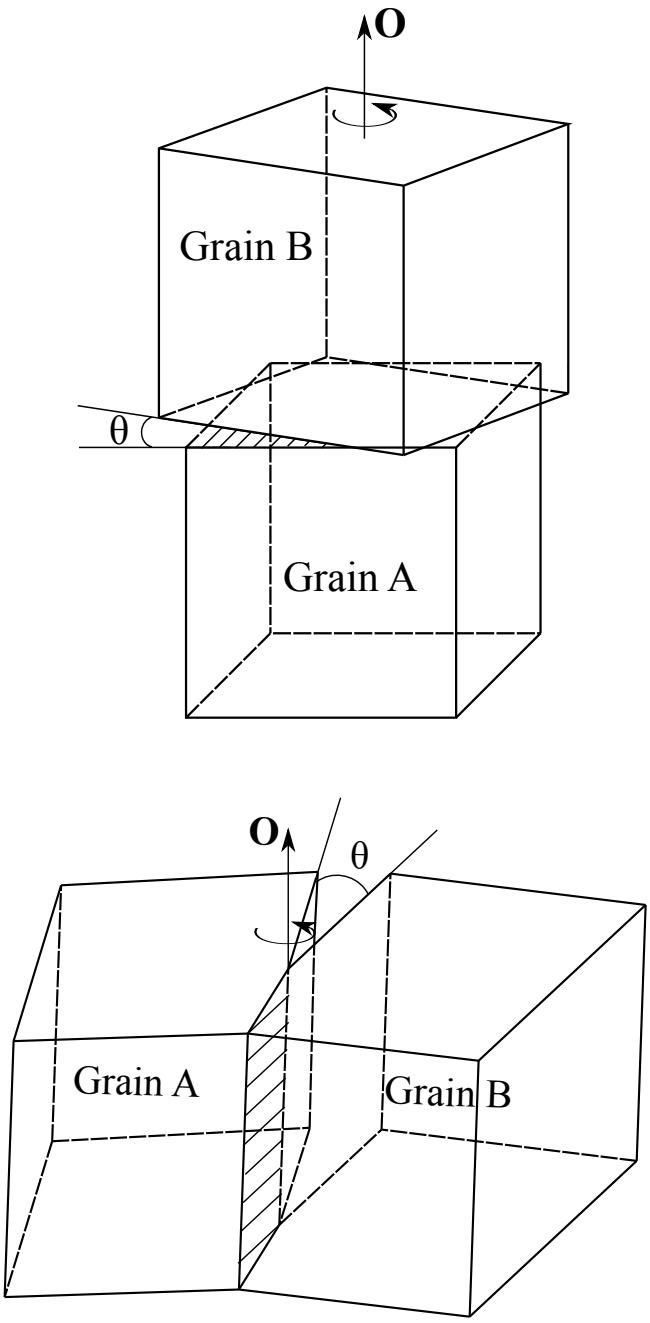

Figure 14: Schematic illustration of twist and tilt grain boundaries. (Top) Twist GB characterised by a rotation of grain B about an axis **o** perpendicular to the grain boundary plane by angle θ. (Bottom) Tilt GB constructed by a rotation of grain B about an axis **o** parallel to the grain boundary plane by angle θ. Equivalently, both grains could be rotated by $\theta/2$ in opposite directions.

Based on the relationship between the rotation axis and the grain boundary plane, tilt and twist GBs can be distinguished [12, 14, 143, 144]. Figure 14 illustrates how tilt and twist grain boundaries are constructed. Rotation of grain B about an axis **O** parallel to the grain boundary normal by an angle θ is required to form a twist GB. A tilt GB is formed when grain B is rotated about an axis **O** perpendicular to the grain boundary normal by an angle θ. For the twist GB, the grain boundary plane is independent of the rotation angle, whereas for the tilt GB the rotation angle determines the grain boundary plane. When the GB plane represents the plane of the mirror symmetry of the crystal lattices of two grains ($\{h_1k_1l_1\} = \{h_2k_2l_2\}$), this boundary is called symmetric [14]. The other grain boundaries are asymmetric. Grain boundaries with a random grain boundary plane and with no special orientation relationship between a rotation axis and a grain boundary plane (also a GB might partially have a tilt/twist character) are called general GBs [11].

Depending on the misorientation angle between two neighbouring grains, grain boundaries are divided into low-angle ($\theta \leq 15°$) and high-angle ($\theta \geq 15°$) GBs [7, 11, 12, 143]. The low-angle grain boundaries can be described as an array of dislocations, separated by patches of strained single crystal [5, 6]. The energy of the corresponding GB can be estimated from the energy and density of dislocations forming a GB. In order to correlate structure, energy and properties of the high-angle grain boundaries, a more complicated description of GBs has to be involved. For example, in the structural unit model [144, 145], a structure of a GB is represented as combinations of basic structural elements (different polyhedra) and the GB energy is estimated from the energy of these structural elements.

Grain boundaries tend to minimise their free energy, and this is usually accomplished by maximising atomic matching (i.e., minimising the number of broken bonds) at the GB [140]. This is why general high-angle grain boundaries exhibit high grain boundary energy relative to the low-angle GBs [14]. However, another type of high-angle but low-energy grain boundaries can be developed during material fabrication. Particular misorientation angles result in the coincidence of the lattice points from each neighbouring grain producing GBs with low excess volume and lower grain boundary energy compared to general high-angle GBs [6, 12]. These grain boundaries are called special GBs. Special GBs show advantages over general grain boundaries such as lower diffusivity, lower susceptibility to solute segregation, greater resistance to GB sliding and fracture, etc. [6, 14].

2.6.2 *Coincidence-site lattice (CSL) model*

The coincidence-site lattice (CSL) model was proposed in 1949 by Kronberg and Wilson and is used to describe the geometry of grain boundaries [146]. A particular

rotation of one grain relative to another grain results in a three-dimensional atomic pattern in which a certain fraction of lattice points coincide in both grains [6]. These lattice points are called coincidence sites. The coincidence sites constitute a periodic lattice called the coincidence site lattice [7, 147]. The CSL is characterised by a parameter Σ, which represents a reciprocal density of the coincidence sites relative to the crystal lattice sites [11, 14]

$$\Sigma = \frac{\text{number of coincidence sites in a primitive CSL unit cell}}{\text{number of all lattice sites in a primitive CSL unit cell}}, \tag{2.39a}$$

or equivalently [7, 140],

$$\Sigma = \frac{\text{volume of a primitive CSL unit cell}}{\text{volume of a crystal unit cell}}. \tag{2.39b}$$

For a cubic system, all possible values of Σ can be found using the Ranganathan [148] equations. For a rotation axis perpendicular to a given plane with the Miller indices (hkl) and any pair of non-negative integer numbers x and y, representing the coordinates of a coincidence site in the lattice (see Figure 15), Σ can be defined as

$$\Sigma = \begin{cases} n, & \text{if } n \text{ is odd} \\ \dfrac{1}{2}n, & \text{if } n \text{ is even,} \end{cases} \tag{2.40}$$

where

$$n = x^2 + Ny^2, \tag{2.41a}$$

and

$$N = h^2 + k^2 + l^2. \tag{2.41b}$$

When n is even, an additional coincidence site is always present in the centre of the CSL (see Figure 15(b)) and a $\frac{1}{2}$ coefficient is required in order to define a correct value of Σ [149].

A rotation angle θ required to form a particular CSL can be found according to [140]

$$\theta = 2\tan^{-1}\left(\frac{y}{x}\right)\sqrt{N}, \tag{2.42}$$

For example, for a cubic lattice rotated about a [001] axis, $N = 1^2 + 0^2 + 0^2 = 1$ (the rotation axis is normal to the plane with the Miller indices $h = 1$, $k = 0$, $l = 0$). Assuming $x = 3$ and $y = 1$, a CSL is formed with Σ which equals

$$\Sigma = \tfrac{1}{2}(3^2 + 1\cdot 1^2) = 5,$$

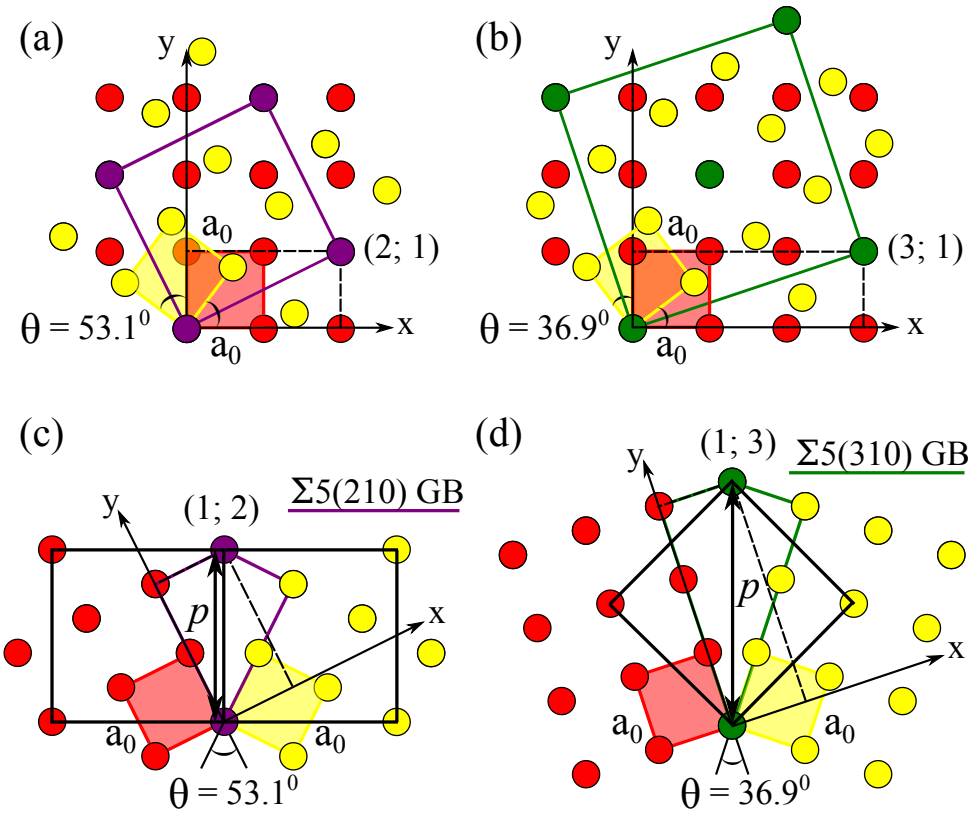

Figure 15: Special high-angle symmetric (a, b) twist Σ5[001], (c) tilt Σ5(210)[001] and (d) tilt Σ5(310)[001] GBs constructed by a rotation of two conventional cubic cells about a [001] axis (perpendicular to the plane of the figure) by an angle (a, c) $\theta = 53.1°$ and (b, d) $\theta = 36.9°$. The GBs are projected along a [001] axis. Coincidence sites are marked by violet and green circles. (a, b) A CSL cell formed by coincidence sites is outlined by solid violet and green lines. The coordinates of the coincidence sites in terms of the lattice constant of a conventional cubic cell a_0 are noted in parentheses. The GB plane is a (001) plane and is parallel to the plane of the figure. (c, d) The GB plane corresponds to a (210) plane and a (310) plane, respectively, and are perpendicular to the plane of the figure. The distances between two coincidence sites in the GB (or structural periodicity, p) equal to the (c) side and (d) diagonal of the primitive CSL cell and are shown by two-headed arrows.

and the rotation angle required to construct this CSL equals

$$\theta = 2\ \tan^{-1}\left(\tfrac{1}{3}\right)\sqrt{1} = 36.9°.$$

However, the same values of Σ can be generated for another combination of x and y, namely if $x = 2$ and $y = 1$ and the same rotation axis. In this case,

$$\Sigma = (2^2 + 1{\cdot}1^2) = 5,$$

and

$$\theta = 2\ \tan^{-1}\left(\tfrac{1}{2}\right)\sqrt{1} = 53.1°.$$

Figure 15(a, b) shows special high-angle twist Σ5[001] grain boundaries constructed from a coincidence site lattice. The GB is projected along a [001] axis (rotation axis) and the GB plane is parallel to the plane of the figure. The misorientation angle between two grains equals 53.1° (Figure 15(a)) and 36.9° (Figure 15(b)). Both rotations result in the same dichromatic pattern due to the four-fold symmetry of a cubic lattice. However, a CSL produced by a 36.9° rotation has also a coincidence point in the centre of a CSL and therefore the unit cell of a CSL outlined by solid green lines can be reduced to a primitive CSL unit cell outlined by solid violet lines.

In contrast to a twist GB, a tilt Σ5[001] grain boundary constructed considering either 36.9° or 53.1° rotation about an [001] axis are not equivalent, see Figure 15(c, d). The former rotation results in the grain boundary plane with the Miller indices (310), whereas considering the latter rotation a (210) grain boundary plane is formed. In order to distinguish between GBs with the same value of Σ but different GB planes, the notation of tilt GBs includes also the Miller indices of the GB plane [140]. In the case of the asymmetric tilt GB, the Miller indices of both grain boundaries have to be noted. The grain boundary plane is perpendicular to the plane of the figure. The distance between coincidence sites in the grain boundary can be calculated using the Ranganathan coordinates [148] according to

$$p = \sqrt{x^2 + y^2}\ \mathrm{a}_0, \tag{2.43}$$

where a_0 is the lattice constant of a conventional cubic cell and p is the structural periodicity. For the tilt Σ5(310)[001] GBs the structural periodicity p equals

$$p = \sqrt{1^2 + 3^2}\ a_0 = \sqrt{10}\ a_0,$$

and corresponds to a diagonal of the primitive CSL cell. In Figure 15(d) the CSL is outlined by solid black lines. The structural periodicity p is shown by a two-headed arrow. Therefore, the lateral dimensions of the tilt Σ5(310)[001] GB correspond to p and a_0.

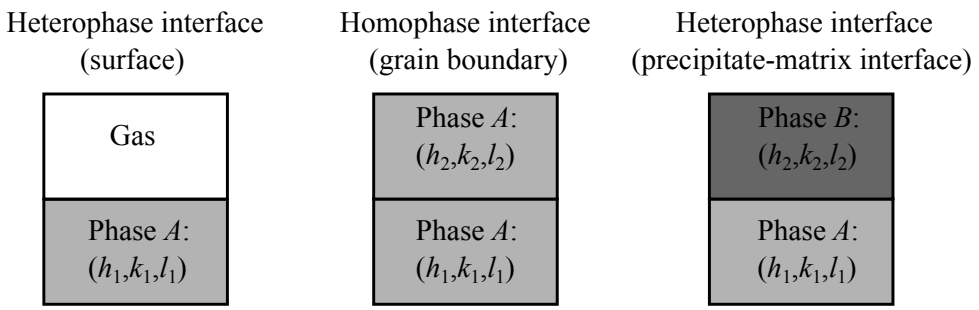

Figure 16: Schematic representation of homophase and heterophase interfaces.

Special GBs are almost exclusively associated with low-Σ CSL relationship ($\Sigma \leq 29$) [145]. However, there is no direct relationship between the value of Σ and specific properties (e.g. energy, solute segregation, fracture stress) of the grain boundaries [11, 14, 150, 151]. The CSL concept is based only on the geometric construction and is not sufficient to predict GB properties [140]. For example, the CSL concept does not account for atomic relaxations, the number of broken bonds at the GB, the energy of the surfaces creating a grain boundary.

In real crystals, a small deviation from the exact rotation relationship results in a drastic change in the long-range coincidence [7, 14]. However, similar to low-angle GBs, where small deviations from the perfect single crystal are accommodated by arrays of dislocations, the bicrystal yields a network of intrinsic GB dislocations which conserve the periodicity of the CSL [7, 140]. The range of existence of low-Σ CSL relationship despite small deviations from the perfect coincidence is defined as [145]

$$\Delta\theta \leq \theta_0 \, \Sigma^{-n}, \tag{2.44}$$

with $\theta_0 = 15°$.

The value of n varies in different studies, however, the most consistent with the experimental observations criterion is $n = \frac{5}{6}$ [152]. Although $\theta_0 = 15°$ is generally used as the largest angle for which the dislocation model can be applied [143, 144], the proper choice of θ_0 depends on the specific property which is investigated [153]. For example, θ_0 can be increased up to 28° when the GB diffusivity is considered [154].

2.6.3 *Thermodynamics of planar defects*

Different interfaces that crystalline solids can form are schematically illustrated on Figure 16. A surface is an example of a solid-gas interface. A surface separates the crystalline phase A and a gas phase. Grain boundary and precipitate-matrix interfaces are examples of solid-solid interfaces. The grain boundary divides two grains of the

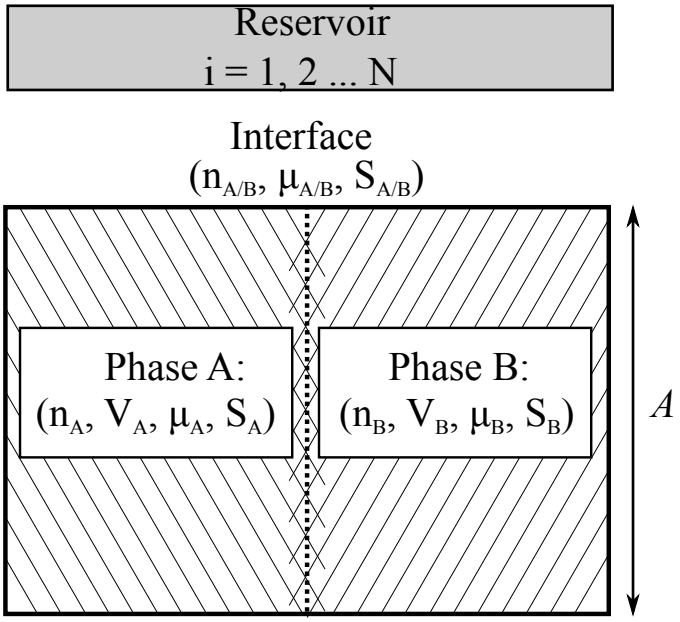

Figure 17: Schematic representation of an interface in equilibrium with an environmental reservoir.

same phase, A, but having different crystallographic orientations. Therefore, GBs are classified as homophase interfaces. In contrast, the surface and the precipitate-matrix interface separate different phases, A and B, and therefore belong to heterophase interfaces.

Homophase and heterophase interfaces belong to the planar interfaces and are described conceptually in the same way. Figure 17 shows a system that consists of two phases, A and B, divided by an interface. Properties of each phase are homogeneous up to the interface. According to Gibbs [155], the interface is considered as dividing plane and,therefore, $V_{\mathrm{A/B}} = 0$. Extensive thermodynamic quantities describing the system can be expressed as a sum of the corresponding quantities for both bulk phases and the interface. For example, the internal energy of the system, U, consists of the internal energies of phase A, phase B and the interface [156]

$$U = U_{\mathrm{A}} + U_{\mathrm{B}} + U_{\mathrm{A/B}}. \tag{2.45}$$

The change of the internal energy of the system in equilibrium (thus, $\mu_{\mathrm{A}} = \mu_{\mathrm{B}} = \mu_{\mathrm{A/B}}$) under constant temperature (T), pressure (P) can be expressed as [157]

$$\mathrm{d}U = T\mathrm{d}S - P\mathrm{d}V + \gamma_{\mathrm{A/B}}\mathrm{d}A + \sum_{i=1}^{N} \mu^{\mathrm{i}}\mathrm{d}n^{\mathrm{i}}, \tag{2.46}$$

where

$$\mathrm{d}S = \mathrm{d}S_{\mathrm{A}} + \mathrm{d}S_{\mathrm{B}} + \mathrm{d}S_{\mathrm{A/B}}, \tag{2.47}$$

$$\mathrm{d}V = \mathrm{d}V_{\mathrm{A}} + \mathrm{d}V_{\mathrm{B}}, \tag{2.48}$$

$$\mathrm{d}n^{\mathrm{i}} = \mathrm{d}n^{\mathrm{i}}_{\mathrm{A}} + \mathrm{d}n^{\mathrm{i}}_{\mathrm{B}} + \mathrm{d}n^{\mathrm{i}}_{\mathrm{A/B}}. \tag{2.49}$$

Here, S is the entropy of the system, V is its volume, $\gamma_{\mathrm{A/B}}$ is the interface energy defined per unit area of the interface, A is the interface area and n^{i} is the number of moles of the component i (i = 1 ... N).

The change in the Gibbs free energy ($G = U + PV - TS$) equals [156]

$$\begin{aligned} \mathrm{d}G = \mathrm{d}U + P\mathrm{d}V + V\mathrm{d}P - T\mathrm{d}S + S\mathrm{d}T = \\ -S\mathrm{d}T + V\mathrm{d}P + \gamma_{\mathrm{A/B}}\mathrm{d}A + \sum_{i=1}^{N} \mu^{\mathrm{i}}\mathrm{d}n^{\mathrm{i}}. \end{aligned} \tag{2.50}$$

The interface energy, $\gamma_{\mathrm{A/B}}$, is defined as a change of the Gibbs free energy of the closed system under constant temperature and pressure [14]

$$\gamma_{\mathrm{A/B}} = \left(\frac{\partial G}{\partial A}\right)_{T,P,n_{\mathrm{i}}}. \tag{2.51}$$

The interface energy, $\gamma_{\mathrm{A/B}}$, describes the work that has to be done in order to bring the species from both bulk phases A and B in contact to create a new interface having an area of 1 m^2.

For electronic-structure calculations within DFT, the interface energy is determined neglecting vibrational contribution to the Gibbs free energy and the entropy of the system [158]. Under these approximations, the Gibbs free energy of the system G is replaced by the total energy of the supercell containing an interface, $E^{\mathrm{supercell}}_{\mathrm{A/B}}$, such that

$$\gamma_{\mathrm{A/B}} = \frac{1}{A}\left(E^{\mathrm{supercell}}_{\mathrm{A/B}} - \sum_{i} N^{\mathrm{i}}\mu^{\mathrm{i}}\right). \tag{2.52}$$

Here, N^{i} is the number of atoms of type i in the supercell and μ^{i} is the chemical potential of the corresponding species.

2.6.4 *Thermodynamics of segregation*

Segregation is the phenomenon by which a material becomes locally enriched by solutes (alloying additives or impurities) at a grain boundary, surface or other interfaces in the form of a solid solution [11]. Supersaturation of the solute-containing grain boundary results in the formation of secondary phase particles called precipitates. Grain boundary precipitation is a continuation of the GB segregation process.

Generally, the formation energy of solutes at grain boundaries is lower compared to those in the bulk. As a consequence, the concentration of solutes at the GBs is higher compared to those in the bulk crystal. The redistribution of solutes is also observed in the vicinity of other planar (surface, phase boundary, stacking fault), linear (dislocation) and point defects (vacancy) in a crystal [159]. Grain boundary segregation can be classified as equilibrium and non-equilibrium [159]. The driving force for equilibrium segregation is to lower the Gibbs free energy of the system [11]. Non-equilibrium segregation occurs during a rapid cooling of the material [141], after which solutes are kinetically trapped. The equilibrium concentration of vacancies is reduced with decreasing temperature. During a rapid cooling over a large temperature range, excess vacancies flow towards the grain boundaries and surfaces which can act as vacancy sinks [160]. Vacancy-solute pairs are also carried to GBs and in this way, the grain boundaries are decorated with solutes.

Qualitatively, equilibrium segregation is described in the same way for all types of interfaces [14]. Dependence of the interface energy on chemical potentials of the components at the interface is described by the Gibbs-Duhem equation [157]

$$S_{\mathrm{A/B}}\mathrm{d}T + \sum_{i=1}^{N} n^{\mathrm{i}}_{\mathrm{A/B}}\mathrm{d}\mu^{\mathrm{i}}_{\mathrm{A/B}} + A\mathrm{d}\gamma_{\mathrm{A/B}} = 0, \tag{2.53}$$

where $S_{\mathrm{A/B}}$ is the interface entropy, $n^{\mathrm{i}}_{\mathrm{A/B}}$ and $\mu^{\mathrm{i}}_{\mathrm{A/B}}$ are the number of moles and the chemical potential of the component i, respectively, and A is the interface area.

At a constant temperature, Eq.(2.53) is transformed into

$$\mathrm{d}\gamma_{\mathrm{A/B}} = -\sum_{i=1}^{N} \Gamma_{\mathrm{i}}\mathrm{d}\mu^{\mathrm{i}}_{\mathrm{A/B}}, \tag{2.54a}$$

where Γ_{i} is the excess of species i, adsorbed at the interface per unit area of an interphase

$$\Gamma_{\mathrm{i}} = \frac{n^{\mathrm{i}}_{\mathrm{A/B}}}{A}. \tag{2.54b}$$

This equation is called the Gibbs adsorption isotherm and it is used for the thermodynamic description of the interface segregation [14, 157]. The equation provides a relation between adsorption Γ_{i}, on one side, and the change of the interfacial energy $\gamma_{\mathrm{A/B}}$ and the chemical potential of the components at the interface, on another side. The Gibbs adsorption isotherm has been used, for example, to determine experimentally the amount of phosphorus segregated at interfaces in α-iron [161]. In the present work the change of the interface energy for different solutes (Zr, Si, O and their combinations) segregated at the twist and tilt $\Sigma 5$ GBs in Mo is shown in Section 4.3.

2.7 THEORETICAL AND ATOMISTIC ASPECTS OF FRACTURE

Fracture is the separation or fragmentation of a solid body into two or more parts under applied stress [6, 162]. Depending on the material response to the applied stress, namely the amount of plastic deformation that occurs at the tip of the crack. Fracture can be classified as brittle or ductile [10, 163, 164]. Brittle fracture is accompanied by no or little plastic deformation and is mainly controlled by cohesive forces between atoms [165]. During brittle fracture a crack propagates very rapidly, as soon as the magnitude of the applied stress reaches its critical value [6, 164]. No increase in the applied stress is required for further crack propagation. In contrast to brittle fracture, ductile fracture is accompanied by extensive plastic deformation in the vicinity of the crack tip [10]. The work for plastic deformation is considerably higher compared to the work required to break cohesive forces between atoms in order to create new crack surfaces [165, 166]. Therefore a ductile fracture demands higher energy to be absorbed before fracture. Moreover, the magnitude of the applied stress has to be increased in order to extend a crack [10].

Depending on the fracture path, fracture in a polycrystalline material can be classified as a transgranular or an intergranular [6, 163, 166]. In transgranular fracture a crack propagates through the grains. For most brittle crystalline materials a transgranular fracture takes place by the separation of atomic bonds along certain crystallographic planes that are characteristic of the crystal structure [10, 163, 164, 166]. This failure mechanism is called cleavage. For example, in body-centred cubic metals, like molybdenum, $\{001\}$ planes are the common cleavage planes [54, 163, 167, 168]. When grain boundaries in the material are weak or embrittled by impurities, a crack will propagate along grain boundaries. This fracture is called an intergranular fracture. In polycrystalline form, molybdenum is considered as “intrinsically brittle”, i.e. the brittleness originates from the bonding strength at the grain boundary [55].

Depending on the fracture path, fracture of an interface can be classified as adhesive and cohesive [164]. In the case of adhesive failure, an interface between materials A and B fails exactly along an interface creating a pure surface of material A and a pure surface of material B. In the case of a cohesive failure, a thin layer of material B (or A) remains on the pure surface of material A (or B). The cohesive fracture appears when the bonds along the interface are sufficiently strong.

Depending on the orientation of the applied stress and the crack, three loading modes can be distinguished. They are marked with Roman numerals from I till III. The loading mode I is called the tensile mode and is characterised by the stress which is perpendicular to the crack surfaces [6, 163]. Tensile stresses are the only stresses that open the crack and separate the surfaces [50]. In modes II and III, the crack surfaces are loaded in shear, representing sliding and tearing modes [6, 50]. In contrast to mode I, in modes II and III the energy received by a system containing a crack is

partially dissipated due to friction of the crack surfaces. Therefore a crack propagates at lower applied stress under loading in mode I [50]. Mode I is the predominant mode in many practical cases [163].

Fracture includes damage accumulation, crack nucleation and crack propagation (also called crack extension or crack growth) [169]. Damage accumulation is associated with the properties of a material, such as its atomic structure, crystal lattice and grain boundaries [6]. Crack nucleation is related to microscopic flaws, microcracks, notches etc. which can be found in a typical solid. These centres of heterogeneity amplify the applied stress and act as stress concentrators (stress razors) [163, 169, 170]. The magnitude of stress amplification depends on the orientation and geometry of a flaw relative to the applied stress [10]. A crack will propagate when a critical stress is achieved in a system, and can be estimated using a Griffith criterion for fracture [169]. The Griffith criterion defines whether for the applied stress and a given geometry of a crack, a crack is stable (stationary) and does not propagate or a crack is unstable and will propagate causing a failure of the body [50].

2.7.1 *Fracture stress*

A critical stress which leads to crack propagation for a crack of initial length $2a$ is called a fracture stress. The fracture stress σ_{F} is equal to [10, 164, 166, 169]

$$\sigma_{\mathrm{F}} = \begin{cases} \sqrt{\dfrac{2\gamma_{\mathrm{s}}E}{\pi a(1-\nu^2)}}, & \text{for plain strain condition} \\ \sqrt{\dfrac{2\gamma_{\mathrm{s}}E}{\pi a}}, & \text{for plain stress condition.} \end{cases} \tag{2.55}$$

Here, γ_{s} is a specific surface energy defined per unit of surface area, E is Young's modulus and ν is a Poisson's ratio. If the magnitude of the applied stress at the tip of one of the flaws is smaller than the fracture stress, $\sigma < \sigma_{\mathrm{F}}$, the crack is stationary and does not extend. If the magnitude of the applied stress exceeds the fracture stress, $\sigma > \sigma_{\mathrm{F}}$, a crack will rapidly propagate which results in fracture.

According to Griffith [171], a criterion for crack propagation can be defined considering an energy balance in the system. Figure 18 shows an infinite plate of elastic material containing a very sharp crack of length $2a$ in the centre of the plate. A plate has a thickness t and is located in a homogeneous tensile stress field σ. When a crack is introduced to a plate, the change in the energy associated with the crack formation (ΔU) can be split into the following contributions [166, 169]

$$\Delta U = \Delta U_{\mathrm{el}} + W + U_{\mathrm{surf}}, \tag{2.56}$$

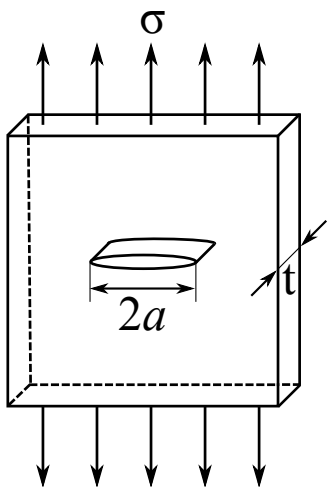

Figure 18: Infinite plate of elastic material containing a very sharp crack of length $2a$ in the centre of the plate. A plate has a thickness t and is loaded with a homogeneous tensile stress field σ.

where ΔU_{el} is the change of the elastic strain energy stored in the plate, W is the external work performed on the system, for example by movement of the loading point [50], and U_{surf} is the surface energy.

For a system, as depicted in Figure 18, the amount of surface energy can be estimated from a total surface area of the crack ($2{\cdot}2a \cdot t$) and a specific surface energy (γ_{s}) defined per unit of surface area [164]

$$U_{\mathrm{surf}} = 2 \cdot 2a \cdot t \cdot \gamma_{\mathrm{s}}. \tag{2.57}$$

The change in the stored elastic strain energy due to the presence of an elliptical crack in the infinite plate can be estimated from the elastic energy per unit volume stored in a solid under stress ($\sigma^2/2E'$) and the volume of the material in which this energy is released ($\pi(2a)a \cdot t$) [6, 50, 172]

$$\Delta U_{\mathrm{el}} = -\frac{\sigma^2}{2E'} \cdot (\pi(2a)a \cdot t) = -\frac{\pi a^2 \sigma^2 t}{E'}, \tag{2.58}$$

where E' corresponds to Young's modulus E for the case of plane stress ("thin" plate) and $E/(1 - \nu^2)$ for the case of plane strain ("thick" plate). The minus sign shows that the elastic strain energy is decreased when a crack is introduced in to a system.

Using Eq. 2.57 and Eq. 2.58, the change in potential energy of the plate associated with the introduction of a crack (Eq. 2.56) can be written as [164]

$$\Delta U = U - U_0 = (2a \cdot 2 \cdot t)\gamma_{\mathrm{s}} - \frac{\pi \sigma^2 a^2 t}{E'}, \tag{2.59}$$

where U_0 is the potential energy of the system without a crack. In the case of an infinite plate, the external work done by movement of the loading point vanishes ($W = 0$) since the size of the crack is negligible compared to the size of the system [50]. Elastic strain-energy contribution decreases the total energy of the system and therefore favours a crack propagation. The surface energy increases the total energy of the system and therefore opposes the crack growth.

When a crack propagates by a length da, the surface energy and the stored elastic strain energy change by [50, 164]

$$\mathrm{d}U_{\mathrm{surf}} = 4\gamma_{\mathrm{s}} t \mathrm{d}a, \tag{2.60}$$

and

$$\mathrm{d}U_{\mathrm{el}} = -\frac{\pi\sigma^2 \cdot 2a \cdot t}{E'}\mathrm{d}a. \tag{2.61}$$

The crack propagates when the released strain energy due to crack extension is sufficient to create two new surfaces with specific surface energies γ_{s}. A criterion predicting the fracture behaviour of a body can be written as [164, 166, 169]

$$\frac{\mathrm{d}U}{\mathrm{d}a} = \frac{\mathrm{d}U_{\mathrm{surf}}}{\mathrm{d}a} + \frac{\mathrm{d}U_{\mathrm{el}}}{\mathrm{d}a} = 0, \tag{2.62}$$

which is known as Griffith equilibrium condition for crack propagation.

Combining Eq. 2.62 with Eq. 2.60 and Eq. 2.61, we receive

$$4t\gamma_{\mathrm{s}} - \frac{\pi\sigma^2 2at}{E'} = 0, \tag{2.63}$$

$$\pi\left(\frac{\sigma^2 a}{E'}\right) = 2\gamma_{\mathrm{s}}. \tag{2.64}$$

The Griffith energy balance equation which determines condition for crack propagation is valid for ideally brittle materials. When crack propagation is accompanied by plastic deformation at the crack tip, the fracture stress is modified by the sum of the specific surface energy, γ_{s}, and work for plastic deformation [166].

2.7.2 *Modelling of brittle fracture*

Fracture can be treated from the viewpoint of stress or energy. For an ideally brittle material the driving force for crack propagation is equal to the total energy that is released during cracking per unit increase in crack size [166]. The released energy Γ is called the fracture energy and it is given by

$$\Gamma = 2\gamma_{\mathrm{s}} - \gamma_{\mathrm{gb}}. \tag{2.65}$$

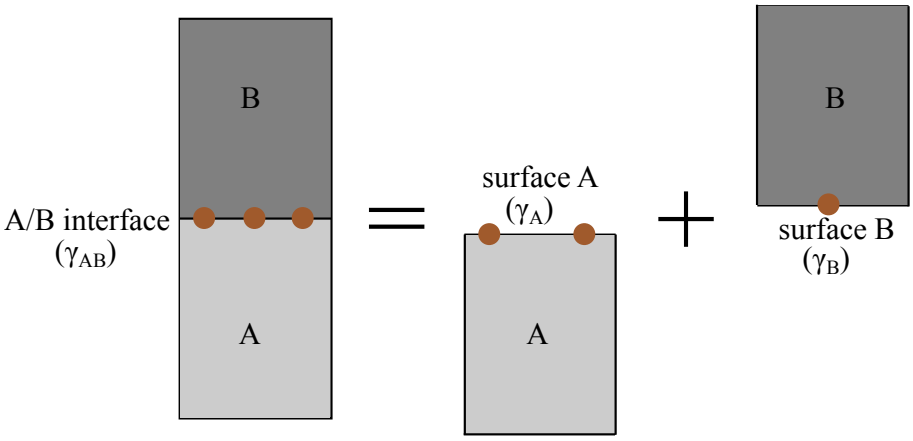

Figure 19: Schematics for computing an ideal work of separation. The interface between materials A and B is split into two surfaces of material A and B, respectively.

Likewise, the driving force for crack propagation can be expressed by means of the critical stress. A crack propagates when the stress at the tip of a crack is higher than a critical stress. In the following both fracture criteria are briefly outlined.

Fracture mechanics principles can be applied to investigate the fracture of interfaces [164]. Conceptually, it is a non-trivial step from calculated total energies to descriptions of the physical process that causes separation of the material and formation of surfaces. Ignoring plastic flow and diffusion processes the reversible work needed to separate the interface into two surfaces is given by the ideal work of separation (W_{sep}^{∞}). It is a fundamental quantity that characterises the strength of an interface [173].

A scheme for computing an ideal work of separation of the interface is shown on Figure 19. The interface between phases A and B is characterised by the interface energy γ_{AB}. Cleaving the interface, two surfaces characterised by surface energy σ_A and σ_B are created. In terms of the interface and surface energies (normalised per area of the interface and surface, respectively), the ideal work of separation is given by the Dupré-equation [174]

$$W_{sep}^{\infty} = (\sigma_A + \sigma_B) - \gamma_{AB}. \tag{2.66}$$

Within the DFT framework, the resistance of an interface against brittle fracture can be quantified by means of the theoretical strength (σ_{th}) using a model of uniaxial tensile loading of the interface [175]. This approach is an alternative to the energy

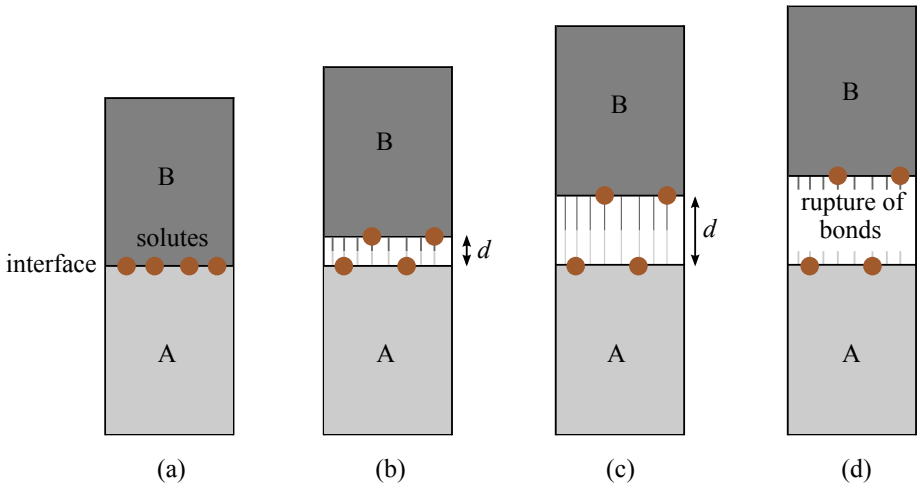

Figure 20: Schematics of uniaxial tensile loading of the interface. An interface separation is stepwise increased by x until phases A and B are not bonded and two surfaces are created.

criterion (W^{∞}_{sep}) and sets the upper bound on the intrinsic bond strength of the interface leaving the energy contributions aside.

Figure 20 shows schematically the uniaxial tensile loading of an interface. The rigid separation of the A/B interface is stepwise increased from its equilibrium value by d until phases A and B are not bonded and correspond to two surface slabs. The corresponding variation of the decohesion energy normalised per interface area A_{int} can be obtained as

$$W_{\text{sep}}(d) = \left(E^{\infty}_{\text{slab}} - E_{\text{slab}}(d)\right)/A_{\text{int}}, \tag{2.67}$$

where $E_{\text{slab}}(d)$ is the total energy of the supercell containing an interface with the interface separation increased by d from its equilibrium interface separation (Figure 20(b,c)). E^{∞}_{slab} is the total energy of the supercell containing two surface slabs, A and B (Figure 20(d)). It is assumed that the strain distribution in front of a propagating crack is not that of a relaxed interface, but closer to the results of a rigid body displacement [99]. After the crack has passed, the newly created surfaces of phase A and B relax to their equilibrium configuration [99]. If solutes are segregated at the interface, after crack propagation they can be distributed on the same or different newly created surfaces. It is important to investigate the solute distribution, especially in the presence on several solute atoms or species. Moreover, solutes change the chemical bonding at the interface influencing the interface strength.

The theoretical strength of an interface (σ_{th}) is obtained by fitting $W_{\mathrm{sep}}(d)$ to an analytical form and identifying the maximum of the derivative of the energy variation

$$\sigma_{\mathrm{th}} = \left(-\frac{\mathrm{d}W_{\mathrm{sep}}(d)}{\mathrm{d}d} \right) \Bigg|_{W''_{\mathrm{sep}}(d)=0}. \tag{2.68}$$

Suitable analytical functions are of the form

$$W_{\mathrm{sep}}(d) = W_{\mathrm{sep}}^{\infty} \cdot e^{-a_1 d} \cdot \sum_{\mathrm{n}=0}^{\mathrm{N}} a_{\mathrm{n}} d^{\mathrm{n}}, \tag{2.69}$$

where d is the deviation of the interface separation from its equilibrium value, $W_{\mathrm{sep}}^{\infty}$ is the ideal work of separation and a_{n} are the fitting parameters. The case where $N = 1$ and $a_0 = 1$ corresponds to the universal binding energy relationship for crystals (UBER) [176].

3

SOLUBILITY OF ZIRCONIUM AND SILICON IN BULK MOLYBDENUM

Published in *Scripta Materialia* 97, 1–4 (2015).

Experimental studies show that microalloying with Zr is an efficient way to increase the fracture toughness, strength and ductility of pure Mo [4, 59, 62–65], binary (Mo-Si) [2, 60] and ternary (Mo-Si-B) [3, 23, 66–68] alloys. Since the solubility limit for Zr in Mo is still a matter of debate, it is unclear if the experimentally observed results can be attributed to grain boundary or bulk effects. Ham [177], for instance, examined Mo arc-cast alloys and found a solubility of 3–5 at.% Zr at 1373 K. Okamoto [178] has reported a value of 10 at.% Zr dissolved in bcc-Mo at 2153 K. Rudy [179] and Brewer [180], in contrast, reported a Zr solubility of 18–20 at.% at around 2223±50 K.

While Zr is increasing the ductility, Si is known to significantly increase the strength due to solid solution strengthening and thus reduce the room-temperature ductility. Most importantly, Si is also improving the oxidation resistance of Mo-Si-B alloys due the formation of a protective borosilicate glass [21, 24, 25, 32]. When the system is supersaturated with silicon, SiO_2 particles are formed at grain boundaries (GBs) at elevated temperatures and passivate the system. Experimental high-temperature measurements report a solubility of ≈4 at.% Si in Mo [181–183].

In this chapter a theoretical assessment of solid solubility of Zr and Si is presented. Knowledge of solid solubility is useful for understanding GB segregation in polycrystalline materials. Qualitatively, the GB enrichment of a solute relative to the bulk is reverse to solid solubility. The solute formation energy is affected by the nature and size of solute and solvent atoms, defining the strength of solute-solvent chemical bonds and the elastic distortions produced by a solute.

3.1 FORMATION ENERGY AND THEORETICAL SOLUBILITY LIMIT

The formation energy ΔE_f of a solute in a host matrix and its solubility c are related according to [184] (see Section 2.5)

$$c = c_0 \exp\left(-\frac{\Delta E_\mathrm{f}}{k_\mathrm{B} T}\right). \tag{3.1}$$

The formation energy ΔE_f of a solute can be obtained by an extrapolation procedure proposed by Mishin *et al.* [136]. DFT calculations are limited to relatively small

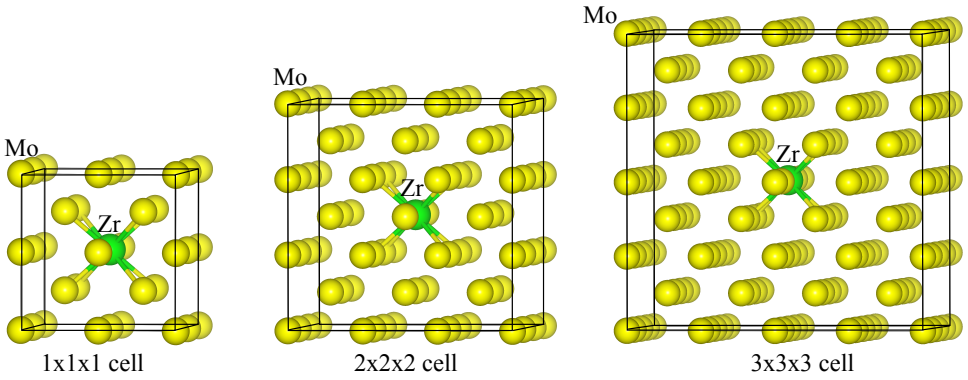

Figure 21: Illustration of supercells, used to determine the solid solubility of Zr (Si) in Mo. Supercells are constructed from different replications of the conventional Mo bcc cell. Yellow spheres represent Mo atoms and green sphere represents Zr atom.

systems containing up to 250–300 atoms, which leads of finite-size effects caused by image interactions. The extrapolation procedure corrects for finite-size effects. At first, the formation energy of Zr and Si is calculated for various supercells constructed from a $(2 \times 2 \times 2)$ to a $(5 \times 5 \times 5)$ replication of the conventional Mo bcc cell with a single substitutional solute atom. The supercells are illustrated on Figure 21. This results in a total of 16 up to 250 atoms and a solute concentration of 6.25 at.% to 0.4 at.%. Afterwards, ΔE_{f} is extrapolated based on the computed data to the energy value, which represents an infinite crystal [136]. Atoms are relaxed under different boundary conditions: (a) constant pressure ($p = 0$) and (b) constant volume.

The formation energy of Zr in bulk Mo is calculated as

$$\Delta E_{\mathrm{f,\,Zr}} = E_{\mathrm{Mo}_x\mathrm{Zr}_y} - y \cdot \epsilon_{\mathrm{Mo_2Zr}} - (x - 2y) \cdot \epsilon_{\mathrm{Mo}}. \tag{3.2}$$

For Si, the formation energy is obtained from

$$\Delta E_{\mathrm{f,\,Si}} = E_{\mathrm{Mo}_x\mathrm{Si}_y} - y \cdot \epsilon_{\mathrm{Mo_3Si}} - (x - 3y) \cdot \epsilon_{\mathrm{Mo}}. \tag{3.3}$$

In Eq.(3.2) and Eq.(3.3), $E_{\mathrm{Mo}_x(\mathrm{Zr,\,Si})_y}$ is the total energy of Mo supercell containing a solute atom. The total energy of bulk molybdenum per Mo atom is represented by ϵ_{Mo}. To minimise errors, both $E_{\mathrm{Mo}_x(\mathrm{Zr,\,Si})_y}$ and ϵ_{Mo} are calculated using the same set of k-points. Mo_2Zr and Mo_3Si act as reservoirs for Zr and Si, respectively. Figure 22 shows the binary Mo-Zr and Mo-Si diagrams presented by H. Okamoto [178, 182]. Mo_2Zr and Mo_3Si phases are the next stable crystalline phases that appear in the binary phase diagrams upon increasing the Zr or Si concentration starting from the pure Mo. This is why they are chosen as reference states for Zr and Si in the present work.

Volume change of a host lattice due to the presence of a point defect (vacancy, interstitial or substitutional atom) is called the relaxation volume, ΔV_{rel}. The relaxation

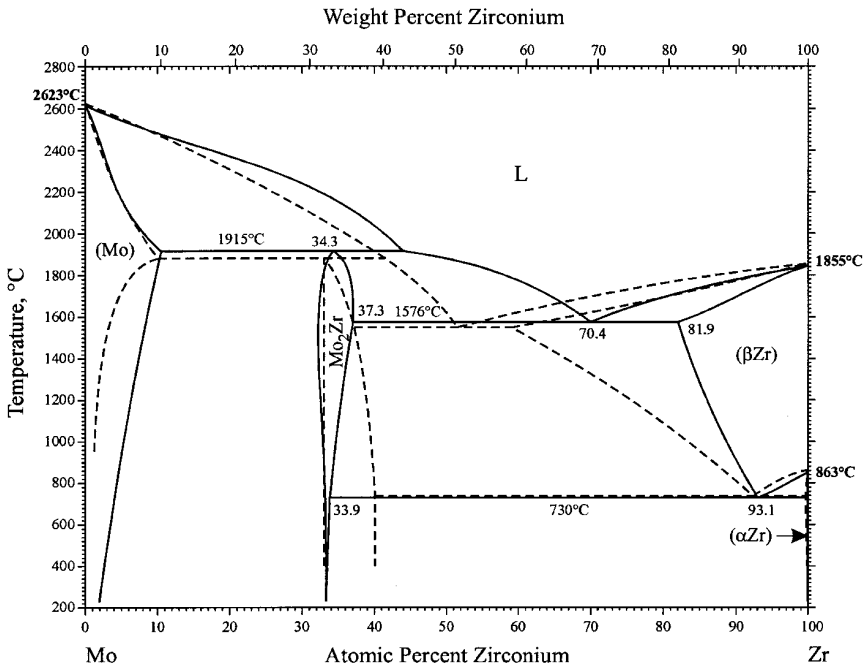

(a)

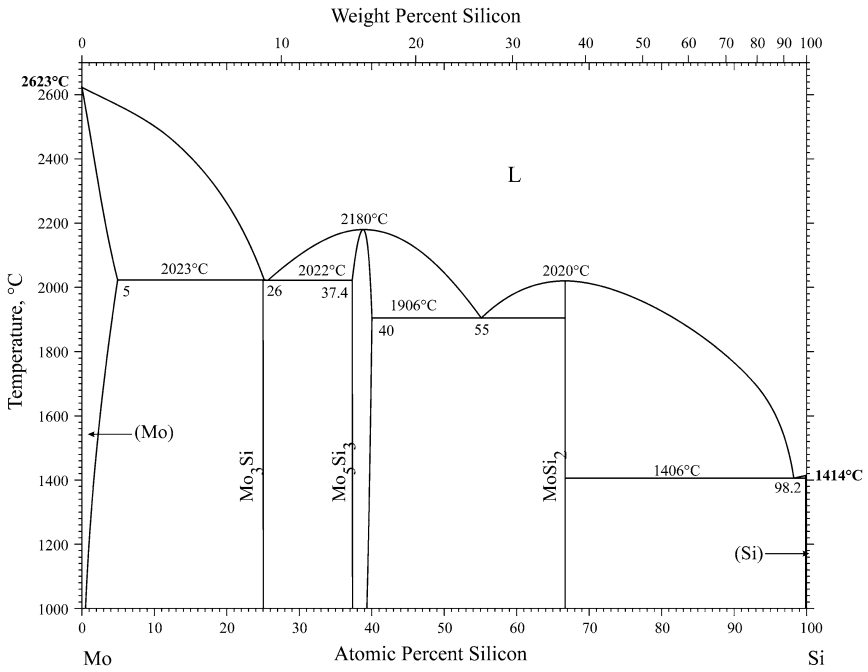

(b)

Figure 22: Binary (a) Mo-Zr and (b) Mo-Si phase diagrams. The figures are originally published by H. Okamoto [178, 182]. ©(2017) reprinted with permission from Springer.

Table 8: Calculated formation energy, formation volume and theoretical solubility limit of Zr and Si in molybdenum at the respective peritectic temperature.

	ΔE_f (eV)	$\Delta V_{rel}/\Omega$	T, K	c (at.%)	c^{exp} (at.%)
Zr	0.27 ± 0.03	0.16	2153±50	23±3	≈3–20 [177, 179, 180]
Si	0.87 ± 0.03	-0.10	2239±50	1.1±0.2	≈4 [181–183]

volume of a point defect contributes to the formation volume ($\Delta V_{rel} \pm \Omega$, where Ω is the atomic volume) and can be directly computed according to [136]

$$\Delta V_{rel} = 1/3 \cdot Tr(P_{\alpha\beta}) V_0 / B_0. \tag{3.4}$$

Here, $p = 1/3 \cdot Tr(P_{\alpha\beta})$ is the hydrostatic part of the stress tensor, that corresponds to the increase in pressure due to the presence of the defect in the material with equilibrium volume V_0 and the bulk modulus B_0. The computational procedure for an accurate description of the bulk modulus and equilibrium lattice constants is described in Section 2.3.1. The corresponding parameters for molybdenum are listed in Table 4.

Figure 23 shows the calculated formation energy ΔE_f of Zr and Si obtained using Eq.(3.2) and Eq.(3.3) as function of the reciprocal number of atoms ($1/N$) in the cell. For each solute atom, two data sets are shown along with linear extrapolations. The red data points correspond to ΔE_f obtained from calculations at constant volume and the black data points correspond to calculations at zero pressure. Independent of the computational settings, the extrapolation of the computed data points gives the same value of ΔE_f. This value represents the formation energy of a solute (Zr, Si) in the dilute limit. For Zr the formation energy converges to $\Delta E_{f,\,Zr} = 0.27 \pm 0.03$ eV and for Si the formation energy corresponds to $\Delta E_{f,\,Si} = 0.87 \pm 0.03$ eV. The positive sign of the formation energy indicates that the dissolution of Zr (Si) from Mo_2Zr (Mo_3Si) into Mo as a solid solution is an endothermic process.

The relaxation volumes of Zr and Si are calculated according to Eq.(3.4) and represent the increase in pressure due to the presence of the solute in a host (solvent) lattice. The relaxation volume ΔV_{rel} is weakly depending on the cell size approaching a value of 0.16 Ω for Zr and -0.10 Ω for Si, where Ω is the atomic volume of Mo. Positive value of the relaxation volume corresponds to an expansion of the cell and negative ΔV_{ref} values corresponds to cell contraction.

The calculated formation energies and the theoretical solubility in a dilute regime are listed in Table 8. The solubility is computed using Eq.(3.1) at the temperature of the peritectic reaction "L + Mo_{bcc} → Mo_2Zr" for Zr and "L + Mo_{bcc} → Mo_3Si" for Si. The experimentally measured solubility of Zr deviates in a wide range. The theoretical solubility for Zr, calculated in this study, supports the experimental finding

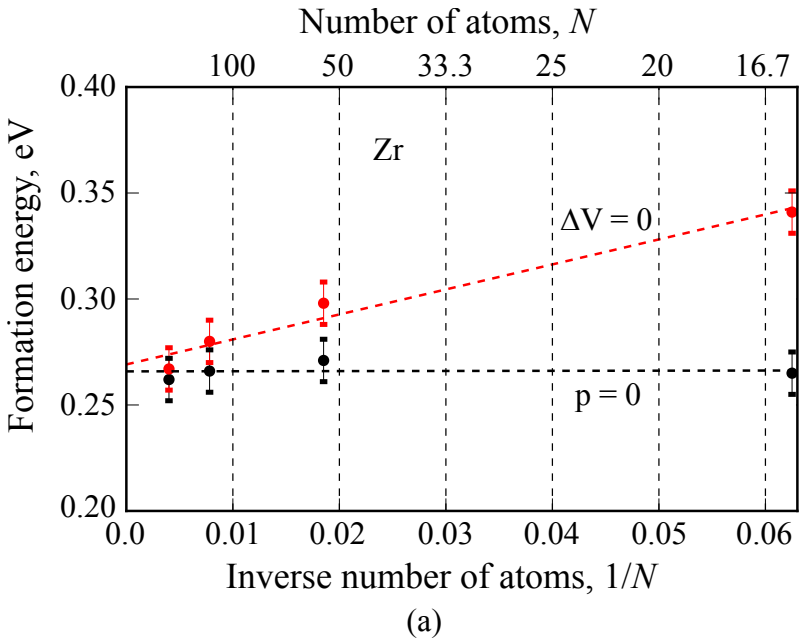

(a)

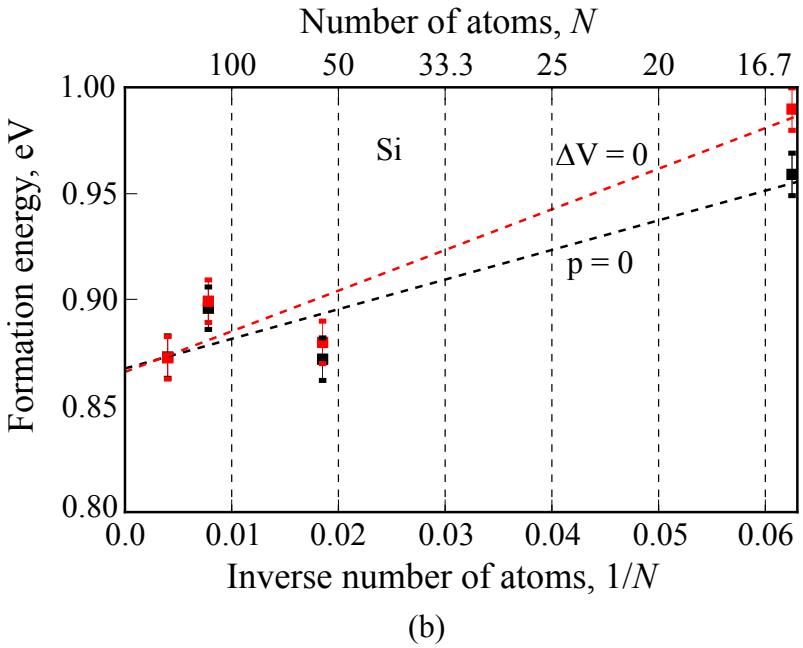

(b)

Figure 23: Calculated formation energy ΔE_f of (a) Zr and (b) Si in molybdenum as function of the inverse number of atoms in the supercell $1/N$. Two types of boundary conditions are considered: $p \approx 0$ and V = const. The energies relating to an infinite crystal are obtained by a linear extrapolation to $1/N \to 0$.

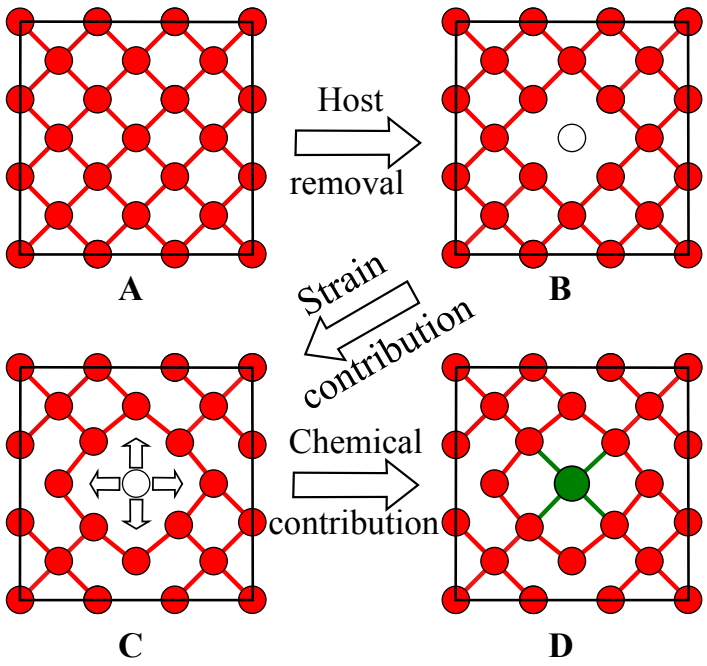

Figure 24: Schematics illustrating individual contributions to the solute formation energy. **A** Pure structure; **A**→**B** Host removal (E_{chem}(Mo)); **B**→**C** Elastic strain contribution (ΔE_{strain}); **C**→**D** Chemical contribution (E_{chem}(solute)).

of Rudy [179] and Brewer *et al.* [180]. It is thus possible to dissolve around 20 at.% Zr under equilibrium conditions. For Si, the theoretical solubility is consistent with reported data and is about 1 at.%.

3.2 STRAIN AND CHEMICAL ANALYSIS

For getting a better understanding, why the Zr and Si solubilities in Mo are considerably different, the calculated formation energy can be subdivided into strain (misfit) and chemical contributions according to Finnis *et al.* [139]. The first term represents the energy stored mechanically due to the size misfit of solutes in the host (solvent) lattice. The second term describes the chemical solute-host atom interaction.

Figure 24 schematically illustrates individual contributions to the formation energy. For a solute occupying a substitutional site in the bulk, a strain energy is stored in the form of broken (Figure 24 (**A**→**B**)) and stretched/compressed host-host bonds (Figure 24 (**B**→**C**)). The chemical bonding contribution to the formation energy describes the bonding strength between the solute and the host atoms. Figure 24 (**C**→**D**) illustrates a chemical bonding formed between a solute and host atoms.

Based on the total energies, investigated by means of DFT calculations, the strain and chemical contributions to the formation energies of solutes can be quantified as follows. The chemical contribution to the binding energy of Mo atoms (or "host removal" energy) is obtained as

$$E_{\text{chem}}(\text{Mo}) = E(\mathbf{B}) - E(\mathbf{A}) + \epsilon_{\text{Mo}}, \tag{3.5}$$

where $E(\mathbf{A})$ is the total energy of the fully relaxed pure system and $E(\mathbf{B})$ is the total energy of the pure system with a Mo vacancy created on the same site which solute atom occupies in **D**. No further relaxations of the structure are allowed. Here, ϵ_{Mo} is the energy per Mo in the bulk. The chemical contribution to the binding energy of solute (Zr, Si) is similarly obtained by

$$E_{\text{chem}}(\text{Zr}) = E(\mathbf{D}) - E(\mathbf{C}) - \epsilon_{\text{Mo}_2\text{Zr}} + 2 \cdot \epsilon_{\text{Mo}}, \tag{3.6}$$

$$E_{\text{chem}}(\text{Si}) = E(\mathbf{D}) - E(\mathbf{C}) - \epsilon_{\text{Mo}_3\text{Si}} + 3 \cdot \epsilon_{\text{Mo}}. \tag{3.7}$$

Here $E(\mathbf{D})$ is the total energy of the fully relaxed system with segregated solute and $E(\mathbf{C})$ is the total energy of the system with the same atomic structure as **D** obtained after removing the solute without any further relaxation of the structure. As before, Mo_2Zr and Mo_3Si phases are used as reservoirs for Zr and Si, respectively. Details are provided in Section 3.1. The overall chemical contribution to the formation energy is thus

$$\Delta E_{\text{chem}} = E_{\text{chem}}(\text{solute}) - E_{\text{chem}}(\text{Mo}), \tag{3.8}$$

and the mechanically stored elastic strain energy is

$$\Delta E_{\text{strain}} = E(\mathbf{C}) - E(\mathbf{B}). \tag{3.9}$$

Figure 25 illustrates the formation energies of Zr and Si solutes along with individual contributions from misfit and chemical bonding. The diagram shows that the highest positive contribution is provided by removal of a Mo atom. In particular, Zr is an attractive bonding partner for Mo. The binding energy of an Mo atom in bulk Mo, $E_{\text{chem, Mo}}$ (red column), and the binding energy of Zr atom in bulk Mo, $E_{\text{chem, Zr}}$ (yellow column), are almost identical. Since Zr is larger than Mo, the incorporation of Zr atom into Mo host lattice causes distortions of the surrounding Mo atoms and therefore leads to a positive energy contribution to the formation energy. Here, ΔE_{strain} equals 0.24 eV. Silicon, in contrast to zirconium, is much smaller in size. Due to the fact that Mo atoms located around a Mo vacancy generally contract, the misfit energy ΔE_{strain} even becomes negative for Si. But energy-consuming host removal can not be counterbalanced by the formation of weaker Mo-Si bonds. This results in a high formation energy and a low solubility of Si in molybdenum.

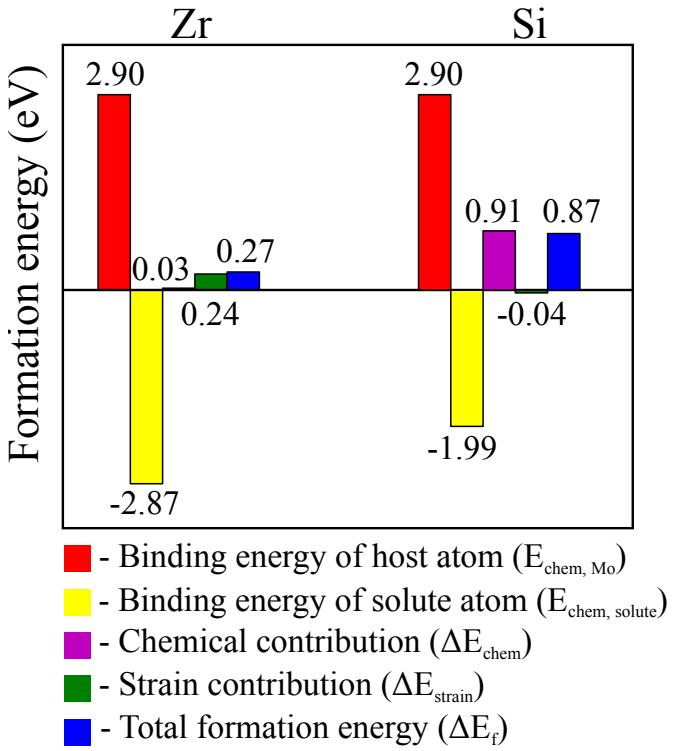

Figure 25: Individual contributions to the formation energy ΔE_{f} of Zr and Si segregated in the Mo bulk.

3.3 ELECTRONIC STRUCTURE ANALYSIS

The bonding between Mo and the solutes can be revealed by analysing the electronic structure of solute containing systems by means of electron densities, Bader charge analysis [125] and density of states (DOS). The analysis is provided using a $3\times3\times3$ replication of the conventional bcc Mo cell. The number of k-points has been increased to yield a smooth DOS. Only for DOS of isolated atoms used as references for solutes, a single point sampling has been used.

Figure 41 shows the redistribution of charge density in the Mo-X (X = Zr, Si) systems relative to the pure Mo system and atomic X. The charge density difference is plotted in the $(1\bar{1}0)$ plane that contains the solute and neighbouring Mo atoms. The red contours correspond to accumulation of electronic charge and the blue contours correspond to the depletion of electronic charge. Figure 41 shows an accumulation of charge with a maximum on the halfway along Mo-Zr and Mo-Si bond lines. According to the colour coding, the Mo-Zr bond is stronger compared to the Mo-Si bond which lies in line with individual chemical contributions to the formation energy, see Figure 25. Using a Bader charge analysis [125] a charge transfer of 1.06 *e* from

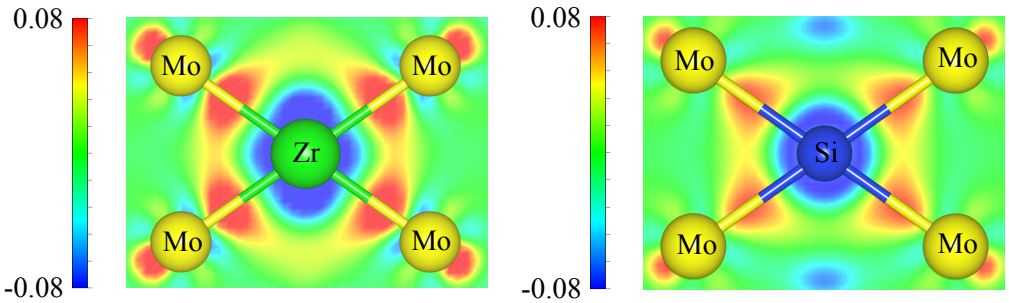

Figure 26: Contour plot of the charge density difference of the Mo-X (X = Zr, Si) systems relative to the pure Mo (Mo+V, where V is a vacancy) and atomic X. The charge density difference is plotted in the $(1\bar{1}0)$ plane containing X and the nearest Mo neighbours. Blue contours correspond to depletion of electronic charge; red contours correspond to its accumulation.

Zr to Mo and 0.44 e from Mo to Si is found. The analysis suggests the mixed ionic-covalent character of the Mo-Zr and Mo-Si bonds. In the Mo-Zr system, the additional charge on Mo is transferred mainly from the first nearest neighbours ($\approx$1.0 e). In the Mo-Si system, the additional charge on Si is transferred from Mo atoms located not only close-by, but also further apart. The ionicity of Zr is considerably higher than the ionicity of Si. Therefore, the Mo-Zr bonds are stronger than Mo-Si bonds, despite of the slight reduction of the metallic bond strength in the Mo-Zr system.

Figure 27 shows total DOS for Mo-Zr (top) and Mo-Si (bottom) systems (black line), Mo-V + Zr(Si) (red line), atomic Zr(Si) (blue line) and the difference between Mo-Zr(Si) and Mo-V + Zr(Si). Here V denotes a Mo vacancy. The analysis shows that, in general, occupation of electronic states at higher energies is reduced while occupation at lower energies is enhanced. The reduction of states close to the Fermi level is considerably more pronounced for Zr than for Si, reflecting the lower formation energy of Zr as compared to Si. There are also indications of Mo-X hybridisation in the DOS. The atomic X peak splits into two, giving a sign of the formation of bonding and antibonding states with similar intensities and indicating the covalency in the Mo-X bond, although it is weak.

3.4 CONCLUSIONS

The formation energy of zirconium and silicon in bcc molybdenum has been calculated using the supercell approach. Extrapolation to the dilute limit yields the formation energy $\Delta E_{\mathrm{f,\,Zr}} = 0.27 \pm 0.03$ eV for zirconium and $\Delta E_{\mathrm{f,\,Si}} = 0.87 \pm 0.03$ eV for silicon.

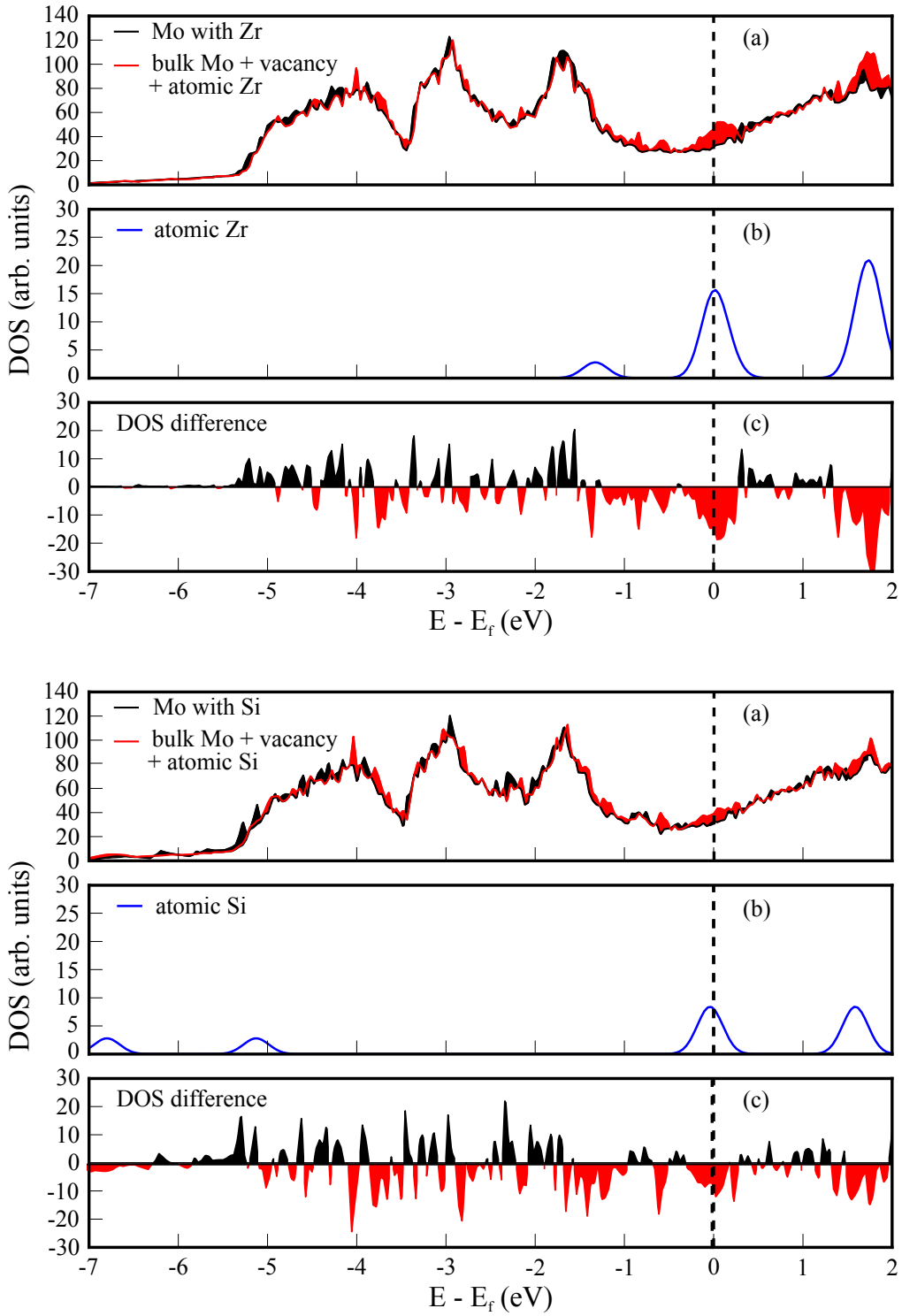

Figure 27: Total density of states (DOS) and the difference in DOS for Mo-Zr (top) and Mo-Si (bottom) systems. (a) Total DOS for Mo-X and for Mo-V + X (V = Mo vacancy). (b) Total DOS of atomic X. (c) Difference in DOS between the Mo-X and Mo-V + X. The filled red area corresponds to a depletion of states in the alloyed system, while the filled black area corresponds to an accumulation of states.

The theoretical solubility limits of zirconium and silicon in molybdenum in this case are estimated to c(Zr) = 23$\pm$3 at.% at 2153 K for zirconium and c(Si) = 1.1$\pm$0.2 at.% at 2239 K for silicon. The calculated values are in line with the upper limit for solubility found experimentally. The large scattering of experimentally measured solubility of zirconium in molybdenum (from 3 at.% to 20 at.%) suggests that not all investigated systems are in equilibrium. The difference in solubility of zirconium and silicon can be explained based on the elastic strain and chemical bonding contributions to the solute formation energy. The bond strength of Zr-Mo bonds is similar to that for Mo-Mo bonds, but incorporation of zirconium into the molybdenum lattice produces large elastic distortions due to the difference in atomic size of both elements. In contrast, the contribution of the elastic strain energy for silicon is negligible. However, silicon is bonded considerably weaker to molybdenum. Bader charge analysis indicates a charge transfer of 1.06 e from zirconium to molybdenum and 0.44 e from molybdenum to silicon, which is consistent with the analysis of chemical-bond contributions to the formation energy of both solutes. The Mo-Zr and Mo-Si bonding is characterised as ionic with weak covalent contributions.

4

SOLUTE SEGREGATION AT MOLYBDENUM GRAIN BOUNDARIES

Parts of this chapter are published in *Journal of Materials Science* 51, 1873–81 (2016).

Strengthening of grain boundaries (GBs) in molybdenum by Zr segregation is one of the potential origins of the experimentally observed improvement of fracture toughness and ductility in Mo-based alloys. An alternative mechanism is the reduction of oxygen concentration at Mo GBs due to the formation of an oxide phase. Since oxygen is a strong embrittler [71], reduction of O would thus be less detrimental to the mechanical properties. Finally, Si microalloying was found crucial for the room-temperature ductility and fracture toughness of Mo [1] and therefore reduction of Si segregation at Mo GBs due to the presence of Zr might be also beneficial for the GB strength.

In this Chapter, segregation of Zr, Si and O to GBs in Mo and their influence on the stability of GBs are addressed. The tendency of solutes to segregate from the bulk to Mo GBs and to Mo surfaces is quantified by comparing with the bulk solubility. In order to evaluate the influence of Zr on Si segregation at Mo GBs, the low-energy segregation sites for both solutes are identified in the dilute limit and upon increasing their concentration. The embrittling potential of Zr, Si and O is evaluated based on the Rice-Wang criterion [76]. According to this criterion, a solute is expected to behave as an embrittler if the energy gain for segregation at the interface from the bulk is smaller than that for segregation at the corresponding surface from the bulk. Contributions to the strain and chemical energy provide helpful insights of the nature of the embrittling/enhancing potential of the solutes. Furthermore, in order to explain why solutes reduce or enhance the GB cohesive strength, the stability of pure and solute containing GBs and surfaces are analysed. The stability is evaluated by evaluating the reduction (increase) in the GB energy (γ_{GB}) and in the surface energy ($\sigma_{\mathrm{Mo}(h,k,l)}$) caused by the presence of a solute.

4.1 MODELS

4.1.1 *Molybdenum bicrystals*

In bcc metals the principal fracture plane is the (001) plane [54, 163, 167, 168]. Therefore, Mo(001) is considered as the dominant Mo surface orientation. Because of

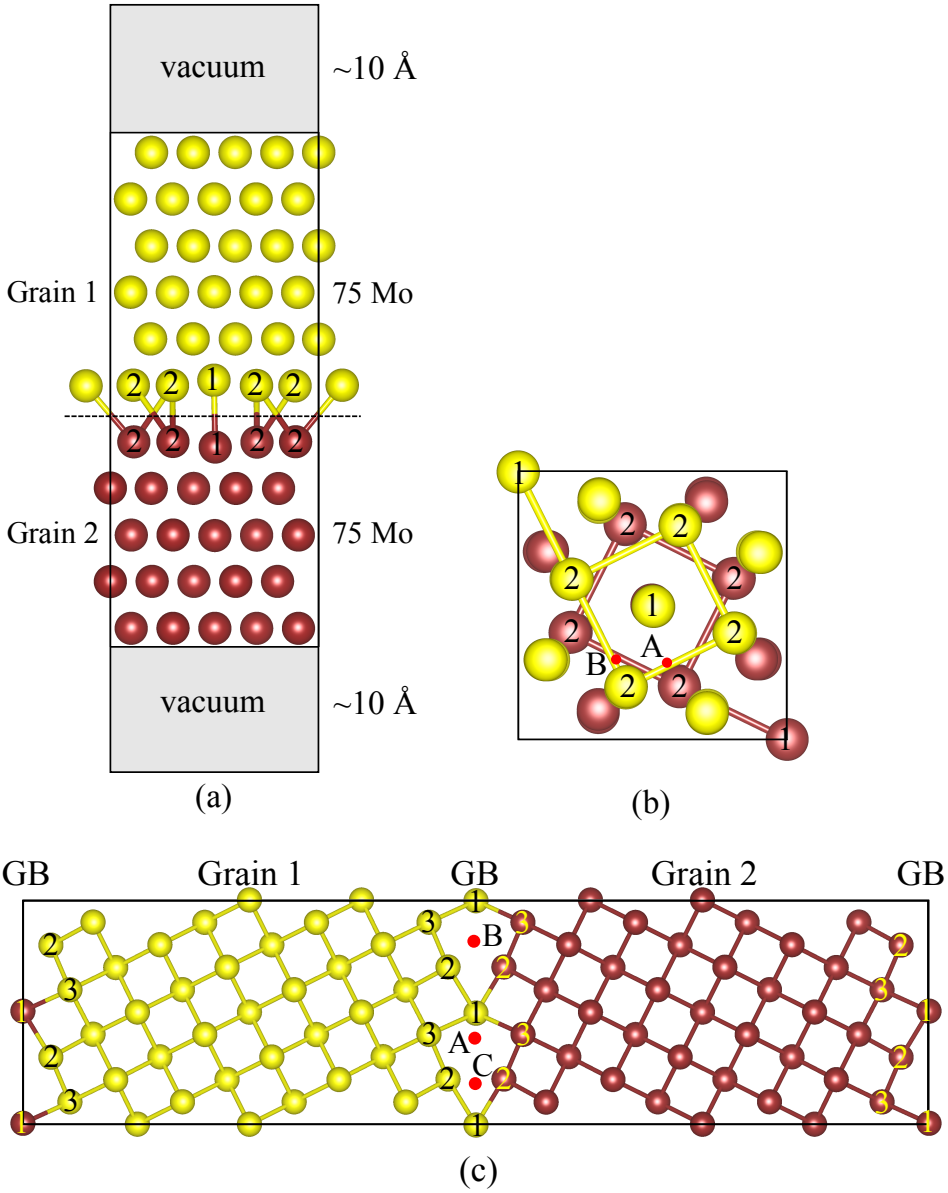

Figure 28: Atomic structure of pure Σ5 GBs in molybdenum. (a) A slab model of a twist Σ5[001] GB including vacuum, projected along the [100] axis; (b) same as (a), but projected along the [001] axis. (c) A periodic supercell model of a tilt Σ5(310)[001] GB, projected along the [001] axis. Atoms belonging to different grains are represented as yellow and dark red spheres. Non-equivalent positions within the GB are marked "1"–"3". Atoms labelled as "1" correspond to coincidence sites. Red circles denoted with letters "A"–"C" correspond to positions, on which oxygen has been inserted.

the computational demands of self-consistent electronic-structure calculations, only bicrystal geometries in relatively small supercells can be investigated. Considered as "intrinsically brittle", Mo polycrystals fracture intergranularly with a fracture path lying along the weakest boundaries [9, 55, 56, 150]. The fracture strength in molybdenum depends markedly on the GB character and impurity segregation [185]. Among special {001} symmetric tilt and twist GBs in molybdenum, Σ5 boundaries appeared to be very brittle [186–188]. Since the type of GB structure has a small effect on the mean segregation tendency of solutes [13, 14], symmetric tilt and twist high-angle Σ5 boundaries constructed from a CSL (see Section 2.6.2) have been chosen in the present study. These boundaries are considered to be representative for weak GB segments in the polycrystalline material.

Figure 28 shows atomistic models of pure twist Σ5[001] and tilt Σ5(310)[001] GBs in CSL geometry. A slab model of a twist Σ5[001] GB including vacuum, projected along the [100] axis and along the [001] axis is illustrated on Figure 28(a, b). A periodic supercell model of a tilt Σ5(310)[001] GB, projected along the [001] axis is shown on Figure 28(c). Atoms belonging to different grains are denoted in different colour.

Both Σ5 GBs are constructed by rotation of the Mo bcc lattice by an angle of 36.9° about the [001] axis. This rotation results in a dichromatic pattern with coincidence of $\frac{1}{5}$ of all lattice sites. For twist Σ5 GB the grain boundary plane is (001) and it is normal to the rotation axis, whereas for tilt Σ5 GB the grain boundary plane is (310) and it is parallel to the rotation axis. The fraction of coincidence sites, rotation axis and the resulting GB plane are included in the notification of a GB, as for example, Σ5[001] and Σ5(310)[001] Mo GB. The twist GB has lateral dimensions of $\sqrt{5} \times \sqrt{5}\, a_{\mathrm{Mo}}$, where a_{Mo} is the lattice constant of the conventional rectangular bcc Mo cell and consists of 150 atoms. The tilt GB has lateral dimensions of $\sqrt{10} \times \sqrt{5}\, a_{\mathrm{Mo}}$ and contains 160 atoms. The equilibrium lattice constant of Mo is listed in Table 4. Within the twist Σ5[001] GB, two non-equivalent sites exist, while there are three non-equivalent sites within the tilt Σ5(310)[001] GB.

The grain boundary energy is computed according to

$$\gamma_{\mathrm{GB}} = \frac{E_{\mathrm{GB}} - N \cdot \epsilon_{\mathrm{Mo}}}{A}, \tag{4.1}$$

where E_{GB} is the total energy of the supercell containing a GB, N is the total number of Mo atoms in the supercell and ϵ_{Mo} is the total energy per atom of bulk Mo. Here, A is the interface area. For the twist GB represented in a slab supercell, surface energies have to be additionally subtracted. The GB energies of tilt Σ5(310)[001] bicrystals are tabulated in Table 9.

Table 9: Comparison of GB energy of a tilt Σ5(310)[001] Mo GB from different computational studies.

Ref.	Method	$\gamma_{\text{tilt GB}}$, J/m^2
Ratanaphan [189]	EAM	1.33
Ochs [190]	d-TB	1.78
Ochs [191]	LDFT	1.82
Tahir [192]	GGA	1.52
Present study	GGA-PBE	1.80

4.1.2 *Mo(001) and Mo(310) surfaces*

Atomistic models of Mo(001) and Mo(310) surfaces are shown on Figure 29. Both surfaces are represented in slab geometry and are projected along the [100] and along the [001] axis, respectively. Mo(001) and Mo(310) surfaces correspond to the GB planes of the twist and tilt Σ5 Mo bicrystals, respectively. Therefore surface models of Mo(001) and Mo(310) are used for calculating the work of separation (see Chapter 5).

The surface energy is calculated using

$$\sigma_{\text{Mo}(hkl)} = \frac{E_{\text{Surface}} - N \cdot \epsilon_{\text{Mo}}}{2A}, \tag{4.2}$$

where E_{Surface} is the total energy of the supercell containing Mo(hkl) surface, N is the total number of Mo atoms in the cell and A is the surface area. The slab is terminated by two equivalent surfaces and therefor a prefactor "2" is used.

The surface energies of Mo(001) and Mo(310) surfaces have been carefully converged with respect to the number of layers (atoms) in the supercell. The corresponding convergence studies are shown in Table 10 for $\sigma_{\text{Mo}(001)}$ and in Table 12

Table 10: Convergence of $\sigma_{\text{Mo}(001)}$ with respect to the number of layers, N_{layers}.

N_{layers}	$\sigma_{\text{Mo}(001)}$, J/m^2
27	3.22
25	3.20
23	3.24
21	3.27
19	3.20

Table 11: Comparison of Mo(001) surface energy , $\sigma_{\text{Mo}(001)}$, in J/m^2 from different computational studies.

Ref.	Method	$\sigma_{\text{Mo}(001)}$, J/m^2
Che [97]	LDA	3.34
Methfessel [193]	FP-LMTO	3.52
Zhang [98]	2NN MEAM	3.26
Wang [194]	GGA-PBE	3.17
Present study	GGA-PBE	3.22

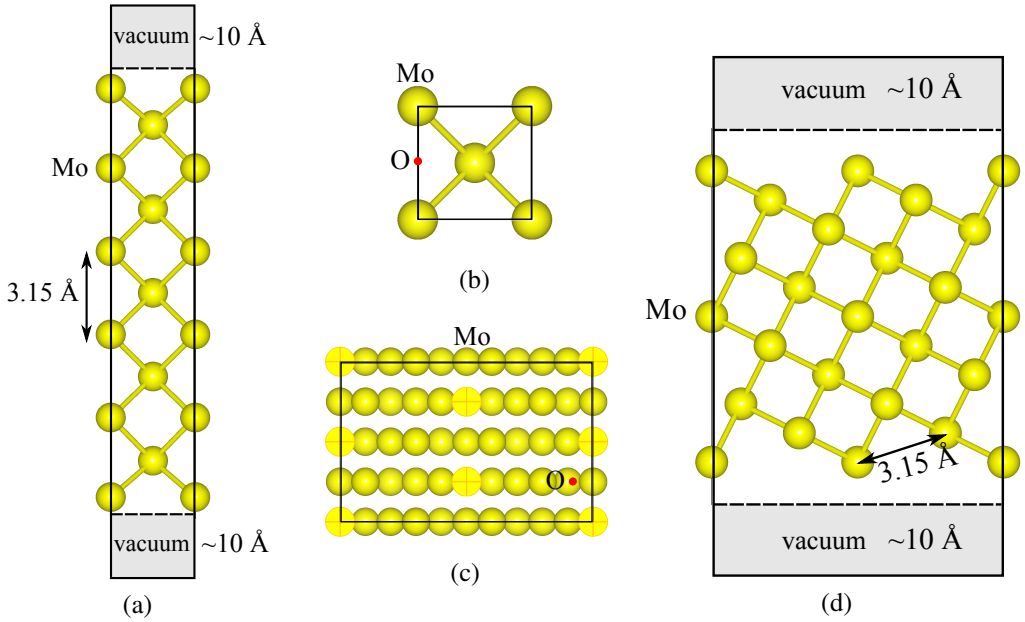

Figure 29: Atomistic models of (a, b) Mo(001) and (c, d) Mo(310) surfaces in slab geometry. The supercells are projected along the (a) [100], (b) [001], (c) [310] and (d) [001] axis, respectively. Yellow spheres represent Mo atoms. Red circles correspond to the low-energy adsorption site for oxygen. Highlighted atoms represent surface atoms.

for $\sigma_{\mathrm{Mo(310)}}$. For Mo(001) the surface energy is converged to 3.22±0.02 J/m^2 in a supercell with 23 layers of Mo per cell (23 Mo atoms). For Mo(310) the surface energy is converged to 3.11±0.01 J/m^2 in a supercell with 21 Mo layers (84 Mo atoms).

Table 11 compares the calculated $\sigma_{\mathrm{Mo(001)}}$ with surface energies, obtained in other computational studies. Our calculated $\sigma_{\mathrm{Mo(001)}}$ is close to the surface energy obtained by Zhang *et al.* [98] and Wang *et al.* [194]. Table 13 lists $\sigma_{\mathrm{Mo(310)}}$ available in the literature. Although this surface is less investigated compared to Mo(001), the value of $\sigma_{\mathrm{Mo(310)}}$ are similar in all studies.

4.2 DRIVING FORCE FOR SEGREGATION OF SOLUTES

4.2.1 *Segregation energies for individual elements*

GB segregation is controlled by the driving force, associated with the energy change when a solute is transferred from a bulk region to the grain boundary. A number of studies show that the solute formation energy varies for different GBs depending on

Table 12: Convergence of $\sigma_{\mathrm{Mo(310)}}$ with respect to the number of layers, N_{layers}.

N_{layers}	$\sigma_{\mathrm{Mo(310)}}$, J/m^2
26	3.12
21	3.11
16	3.10

Table 13: Comparison of Mo(310) surface energy , $\sigma_{\mathrm{Mo(310)}}$, in J/m^2 from different computational studies.

Ref.	Method	$\sigma_{\mathrm{Mo(310)}}$, J/m^2
Wang [194]	GGA-PBE	3.09
Tahir [192]	GGA	3.12
Present study	GGA-PBE	3.11

their atomic structure and for different sites within the same grain boundary depending on the excess volume, coordination number etc. [11].

The formation energy for Zr is obtained from

$$\Delta E_{\mathrm{f,\,Zr}} = E_{\mathrm{GB\,+\,y\cdot Zr}} - E_{\mathrm{GB}} - y \cdot \epsilon_{\mathrm{Mo_2Zr}} + (1+2y) \cdot \epsilon_{\mathrm{Mo}}, \tag{4.3}$$

for Si from

$$\Delta E_{\mathrm{f,\,Si}} = E_{\mathrm{GB\,+\,y\cdot Si}} - E_{\mathrm{GB}} - y \cdot \epsilon_{\mathrm{Mo_3Si}} + (1+3y) \cdot \epsilon_{\mathrm{Mo}}, \tag{4.4}$$

and for O from

$$\Delta E_{\mathrm{f,\,O}} = E_{\mathrm{GB\,+\,y\cdot O}} - E_{\mathrm{GB}} - \frac{y}{3} \cdot \epsilon_{\mathrm{MoO_3}} + \frac{y}{3} \cdot \epsilon_{\mathrm{Mo}}, \tag{4.5}$$

where E_{GB} and $E_{\mathrm{GB\,+\,y\cdot solute}}$ are the total energies of the pure and solute containing GB supercells, respectively. Here, ϵ_{Mo} is the total energy per atom of bulk Mo, whereas $\epsilon_{\mathrm{Mo_2Zr}}$, $\epsilon_{\mathrm{Mo_3Si}}$ and $\epsilon_{\mathrm{MoO_3}}$ are the total energies per formula unit of bulk Mo_2Zr, Mo_3Si and MoO_3 being the reservoirs for Zr, Si and O, respectively. The

Table 14: Change in the formation energy $\Delta E_{\mathrm{f,\,solute}}$ of Zr and Si segregating at the GB relative to Mo bulk ($E^{\mathrm{bulk}}_{\mathrm{f,\,Zr}}$ = 0.27 eV and $E^{\mathrm{bulk}}_{\mathrm{f,\,Si}}$ = 0.83 eV). Gain in energy corresponds to negative values. All numbers are given in eV. Segregation sites of solutes are shown on Figures 28.

	Twist Σ5[001]		Tilt Σ5(310)[001]			Surface	
	Position "1"	Position "2"	Position "1"	Position "2"	Position "3"	Mo(001)	Mo(310)
Zr	+0.15	-0.45	-0.51	-0.17	-0.15	-1.33	-1.25
Si	-0.77	-0.48	+0.12	-0.63	-0.23	-1.47	-1.42

choice of the reservoirs is outlined in Section 3.1. We emphasise that the calculated formation energy depends on the exact position of the solute in the GB.

It has been shown in a number of studies that GB segregation is site specific [13, 138, 156, 195]. As highlighted in Tables 14, this also applies to Zr and Si, segregated at GBs in Mo. Table lists the formation energies of Zr and Si ($\Delta E_{\text{f, solute}}$) for individual sites within the twist Σ5[001] and the tilt Σ5(310)[001] Mo GBs and compares them with the formation energies of solutes at the corresponding surfaces, Mo(001) and Mo(310). All numbers are given relative to the bulk value. Zr and Si are inserted at the GB and at the surface substitutionally. Incorporation of solutes at Mo surfaces is found to be more energetically favourable compared to solutes adsorption. Detailed atomic structures of the twist and tilt Σ5 GBs with non-equivalent segregation sites are shown on Figure 28.

The change of the formation energy ΔE_{f}, summarised in Table 14–15, provides a measure for the driving force for Zr, Si and O segregation towards a GB or a surface. Zr being an oversized solute prefers to occupy sites offering more excess volume, while Si being smaller than Mo segregates at the sites having a more dense atomic environment. Although position "1" corresponds to a coincidence site in both GB geometries, the formation energy of Zr at site "1" in the twist GB is high. This observation can be explained by the relative arrangement of two grains. Two coincidence sites in both grains are located ontop of each other offering less excess volume compared to other sites. Incorporation of Zr and Si into Mo(001) or Mo(310) surfaces is, however, more favourable than GB segregation independent of the position. Solute segregation at the surface is accompanied by saturation of dangling bonds at the surface and the elimination of the elastic strain energy due to the size misfit of a solute in a solvent matrix. At the GB, the number of dangling bonds is smaller compared to the surface and also the elastic strain energy can be only partially eliminated. This results in the higher driving force Zr and Si segregation at the surface compared to the GB.

The driving force for Zr and Si segregation at the GB (surface) is visualised by computing the formation energy of a solute, $\Delta E_{\text{f, solute}}$, for different positions as a function of the distance to the GB. Figure 30 illustrates the variation of $\Delta E_{\text{f, solute}}$ for (a) twist Σ5[001] and (b) tilt Σ5(310)[001] GBs in molybdenum. The corresponding GBs are shown on the bottom of the figure. For the twist GB, a soluteatom is moved from the GB to the surface through the bulk. For the tilt GB, a solute is transferred from one GB to another GB. At the GBs, Zr and Si occupy low-energy segregation sites, which have been previously identified (see Table 14). Afterwards, solutes follow the path denoted by green atoms on the bottom of Figure 30. In both GBs the curves indicate a significant driving force towards segregation of Zr and

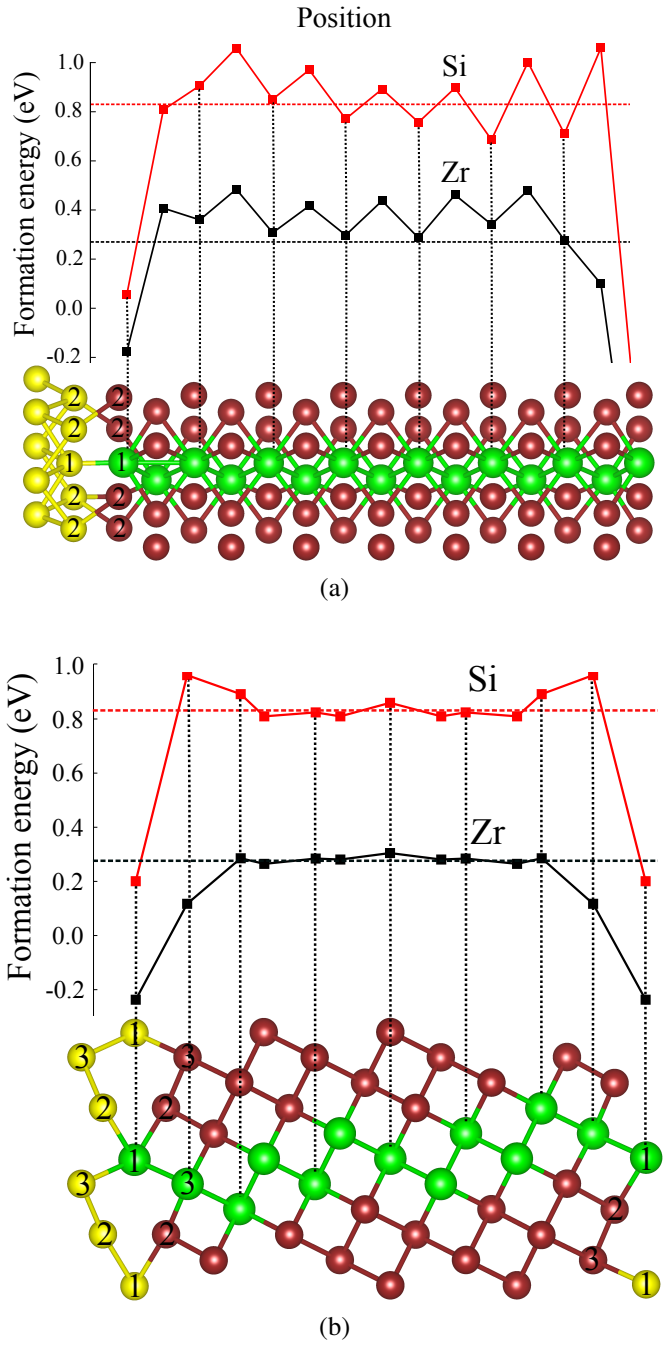

Figure 30: The formation energy of Zr and Si segregated at (a) twist Σ5[001] and (b) Σ5(310)[001] Mo GB as a function of the distance to the grain boundary. Yellow and dark red spheres represent Mo atoms that belong to different grains. Zirconium atoms are denoted in green. Zr and Si atoms are located on the energetically preferred sites within the GB. Numbers "1"–"3" indicate non-equivalent sites within the GB. Site "1" is the coincidence site.

Table 15: Change in the formation energy $\Delta E_{\mathrm{f,\,O}}$ of oxygen segregating at the GB relative to Mo bulk. Gain in energy corresponds to negative values. All numbers are given in eV. Oxygen adsorption sites are shown on Figures 28–29.

	Twist Σ5[001]		Tilt Σ5(310)[001]			Surface	
	Position "A"	Position "B"	Position "A"	Position "B"	Position "C"	Mo(001)	Mo(310)
O	-2.09	-2.02	-2.01	-1.44	-2.32	-3.96	-4.27

Si solutes at the GB (or at a surface, if present). The formation energies of solutes located in the layer next to the GB or next to the surface strongly increase. Upon further penetration of the solutes into the bulk, the formation energies increase to $\Delta E^{\mathrm{bulk}}_{\mathrm{f,\,Zr}} = 0.27$ eV and $\Delta E^{\mathrm{bulk}}_{\mathrm{f,\,Si}} = 0.83$ eV. These values are in agreement within an errorbar with our calculations for solutes in the bulk (Section 3.1). Small peaks close to the tilt GB indicate the thermodynamic barrier for Si segregation. In order to segregate at low-energy site at the tilt GB (position "2"), Si has to occupy at first energetically unfavourable sites, which gives rise to the small thermodynamic barrier for Si segregation.

Zirconium and silicon show similar behaviour for both twist and tilt GB geometries. Since the segregation tendency is significant even for these densely packed GBs it is safe to assume a similar behaviour for other orientations [13, 14]. Another important fact is that the formation energy of Zr located in a GB is negative. Thus, the concentration of Zr in GBs is not determined by the configurational entropy (and thus does not depend on temperature). It is determined only by the number of energetically preferred sites within the GB. The oscillatory behaviour of the formation energies is associated with the change in the charge density induced by the surfaces (surface resonance). Details concerning Friedel oscillations are given in Section 2.4.4.

Impurities like oxygen, dissolved interstitially, strongly affect the mechanical properties of the bcc refractory metals. By segregating to the GBs in molybdenum, oxygen decreases the GB cohesion [71] and promotes brittle intergranular fracture [57]. The change in the formation energy of oxygen segregating from the Mo bulk to the GBs or from the Mo bulk to the surface is listed in Table 15. Oxygen always occupies interstitial sites at the GBs and at the surface. Different positions, on which oxygen has been inserted in the GB, are shown as red circles and denoted with numbers "A"–"C" on Figure 28. The low-energy adsorption sites for oxygen at the Mo surface are shown on Figure 29. Similar to Zr and Si, oxygen segregation to Mo surfaces is stronger compared to the GB segregation. At the GB oxygen prefers to occupy

interstitial sites exhibiting more excess volume. However, the tendency of oxygen to segregate at the GB is considerably higher compared to Zr and Si, for both GBs and for surfaces.

Based on the calculated data, the hierarchy of the driving force for Zr, Si and O segregating to Mo GBs (see Tables 14–15) corresponds to $\Delta E_{\mathrm{f,\,O}} \gg \Delta E_{\mathrm{f,\,Si}} > \Delta E_{\mathrm{f,\,Zr}}$, whereas the trend for solubility in Mo is $c_{\mathrm{O}} \ll c_{\mathrm{Si}} < c_{\mathrm{Zr}}$. The solid solubility of O in Mo is extremely small, approximately 200 ppm at 1900 °C [196]. The solubility of Zr and Si is discussed in Chapter 3. The theoretical results support the inverse correlation between the solid solubility and the solute tendency to segregate to the GB. A similar behaviour is observed for surface segregation.

The segregation energies are also useful as an indicator for embrittlement induced by the solute segregation. Following the Rice-Wang theory [76], for a sub-monolayer coverage an embrittling potential of a solute is given by

$$\Delta E_{\mathrm{EP}} = \Delta E_{\mathrm{f,\,GB}} - \Delta E_{\mathrm{f,\,Surface}}. \tag{4.6}$$

This corresponds to a difference in the formation energy, when a solute is moved from the bulk to a grain boundary, $\Delta E_{\mathrm{f,\,GB}}$, compared to one moved from the bulk to the corresponding surface, $\Delta E_{\mathrm{f,\,Surface}}$. If ΔE_{EP} is positive, a solute is expected to behave as an embrittler.

The embrittling potential of Zr, Si and O for both GBs is positive and embrittle Mo GBs. For the twist GB, it corresponds to $\Delta E_{\mathrm{EP,\,Zr}} = 0.88$ eV for Zr, $\Delta E_{\mathrm{EP,\,Si}} = 0.70$ eV for Si and $\Delta E_{\mathrm{EP,\,O}} = 1.87$ eV for O (see Tables 14–15). For the tilt GB, the embrittling potentials are $\Delta E_{\mathrm{EP,\,Zr}} = 0.74$ eV for Zr, $\Delta E_{\mathrm{EP,\,Si}} = 0.79$ eV for Si and $\Delta E_{\mathrm{EP,\,O}} = 1.95$ eV for O. Zirconium is found to be a stronger embrittler compared to Si for grain boundaries with more densely packed atomic structure. For GBs possessing more excess volume, the embrittling potential of both solutes, Zr and Si, is equivalently strong. Oxygen is found to be an extremely strong embrittler of molybdenum.

4.2.2 *Solute interaction*

In multicomponent systems with two or more solute species, the segregation of one solute might be affected by the presence of another solute due to site competition (if present) and attractive or repulsive interactions between solutes [11]. A solute may also disturb the host lattice and in this way influence the segregation of another solute [141]. GB segregation on one side of a GB also depends on the on the composition on the other side of the GB [156]. In the alloy containing both Zr and Si, the segregation behaviour depends on the mutual interaction of both solutes, attractive or repulsive, and the site competition. In Section 4.2 it has been shown that low-energy

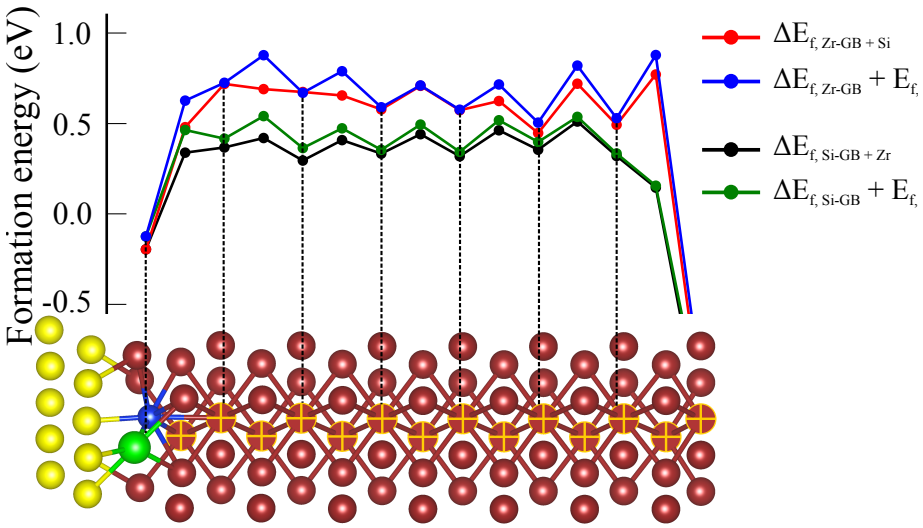

Figure 31: The formation energy of Zr in the presence of Si at the GB ($\Delta E_{\text{f, Si-GB + Zr}}$) and Si in the presence of Zr at the GB ($\Delta E_{\text{f, Zr-GB + Si}}$) segregated at twist Σ5[001] Mo GB as function of the distance to the grain boundary. The green and blue curves represent a sum of individual formation energies of Zr and Si for each position of solutes, $\Delta E_{\text{f, Si-GB}}$+$E_{\text{f, Zr}}$ and $\Delta E_{\text{f, Zr-GB}}$+$E_{\text{f, Si}}$, respectively. Yellow and red spheres represent Mo atoms that belong to different grains. Zirconium atom is denoted in green and silicon atom is denoted in blue. Highlighted Mo atoms show a path of Zr (Si) moved from the GB to the surface through the bulk. At the GB, Zr and Si atoms occupy low-energy segregation sites.

segregation sites for Zr and Si in a dilute regime are different for both twist and tilt geometries. In the following Section 4.2.2, the GBs containing a higher concentration of Zr and Si solutes are investigated.

At first, the influence of Zr (Si) on the driving force for segregation for Si (Zr) has been evaluated. As before, the driving force is estimated by transferring Si layer by layer from the GB to the Mo(001) surface through the bulk, while Zr remains at the GB and *vice versa*. For each position the formation energy of Si in the presence of Zr at the GB ($\Delta E_{\text{f, Zr-GB + Si}}$) and of Zr in the presence of Si at the GB ($\Delta E_{\text{f, Si-GB + Zr}}$) is calculated according to

$$\Delta E_{\text{f, Zr + Si}} = E_{\text{GB + y·Zr + z·Si}} - E_{\text{GB}} - y \cdot \epsilon_{\text{Mo}_2\text{Zr}} - z \cdot \epsilon_{\text{Mo}_3\text{Si}} + (2 + 2y + 3z) \cdot \epsilon_{\text{Mo}}, \tag{4.7}$$

where $E_{\text{GB + y·Zr + z·Si}}$ is the total energy of the GB supercells with substitutional solutes and E_{GB} is the total energy of the pure GB supercells. Here, ϵ_{Mo} is the total energy per atom of bulk Mo, whereas $\epsilon_{\text{Mo}_2\text{Zr}}$, $\epsilon_{\text{Mo}_3\text{Si}}$ and ϵ_{MoO_3} are the total energies

per formula unit of bulk Mo_2Zr, Mo_3Si and MoO_3 being the reservoirs for Zr, Si and O, respectively. The choice of the reservoirs is discussed in Section 3.1.

Figure 31 shows the resulting formation energies of Zr and Si. The atomic structure of the GB with segregated atoms is shown on the bottom of the figure. Both solutes are located at energetically favourable segregation sites at the GB (site "2" for Zr and site "1" for Si, see Figure 28). The path is indicated by highlighted Mo atoms in the figure. The black curve represents the driving force for Zr segregation in the presence of Si at the GB and the red curve represents the driving force for Si segregation in the presence of Zr at the GB. The sum of the corresponding individual formation energies of Zr and Si at the GB and moving through the grain is shown for comparison (green and blue curves). Both curves coincide approximately in the middle of the slab which corresponds to the bulk. In the presence of the Zr (Si) at the GB, the formation energy of Si (Zr) is decreased favouring GB segregation. As before, the formation energy of both solutes is considerably smaller at the GB and at the surface compared to the bulk. The negative values of the formation energy at the GB suggest that the concentration of Zr and Si atoms in the GB is determined by the number of low-energy segregation sites within the GB. The oscillatory behaviour of the formation energy, caused by a long-range surface resonance is discussed in Section 2.4.4.

Further, the interaction of Zr and Si solutes, located at the GB within one grain and solutes interactions across the GB are investigated in twist and tilt GBs. Figures 32–33 show the atomic structure of twist and tilt Mo bicrystals with one Zr atom and one Si atom segregated at the GB, viewed along the [100] axis ("side view") and along the [001] axis ("top view"). For each configuration the formation energy of both solutes ($\Delta E_{\mathrm{f,\,Zr+Si}}$) are calculated using Eq.(4.7).

The segregation tendency of Zr and Si, computed relative to the bulk ($\Delta E_{\mathrm{f,\,Zr+Si}} - \Delta E^{\mathrm{bulk}}_{\mathrm{f,\,Zr+Si}}$) is negative and indicates that the segregation of Zr and Si to the GB from the bulk is energetically highly preferred. For all investigated configurations, the energy gain varies approximately in the same range ($\sim$-0.9 eV to $\sim$-1.3 eV) for the twist and for the tilt GBs. The lowest-energy segregation sites of Zr and Si combination correspond to configuration "1" for both GBs (see Figures 32–33), and exhibit negative formation energy $\Delta E_{\mathrm{f,\,Zr+Si}}$. In the twist GB, this corresponds to Zr and Si occupying sites that have been identified as the lowest-energy segregation sites for each solute species and are located within one grain. In the tilt GB, this corresponds to Si occupying the lowest-energy segregation site and Zr located close-by. The analysis of the optimised GB structure reveals that the neighbouring Mo atoms contract around Si, since Si is smaller in size than Mo, and thus creating excess volume for Zr incorporation.

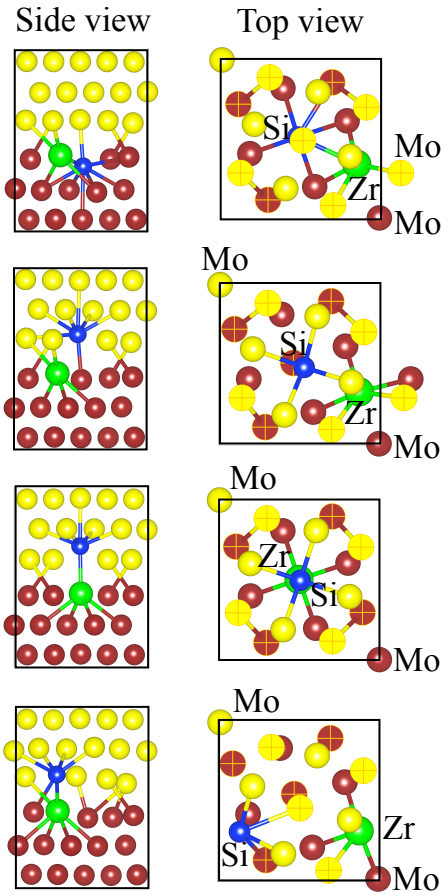

Configuration "1":

$E_{f,\,Zr+Si}$ = -0.20 eV

E_{assoc} = -0.08 eV

$E_{f,\,Zr+Si} - E^{bulk}_{f,\,Zr+Si}$ = -1.19 eV

Configuration "2":

$E_{f,\,Zr+Si}$ = 0.06 eV

E_{assoc} = +0.19 eV

$E_{f,\,Zr+Si} - E^{bulk}_{f,\,Zr+Si}$ = -0.93 eV

Configuration "3":

$E_{f,\,Zr+Si}$ = 0.14 eV

E_{assoc} = +0.27 eV

$E_{f,\,Zr+Si} - E^{bulk}_{f,\,Zr+Si}$ = -0.85 eV

Configuration "4":

$E_{f,\,Zr+Si}$ = 0.15 eV

E_{assoc} = +0.28 eV

$E_{f,\,Zr+Si} - E^{bulk}_{f,\,Zr+Si}$ = -0.84 eV

Figure 32: Close-up of the twist Σ5[001] GB in Mo with one Zr and one Si atom occupying different positions at the GB. The GBs are projected along the [100] axis ("side view") and along the [001] axis ("top view"). Yellow and red spheres represent molybdenum atoms that belong to different grains. Green spheres represent zirconium atoms and blue spheres represent silicon atoms. Highlighted atoms correspond to Mo atoms that form a GB. The formation energy of both solutes located in bulk Mo $\Delta E^{bulk}_{f,\,Zr+Si}$ = = 0.99 eV. The formation energy of Zr and Si ($\Delta E_{f,\,Zr+Si}$), association energy of both solutes (E_{assoc}) and the driving force for GB segregation ($\Delta E_{f,\,Zr+Si} - \Delta E^{bulk}_{f,\,Zr+Si}$) are given for each configuration. The negative driving force indicates that Zr and Si segregation to from the bulk to the GB is energetically preferred. The negative association energy reveals the attractive interaction between Zr and Si.

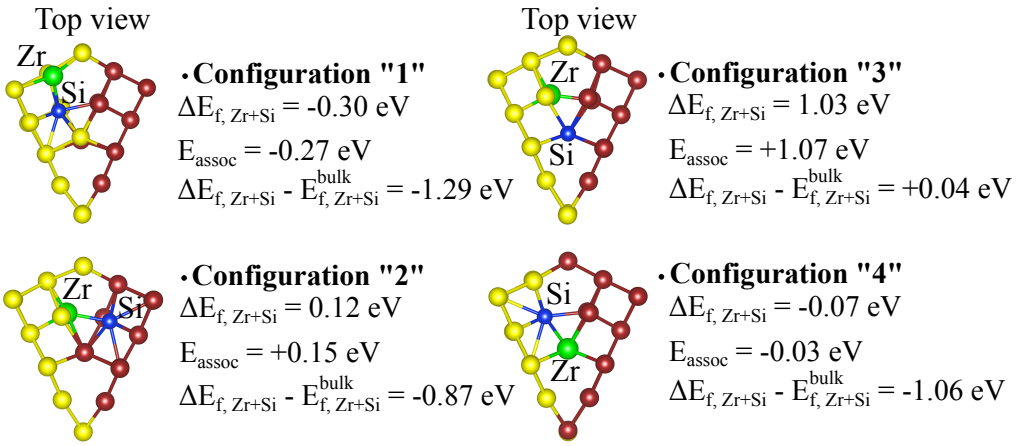

Figure 33: Close-up of the tilt Σ5(310)[001] Mo GB with one Zr and one Si atom occupying different positions at the GB. The GBs are viewed along the [001] axis. Colour coding: see Figure 32. The formation energy of both solutes located in bulk Mo $\Delta E^{bulk}_{f,\,Zr+Si}$ = = 0.99 eV. The formation energy of Zr and Si ($\Delta E_{f,\,Zr+Si}$), association energy of both solutes (E_{assoc}) and the driving force for GB segregation ($\Delta E_{f,\,Zr+Si} - \Delta E^{bulk}_{f,\,Zr+Si}$) are given for each configuration. The negative driving force indicates that Zr and Si segregation to from the bulk to the GB is energetically preferred. The negative association energy reveals the attractive interaction between Zr and Si.

The association energy of Zr and Si (E_{assoc}) is computed as a difference between $\Delta E_{f,\,Zr+Si}$ and individual formation energies for the low-energy segregation site at the GB

$$E_{assoc} = \Delta E_{f,\,Zr+Si} - \Delta E^{fav}_{f,\,Zr} - \Delta E^{fav}_{f,\,Si}. \tag{4.8}$$

The results reveal that the association energy of Zr and Si is negative for the lowest-energy segregation sites of Zr and Si combination (configuration “1” in the twist GB and configurations “1” and “4” in the tilt GB, see Figures 32–33). The negative association energy indicates that it is energetically preferred for both solutes to segregate at the GB and occupy neighbouring sites. The interaction between Zr and Si is attractive.

The site preference of Zr and Si and their driving force for segregation at the GB are affected by the concentration and the mutual distribution of solutes in the GB. For example, the formation energy of one Si and two Zr atoms is computed as $\Delta E_{f,\,2Zr+Si}$ = -0.54 eV in the twist GB and $\Delta E_{f,\,2Zr+Si}$ = -0.62 eV in the tilt GB. The interaction between Si and Zr atoms is attractive in both bicrystals. However, when the same combination of solutes is distributed on both sides of the GB, the formation energy increases and becomes highly positive. For example, $\Delta E_{f,\,2Zr+Si}$ = 0.25 eV per

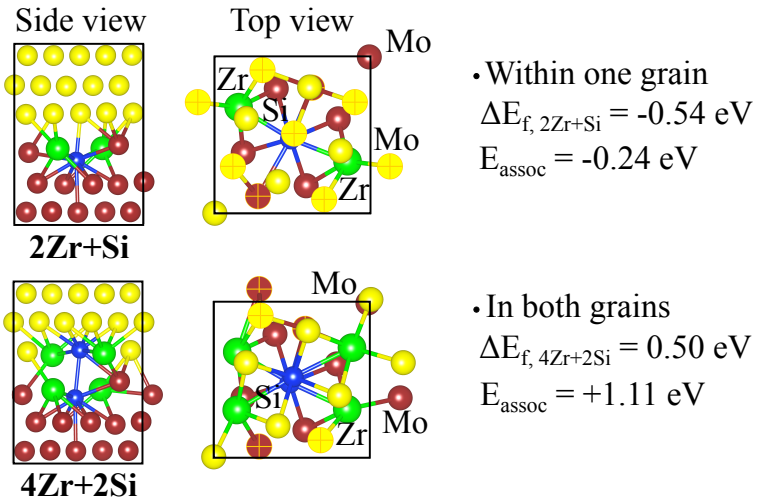

Figure 34: Atomic structure of the twist Σ5[001] Mo GB with one Si and two Zr atoms segregated at the GB and occupying energetically preferred positions. Top panel: all solutes are distributed within one grain. Bottom panel: solutes are located on each side of the GB. The GBs are viewed along the [100] axis ("side view") and along the [001] axis ("top view"). Colour coding: see Figure 32. The formation energy of two Zr and one Si atoms ($\Delta E_{f,\ 2Zr+Si}$) and the corresponding association energy of solutes combination (E_{assoc}) are given for each configuration. The negative association energy indicates the attractive interaction between Zr and Si. For convenience, only few atomic layers close to GB are shown.

combination of one Si and two Zr atoms in the twist GB. The atomic structure of the twist and the tilt Σ5 Mo GBs with different concentration of Zr and Si, distributed within one grain or within both grains is shown on Figures 34–35.

Careful investigation of solute formation energies and their mutual positions reveals that the distribution of silicon atoms on both sides of the GB in the vicinity of each other is energetically unfavourably resulting in high positive formation energies. Si being smaller compared to Mo, when located at the GB penetrates deeper inside a grain and also contracts Mo atoms around it. Two silicon atoms located on different sides of the GB, behave in the same way but in the opposite directions and, in this way, forcing another Si atom to stay closer to the GB, which is unfavourable.

In a general GB, the arrangement of atoms is more open. Due to the negative formation energy of Zr at GB sites offering more excess volume, at lower temperatures the higher Zr concentration is expected at the GBs compared to Si concentration. Since the interaction between Zr and Si atoms is attractive, the segregation of Si is expected to start at lower temperatures compared to the system without Zr. Silicon, located in a GB, however, repels other silicon atoms from segregation to the other side

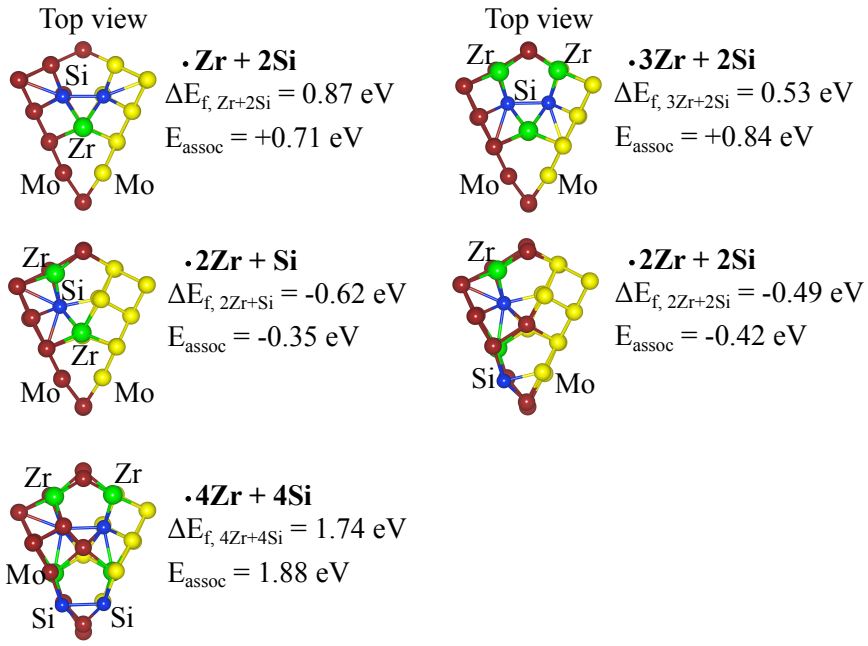

Figure 35: Atomic structure of the tilt Σ5(310)[001] Mo GB with different concentration of Zr and Si atoms at the GB. Solutes are distributed within one grain or on each side of the GB. The GBs are viewed along the [001] axis ("top view"). Colour coding: see Figure 32. The formation energies of different combination of solutes and the corresponding association energies are given for each configuration. For convenience, only atoms at and close to the GB are shown. The negative association energy reveals the attractive interaction between Zr and Si.

of the GB and allows the segregation of Si atoms on other low-energy segregation sites within the same grain. Distribution of Zr atoms close to Si atoms within one grain is found to be energetically preferred. The site competition between Si and Zr atoms is found for increased concentration of solutes in the more densely packed GBs.

4.3 ENERGY OF GRAIN BOUNDARIES

Solute segregation at grain boundaries affect the grain boundary stability and properties. The thermodynamic stability of GBs is characterised by the grain boundary energy, γ_{GB} (see Eq.(4.1) for the case of pure Mo GBs). The GB energy is also strongly correlated with the level of solute segregation at the GB [14]. Therefore, changes in GB energy also reflect the segregation tendency of a solute for a particular

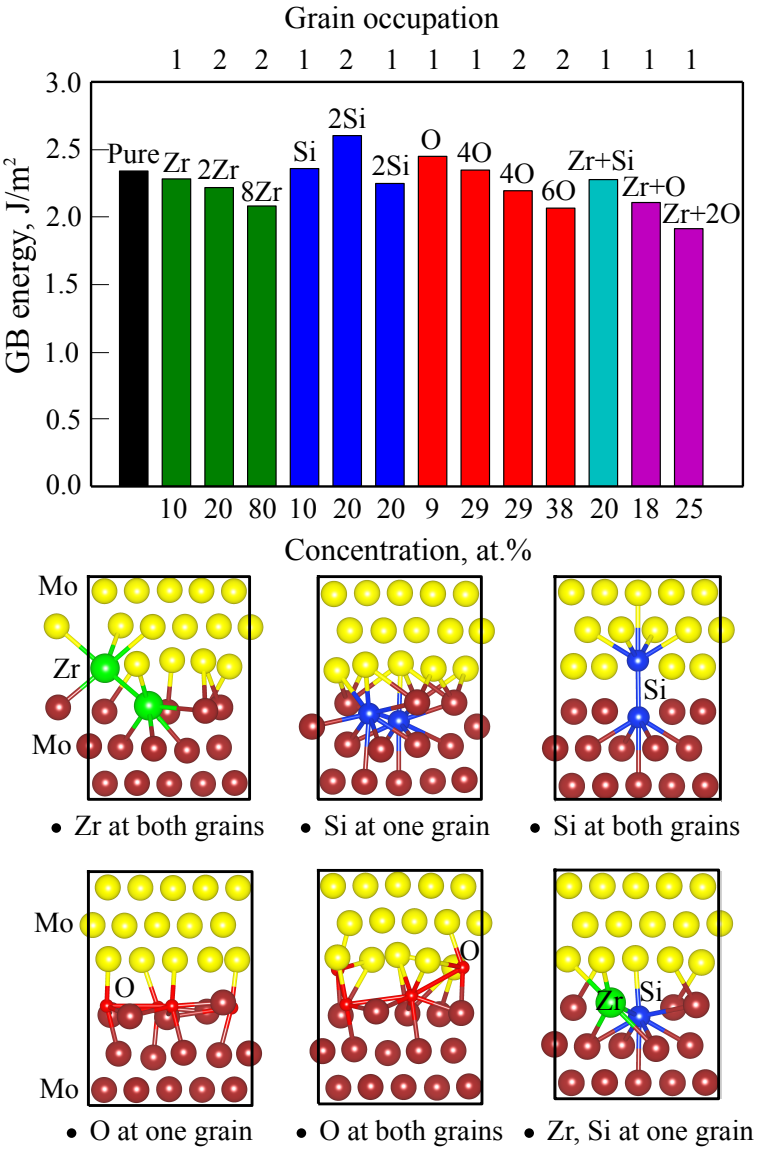

Figure 36: Grain boundary energy of pure and solute containing twist Σ5[001] Mo GB. Zr and Si are inserted substitutionally and occupy the low-energy positions, whereas oxygen is inserted interstitially. The concentration of solutes is given with respect to the number of atoms that form a GB (ten Mo atoms). Numbers on the top panel correspond to location of the solute within one grain ("1") or at both sides of the GB ("2"). Atomistic models of different GBs are shown on the bottom of the figure. Yellow and dark red spheres represent Mo atoms that belong to different grains. Zirconium atoms are denoted in green, silicon in blue and oxygen is red.

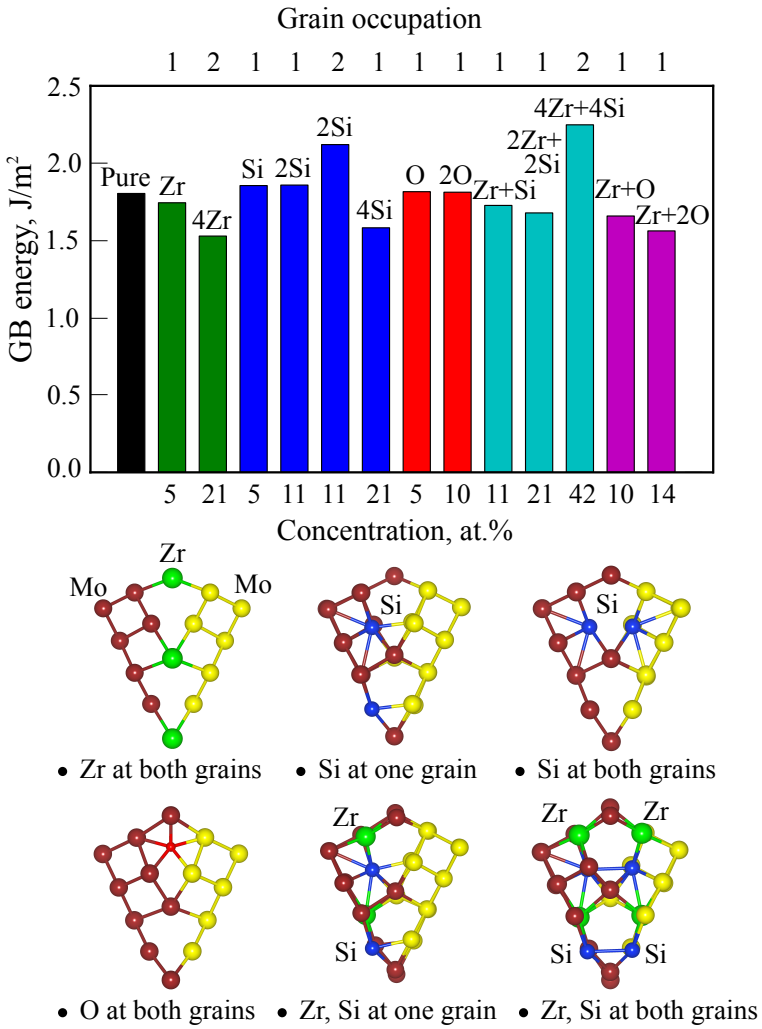

Figure 37: Grain boundary energy of pure and solute containing tilt Σ5(310)[001] Mo GB. Zr and Si are inserted substitutionally and occupy the low-energy positions, whereas oxygen is inserted interstitially. The concentration of solutes is given with respect to the number of atoms that form a GB (nineteen Mo atoms). Numbers on the top panel correspond to location of the solute within one grain (“1”) or at both sides of the GB (“2”). Atomistic models of different GBs are shown on the bottom of the figure. Colour coding: see Figure 36.

GB site indicating site-specific solute segregation. The reduction in γ_{GB} is the most pronounced when the solute segregation at GBs is strong.

The grain boundary energy of the GB containing a solute is defined as

$$\gamma_{\mathrm{GB\,+\,solute}} = \frac{1}{A}\left(E_{\mathrm{GB\,+\,y\cdot solute}} - (N - k\cdot y)\cdot \epsilon_{\mathrm{Mo}} - y\cdot \mu_{\mathrm{solute}}\right), \tag{4.9}$$

and the surface energy of the surface with segregated solute is

$$\sigma_{\mathrm{Surface\,+\,solute}} = \frac{1}{2A}\left(E_{\mathrm{Surface\,+\,y\cdot solute}} - (N - k\cdot y)\cdot \epsilon_{\mathrm{Mo}} - y\cdot \mu_{\mathrm{solute}}\right). \tag{4.10}$$

The chemical potential for Zr is calculated according to

$$\mu_{\mathrm{Zr}} = \epsilon_{\mathrm{Mo_2Zr}} - 2\cdot \epsilon_{\mathrm{Mo}}, \tag{4.11}$$

for Si

$$\mu_{\mathrm{Si}} = \epsilon_{\mathrm{Mo_3Si}} - 3\cdot \epsilon_{\mathrm{Mo}}, \tag{4.12}$$

and for O

$$\mu_{\mathrm{O}} = \frac{1}{3}\left(\epsilon_{\mathrm{MoO_3}} - \epsilon_{\mathrm{Mo}}\right). \tag{4.13}$$

In the equation $k = 1$ for solute inserted substitutionally (Zr, Si) and $k = 0$ if a solute occupies interstitial site (O). Here, $E_{\mathrm{GB\,+\,y\cdot solute}}$ and $E_{\mathrm{Surface\,+\,y\cdot solute}}$ are the total energies of the GB and surface with segregated solute, respectively. N is the total number of Mo atoms in the supercell and ϵ_{Mo} is the total energy per atom of bulk Mo. The GB energy is defined per unit area of the grain boundary, A. Mo_2Zr, Mo_3Si and MoO_3 phases have been chosen as reference states for Zr, Si and O. Details are provided in Section 3.1. MoO_3 is used since it is the principal stable oxide phase [197].

In the following, the changes in the grain boundary energy ($\gamma_{\mathrm{GB+solute}}$) and in the surface energy ($\sigma_{\mathrm{Surface+solute}}$) induced by solute segregation are investigated. As discussed in Section 2.7.2, ideal brittle fracture can be modelled based on total energies by computing the reversible work needed to separate the interface into two surfaces called the work of separation (see Eq.(2.66)). After cleavage, solutes segregated at a GB will decorate one of the newly created surfaces (see Figure 20). In the case when several solute atoms or different solute species are segregated at the GB, the final distribution of solutes at the surfaces depends on site competition and mutual interactions between solutes. The work of separation is discussed further in Chapter 5. Here, the stability of grain boundaries and surfaces are described.

The GB energy of the pure and solute containing twist $\Sigma5[001]$ and tilt $\Sigma5(310)[001]$ Mo GBs is shown on Figures 36–37. Zr and Si in different concentration, their combination and the presence of oxygen are considered. The GB structures are shown on

the bottom panel. The results show that Zr segregation at low-energy segregation sites always decreases the GB energy and thus stabilise the Mo GB. The reduction in γ_{GB} scales proportionally with the Zr concentration at the GB. This result is independent of the GB structure. Moreover, assuming an open system with oxygen supply, the GB energy is reduced when Zr and oxygen decorate the GB compared to the case when only Zr or O is present at the GB,

$$\gamma_{GB+Zr+O} < \frac{1}{2}(\gamma_{GB+Zr} + \gamma_{GB+O}). \tag{4.14}$$

Using Mo_2Zr and MoO_3 as references for Zr and oxygen, the GB energy is equal to

$$2.11\ \text{J/m}^2 < \tfrac{1}{2}(2.28\ \text{J/m}^2 + 2.45\ \text{J/m}^2).$$

The reduction in the GB energy indicates that gettering oxygen by Zr at the GB is energetically favourable.

In the presence of Si at the GBs, the GB energy slightly increases reflecting a small positive formation energy of Si at the energetically preferred segregation site. Increasing the Si content at the GB, the GB energy can be reduced or increased, depending on the mutual distribution of Si atoms. Consistent with finding in Section 4.2.2, the results show that Si atoms prefer to occupy sites on the same side of the GB, thus reducing the GB energy. The distribution of Si atoms ontop of each other on both sides of the GB is energetically unfavourable, which is reflected by an increase in γ_{GB} (for example, by 11% at the twist GB). A mutual distribution of oxygen atoms also affects pronouncedly the GB energy and its stability. For example, the twist GB containing four oxygen atom within one grain exhibits the same GB energy as a pure twist GB, whereas segregation of two oxygen atoms on both sides of the GB (see structures at the bottom panel in Figure 36) reduces γ_{GB} by 6%. Due to the large excess volume inside the tilt GB, segregation of few oxygen atoms does not affect the GB much. The interplay between Zr and Si atoms located at the GB is also important for the GB stability.

As a next step, the influence of solute segregation on the stability of Mo surfaces is investigated. When a twist Σ5 GB is cleaved, two Mo(001) surfaces are created. Cleavage of tilt Σ5 GB results into formation of two Mo(310) surfaces. The atomic structures of Mo(001) and Mo(310) surfaces are shown on Figure 29. The variation of surface energy of the Mo(001) and Mo(310) surfaces with different segregated species is illustrated on Figures 39–38. In contrast to GBs, surface segregation always reduces the surface energy for both surfaces. The reduction in σ_{Mo} is proportional to the number of segregated atoms. For example, segregation of one Zr atom on the surface causes a reduction in $\sigma_{Mo(001)}$ by 11%, whereas for four Zr atoms $\sigma_{Mo(001)}$ decreases already by 33%. The magnitude of surface energy reduction is slightly more

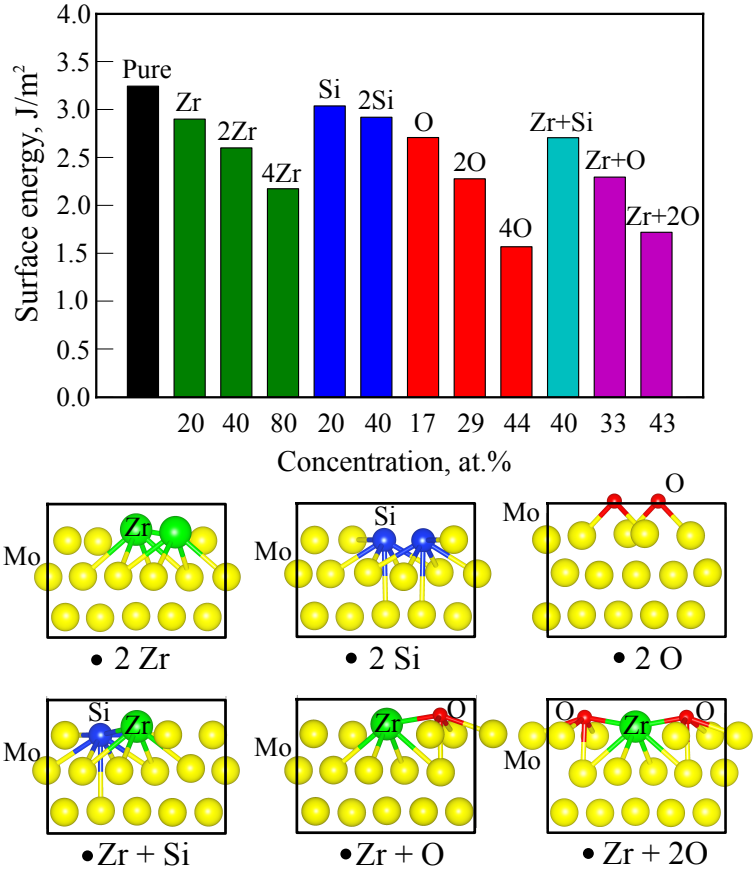

Figure 38: Surface energy of pure and solute containing Mo(001) surfaces. Zr and Si are inserted substitutionally and oxygen is adsorbed on the surface. Colour coding: see Figure 36.

pronounced for the Mo(001) surface compared to the Mo(310) surface, especially for Zr segregation, also in the presence of two oxygen atoms. The concentration of solutes per unit surface area is higher at the Mo(001) surface resulting in a slightly stronger image interaction.

4.4 STRAIN AND CHEMICAL ANALYSIS

The driving force for solute segregation is controlled by two counterbalancing contributions. The first contribution is the elimination of the elastic strain energy, ΔE_{strain}, caused by a solute misfit in the solvent lattice. The second contribution accounts for changes in the binding energy due to the presence of solute atom, ΔE_{chem}. Decomposition of solutes formation energies into the elastic strain energy and chemical bond

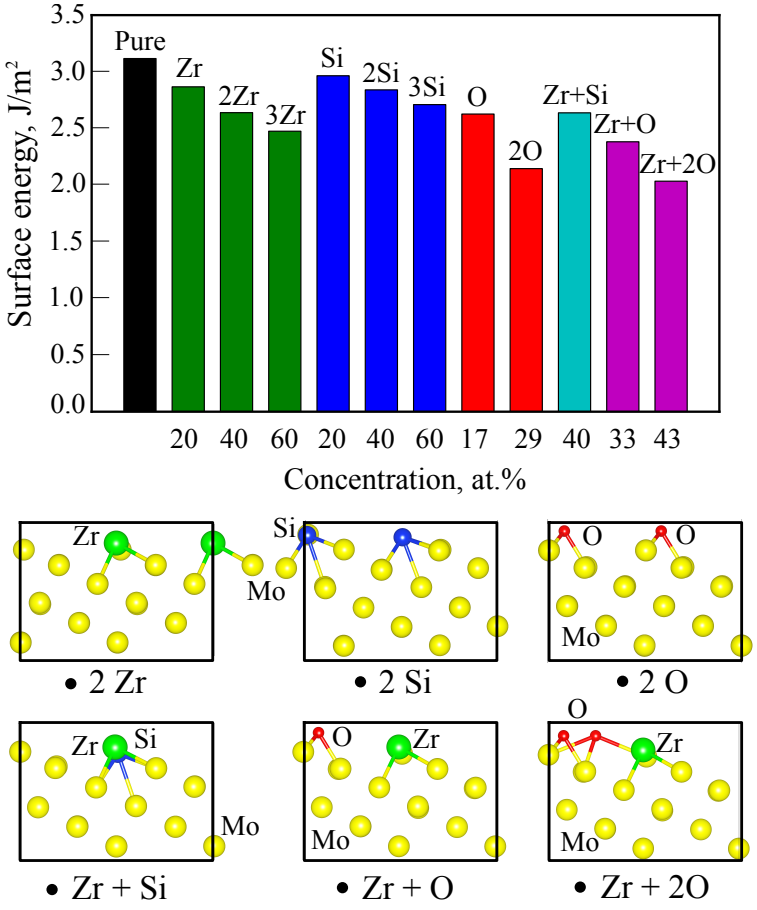

Figure 39: Surface energy of pure and solute containing Mo(310) surfaces. Zr and Si are inserted substitutionally and oxygen is adsorbed on the surface. Colour coding: see Figure 36.

energy allows to shed some light on the origin of the embrittling/enhancing behaviour of a solute.

Figure 40 shows the formation energies of Zr and Si solutes along with individual contributions from elastic strain and chemical bonding. The chemical contribution to the binding energy for Mo ($E_{\text{chem, Mo}}$) is denoted in red and those for a solute ($E_{\text{chem, solute}}$) is denoted in yellow. Chemical contribution (ΔE_{chem}) is computed as a difference between $E_{\text{chem, solute}}$ and $E_{\text{chem, Mo}}$ and is denoted in purple. A green column corresponds to mechanically stored strain energy (ΔE_{strain}) and the blue column represents the total formation energy of a solute. In both GB geometries Zr and Si are inserted substitutionally on the lowest-energy segregation sites. Since Si and Zr prefer different sites for segregation at both GBs, $E_{\text{chem, Mo}}$ differs in the

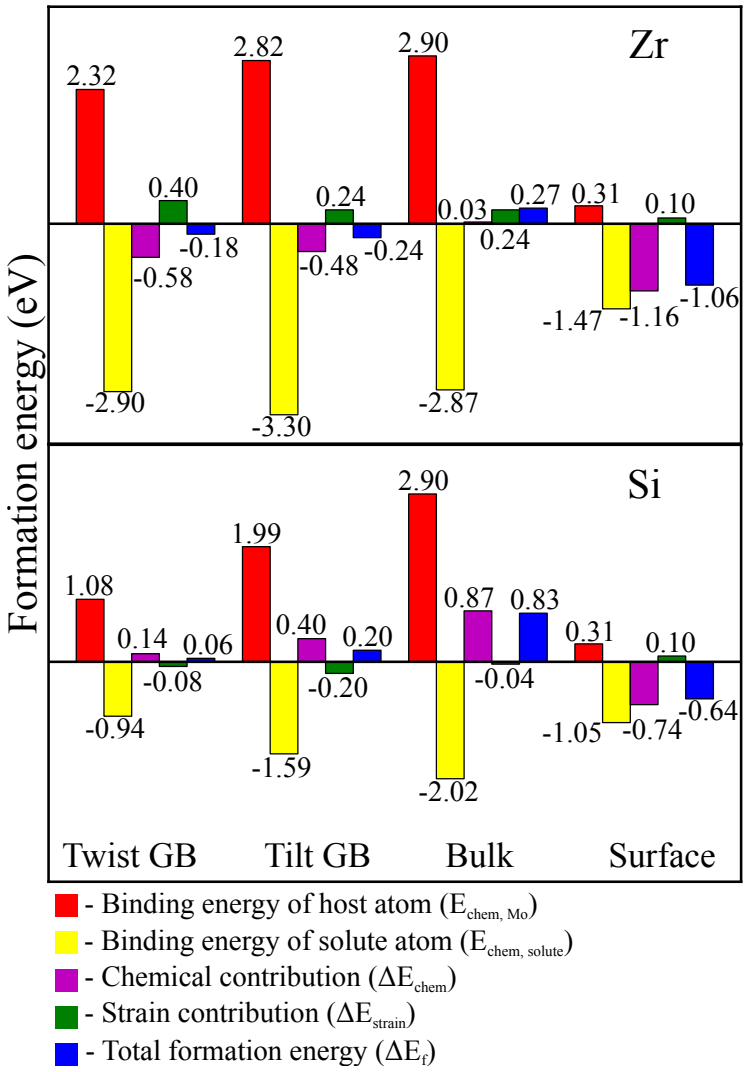

Figure 40: Contributions to the formation energy of Zr and Si segregated at twist and tilt Mo GB, in the Mo bulk and at Mo(001) surface. Solutes occupy energetically preferred sites at the GBs.

Si and Zr analysis. Computational details concerning all contributions are given in Section 3.2.

The negative value of ΔE_{chem} for Zr indicates that Zr is chemically a strong enhancer of Mo. Chemical contribution to the Zr-Mo binding energy is 0.58 eV, 0.48 eV and 1.16 eV lower (which means stronger) at the twist and tilt GBs and at Mo(001) surface compared to pure system, respectively. In contrast, the elastic strain energy exhibits positive values for all investigated systems, possessing the smallest value at the surface, ΔE_{strain} = 0.10 eV, and the largest value at the twist GB, ΔE_{strain} = 0.40 eV. According to Rice and Wang [76], a solute is expected to behave as an embrittler if its formation energy at the interface is higher than the formation energy at the corresponding surface. In total, the formation energy of Zr is higher at the GB (-0.18 eV for twist GB) compared to the corresponding Mo(001) surface (-1.06 eV) and Zr behaves as a weak intrinsic embrittler. The origin of embrittling behaviour of Zr arises from the elastic strain energy associated with the large atomic radius of Zr. The misfit energies at the twist GB is larger than the misfit energies at the tilt GB and in the bulk Mo. This is directly connected to the structure of the twist GB which is more constrained (more densely packed) and the large Zr is producing more lattice strain. Thus, extrapolation to the case of a general GB presumes that the strain energy contribution becomes much smaller, while the chemical energy contribution should be comparable.

Silicon, in contrast to zirconium, is much smaller in size. Due to the fact that Mo atoms located around a Mo vacancy generally contract, the strain energy even becomes negative for Si, ΔE_{strain} = -0.08 eV for the twist GB and ΔE_{strain} = -0.20 eV for the tilt GB. However, Si is a much less attractive chemical bonding partner for Mo. The difference in chemical contribution to the Mo-Mo and Mo-Si binding energies is positive and varies in the range from 0.14 eV till 0.40 eV for different GB geometries. In the bulk Mo ΔE_{chem} rises up to 0.87 eV. In total, similar to Zr, the formation energy of Si is lower at Mo(001)surface (-0.64 eV) compared to those at the GB (0.06 eV for the twist GB). Silicon also embrittles Mo, but due to weak chemical bonds.

The interplay between chemical bonding and size-related elastic strain energies determines the overall (embrittling or enhancing) behaviour of solutes. A potential candidate for GB strengthening in Mo should show a Zr-like chemistry, on one hand, and should have a small atomic radius, on the other hand. It is likely that a small-sized solute will rather segregate at a GB than at a surface, because of the more dense atomic environment in a GB. Scheiber *et al.* [75] has investigated the embrittling/enhancing potential (ΔE_{EP}) of transition metals (from Sc to Hg) on $\Sigma 3(110)[\bar{1}11]$ GB in molybdenum. This study reveals that the elements in the centre of the d-band, namely Cr, Mn, Fe, Co, Ni, Ru, Rh, Os and Ir act as strong enhancers of molybdenum GB. Tran *et al.* [74] have investigated the embrittling/enhancing potential of transition metals in twist and tilt $\Sigma 5$ bicrystals in molybdenum. The

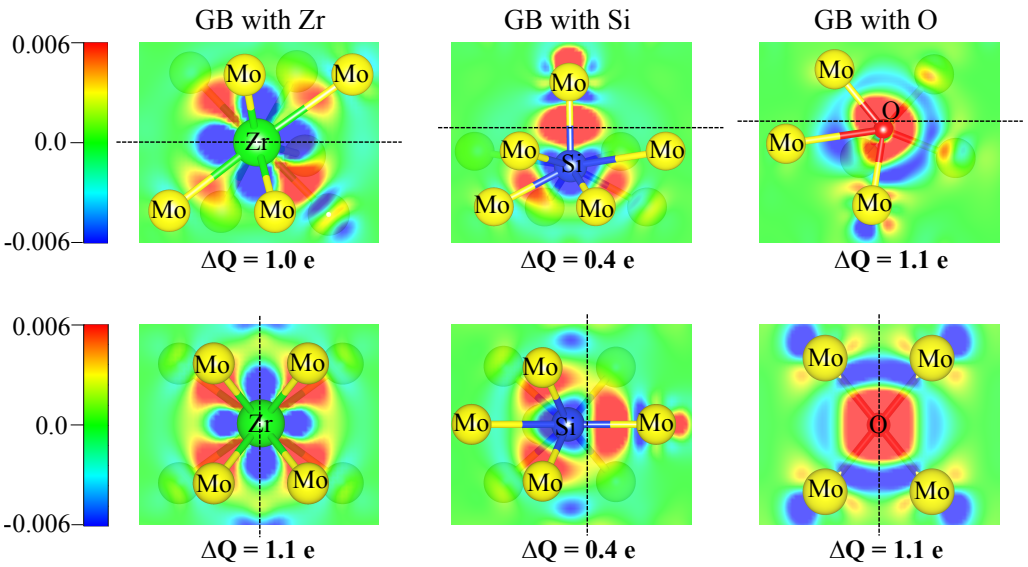

Figure 41: Bonding nature of solutes in twist Σ5[001] (top panel) and tilt Σ5(310)[001] (bottom panel) GBs in molybdenum. Contour plot of the charge density difference (computed using Eq.(4.15)) indicates depletion of electronic charge (blue contours) or its accumulation (red contours) in the solute containing GBs. ΔQ corresponds to the change of charge on the solute to (from) neighbouring Mo atoms in units of e. Black dashed lines represent grain boundary planes.

authors claim that Ta, Re, Os and W have a weak strengthening effect on Mo tilt Σ5(310)[001] and Mn, Fe, Co and Nb have reasonable strengthening effects on the twist Σ5[001] Mo GB. All listed elements are smaller or similar in size than Mo, which should result in a partial or complete elimination of the strain energy contribution. The authors emphasise the importance of considering both chemical and elastic contributions of the segregation energies in phenomenological models aiming to predict the embrittling potential of solutes. Unfortunately, the individual contributions to the formation energies of solutes has not been provided.

4.5 ELECTRONIC STRUCTURE ANALYSIS

A well-known consequence of solute segregation at grain boundaries is the GB embrittlement caused by a reduction of GB cohesion induced by solutes. One of the origins of the solute-induced embrittlement is charge redistribution [14]. If more electronegative atoms segregate at the GB, they withdraw electrons from the metal d-band and weaken the strength of metallic bond. If the bonds across GBs are weakened,

the GBs fails in a brittle manner. A potential GB strengthener is a solute that forms strong bonds perpendicular to the GB.

The bonding nature between Mo and the solutes is investigated using charge-density differences and a Bader charge analysis [125]. In detail, the charge-density differences are computed as

$$\Delta n = n_{\mathrm{GB+X}} - n_{\mathrm{GB+V}} - n_{\mathrm{X}}, \tag{4.15}$$

where $n_{\mathrm{GB+X}}$ and $n_{\mathrm{GB+V}}$ are the charge density of Mo GBs containing X (X = Zr, Si, O) or a vacancy, respectively. Here, n_{X} the charge density of the isolated X atom.

Figure 41 shows a contour plot of the charge density difference of the twist Σ5[001] (top panel) and tilt Σ5(310)[001] (bottom panel) Mo GBs containing Zr, Si and O. The grain boundary plane is indicated by the dashed black line. Figure 41 shows an accumulation of charge with a maximum located halfway along Mo-Zr and Mo-Si bond lines. For Mo-O system, charge is transferred closer to oxygen atom. The analysis of the bond strength shows a charge transfer from Zr to Mo of 1.0–1.1 *e* in the twist and tilt GBs. The additional charge is distributed within the neighbouring Mo atoms, located at a distance of ∼2.70–3.15 Å. In the Mo-Si system 0.4 *e* is transferred from Mo atoms to Si, same in both GBs. In the Mo-O system a charge transfer of 1.1 *e* from Mo to O is identified in both GB geometries. The individual Mo-Zr bonds are stronger compared to Mo-Si bonds, which is consistent with the analysis of chemical bonding contributions investigated in Section 4.4. In general, individual Mo-O bonds are stronger compared to Mo-Zr bonds, which is in line with electronegativity of elements. Mo-Zr and Mo-Si bonds are identified as mixed ionic-covalent bonds, whereas Mo-O bond is ionic.

Atomic structure of the GB and the position where the solute is located influence on the electronic structure and charge distribution in the system. In particular, size of the region that participates in charge transfer from (to) a solute is larger in the twist GB compared to that in the tilt GB. In the tilt GB the charge from (to) a solute is mainly transferred from the neighbouring Mo atoms located at a distance of ∼2.70–3.15 Å, while in the twist GB this region is larger.

Figure 41 shows that zirconium creates strong bonds with Mo atoms located both within the grain and across the GB. The GB plane is represented by a black dashed line. As shown by the strain and chemical bonding analysis given in Section 4.4, embrittlement of Mo GBs due to Zr segregation is related to elastic distortions produced by Zr at the GBs. Zr pushes apart atoms across the GB and thus weaken the bonding between two grains. In Mo-Si and Mo-O systems, the charge transfer from Mo atoms located across the GB weakens the strength of metallic bond and thus promotes the GBs failure in a brittle manner. Oxygen acts as a stronger embrittlement compared to Si.

4.6 CONCLUSIONS

In the present chapter the segregation tendency of zirconium, silicon and oxygen at molybdenum grain boundaries is investigated. Molybdenum Σ5 tilt and twist grain boundaries in bicrystal geometry are chosen as structural models. Both solutes and oxygen show a strong tendency to segregate to grain boundaries or to surfaces, if low-energy segregation sites (for Zr and Si) are available. The hierarchy of the segregation tendency corresponds to $\Delta E_{\mathrm{f,\,Zr}} < \Delta E_{\mathrm{f,\,Si}} \ll \Delta E_{\mathrm{f,\,O}}$. Qualitatively, the grain boundary segregation tendency is inverse to the solid solubility. The site preferences for solutes at a grain boundary has been identified. Zirconium occupies sites showing more excess volume and silicon occupies more densely packed lattice sites. This is why no site competition between zirconium and silicon is identified in the dilute limit. The competition between zirconium and silicon for segregation sites is found in more densely-packed grain boundaries upon increasing silicon concentration. The presence of zirconium at the grain boundary promotes the segregation of silicon at the grain boundary and *vice versa*.

Solute segregation at the grain boundary (surface) affects the grain boundary (surface) stability. This is reflected by changes in the grain boundary (surface) energy. Solute segregation at the surface always reduces the surface energy stabilising the surface. When a solute is located at the grain boundary, the grain boundary energy can be reduced or increased, depending on the segregation site and distribution of solutes. The number of dangling bonds at the surface is higher compared to that at the grain boundary and therefore the binding at the surface is stronger. The elastic distortion due to solute incorporation to the lattice is more pronounced at the grain boundary compared to the surface.

The influence of solutes and of oxygen on grain boundary embrittlement is evaluated by means of the Rice-Wang criterion. Since zirconium and silicon prefer to segregate at the surface compared to the grain boundary in molybdenum, they behave as embrittles of molybdenum grain boundaries. The analysis of elastic strain and chemical bond contributions shows that the strain energy required to accommodate zirconium at the grain boundaries counteracts the gain in chemical (bonding) energy and therefore zirconium behaves as a embrittler of molybdenum. In contrast to zirconium, silicon embrittles molybdenum grain boundaries since it substitutes strong Mo-Mo bonds with weaker Mo-Si bonds. The overall embrittling behaviour of zirconium can be minimised in the presence of grain boundaries that provide more excess volume or by using solutes with a Zr-like chemistry but smaller atomic radius.

5

GRAIN BOUNDARY COHESION

Parts of this chapter are published in *Journal of Materials Science* 51, 1873–81 (2016).

In the present Chapter the influence of solutes on the cohesive strength of grain boundaries in molybdenum is investigated. Ductility and fracture toughness of materials are limited by GB decohesion, which can be manipulated by solute segregation. Grain boundary segregation induces changes in the atomic structure and chemical bonding within the decorated GB and affects the GB cohesive strength. The stability of the Mo GB against brittle fracture has been investigated. Based on total energies the embrittlement of GBs by solute segregation is predicted by means of the ideal work of separation given by the Dupré-equation. Leaving the energy contributions aside, an alternative approach is to analyse the theoretical strength of the interface, which describes the maximum strength of a chemical bond between atoms [163]. Using energy-based and stress-based criteria it is possible to measure the influence of solutes on the GB resistance to fracture.

In this chapter, the work of separation and the theoretical strength of twist and tilt Σ5 Mo GBs containing solutes (Zr, Si) and oxygen in different concentrations and various combinations of solutes are evaluated.

5.1 IDEAL WORK OF SEPARATION

Intergranular fracture passes through by breaking the weakest bonds at the interface. In order to find the lowest-energy fracture path, different cleavage planes and distribution of the segregated species at the newly created fracture surfaces have to be carefully investigated. The stability of GBs with segregated solutes is first evaluated by means of the ideal work of separation, $W_{\mathrm{sep}}^{\infty}$, described in detail in Section 2.7.2. Figures 42–48 illustrate the atomic structure of twist and tilt Σ5 grain boundaries containing Zr, Si and O in different concentration, as well as combination of solutes, investigated in the present study. GB cleavage with and without further structural relaxation of the resulting surfaces is considered. The latter procedure can be considered as a measure for the chemical contribution to the $W_{\mathrm{sep}}^{\infty}$.

The work of separation is summarised in Table 17 for twist and in Table 16 for tilt Σ5 bicrystals. The results show that alloying the GB with Zr, Si, O or any of the considered combinations generally decreases (or at least does not significantly

Table 16: Work of separation W_{sep}^{∞} in J m^{-2} for the pure and alloyed twist Σ5[001] GB in molybdenum.

	Twist (rigid)	Twist (relaxed)
Pure GB	4.64	4.06
Zr	4.29	3.82
Si	4.44	3.88
O	4.21	3.50
2Zr	4.10	3.56
8Zr	2.60	2.22
2Si	5.54	3.88
4Si	3.71	2.91
2O	3.98	3.15
4O	3.48	2.53
5O	2.87	2.09
6O	2.59	2.11
Zr+Si	4.15	3.63
2Zr+Si	4.24	3.38
4Zr+2Si	3.08	2.19
Zr+O	3.87	3.38
Zr+2O	3.59	2.98

Table 17: Work of separation W_{sep}^{∞} in J m^{-2} for the pure and alloyed tilt Σ5(310)[001] Mo GB.

	Tilt (rigid)	Tilt (relaxed)
Pure GB	5.35	4.44
Zr	5.05	4.26
Si	5.47	4.50
O	5.20	4.27
4Zr	4.58	3.94
8Zr	4.62	3.80
2Si	4.90	4.11
4Si	4.87	4.14
2O	5.01	4.11
4O	4.10	2.80
Zr+Si	5.01	4.18
2Zr+Si	5.11	4.38
3Zr+2Si	4.57	3.82
2Zr+2Si	4.59	3.81
4Zr+4Si	4.31	3.43
Zr+O	5.31	4.10
Zr+2O	4.64	3.93

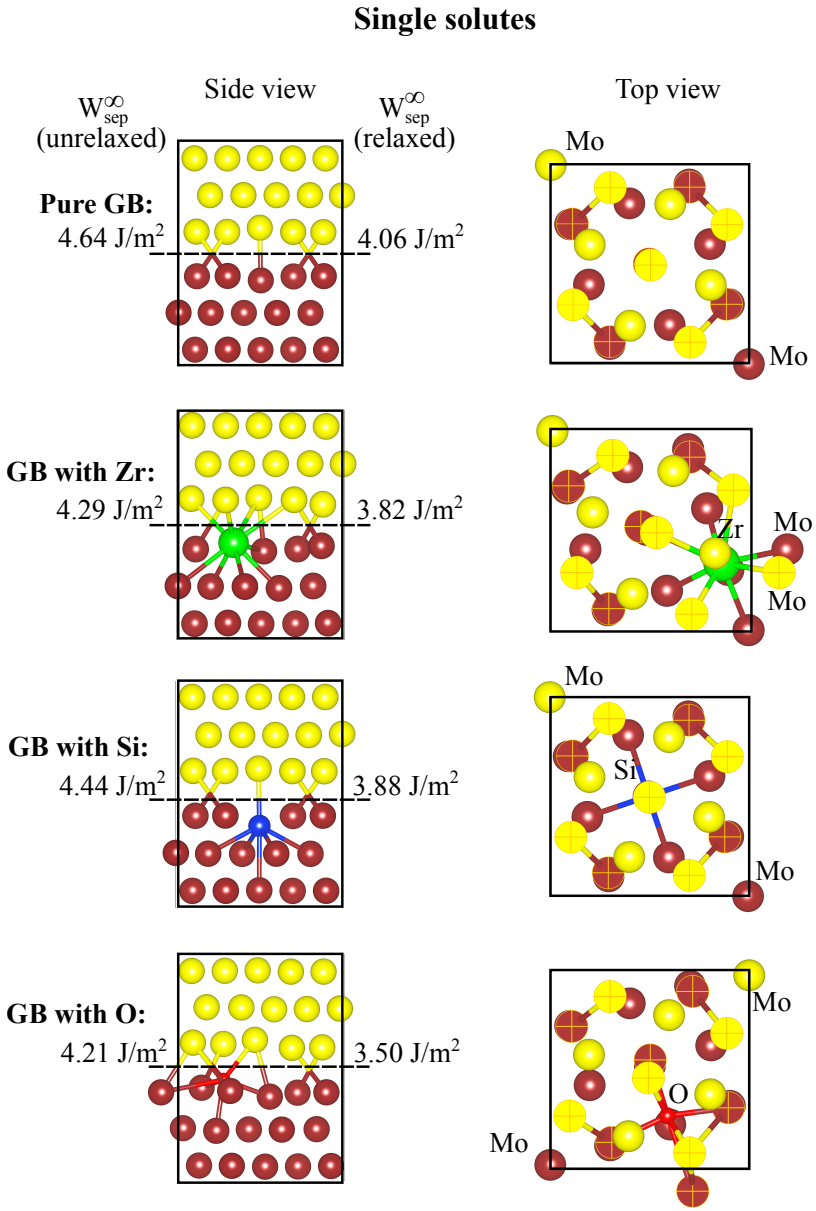

Figure 42: Close-up of the pure and solutes containing twist Σ5[001] Mo grain boundary, projected along the [100] axis ("Side view") and along the [001] axis ("Top view"). Molybdenum atoms that belong to different grains are represented as dark red (for grain I) and yellow (for grain II) spheres. Green spheres denote zirconium atoms, blue ones denote silicon atoms and red spheres denote oxygen atoms. Atoms that form a GB are highlighted. Black dashed lines indicate the cleavage planes. Numbers show the ideal work of separation for a given cleavage plane: rigid W^{∞}_{sep}(rigid) is reported on the left-hand side and relaxed W^{∞}_{sep}(relaxed) is reported on the right-hand side of the GB.

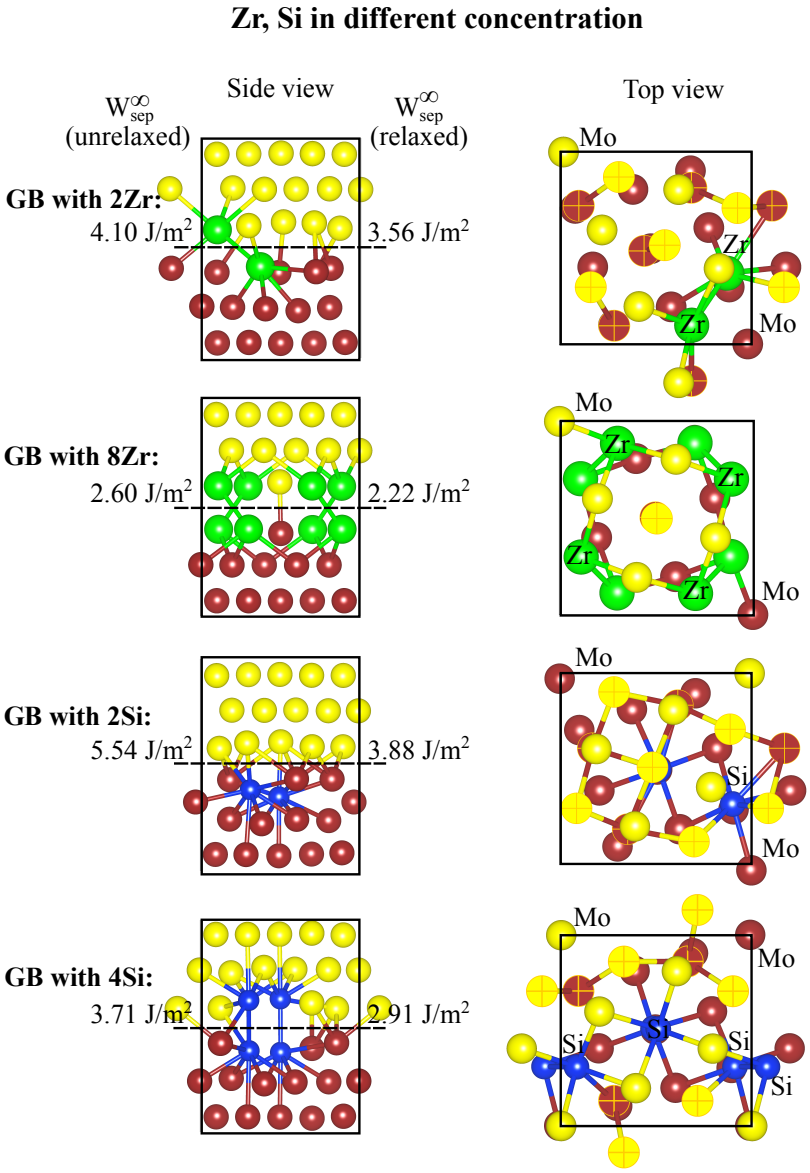

Figure 43: Close-up of the pure and solutes containing twist Σ5[001] Mo grain boundary, projected along the [100] axis ("Side view") and along the [001] axis ("Top view"). Colour coding: see Figure 42. Black dashed lines show cleavage planes. Numbers show the ideal work of separation for a given cleavage plane: rigid W_{sep}^{∞}(rigid) is reported on the left-hand side and relaxed W_{sep}^{∞}(relaxed) is reported on the right-hand side of the GB.

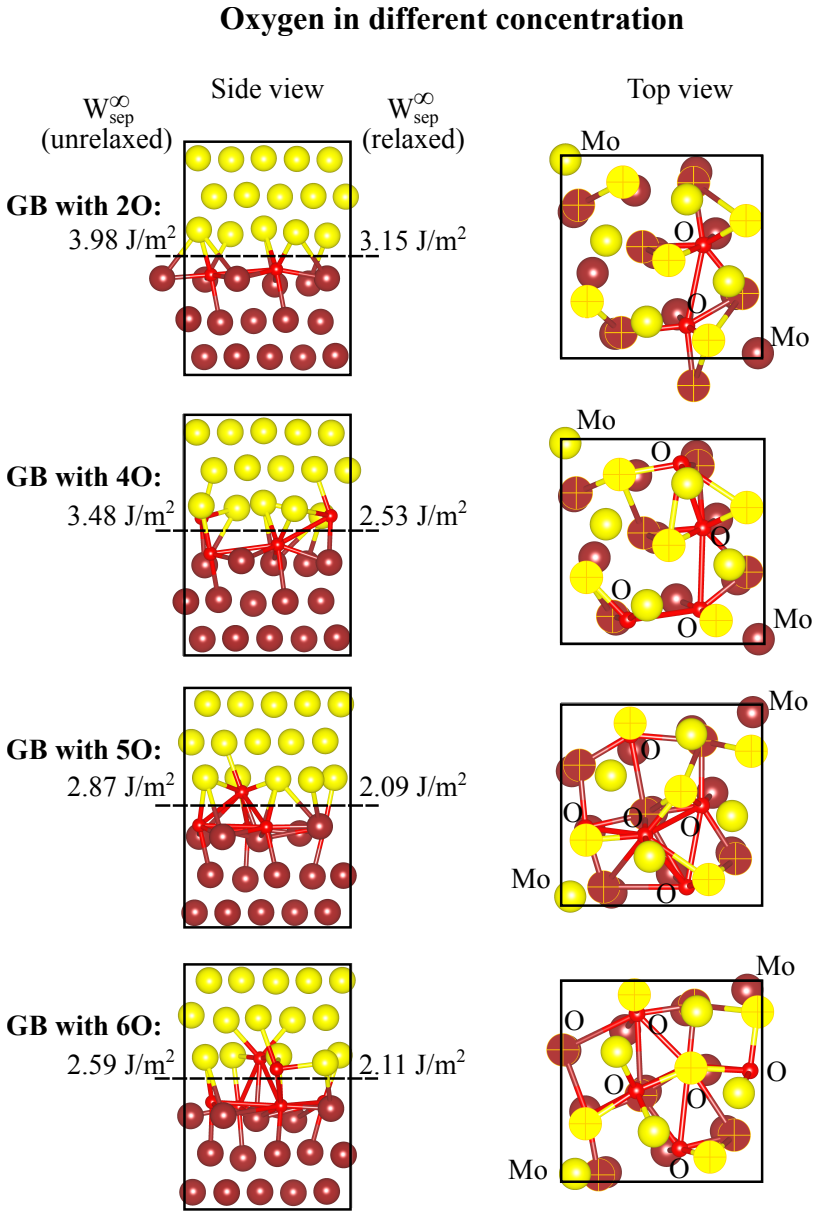

Figure 44: Close-up of the pure and solutes containing twist Σ5[001] Mo grain boundary, projected along the [100] axis ("Side view") and along the [001] axis ("Top view"). Colour coding: see Figure 42. Black dashed lines show cleavage planes. Numbers show the ideal work of separation for a given cleavage plane: rigid W_{sep}^{∞}(rigid) is reported on the left-hand side and relaxed W_{sep}^{∞}(relaxed) is reported on the right-hand side of the GB.

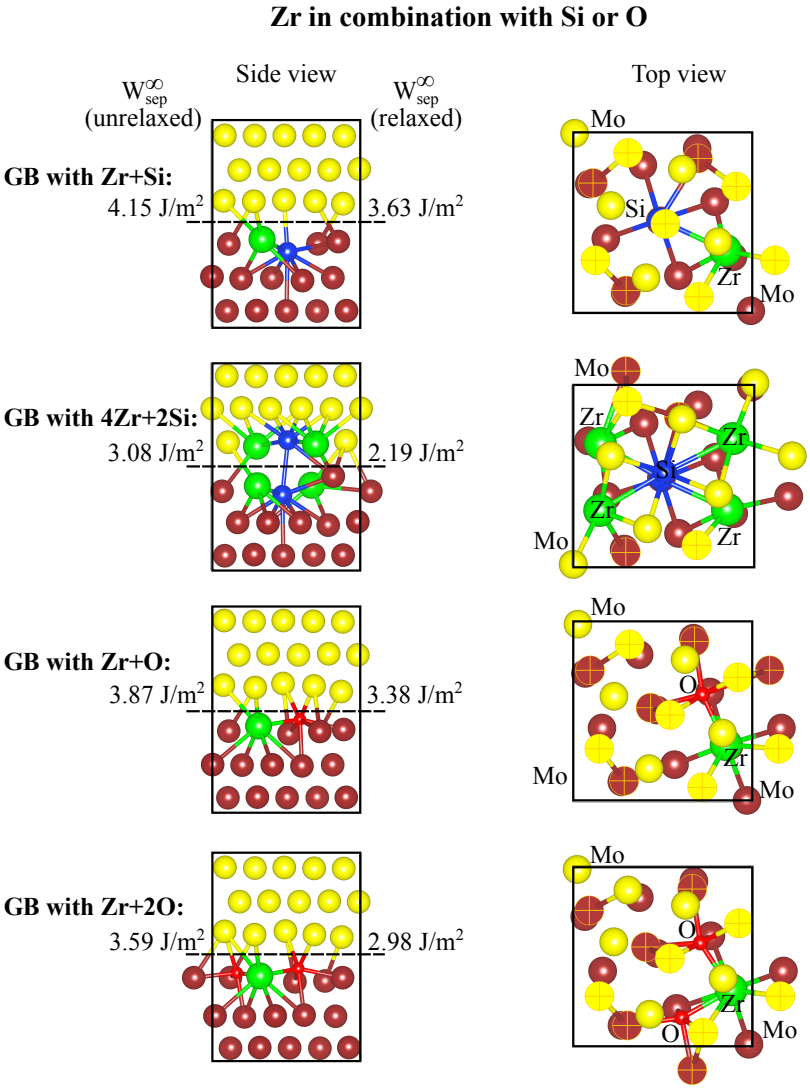

Figure 45: Close-up of the pure and solutes containing twist Σ5[001] Mo grain boundary, projected along the [100] axis ("Side view") and along the [001] axis ("Top view"). Colour coding: see Figure 42. Black dashed lines show cleavage planes. Numbers show the ideal work of separation for a given cleavage plane: rigid W_{sep}^{∞}(rigid) is reported on the left-hand side and relaxed W_{sep}^{∞}(relaxed) is reported on the right-hand side of the GB.

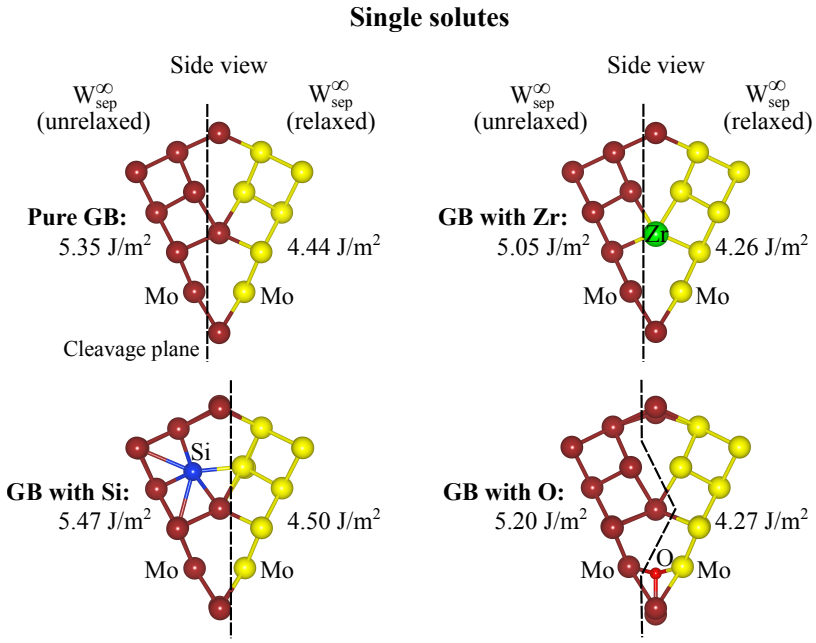

Figure 46: Close-up of the pure and solutes containing tilt Σ5(310)[001] Mo grain boundary, projected along the [100] axis ("Side view") and along the [001] axis ("Top view"). Colour coding: see Figure 42. Black dashed lines show cleavage planes. Numbers show the ideal work of separation for a given cleavage plane: rigid W^{∞}_{sep}(rigid) is reported on the left-hand side and relaxed W^{∞}_{sep}(relaxed) is reported on the right-hand side of the GB.

increase) W^{∞}_{sep}. In line with the Rice-Wang theory [76], the decrease in W^{∞}_{sep} is generally larger for Zr than for Si, independent of whether we consider unrelaxed or relaxed W^{∞}_{sep} and independent of the particular GB. The decrease in the work of separation is evidencing that the energy released during structural relaxation will facilitate the fracture of the GB [198]. This decrease is proportional to the amount of solute atoms at the GB and in general is more pronounced for the twist GB than for the tilt GB. This difference is caused both by the GB structure and by the lower concentration of solutes at the tilt GB due to its larger interface area. When Zr and Si or Zr and O is segregated at the GB, the lowest cleavage energy is found when the cleavage plane passes through the GB leaving all solutes on the same newly created surface.

The work of separation also reflects the finding that the mutual distribution of solutes affects the stability of GBs significantly. This effect is most pronounced for silicon and oxygen. For example, two silicon atoms segregated at the twist GB and located on one side of the GB decrease W^{∞}_{sep} by 4%, while segregation of two Si atoms

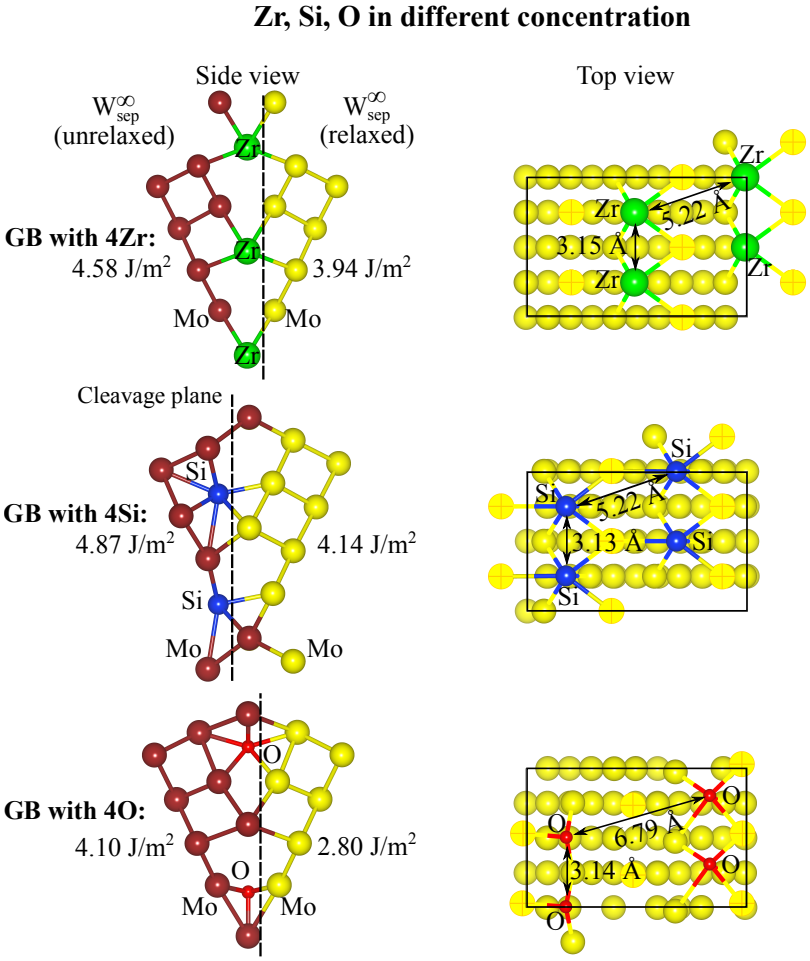

Figure 47: Close-up of the pure and solutes containing tilt Σ5(310)[001] Mo grain boundary, projected along the [100] axis ("Side view") and along the [001] axis ("Top view"). Colour coding: see Figure 42. Black dashed lines show cleavage planes. Numbers show the ideal work of separation for a given cleavage plane: rigid W^{∞}_{sep}(rigid) is reported on the left-hand side and relaxed W^{∞}_{sep}(relaxed) is reported on the right-hand side of the GB.

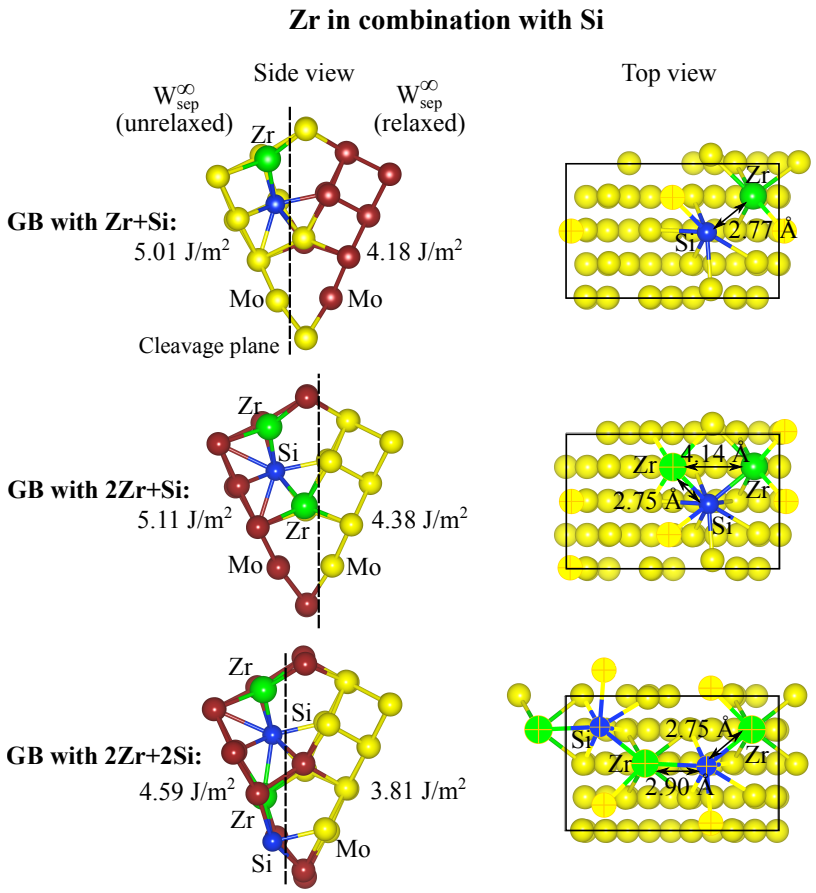

Figure 48: Close-up of the pure and solutes containing tilt Σ5(310)[001] Mo grain boundary, projected along the [100] axis ("Side view") and along the [001] axis ("Top view"). Colour coding: see Figure 42. Black dashed lines show cleavage planes. Numbers show the ideal work of separation for a given cleavage plane: rigid W^{∞}_{sep}(rigid) is reported on the left-hand side and relaxed W^{∞}_{sep}(relaxed) is reported on the right-hand side of the GB.

on the same sites but located on both sides of the GB each results into a reduction of W_{sep}^{∞} by 28% (see Figure 43). Two silicon atoms, segregated at the same grain in the twist GB, penetrate deeper inside the grain and cause rearrangement of Mo atoms at the GB. Because of this rearrangement the rigid W_{sep}^{∞} for the GB is increased compared to the pure GB. Segregation of Si at the tilt GB causes a slight increase of W_{sep}^{∞} of about 1%. Afterwards the work of separation decreases with increasing Si concentration. Experimentally, for small Si concentrations (0.34 at.%) solid solution softening was observed at room temperature and below. With increasing Si concentration, the room-temperature ductility and fracture toughness dropped precipitously. This is attributed to the increase in strength due to Si, and a transition from transgranular to intergranular fracture [1].

For O at the tilt GB, the work of separation decreases at around 4%, the same as for Zr. But according to the embrittling potential ($\Delta E_{EP,\,Zr} = 0.88$ eV and $\Delta E_{EP,\,O} = 1.87$ eV), oxygen is a stronger embrittler of Mo than Zr. This disagreement comes from the fact that the surface created after cleaving the pure GB is not the same as the surface created after cleaving the GB with oxygen. If W_{sep}^{∞} without and with oxygen is compared for the same surface cuts, the decrease in the work of separation is around 8%. However, this kind of cut is not favourable for a pure tilt GB.

The analysis based on energetical considerations suggests that the pure Mo GBs are the most stable against brittle fracture. The GBs decorated with solutes or with oxygen show a decrease in work required for their fracture. Smaller W_{sep}^{∞} favours brittle fracture, whereas a larger W_{sep}^{∞} makes it difficult [199].

So far, the increase in ductility of Mo and Mo-based alloys, observed experimentally, cannot be simply explained by grain boundary strengthening due to solute segregation.

5.2 THEORETICAL STRENGTH

An alternative to the energy criterion (work of separation) is the analysis of the theoretical strength, σ_{th}, calculated from the stress needed to separate adjacent grains [56]. The theoretical strength of a material describes the maximum strength of a chemical bond between atoms [163]. In this way the bound on the maximum cohesive strength of molybdenum GB is set and it can be shown in which manner solutes affect σ_{th} leaving the energy contributions aside. The ideal brittle cleavage is modelled by stepwise rigid increase of the GB separation until two surfaces are created and represents the uniaxial loading of the system (the shear stress contributions in two other directions are neglected).

The top panels of Figures 49–51 show the energy variation obtained by stepwise separating the pure and solutes containing twist $\Sigma 5[001]$ Mo GB into two surfaces. The GB containing Zr, Si, O (from one to six oxygen atoms) and combination of Zr

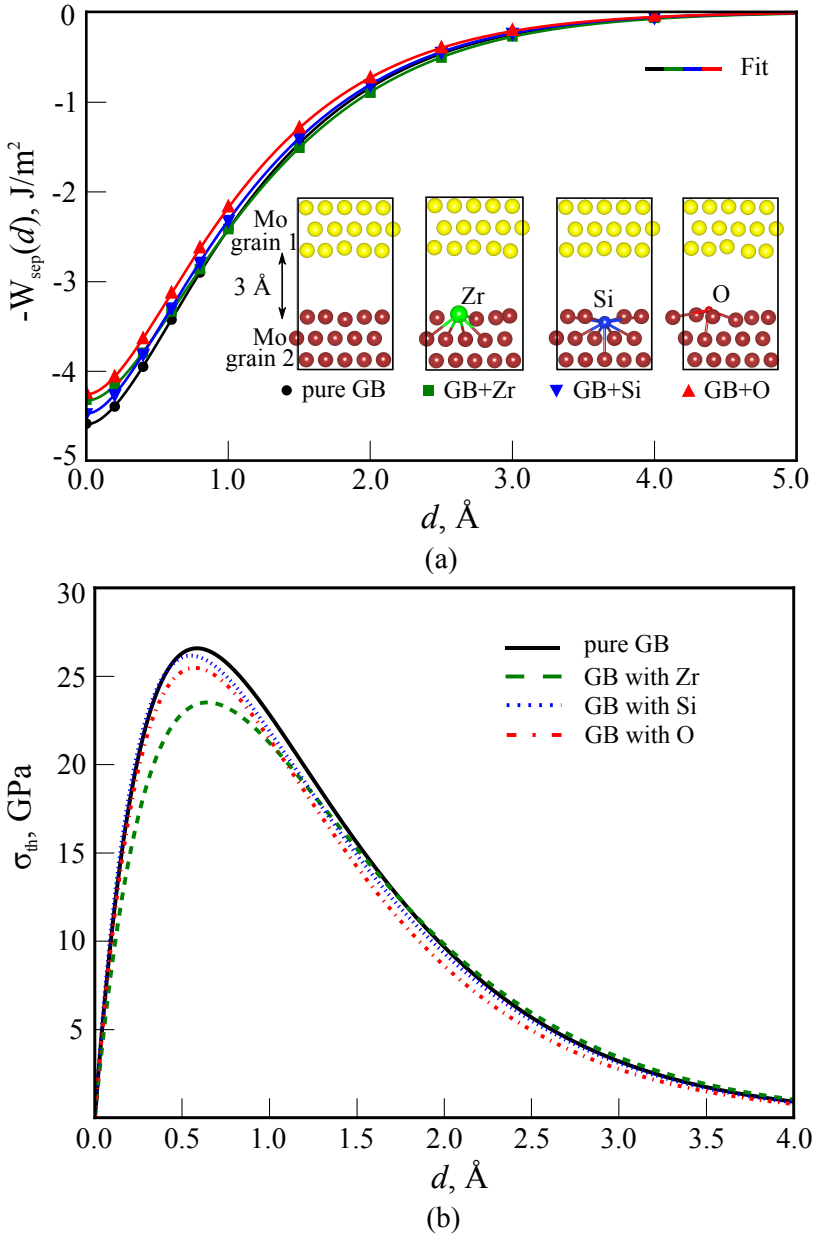

Figure 49: The uniaxial loading of the pure twist Σ5[001] Mo GB and one containing Zr, Si and O. (a) Variation of $W_{sep}(d)$ computed as a function of rigid increase of GB separation. Circles correspond to calculated data points and the solid curves are obtained by fitting the data to Eq.(2.69). (b) Stress versus grain separation for the pure Mo GB (black curve) and one containing Zr (green curve), Si (blue curve) and O (red curve).

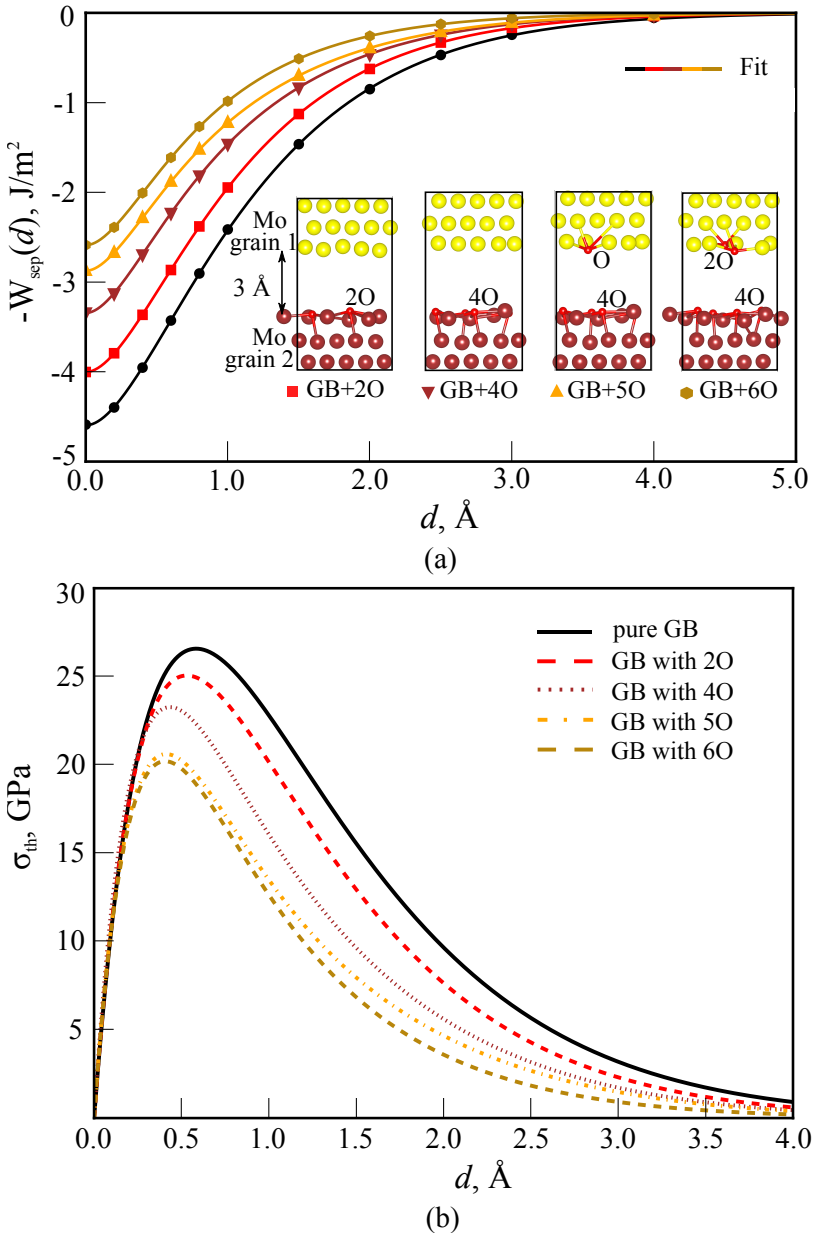

Figure 50: The uniaxial loading of the pure twist Σ5[001] Mo GB and one containing O in different concentration (from two to six atoms). Oxygen atoms are inserted interstitially and are distributed on one or on both sides of the GB. (a) Variation of $W_{sep}(d)$ computed as a function of rigid increase of GB separation. Circles correspond to calculated data points and the solid curves are obtained by fitting the data to Eq.(2.69). (b) Stress versus grain separation for the pure Mo GB (black curve) and one containing two O atoms (red curve), four O atoms (brown curve), five oxygen atoms (gold curve) and six oxygen atoms (dark gold curve).

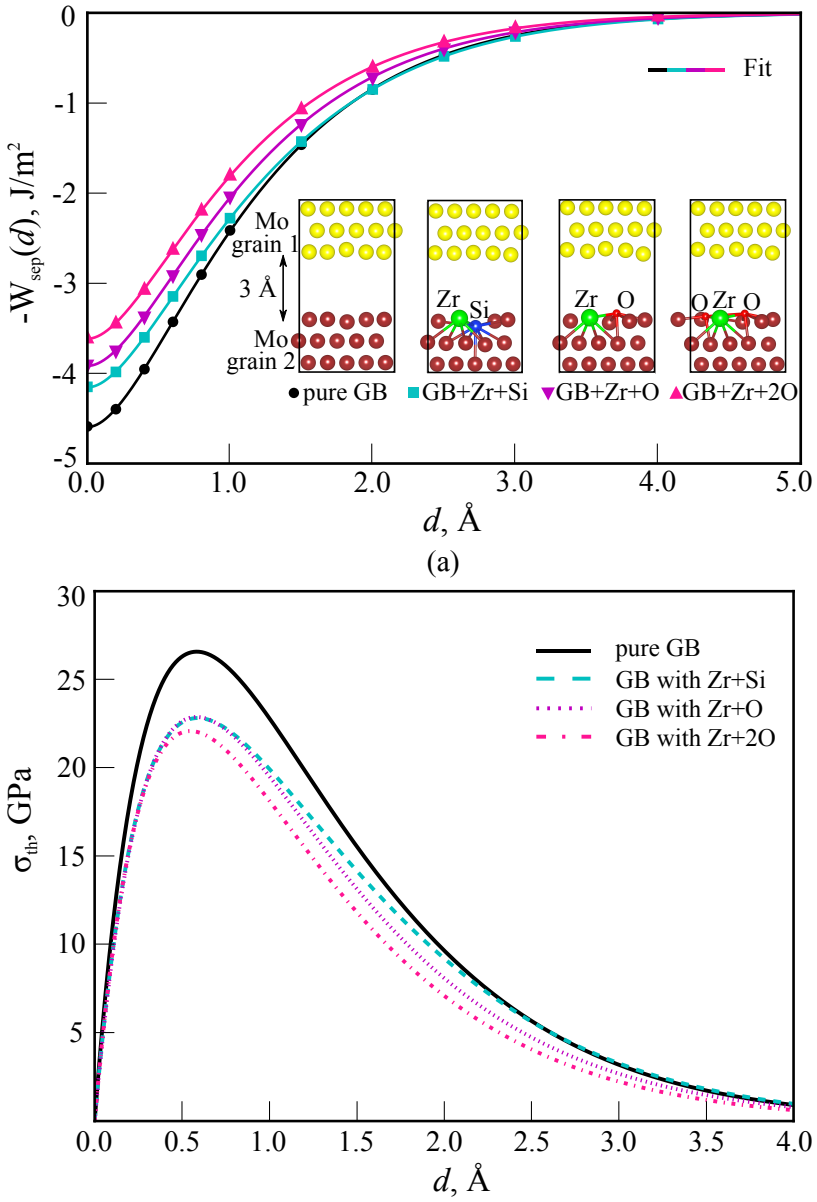

Figure 51: The uniaxial loading of the pure twist Σ5[001] Mo GB and one containing Zr in the presence of Si or O. (a) Variation of $W_{sep}(d)$ computed as a function of rigid increase of GB separation. Circles correspond to calculated data points and the solid curves are obtained by fitting the data to Eq.(2.69). (b) Stress versus grain separation for the pure Mo GB (black curve) and one containing Zr and Si at the GB (cyan curve), Zr in the presence of one oxygen (magenta curve) and Zr in the presence of two O atoms at the GB (pink curve).

with Si and Zr with O are considered. Each circle corresponds to a single calculation performed for a particular GB separation and the solid lines are obtained by fitting the data points to Eq.(2.69). The bottom panel of each figure shows the derivative of the $W_{sep}(d)$ curve and represents stress acting on the facets of the crack.

Table 18: Theoretical strength in GPa for pure and solutes containing twist Σ5[001] Mo GB obtained from uniaxial loading.

	σ_{th}, GPa
Pure GB	27
Zr	23
Si	26
O	25
2O	25
4O	23
5O	21
6O	20
Zr+Si	23
Zr+O	23
Zr+2O	22

Table 18 summarises the calculated theoretical strength for the twist GB. In the presence of Zr, Si or O and their combinations at the GB, the GB strength decreases and the slope of the curve is not as steep as in the case of pure Mo GB. For example, Zr segregation at the GB reduces σ_{th} by 15%, Si segregation by 4% and O segregation by 7%. Based on the stress criterion, the presence of oxygen at the twist GB in a very dilute concentration affects the GB strength less compared to the presence of Zr. The situation, however, changes when the concentration of oxygen increases. It should be pointed out that the distribution of oxygen at both sides of the GB has been found to be significantly more detrimental compared to monolayer oxygen coverage, considered here and shown in Figure 50.

The results based on the stress criterion (σ_{th}) are consistent with those obtained for energy criterion (W^{∞}_{sep}) and show that the pure GB is energetically the most stable. All investigated solutes and the presence of oxygen embrittle the GBs in molybdenum. Experimentally, zirconium has been shown to reduce the O content at Mo GBs significantly by capturing and formation of ZrO_2 [2–4, 68, 80]. ZrO_2 (zirconia) particles of nm size have been found both at the GBs and in grain interior. In order to shed some light on the origin of improved fracture toughness and ductility in Mo-based alloys with addition of Zr, the strength of zirconia-molybdenum interfaces in molybdenum are investigated in Chapter 6.

5.3 CONCLUSIONS

The influence of solutes (Zr, Si) and of oxygen on the cohesive strength of grain boundaries in molybdenum is investigated in the present chapter. The work required to cleave molybdenum grain boundaries decreases in the presence of solutes. Solute

segregation also reduces the theoretical strength of the grain boundaries. The reduction in the grain boundary strength scales with the concentration of segregated species. Upon increasing solute concentration the mutual distribution of solutes significantly affects their embrittling behaviour. Oxygen is found to be more detrimental to mechanical properties of molybdenum grain boundaries compared to zirconium and silicon. This result is consistent with the analysis of the Rice-Wang embrittling potential, provided in Section 4.2. Thus, based on energy and stress criteria, the pure molybdenum grain boundary is considered as the most stable against brittle fracture.

6

ZIRCONIA/MOLYBDENUM INTERFACES

In Chapter 5, the influence of solutes (Zr, Si) and of oxygen on the cohesive strength of GBs in molybdenum in twist and tilt bicrystals by means of electronic-structure calculations based on density functional theory (DFT) has been investigated. It was shown that Zr and Si preferably segregate to the grain boundaries if the low-energy insertion sites are available. At the same time, both species act as weak embrittlers of the Mo GBs and in the presence of oxygen show even more detrimental influence on the GB cohesion. Thus, the experimentally observed improvement of fracture toughness, strength and ductility in Mo cannot be simply explained by grain boundary strengthening due to solute segregation and other possibilities need to be considered.

In general, oxides and metals often form interfaces with enhanced strength compared to the individual constituent phases. For example, Nb and α-Al_2O_3 form a stable interface with high adhesive strength due to strong bonds with a high degree of ionic character [200, 201]. Strong adhesion is also found for interfaces between Al_2O_3, ZrO_2, HfO_2 oxides and other transition metals [77–79]. Also, zirconium tends to capture oxygen and form ZrO_2 (zirconia). Zirconia precipitates of nanometre size have been found experimentally at GBs and in the grain interior [2–4, 68, 80]. However, there is no data available on the strength and stability of zirconia/molybdenum interfaces. This is why, in the present Chapter DFT calculations are used to investigate the thermodynamics and mechanical properties of ZrO_2/Mo interfaces. The interface to thick ZrO_2 layers corresponding to precipitates and also ultrathin ZrO_2 films embedded between Mo grains are considered.

6.1 MODELS

6.1.1 *Interface geometries*

Heterogeneous interface modelling has a crystalline and atomic aspects [202]. The crystalline aspect is determined by the overall strain in the system and requires matching the lattice constants of two phases when the interface is formed. The atomic aspect includes the strength of chemical bonds at the interface and structure of the interface [203]. In bcc metals the principal fracture plane is the (001) plane [54, 163, 167, 168]. This is why, Mo(001) is considered as the dominant Mo surface orientation on which ZrO_2 may grow. As discussed in Section 6.1.2, the most stable ZrO_2

Table 19: A mismatch between lattice constants and lattice angle of Mo(001) and low-index facets (h,k,l<3) of the t-ZrO_2, computed using Eqs.(6.1−6.3). The planar density of facets for oxygen (ρ_O) and zirconium (ρ_{Zr}) atoms, computed using Eq.(6.4), and the stacking sequence are given for each facet.

Facet	Δa, %	Δc, %	$\Delta\alpha$, %	ρ_{Zr}, atoms/(Å)^2	ρ_O, atoms/(Å)^2	Stacking sequence
(001)	**3.0**	**3.0**	**0.0**	**0.076**	**0.076**	[Zr–O–O]
(100), (010)	1.0	2.1	3.9		0.158	[Zr+2O]
(110)	3.9	3.9	1.2	0.075	0.150	[2Zr–4O]
(101), (011)	3.0	1.0	3.5	0.087	0.087	[2Zr–2O–2O]
(111)	3.2	2.5	1.5	0.034	0.067	[Zr–2O]
(210), (120)	8.3	0.7	2.4		0.071	[Zr+2O]
(201), (021)	2.6	5.0	1.3	0.025	0.050	[Zr–2O]
(102), (012)	4.4	1.4	5.0		0.093	[Zr+2O]
(211)	3.0	4.8	8.5	0.045	0.045	[2Zr–2O–2O]
(112)	4.4	0.7	1.3		0.16	[2Zr+4O]
(121)	3.0	4.8	8.5	0.045	0.045	[2Zr–2O–2O]
(122), (212)	**0.7**	**1.4**	**0.1**		**0.060**	[Zr+2O]
(221)	6.3	1.8	2.8	0.018	0.036	[Zr–2O]
(311), (131)	**1.0**	**2.1**	**1.0**	**0.016**	**0.032**	[Zr–2O]
(113)	2.1	3.0	4.2		0.063	[Zr+2O]
(123)	4.0	9.0	7.9	0.035	0.035	[2Zr–2O–2O]
(132)	3.9	2.4	4.3		0.092	[2Zr+4O]
(312)	3.1	1.0	4.7		0.092	[2Zr+4O]
(321), (231)	3.9	3.2	2.2	0.029	0.029	[2Zr–2O–2O]
(213)	2.1	9.0	6.1	0.035	0.035	[2Zr–2O–2O]
(310), (130)	1.2	1.0	7.5	0.033	0.066	[2Zr–4O]
(103), (013)	**3.0**	**1.2**	**0.2**	**0.046**	**0.023**	[2Zr–O–O–O–O]
(023), (203)	3.0	7.1	0.0	0.018	0.036	[Zr–2O]
(032), (302)	3.0	5.1	6.1		0.048	[Zr+2O]

polymorph at the characteristic synthesis conditions (T = 1500°C–1980°C, 1 atm) is tetragonal t-ZrO_2 [110, 204]. Thus, based on the calculated lattice parameters the mismatch between Mo(001) and t-ZrO_2(hkl) for h,k,l < 3 is investigated.

A mismatch of all low-index facets (h,k,l<3) of t-ZrO_2 and Mo(001) is computed using

$$\Delta a = \frac{a_{\mathrm{Mo}} - a_{\mathrm{ZrO_2}}}{a_{\mathrm{Mo}}} \times 100\%, \tag{6.1}$$

$$\Delta c = \frac{a_{\mathrm{Mo}} - c_{\mathrm{ZrO_2}}}{a_{\mathrm{Mo}}} \times 100\%, \tag{6.2}$$

$$\Delta \alpha = \frac{\alpha_{\mathrm{Mo}} - \alpha_{\mathrm{ZrO_2}}}{\alpha_{\mathrm{Mo}}} \times 100\%. \tag{6.3}$$

Here, $a_{\mathrm{ZrO_2}}$ and $c_{\mathrm{ZrO_2}}$ are the computed lattice constants of tetragonal zirconia in the [100] and in the [001] directions, respectively. The parameter $\alpha_{\mathrm{ZrO_2}}$ represents the lattice angle. The molybdenum lattice constant is a_{Mo} and the cell angle is α_{Mo}. In the following, $a_{\mathrm{ZrO_2}}$ = 3.626 Å, $c_{\mathrm{ZrO_2}}$ = 5.225 Å (see Table 5) for t-ZrO_2 and a_{Mo} = 3.15 Å for molybdenum (see Table 4).

The planar atomic density of a facet is obtained according to

$$\rho_{\mathrm{Zr\ (O)}} = \frac{\text{Number of Zr (O) atoms}}{\text{Surface area}}. \tag{6.4}$$

Atoms are considered to belong to one layer, if the difference in their coordinates along the z-axis, Δz, is smaller than 0.3 Å.

Table 19 summarizes the computed mismatch for low-index facets (h,k,l<3) of t-ZrO_2 with Mo(001). Facets with mismatch in lattice constants and angle smaller than 3% are marked in bold. The planar density is computed for oxygen (ρ_{O}) and for zirconium (ρ_{Zr}) atoms using Eq.(6.4). The stacking sequence of each facet is also given in the table. A minimal mismatch reduces the mechanical stress at the interface while a maximum planar atomic density increases the number of chemical bonds across the interface. Here, (001), (122), (212), (311), (131), (103), (013) zirconia surfaces satisfy the condition of Δa < 3%, Δb < 3% and $\Delta \alpha$ < 3%. Among these facets the (001) facet has the highest planar atomic density. This is why, based on the mismatch of lattice parameters and the planar atomic density of the facets, Mo(001)/t-ZrO_2(001) system has been chosen and is further investigated in the present work.

Along the [001] direction, the stacking sequence for t-ZrO_2 can be described as R–[O–Zr–O]–R, where R = O–Zr–O (see Figure 9). This suggests three possible terminating surfaces along the [001] direction, namely a metallic Zr surface layer (R–O–Zr), a stoichiometric Zr–O surface layer (R–O–Zr–O) or an O-rich O layer

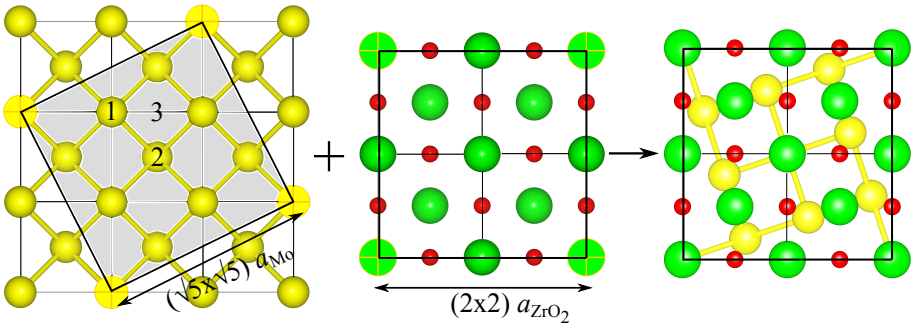

Figure 52: Construction of the zirconia/molybdenum interface, viewed from the top. The molybdenum cell is constructed from a $(\sqrt{5} \times \sqrt{5})$ replication of the conventional rectangular bcc Mo cell (a_{Mo} = 3.15 Å). The cell of tetragonal zirconia is constructed from a (2×2) replication of the rectangular tetragonal zirconia cell (a_{ZrO_2} = 3.626 Å). High-symmetry positions within the Mo(001) surface are marked "1"–"3" and correspond to ontop, hollow and bridge sites, respectively. Yellow spheres represent molybdenum atoms, green spheres represent Zr atoms and red spheres indicate O atoms.

(R–O–Zr–O–O). Details of the O–Zr–O repetition unit is shown on Figure 9. For the interface, all three terminations are considered.

Figure 52 shows the geometry of the zirconia/molybdenum interface on the atomic scale. In order to match a Mo(001) and a t-ZrO_2 a $(\sqrt{5} \times \sqrt{5})$ replication of the conventional rectangular bcc Mo cell and a (2×2) replication of the rectangular tetragonal zirconia cell are used. The Mo(001) substrate is characterised by three high-symmetry positions and the t-ZrO_2(001) surface is characterised by two high-symmetry positions for Zr and two for O. Each high-symmetry position in the t-ZrO_2 cell can be placed on top of any of the high-symmetry positions of Mo. Excluding equivalent structures, three structurally distinct configurations for each interface composition are investigated.

In this study, the interface to thick ZrO_2 layers corresponding to precipitates and also ultrathin ZrO_2 films embedded between Mo grains are considered. Figure 53 shows atomistic models of the corresponding interfaces. Since the thickness of the zirconia precipitates, observed experimentally, is in the nanometre range and thus considerably smaller compared to the grain size of molybdenum (micrometres), the dimensions of the interface cell along the [100] and along the [010] directions are fixed to the lattice constant computed for molybdenum, independent of the number of zirconia layers.

For describing the interface with a precipitate (Figure 53(a)), a slab geometry representing a Mo(001) grain in contact with a t-ZrO_2(001) precipitate is used. These

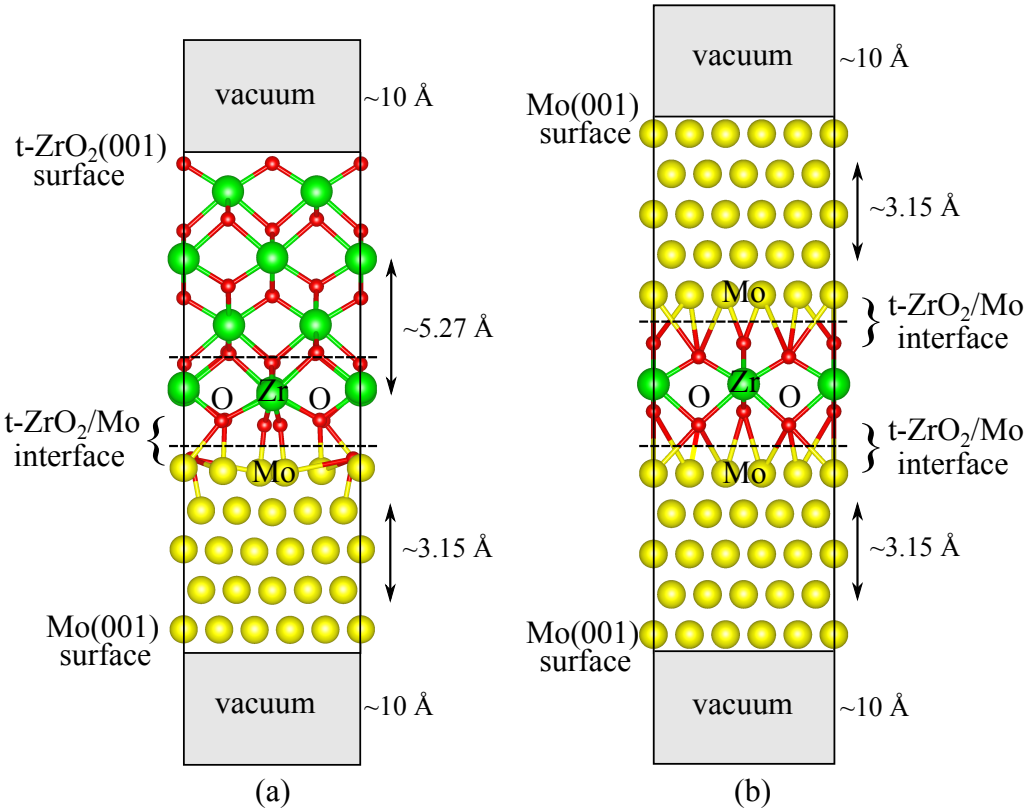

Figure 53: Atomistic models of (a) zirconia precipitate on a molybdenum grain and (b) zirconia ultrathin film embedded between molybdenum grains. Black dashed lines indicate cleavage planes for intergranular (along the interface) and transgranular (across the particle) brittle fracture.

systems contain one interface, one Mo(001) surface and one t-ZrO_2(001) surface. The latter is always terminated stoichiometrically while the interfacial composition varies. The slab contains fifteen Mo layers (75 Mo atoms) and seven stoichiometric zirconia layers (28 Zr atoms and 56 O atoms). For modelling the case of an ultrathin film (Figure 53(b)), a sandwich geometry containing two interfaces and two Mo(001) surfaces is used. The supercell consists of thirty Mo layers (fifteen on each side) and a monolayer of stoichiometric zirconia (four zirconium atoms and eight oxygen atoms) with two to four excess oxygen atoms per interface. The composition at the interface is varied.

Figure 54 details the atomic structure of the optimised interfaces between zirconia precipitate and molybdenum grain. The interfaces with different terminations (O-rich, stoichiometric and Zr-rich) are visualised. These interface structures represent the lowest-energy configurations among possible arrangements of zirconia on molyb-

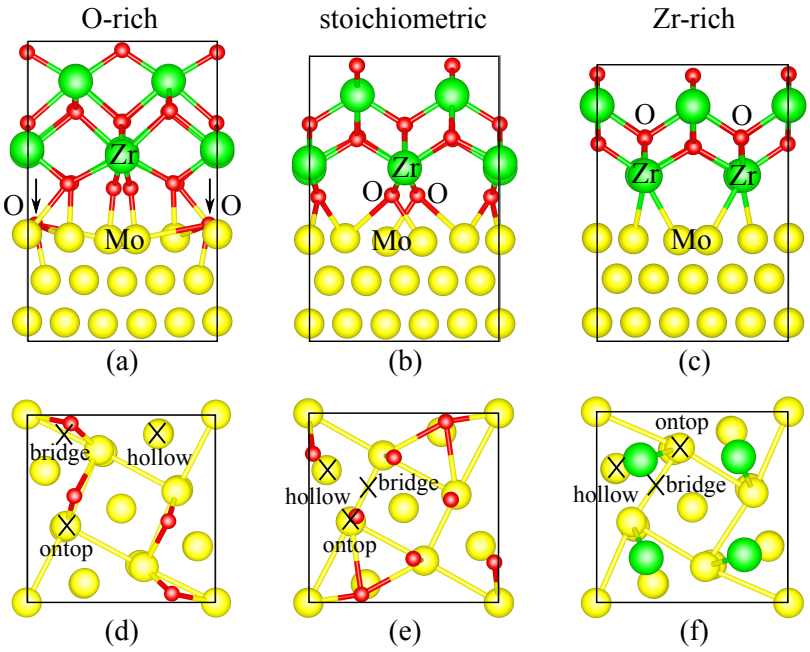

Figure 54: The atomic structure of the optimised interfaces between zirconia precipitate and molybdenum grain. (a), (d) O-rich interface; (b), (e) stoichiometric interface and (c), (f) Zr-rich interface. Top panel shows a projection of the interface along the [100] axis and bottom panel shows the interfaces projected along the [001] axis. Black arrows indicate oxygen atoms that penetrate inside the molybdenum grain after structure optimisation. Colour coding: see Figure 52.

denum (see Figure 52). For convenience, only the first few layers of zirconia and molybdenum are depicted on the figure. Black arrows indicate two oxygen atoms that penetrate inside the molybdenum grain after structure optimisation.

6.1.2 *Surface models*

Figure 55 shows atomistic models of a t-ZrO_2(001) surface in a slab geometry, projected along the [100] axis. As discussed in a previous section, cut along the [001] direction, zirconia can exhibit three terminations. The corresponding cleavage planes are represented by black dashed lines on the figure. The stoichiometric t-ZrO_2(001) surface is terminated with four atoms per surface. An O-rich surface contains eight oxygen atoms and Zr-rich surface is terminated with four zirconium atoms.

The surface energy of the stoichiometric t-ZrO_2(001) is carefully converged with respect to the number of layers. The results are listed in Table 20. The surface slab consisted of nine zirconia layers (nine Zr atoms and eighteen O atoms) is required to

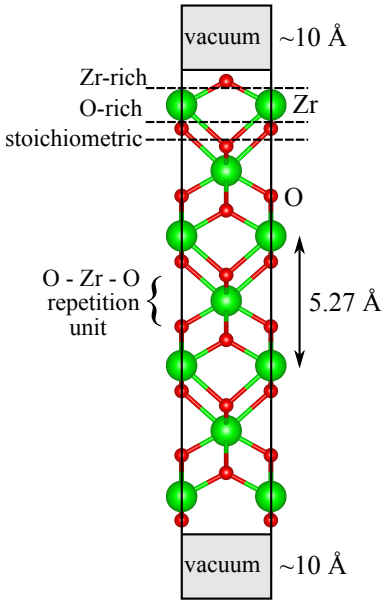

Figure 55: Atomistic model of a t-ZrO_2(001) surface in a slab geometry. The supercell is projected along the [100] axis. Black dashed lines correspond to the cleavage planes required to create stoichiometric, Zr-rich and O-rich (001) zirconia surfaces. Green spheres represent Zr atoms and red spheres indicate O atoms.

converge $\sigma_{\text{t-ZrO}_2(001)}$ to 1.159±0.003 J/m^2. Table 21 compares the calculated surface energy of the stoichiometric zirconia with other computational studies. The value of $\sigma_{\text{t-ZrO}_2(001)}$ available in the literature varies significantly, from 0.79 J/m^2 to 1.58 J/m^2. Our calculated surface energy lies approximately in the middle of this range, close to the values computed by Iskandarova [207].

The surface energy of non-stoichiometric zirconia surfaces is obtained combining the DFT total energies and thermochemical data. The thermodynamic stability diagram of t-ZrO_2(001) is shown in Figure 56 as a function of the oxygen chemical potential and the oxygen partial pressure, calculated using Eq.(6.5) and Eq.(6.7a)–Eq.(6.7b). The results show that independent of μ_O the stoichiometric termination is always preferred, which is consistent with the study of Eichler [208]. This is why in our interface models the zirconia surface is always stoichiometric, independent of the interface terminations. The value of the surface energy calculated in the present work and available in literature are given in Table 21.

A solid-gas interface (surface) is in equilibrium with the environment which can act as a reservoir. A surface grows by exchanging atoms with the environment. Thermodynamic stability of the surface relative to the bulk phases is determined

Table 20: Convergence of $\sigma_{\text{t-ZrO}_2(001)}$ with the number of layers.

N_{layers}	$\sigma_{\text{t-ZrO}_2(001)}$, J/m^2
17	1.159
15	1.159
13	1.159
11	1.158
9	1.154
7	1.135
5	1.064

Table 21: Comparison of t-ZrO_2(001) surface energy, $\sigma_{\text{t-ZrO}_2(001)}$, in J/m^2 from different computational and experimental studies.

	Method	$\sigma_{\text{t-ZrO}_2(001)}$, J/m^2
Christensen [205]	LDA	1.577
Christensen [202]	GGA	0.785
Hofmann [206]	GGA	1.453
Iskandarova [207]	PW91 TM	1.195
Iskandarova [207]	PW91 US	1.130
Eichler [208]	GGA	1.110
Present study	GGA-PBE	1.159

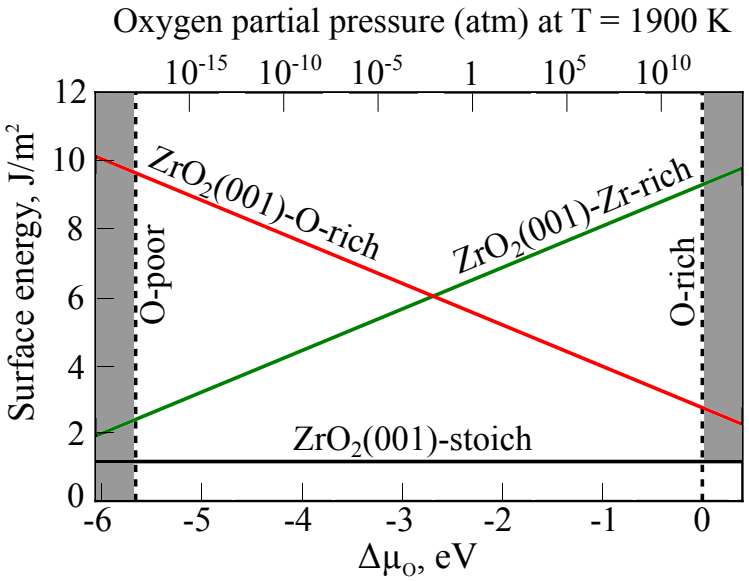

Figure 56: Surface energy $\sigma_{\text{t-ZrO}_2(001)}(T, p)$ of t-ZrO_2(001) as a function of the oxygen chemical potential. The dashed vertical lines indicate the allowed range of the oxygen chemical potential. In the top x axis, the oxygen chemical potential is expressed in terms of oxygen partial pressure at a fixed temperature of T = 1900 K.

assuming it being in contact with an oxygen atmosphere described by an oxygen pressure p and temperature T. On the basis of total energies obtained from DFT calculations, the surface energy $\sigma_{\text{t-ZrO}_2}$ is defined as [158]

$$\sigma_{\text{t-ZrO}_2} = \frac{1}{2A}[E^{\text{surf}}_{\text{slab}}(0\ \text{K}) - N_{\text{Zr}}E^{\text{bulk}}_{\text{ZrO}_2}(0\ \text{K}) - (N_{\text{O}} - 2N_{\text{Zr}})\mu_{\text{O}}(T,p)], \tag{6.5}$$

where $E^{\text{surf}}_{\text{slab}}(0\ \text{K})$ is the total energy of the supercell containing a surface; $E^{\text{bulk}}_{\text{ZrO}_2}(0\ \text{K})$ is the total energy of the bulk tetragonal zirconia. The number of Zr and O atoms in the supercell and the chemical potential of the corresponding atomic species are defined as N_{Zr} and N_{O}, μ_{Zr} and μ_{O}, respectively. The surface energy is normalised to energy per unit area.

The range of oxygen chemical potential can be established using thermodynamic bounds via the chemical potentials of atoms in the system. For a metal oxide a suitable lower boundary of μ_{O}, called *O-poor limit*, is defined by the decomposition of the oxide into the pure metal and gas phase oxygen. An upper bound of the oxygen chemical potential, called *O-rich limit*, is given by the condensation of the gaseous component on the surface [158]

$$\begin{aligned} \frac{1}{2}[E^{\text{bulk}}_{\text{ZrO}_2}(0,0) - E^{\text{bulk}}_{\text{Mo}}(0,0)] \leq \mu_{\text{O}}(T,p) \\ \leq \frac{1}{2}[E^{\text{bulk}}_{\text{ZrO}_2}(0,0) - E^{\text{bulk}}_{\text{Mo}}(0,0)] - \frac{1}{2}\Delta G^{\text{f}}_{\text{ZrO}_2}(0,0). \end{aligned} \tag{6.6}$$

Here, $\Delta G^{\text{f}}_{\text{ZrO}_2}$ is taken from thermochemical tables (NIST-JANAF) [209].

In order to connect the oxygen chemical potential with experimentally accessible quantities, we assume that the O_2 gas in the probe forms an ideal-gas-like reservoir. The temperature and pressure dependence of the oxygen chemical potential can be therefore expressed as

$$\mu_{\text{O}}(T,p) = \mu_{\text{O}}(0\ \text{K}, p^0) + \Delta\mu_{\text{O}}(T,p^0) + \frac{1}{2}k_{\text{B}}T\ln\frac{p}{p^0}, \tag{6.7a}$$

where

$$\begin{aligned} \Delta\mu_{\text{O}}(T,p^0) = \frac{1}{2}[H(T,p^0,\text{O}_2) - H(0\ \text{K},p^0,\text{O}_2)] \\ -\frac{1}{2}[S(T,p^0,\text{O}_2) - S(0\ \text{K},p^0,\text{O}_2)]. \end{aligned} \tag{6.7b}$$

We define the zero reference state of oxygen as $\mu_{\text{O}}(0\ \text{K},\ p^0) = \frac{1}{2}[g^{\text{bulk}}_{\text{ZrO}_2}(0,\ 0)$ - $g^{\text{bulk}}_{\text{Zr}}(0,\ 0)$ - $\Delta G^{\text{f}}_{\text{ZrO}_2}(0,\ 0)] \equiv 0$. For standard pressure, p^0 = 1 atm, the entropy and enthalpy of oxygen are tabulated in thermochemical tables [209]. Thus, the oxygen chemical potential can be obtained for any given (T, p) pair.

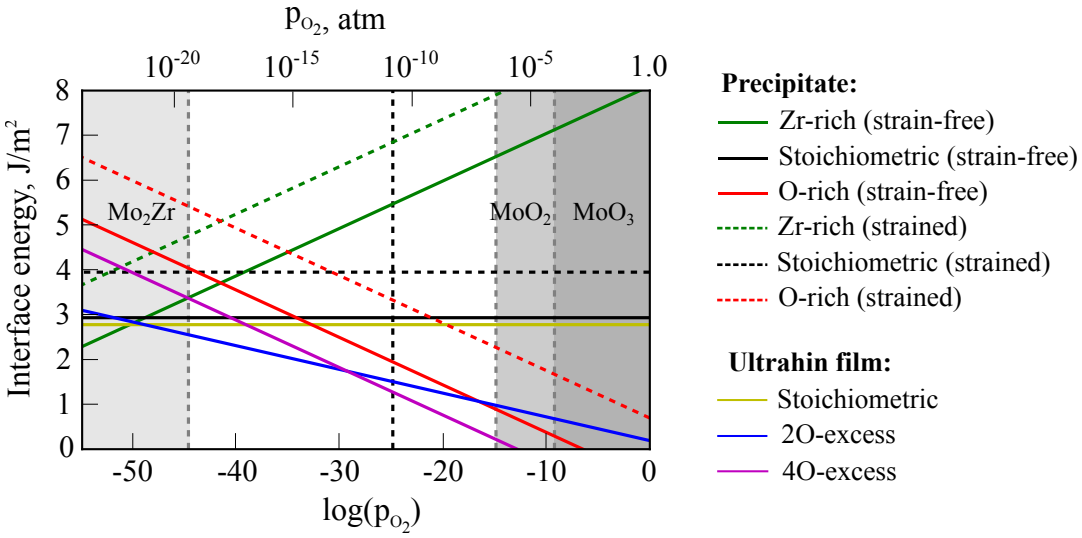

Figure 57: The calculated interface energy diagram for t-ZrO_2(001)/Mo(001) precipitate and ultrathin film at 1900 K. The oxygen partial pressure is determined from the Zr activity by using Eq.(6.12). The grey area separated by dark grey dashed lines indicates the formation of Mo_2Zr, MoO_2 and MoO_3 phases. The dashed black vertical line in the middle denotes the oxygen pressure during powder metallurgical synthesis.

6.2 STABILITY AND STRUCTURE OF INTERFACES

As discussed in Section 6.1.1, the structure of zirconia along the [001] direction suggest three possible terminating surfaces that can form the interface. In order to evaluate the stability of interfaces, the interface energy diagram is computed for the allowed range of the oxygen chemical potential. Figure 57 shows the calculated diagram for the precipitate and the ultrathin film. Both interface models are shown on Figure 53. If the strain contribution $\epsilon^{\text{strain}}_{ZrO_2}$ is included in Eq.(6.8), the resulting interface energy is strain-free. Similar, if $\epsilon^{\text{strain}}_{ZrO_2}$ is ignored in Eq.(6.8), the resulting interface energy is strained. Contrary to the t-ZrO_2(001) surface (see Figure 56), the stoichiometric interfaces are never favoured. The dashed black vertical line indicates the oxygen pressure during powder metallurgical synthesis, obtained from the Zr activity. Around this value, the O-rich interfaces are stabilised for both, the precipitate and the ultrathin film. The strain energy plays a significant role only for the zirconia precipitate. Increasing the precipitate thickness, the O-rich interface becomes less stable compared to the pure and Zr-containing Mo grain boundaries (see Figure 36).

The thermodynamic stability of the various interfaces is determined by combining DFT total energies with thermochemical data. In particular, the interface energy $\gamma_{\text{t-ZrO}_2/\text{Mo}}$ is computed according to [210]

$$\gamma_{\text{t-ZrO}_2/\text{Mo}} = \frac{1}{nA_{\text{int}}}\Big[E^{\text{int}}_{\text{slab}} - N_{\text{Mo}}\epsilon^{\text{bulk}}_{\text{Mo}} - \frac{N_{\text{O}}}{2}(\epsilon^{\text{bulk}}_{\text{ZrO}_2} + \epsilon^{\text{strain}}_{\text{ZrO}_2}) - (N_{\text{Zr}} - \frac{N_{\text{O}}}{2})(\mu^{\text{bulk}}_{\text{Zr}}(0\text{ K}) + \Delta\mu_{\text{Zr}}(T))\Big] - m\sigma_{\text{Mo}(001)} - k\sigma_{\text{t-ZrO}_2(001)}. \tag{6.8}$$

Here, $E^{\text{int}}_{\text{slab}}$ is the total energy of the slab supercell containing an interface; $\epsilon^{\text{bulk}}_{\text{Mo}}$ and $\epsilon^{\text{bulk}}_{\text{ZrO}_2}$ are the total energies of the bulk molybdenum and bulk tetragonal zirconia per formula unit; $\epsilon^{\text{strain}}_{\text{ZrO}_2}$ is the strain energy per formula unit stored in zirconia when it is subject to the same lateral strain as in the interface. The interface energy is normalized to an energy per unit area by dividing through the interface area A_{int}. Here, N_{i} and μ_{i} are the number of atoms and the chemical potential of the constituents (i = Mo, Zr, O), respectively. $\sigma_{\text{Mo}(001)}$ and $\sigma_{\text{t-ZrO}_2(001)}$ are the surface energies of the Mo(001) and the stoichiometric t-ZrO_2(001) surfaces, respectively. In case of the zirconia precipitate, the interface supercell contains one t-ZrO_2(001)/Mo(001) interface and two surfaces (Mo(001) and stoichiometric t-ZrO_2(001) surfaces), whereas in the case of zirconia ultrathin film the interface supercell consists of two zirconia/molybdenum interfaces and two molybdenum surfaces (see Figure 53). Thus, the factors $n = m = k = 1$ are used for the zirconia precipitate and $n = m = 2$, $k = 0$ are used for the zirconia ultrathin film. The bulk Mo and t-ZrO_2 are calculated using the cell of the same lateral dimensions as the interface cell.

The strain energy per formula unit stored in t-ZrO_2, $\epsilon^{\text{strain}}_{\text{ZrO}_2}$, is computed as the difference between strained ($E^{\text{strained}}_{\text{ZrO}_2}$) and strain-free ($E^{\text{strain-free}}_{\text{ZrO}_2}$) bulk tetragonal zirconia and is normalized by the number of ZrO_2 formula units

$$\epsilon^{\text{strain}}_{\text{ZrO}_2} = (E^{\text{strained}}_{\text{ZrO}_2} - E^{\text{strain-free}}_{\text{ZrO}_2})/N_{\text{units}}. \tag{6.9}$$

In Eq.(6.8) $\Delta\mu_{\text{Zr}}(T)$ is defined as $\Delta\mu_{\text{Zr}}(T) = \mu_{\text{Zr}}(T) - \mu^{\text{bulk}}_{\text{Zr}}(0\text{ K})$, and $\mu^{\text{bulk}}_{\text{Zr}}(0\text{ K})$ is the chemical potential of the bulk zirconium, determined at 0 K. The $\Delta\mu_{\text{Zr}}(T)$ shows the deviation of the Zr chemical potential at the interface from that of the bulk Zr [211]

$$\Delta\mu_{\text{Zr}}(T) = k_{\text{B}}T\ln a_{\text{Zr}} + \Delta^{\text{bulk}}_{\text{Zr}}(T), \tag{6.10}$$

where k_{B} is the Boltzmann constant and a_{Zr} is the activity of Zr. The quantity $\Delta^{\text{bulk}}_{\text{Zr}}(T)$ characterises the dependence of the chemical potential of bulk Zr on temperature and is defined according to

$$\Delta^{\text{bulk}}_{\text{Zr}}(T) = (H^{\text{bulk}}_{\text{Zr}}(T) - H^{\text{bulk}}_{\text{Zr}}(0\text{ K})) - TS^{\text{bulk}}_{\text{Zr}}(T), \tag{6.11}$$

where $H^{\text{bulk}}_{\text{Zr}}$ is the enthalpy of bulk Zr at temperature T and $S^{\text{bulk}}_{\text{Zr}}$ is its entropy.

The environmental dependence of the Zr activity and the oxygen partial pressure can be established using the Gibbs free energy of ZrO_2 formation [210]

$$k_B T \ln p_{O_2} = \Delta G_{f,\,ZrO_2} - k_B T \ln a_{Zr}, \tag{6.12}$$

in accordance with the reaction O_2(gas) + Zr(solid) = ZrO_2(solid). Similar, when MoO_3 is formed, the oxygen partial pressure is

$$\frac{3}{2} k_B T \ln p_{O_2} = \Delta G_{f,\,MoO_3} - k_B T \ln a_{Mo}, \tag{6.13}$$

for $\frac{3}{2}O_2$(gas) + Mo(solid) = MoO_3(solid). The range of oxygen partial pressure required for the formation of zirconia is bounded by the formation of molybdenum oxides (MoO_2, MoO_3) and by the formation of Mo_2Zr. $\Delta G_{f,\,ZrO_2}$, as well as enthalpy and entropy of bulk Zr are tabulated in thermochemical tables (NIST-JANAF) [209].

Figure 58 shows a close up of the fully optimised O-rich zirconia/molybdenum interfaces, which are thermodynamically relevant at the characteristic synthesis conditions of Mo-based alloys (see Figure 57). In case of the precipitate, four oxygen atoms at the interface occupy ontop positions and another four oxygen atoms occupy hollow positions, whereas in case of the ultrathin film both oxygen and zirconium atoms undergo more pronounced relaxations during structure optimisation. In both structures, two oxygen atoms located at the interface penetrate inside the molybdenum grain. These atoms are denoted by black arrows on the figure. Mechanical properties of both systems are characterised in Section 6.3.1.

Based on the interface energy of the zirconia ultrathin film, $\gamma_{\text{t-}ZrO_2(001)/Mo(001)}$, and the grain boundary energies of the Mo GB containing a monolayer of Zr, $\gamma_{GB+Zr}^{monolayer}$, and the Mo GB containing a monolayer of oxygen, $\gamma_{GB+O}^{monolayer}$, the stability of the ultrathin zirconia film is investigated. Assuming an open system with oxygen supply, the relationship between the interface energy and the grain boundary energies of the corresponding GBs

$$\gamma_{\text{t-}ZrO_2(001)/Mo(001)} < \frac{1}{5}(\gamma_{GB+Zr}^{monolayer} + 4 \cdot \gamma_{GB+O}^{monolayer}). \tag{6.14}$$

As shown on Figure 58(b), the O-rich ultrathin film contains sixteen oxygen atoms and four zirconium atoms per unit interface area, whereas the monolayer of Zr (O) at the GB corresponds to four atoms. The prefactor $\frac{1}{5}$ normalises the GB energy per unit of the GB area. The results correspond to

$$\sim 1.40\ \text{J/m}^2 < \sim 2.20\ \text{J/m}^2.$$

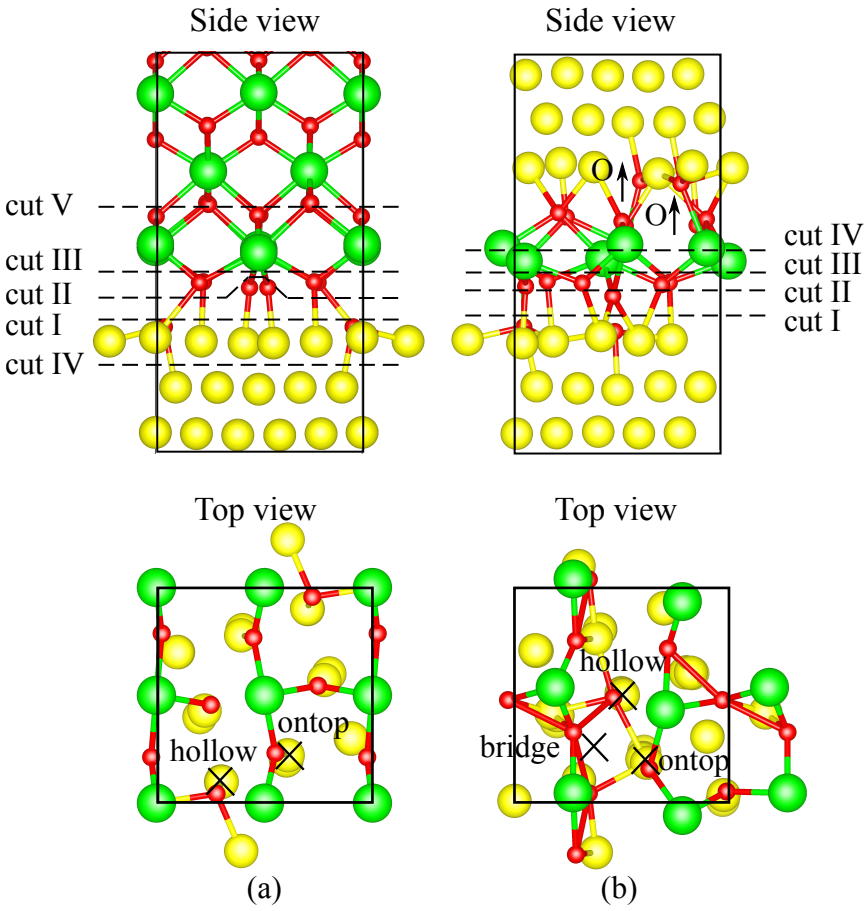

Figure 58: A close up of the atomic structure of (a) the O-rich zirconia precipitate and molybdenum interface and (b) the O-rich zirconia ultrathin film embedded between molybdenum grains. The structures correspond to the thermodynamically relevant interfaces and are fully optimised. Each zirconia/molybdenum interface has four excess oxygen atoms per interface. The top panel shows a projection of the interface along the [100] axis and the bottom panel shows the interface projected along the [001] axis. The dashed black lines represent cleavage planes used for calculating the ideal work of separation (see Section 6.3.1). Colour coding: see Figure 52.

The ultrathin film is more stable compared to Mo GB decorated with a monolayer of Zr and a monolayer of oxygen. The reduction of the GB energy can stabilise small grains during the alloy fabrication and thus lead to grain refinement.

6.3 ADHESION OF THE ZIRCONIA/MOLYBDENUM INTERFACE

6.3.1 *Ideal work of separation*

As before, energy-based and stress-based criteria for brittle fracture are applied in order to evaluate the strength of the interfaces. The ideal work of separation is defined by comparing the total energies of a system with two surfaces and that in which they are in contact [139],

$$W_{\text{sep}}^{\infty,\text{strained}} = \frac{1}{A_{\text{int}}}[E_{\text{Mo(001)}} + E_{\text{t-ZrO}_2\text{(001)}} - E_{\text{t-ZrO}_2\text{(001)/Mo(001)}}], \tag{6.15}$$

and

$$W_{\text{sep}}^{\infty,\text{strain-free}} = \frac{1}{A_{\text{int}}}[E_{\text{Mo(001)}} + (E_{\text{t-ZrO}_2\text{(001)}} - N_{\text{units}}\epsilon_{\text{ZrO}_2}^{\text{strain}}) - E_{\text{t-ZrO}_2\text{(001)/Mo(001)}}], \tag{6.16}$$

where $E_{\text{Mo(001)}}$ and $E_{\text{ZrO}_2\text{(001)}}$ are the total energies of the Mo(001) and t-ZrO_2(001) slabs created by cleaving the t-ZrO_2(001)/Mo(001) interface into two parts and A_{int} is the total interface area. N_{units} is the number of stoichiometric zirconia units.

During the interface separation, strain energy can be released. The strain energy is grain-size dependent and can be partially or fully relaxed during crack propagation. Figure 59 shows schematically how the work of separation is calculated. The strained work of separation, $W_{\text{sep}}^{\infty,\text{strained}}$, is computed with respect to the surface slabs subject to the same lateral strains as the interface cell. The strain-free work of separation, $W_{\text{sep}}^{\infty,\text{strain-free}}$, is computed with respect to the strain-free surface slabs possessing the equilibrium lattice constants of the corresponding bulk phases. According to the Griffith criterion of brittle fracture a small W_{sep}^{∞} favors brittle fracture, whereas a larger W_{sep}^{∞} makes it difficult [136].

The work of separation strongly depends on the cleavage plane and, this is why, different cleavage planes are investigated for the interface models. In the side views on Figure 58, various potential cleavage planes are indicated. In case of the precipitate, cleavage planes I, II and III lead to O-covered Mo(001) surface and O-rich, stoichiometric and Zr-rich t-ZrO_2(001) surfaces. The degree of oxygen coverage at Mo(001) thereby increases from cut I to III. Cut IV leaves a monolayer of molybdenum on the zirconia surface. Another possibility is to perform a cut through the

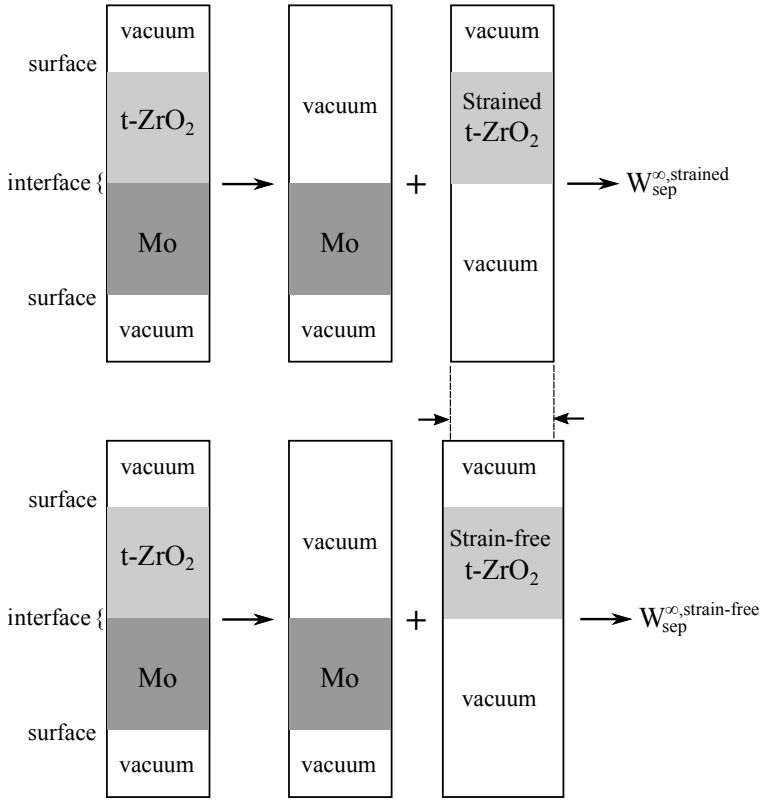

Figure 59: Schematics for the strained and strain-free ideal work of separation.

actual t-ZrO_2 precipitate leaving an ultrathin zirconia film on the Mo(001) surface. The corresponding cleavage plane is indicated by cut V. In the ultrathin film cut I, II and III are non symmetric and yield to an O-covered Mo(001) and a Mo(001) surface covered with off-stoichiometric t-ZrO_2 overlayer; cut IV is symmetric separating the t-ZrO_2 film in its central plane.

Table 22 lists the calculated ideal work of separation corresponding to different individual cuts, shown on Figure 58. Strained and strain-free W_{sep}^{∞}, calculated using Eqs.(6.15)-(6.16), are compared with that calculated for pure and solutes containing twist GB in molybdenum, listed in Table 23. The work of separation depends markedly on the way the interface is cleaved. For example, the precipitate is strongly adhered to the Mo grain if the crack propagates along the cut I, III or IV. Nevertheless, the zirconia precipitate is unstable against brittle fracture when the crack creates a stoichiometic t-ZrO_2(001) surface which is energetically extremely favourable (see Figure 56). This failure is represented by cut II (intergranular fracture) and by cut V (transgranular fracture).

Table 22: The calculated ideal work of separation W_{sep}^{∞} in J/m^2 for the zirconia precipitate interface and the zirconia ultrathin film. $W_{sep}^{\infty,\text{ strained}}$ is computed with respect to the zirconia, which is subject to the same lateral strain as the interface supercell (see Figure 59). $W_{sep}^{\infty,\text{ strain-free}}$ is calculated with respect to strain-free zirconia.

System	Rigid		Relaxed
	$W_{sep}^{\infty,\text{ strained}}$	$W_{sep}^{\infty,\text{ strain-free}}$	$W_{sep}^{\infty,\text{ strained}}$
Precipitate:			
Cut I[a]	4.96	3.62	4.44
Cut I[b]	4.74	–	4.37
Cut II[a]	2.75	1.40	0.92
Cut III[a]	10.62	9.28	-
Cut IV[a]	7.42	6.08	-
Cut V[a]	2.71	1.36	2.02
Thin film:			
Cut I[a]	4.88	4.73	2.62
Cut II[a]	3.42	3.27	1.70
Cut III[a]	10.45	10.30	4.42
Cut IV[a]	7.18	7.03	2.41

a Lattice parameters of the oxide phase are adjusted to those of molybdenum.
b Lattice parameters of molybdenum are adjusted to those of zirconia.

Similar results are obtained for the ultrathin film. The smallest value of W_{sep}^{∞} is physically the most relevant and it exhibits 3.42 J/m^2. This cut (cut II on Figure 58) creates a molybdenum surface with three adsorbed oxygen atoms and a zirconia surface with a composition close to the stoichiometric surface. A dramatic drop in W_{sep}^{∞} is observed when the newly created surfaces are allowed to relax. In this case, the ultrathin film becomes unstable due to uncompensated charges and this is why it undergoes pronounced structural rearrangements of O, Zr and Mo atoms. For ultrathin films, the relaxed W_{sep}^{∞} does not give a proper estimate for mechanical stability of the film.

The strain-free work of separation, $W_{sep}^{\infty,\text{ strain-free}}$, represents a limiting case, when the elastic strain energy stored in zirconia, is fully released. The table shows that the work of separation is decreased for the strain-free W_{sep}^{∞} compared to that containing strain and thus promotes the crack propagation. However, in reality the precipitate is connected to several surrounding molybdenum grains and the amount of strain energy that can be released during the interface separation depends on the mechanical boundary conditions. Under constrains of other molybdenum grains, it is unlikely

Table 23: The calculated ideal work of separation W_{sep}^{∞} in J/m^2 for pure and solute containing twist Σ5[001] Mo GB.

System	W_{sep}^{∞}, J/m^2	
	(rigid)	(relaxed)
Twist GB:		
pure	4.64	4.06
O	4.21	3.50
2O	3.98	3.15
4O	3.48	2.53
6O	2.59	2.11
Zr	4.29	3.82
Zr+O	3.87	3.38
Zr+2O	3.59	2.98

that the zirconia precipitate can be relaxed to its equilibrium lattice parameters. The elastic strain energy most likely can be only partially released.

Based on the energy criterion the pure Mo grain boundary is thermodynamically the most stable and possesses the highest work of separation of 4.64 J/m^2. In the presence of Zr or O at the GB, the W_{sep}^{∞} decreases indicating that the cohesive strength of the GB is reduced promoting a brittle failure along the GB. In the case of zirconia systems, the cleavage that creates a stoichiometric t-ZrO_2 surface will always possess a low W_{sep}^{∞}.

6.3.2 *Theoretical strength*

An alternative approach to the energy criterion is the analysis of the theoretical strength, σ_{th}. The theoretical strength of a material describes the maximum strength of a chemical bond between atoms [163]. Figure 60 shows the statically calculated work of separation as function of the interlayer distance. On the bottom panel the corresponding stress-strain curves are shown, where the stress is obtained by differentiation of the work of separation with respect to the interlayer distance. Similar stress-strain curves for pure and solutes containing twist Σ5[001] Mo GB is also shown on Figures 49–51.

Table 24 summarises the calculated theoretical strength for different cuts (see Figure 58). Although the interface between zirconia precipitate and molybdenum grain is strong, the crack propagates along the path with the lowest resistance which corresponds to cut II (intergranular fracture) and cut V (transgranular fracture). The

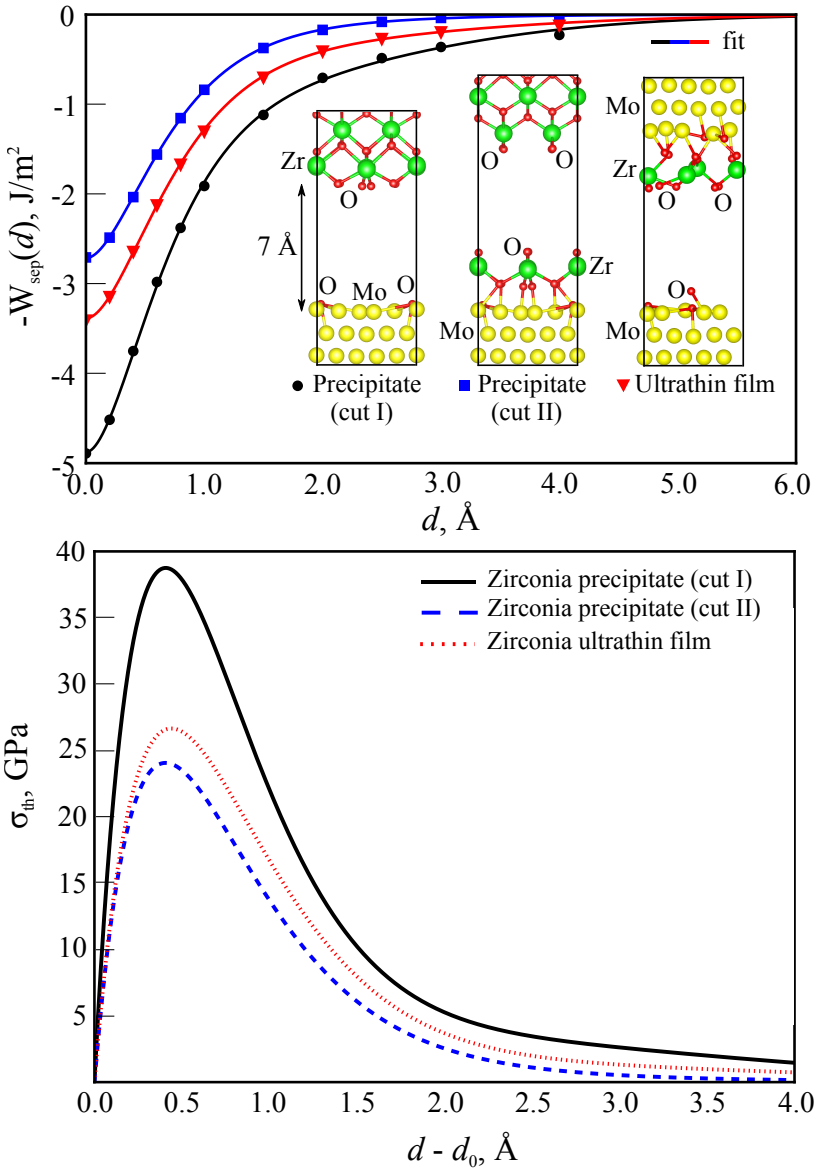

Figure 60: Uniaxial stretching of zirconia/molybdenum interfaces for the zirconia precipitate and for the zirconia ultrathin film. (a) Variation of the statically calculated work of separation as function of interface separation. The circles correspond to calculated data points and the solid curves are obtained by fitting the data to Eq.(2.69). Cuts I and II are shown for the precipitate and cut II is considered for the ultrathin film. (b) Stress versus interface separation obtained by differentiation of the curves illustrated on the top panel.

Table 24: Theoretical strength σ_{th} in GPa for the zirconia/molybdenum interfaces.

System	σ_{th}, GPa
Precipitate:	
Cut I[a]	39
Cut I[b]	38
Cut II[a]	22
Cut V[a]	24
Ultrathin film:	
Cut II	27

a Lattice parameters of the oxide phase are adjusted to those of molybdenum.

b Lattice parameters of molybdenum are adjusted to those of zirconia.

Table 25: Theoretical strength σ_{th} in GPa for pure and solutes containing twist Σ5[001] Mo GB.

System	σ_{th}, GPa
Twist Σ5[001] GB:	
pure	27
O	25
2O	25
4O	23
6O	20
Zr	23
Zr+O	23
Zr+2O	22

ultrathin film of zirconia exhibits a theoretical strength σ_{th} of around 27 GPa, which is comparable to value obtained for the pure Mo. This indicates that the bond strength of both systems are comparable. When the GB is decorated with solutes, the GB strength is reduced. The reduction in σ_{th} scales proportionally to the amount of the segregated atoms (see Table 25).

6.4 CONCLUSIONS

Density-functional theory calculations of thermodynamic stability and mechanical properties of t-ZrO_2(001)/Mo(001) interfaces are investigated. The interfaces to thick ZrO_2 layers corresponding to precipitates and also to ultrathin ZrO_2 films embedded between molybdenum grains have been examined. Around the value of the oxygen pressure at experimental synthesis conditions, obtained from the zirconium activity, the oxygen-rich interfaces are stabilised for both, the precipitate and the ultrathin film. For more objective estimate of the interface adhesive strength, energy-based (work of separation) and stress-based (theoretical strength) criteria for brittle fracture are applied. The results reveal that work of separation markedly depends on the cleavage plane and different cuts have to be carefully examined. The lowest energy for crack propagation is obtained for the cut that creates a stoichiometic t-ZrO_2(001) surface. For the ultrathin film, the cleavage plane possessing the lowest work of separation and stress passes through the film leaving a monolayer oxygen coverage on one of the grains. After cleavage, zirconia ultrathin film becomes unstable due to

uncompensated charges and therefore relaxed work of separation does not properly estimate the interface stability. Based on the theoretical strength, the stress required to cleave the ultrathin zirconia film is equal to that for the pure molybdenum Mo grain boundary.

The results reveal that addition of zirconium to molybdenum-based alloys can strengthen molybdenum grain boundaries that contain oxygen by forming an ultrathin zirconia film between molybdenum grains. Choosing oxidised molybdenum grain boundary systems as references (molybdenum with segregated oxygen), an increase of the theoretical strength up to 25% can be inferred upon formation of ultrathin ZrO_2 film between molybdenum grains.

7

SUMMARY AND CONCLUSIONS

The main focus of this thesis was the investigation of the influence of solute segregation and the presence of zirconia (ZrO_2) interfaces on the properties of grain boundaries in molybdenum using density functional theory calculations. The key findings are summarised below.

- ***Solid solubility of zirconium and silicon.***

The theoretical solid solubility of zirconium and silicon in molybdenum for a diluted system are estimated and are equal to c(Zr) = 23$\pm$3 at.% at 2153 K for zirconium and c(Si) = 1.1$\pm$0.2 at.% at 2239 K for silicon. The calculated values are in line with the upper limit for solubility found experimentally. The large scattering of experimentally measured solubility of zirconium in molybdenum (from 3 at.% to 20 at.%) suggests that not all investigated systems are in equilibrium.

The difference in solubility of zirconium and silicon can be explained based on the elastic strain and chemical bonding contributions to the solute formation energy. The bond strength of Zr-Mo bonds is similar to that for Mo-Mo bonds, but incorporation of zirconium into the molybdenum lattice produces large elastic distortions due to the difference in atomic size of both elements. In contrast, the contribution of elastic strain energy for silicon is negligible. However, silicon is bonded considerably weaker to molybdenum. Bader charge analysis indicates a charge transfer of 1.06 e from zirconium to molybdenum and 0.44 e from molybdenum to silicon, which is consistent with the analysis of chemical-bond contributions to the formation energy of both solutes. The Mo-Zr and Mo-Si bonding is characterised as ionic with weak covalent contributions.

- ***Driving force for zirconium, silicon and oxygen segregation.***

A strong driving force for segregation of zirconium, silicon and oxygen from the bulk to the grain boundaries in molybdenum is identified, if the corresponding low-energy insertion sites (for zirconium and silicon) are available. Oxygen occupies interstitial sites at the grain boundaries. The hierarchy of the segregation tendency corresponds to $\Delta E_{\mathrm{f,\,Zr}} < \Delta E_{\mathrm{f,\,Si}} \ll \Delta E_{\mathrm{f,\,O}}$. Qualitatively, the grain boundary segregation tendency is inverse to the solid solubility.

The negative formation energy of zirconium located in a grain boundary indicates that the concentration of zirconium in grain boundaries is not determined by the

configurational entropy and, thus, does not depend on temperature. It is determined only by the number of energetically preferred sites within the grain boundary.

- ***Embrittling potential of zirconium, silicon and oxygen.***

The embrittling potential ΔE_{EP} of solutes is evaluated based on the Rice-Wang criterion. Oxygen is found to be an extremely strong embrittler of molybdenum grain boundaries. The detrimental influence of oxygen on the grain boundaries cohesive strength has been also identified experimentally by Kumar and Eyre [57] and theoretically by Janisch *et al.* [71] and by Scheiber *et al.* [72].

Zirconium is found to be a stronger embrittler compared to silicon for grain boundaries with more densely packed atomic structure. For grain boundaries possessing more excess volume, the embrittling potential of both solutes, zirconium and silicon, is equivalently strong. Oxygen is found to be an extremely strong embrittler of molybdenum.

- ***Site competition between zirconium and silicon.***

In the dilute regime no site competition between zirconium and silicon has been found. The analysis of the site preference of zirconium and silicon shows that both solutes segregate at different sites at the grain boundary: zirconium occupies sites possessing more excess volume and silicon occupies more densely packed lattice sites. Moreover, in the presence of one of the solute species at the grain boundary, the formation energy of another solute close to the grain boundary decreases.

With increasing silicon concentration, the solute formation energies depend significantly on the distribution of solutes. If the first silicon atom already occupies the lowest-energy segregation site at the grain boundary, the second silicon atom is forced to occupy sites with higher formation energies and therefore compete for these positions with zirconium.

- ***Elastic strain and chemical energies.***

The strain energy required to accommodate zirconium at the grain boundaries counteracts the gain in chemical (bonding) energy and therefore zirconium behaves as a weak intrinsic embrittler of molybdenum. In contrast to zirconium, silicon embrittles molybdenum grain boundaries since it substitutes strong Mo-Mo bonds with weaker Mo-Si bonds. The overall embrittling behaviour of zirconium can be minimised in the presence of grain boundaries that provide more excess volume or by using solutes with a Zr-like chemistry but smaller atomic radius.

- ***The influence of zirconium, silicon and oxygen segregation on the cohesive strength of molybdenum grain boundaries.***

The resistance of the pure and solute containing molybdenum grain boundaries against brittle fracture has been investigated by means of the ideal work of separation (energy criterion) and theoretical strength (stress criterion). Results obtained using both methods are consistent and indicate that pure molybdenum grain boundaries are the most stable. The cohesive strength of grain boundaries decrease as soon as any of the chosen species (Zr, Si), their combination or oxygen decorate the grain boundary. Since the grain boundary cohesion determines the ductility of the material, segregation of zirconium at the grain boundaries is not responsible for the increase in ductility of molybdenum and molybdenum-based alloys, observed experimentally.

- ***Influence of zirconia on the cohesive strength of grain boundaries in molybdenum.***

The amount of residual oxygen in molybdenum-based alloy after mechanical alloying varies in the range of approximately 200–500 wt.ppm [2]. One of the beneficial effects of zirconium addition is that zirconium reduces the oxygen content at Mo grain boundaries significantly. Zirconium getters oxygen forming nanometre-size ZrO_2 precipitates that have been found experimentally both at the grain boundaries and in grain interior [2–4, 68, 80].

The presence of stronger zirconia/molybdenum interface can potentially explain experimental findings. The results reveal that (i) despite the strongly adhered t-ZrO_2(001)/Mo(001) interface between zirconia precipitate and molybdenum grain, the precipitate tends to fail creating a stoichiometric t-ZrO_2(001) surface; (ii) the stress required to separate the zirconia ultrathin film on molybdenum grain is equal to the stress needed for separation of the pure molybdenum grain boundary.

- ***Interaction of crack with precipitate.***

Considering mechanisms that contribute to toughening in real materials, particles with smaller Young's modulus (in our case it is tetragonal zirconia with E = 201 GPa [212]) being distributed in the matrix with higher Young's modulus (E = 317 GPa for molybdenum [52, 213]) will attract crack due to the stress raise in the vicinity of the particle [214]. If the fracture plane along which the crack propagate is less favourably oriented relative to the molybdenum grain, a larger stress has to be applied for crack propagation. The crack can be also deflected to the zirconia/molybdenum interface which is shown to be very strong.

- ***Grain refinement.***

The improved ductility in molybdenum-based alloys has been observed also with addition of $MgAl_2O_4$ spinel particles [215, 216]. These studies claim that the ductility

gain is mainly caused by the grain size refinement. Zirconium is a well-known grain-refining element [70]. The present study also shows that the energy of molybdenum grain boundaries is reduced with addition of zirconium and is more pronounced, if more zirconium is present at the grain boundary. The reduction in the grain boundary energy can stabilise small grains during alloy fabrication, resulting in grain refinement.

Saage *et al.* [2] argue that the grain refinement is not sufficient to allow for room-temperature ductility in Mo-based alloys. Since oxygen at the molybdenum grain boundaries is highly detrimental, a proper alloying additive to molybdenum must prevent segregation of oxygen to the grain boundaries, as well as to refine the grain size [217]. Formation of ultrathin zirconia film between molybdenum grain satisfies both requirements. The interface energy of zirconia ultrathin film is lower compared to the grain boundary energy for molybdenum grain boundary decorated with a monolayer of zirconium and a monolayer of oxygen. The formation of the ultrathin film also leads to the grain refinement. In addition, the amount of oxygen segregating at the grain boundaries is decreased resulting in enhancement of the grain boundary strength.

In conclusion, atomistic modelling can currently not substantiate that the experimentally observed strengthening of molybdenum upon addition of zirconium is a direct solute effect leading to an increase of the cohesive strength of molybdenum grain boundaries. In fact, our results reveal that addition of zirconium to molybdenum-based alloys can strengthen molybdenum grain boundaries that contain oxygen by forming an ultrathin zirconia film between molybdenum grains. Choosing oxidised molybdenum grain boundary systems as references (molybdenum with segregated oxygen), an increase of the theoretical strength up to 25% can be inferred upon formation of ultrathin ZrO_2 film between molybdenum grains. Moreover, due to the strong embrittling potential of oxygen at molybdenum grain boundaries, the reduction of oxygen at molybdenum grain boundaries contribute to the overall improvement of the grain boundaries cohesive strength.

A more detailed understanding of the influence of zirconium microalloying on the molybdenum and molybdenum-based alloys requires further experimental and theoretical investigations of (i) another possible zirconia/molybdenum interface terminations present in the material; (ii) the chemical composition of molybdenum grain boundaries in terms of oxygen and silicon concentration and (iii) the contribution of the grain size refinement to the ductility improvement.

ERKLÄRUNG - DISCLAIMER

Hiermit versichere ich an Eides statt, dass ich die vorliegende Arbeit selbstständig und nur unter Verwendung der angegebenen Hilfsmittel angefertigt habe. Alle Stellen, die aus Quellen entnommen wurden, sind als solche kenntlich gemacht. Von mir wurde weder an der Technischen Universität Darmstadt noch an einer anderen Hochschule ein Promotionsversuch unternommen.

Darmstadt, den 13. März 2017

Olena Lenchuk

DANKSAGUNG - ACKNOWLEDGEMENTS

Throughout time of my study as a PhD student I met many people who supported me and who I feel thankful to:

- My Doktorvater **Prof. Karsten Albe**, for choosing me to carry out this research project, for guidance, motivation and valuable discussions of the results. Thank you for being always ready to answer any scientific and private questions, inspiring to think critically and for being always patient to correct my always-wrong-placed "the/a" articles. Thank you for improving my story-telling skills, although I hardly have chances to win the Nobel Prize in literature.
- co-referee of my Ph.D. thesis, **Prof. Martin Heilmaier**, for the opportunity for collaboration within the research project "Beyond Ni-base superalloys" and for helpful advices, suggestions and comments on the research. I really appreciate that you agreed to revise my Ph.D. thesis.
- My Ph.D. committee, **Prof. Karsten Durst** and **Prof. Matthias Öchsner**, for serving as my committee members and for useful comments about my study.
- The best office mate I have ever had, **Dr. Jochen Rohrer**. This thesis would not have been possible without your support, valuable advices, critical view on the research and never-ending optimism. Thank you for teaching me python and of course for proof-reading of my thesis.
- **Maria Azim and Dr. Bronislava Gorr** for sharing research of 5-3 Mo-silicides and improving my knowledge of the material's oxidation resistance. Thank you for really nice collaboration, fruitful discussions and cheerful phone talks.
- **The members of the research group *FOR* 727 "Beyond Ni-base superalloys"** for the very nice collaboration, friendly atmosphere and interesting research-group meetings and conferences. I learnt a lot about the alloy systems Mo-Si-B, especially about gentle "moly".
- **Materials Modelling group** for a really nice working atmosphere, stimulating discussions during group seminars and the excellent opportunity to improve my German and English.

- Special thank you to **Kai-Christian Meyer** for pleasant talks, fun and inspiration to learn chess better.
- **Conny Kalcher** for being always friendly, open and ready to help, especially with bikes. It was fun to be a part of a running team and to do sports together (although, shortly).
- **Dr. Yuri Genenko and Ukrainian-Armenian-fraction** for being always friendly, motivating and incredibly erudite. Thank you for tea and cakes.
- **Renate Hernichel und Gabriele Rühl** for support with administrating questions and for your help in organisation.
- **German Research Foundation** for finantial support and **John von Neumann Institute for Computing** and **Lichtenberg High Performance Computer** for providing computational time.
- **Dr. Anton Romanenko** for being always on my side and manfully adopting domestic duties whenever I was busy.
- **Olga Ishchuk** and **Dr. Christian Hubert** for all fun we had together. Thank you for inspiring me to come to Germany and to study here.
- **My family** in Kiev for being always supportive and proud of me.

CURRICULUM VITAE

Personal Data

Name	Olena Lenchuk
Birth	02 October 1986 Kiev, Ukraine
Address	Frankfurter Str. 41 64293 Darmstadt

University Education

06/2017	Defence of PhD-Thesis
since 11/2011	**PhD Thesis:** "*Density-functional theory calculations of solutes in molybdenum grain boundaries*" Materials Modelling Division (Prof. K. Albe), Technische Universität Darmstadt, Darmstadt, Germany
02/2010	**Master of Science in Applied Physics**, Master Thesis: "*Computer modelling of transfer processes during combine diffusion and kinetic combustion of natural gas*" Division of Applied Physics (Prof. N. Fialko), National Aviation University, Kiev, Ukraine
09/2008–02/2010	**Studies:** Applied Physics, National Aviation University, Kiev, Ukraine
09/2004–06/2008	**Bachelor of Science in Applied Physics**, National Aviation University, Kiev, Ukraine

Research Experience

08/2011–09/2015	**Research Associate** (Wissenschaftlicher Mitarbeiterin), Materials Modelling Division (Prof. K. Albe), Technische Universität Darmstadt, Darmstadt, Germany
02/2010–07/2010	**Research Scientist** Division of Applied Physics, National Aviation University, Kiev, Ukraine
09/2005–02/2010	**Research Assistant** (Studentische Hilfskraft), Institute of Engineering Thermophysics of National Academy of Sciences of Ukraine Kiev, Ukraine

School Education

09/1994–06/2004	High School Graduation (*Abitur*), General Secondary School Nr. 263 Kiev, Ukraine

Awards

09/2016	Award of the *1st* Prize in PhD Thesis Presentation Contest German-Ukrainian Academic Society Berlin, Germany

Publications Based on the Present Dissertation

Peer-Reviewed Articles:

1. **O. Lenchuk**, J. Rohrer, K. Albe, *Cohesive strength of zirconia/molybdenum interfaces and grain boundaries in molybdenum: A comparative study*, Acta Materialia **135** (2017) 150–157.

2. **O. Lenchuk**, J. Rohrer, K. Albe, *Atomistic modelling of zirconium and silicon segregation at twist and tilt grain boundaries in molybdenum*, Journal of Materials Science **51** (2016) 1873–81.

3. **O. Lenchuk**, J. Rohrer, K. Albe, *Solubility of zirconium and silicon in molybdenum studied by first-principles calculations*, Scripta Materialia **97** (2015) 1–4.

4. M.A. Azim, H.-J. Christ, B. Gorr, T. Kowald, **O. Lenchuk**, K. Albe and M. Heilmaier, *Effect of Ti addition on the thermal expansion anisotropy of* Mo_5Si_3, Acta Materialia **132** (2017) 25–34.

5. M.A. Azim, B. Gorr, H.-J. Christ, **O. Lenchuk**, K. Albe, D. Schliephake, M. Heilmaier, *Effect of Ti content and nitrogen on the high-temperature oxidation behavior of* $(Mo,Ti)_5Si_3$, Intermetallics **90** (2017) 103–112.

Proceedings:

6. **O. Lenchuk**, J. Rohrer, K. Albe, *Atomistic modelling of Zr segregation in symmetric grain boundaries of molybdenum*, in Proceedings of the NIC Symposium, FZ Jülich GmbH, **47** (2014) 267–274, ISBN 978–3–89336–933–1.

International Conferences and Workshops

1. **O. Lenchuk**, J. Rohrer, K. Albe, *Atomistic modeling of Zr, Si segregation at twist and tilt grain boundaries in molybdenum* (Oral Presentation), TMS Annual Meeting, San Diego, USA, 2014.

2. **O. Lenchuk**, J. Rohrer, K. Albe, *Atomic modeling of zirconium segregation at molybdenum grain boundaries* (Poster), Beyond Nickel-Based Super Alloys, Bad Berneck, Germany, 2013.

3. **O. Lenchuk**, J. Rohrer, K. Albe, *Solubility of zirconium and silicon in molybdenum* (Poster), The CAMD Summer School on the *Electronic Structure Theory and Materials Design*, TU Lyngby, Denmark, 2012.

BIBLIOGRAPHY

[1] D. Sturm, M. Heilmaier, J. Schneibel, P. Jéhanno, B. Skrotzki, H. Saage, The influence of silicon on the strength and fracture toughness of molybdenum, Mater. Sci. Eng.: A 463 (2007) 107–114.

[2] H. Saage, M. Krüger, D. Sturm, M. Heilmaier, J. Schneibel, E. George, L. Heatherly, C. Somsen, G. Eggeler, Y. Yang, Ductilization of Mo-Si solid solutions manufactured by powder metallurgy, Acta Mater. 57 (2009) 3895–3901.

[3] J. Schneibel, P. Tortorelli, R. Ritchie, J. Kruzic, Optimization of Mo-Si-B intermetallic alloys, Metall. Mater. Trans.: A 36 (2005) 525–531.

[4] J. Fan, M. Lu, H. Cheng, J. Tian, B. Huang, Effect of alloying elements Ti, Zr on the property and microstructure of molybdenum, Int. J. Refract. Met. H. 27 (2009) 78–82.

[5] R. Reed-Hill, R. Abbaschian, Physical Metallurgy Principles, The PWS-Kent Series in Engineering, 3rd ed., PWS-Kent, Boston, 1992.

[6] M. Meyers, K. Chawla, Mechanical Behavior of Materials, 2nd ed., Cambridge University Press, 2009.

[7] G. Gottstein, Physical Foundations of Material Science, Springer, Berlin, 2004.

[8] D. Molodov (Ed.), Microstructural Design of Advanced Engineering Materials, Wiley-VCH, Weinheim, 2013.

[9] T. Watanabe, Grain boundary engineering: Historical perspective and future prospects, J. Mater. Sci. 46 (2011) 4095–4115.

[10] J. W.D. Callister, Materials Science and Engineering: An Introduction, 6th ed., Wiley, New York, 2003.

[11] L. Priester, Grain Boundaries: From Theory to Engineering, volume 172 of *Springer Series in Materials Science*, Springer, 2013.

[12] V. Randle, The Measurement of Grain Boundary Geometry, Electron Microscopy in Materials Science Series, Inst. of Physics Publ., Bristol, 1993.

[13] S. Hofmann, P. Lejček, Solute segregation at grain boundaries, Interfaces Sci. 3 (1996) 241–267.

[14] P. Lejček, Grain Boundary Segregation in Metals, volume 136 of *Springer Series in Materials Science*, Springer, 2010.

[15] M. Boyce, Gas Turbine Engineering Handbook, 4th ed., Butterworth-Heinemann, Oxford, 2012.

[16] T. Giampaolo, Gas Turbine Handbook: Principles and Practice, 4th ed., The Fairmont Press, Lilburn, 2009.

[17] B. Pearce, Economic performance of the airline industry, Technical Report, The International Air Transport Association (IATA), 2015.

[18] R. Flack, Fundamentals of Jet Propulsion with Applications, Cambridge university press, Cambridge, 2005.

[19] R. Reed, The Superalloys: Fundamentals and Applications, Cambridge university press, Cambridge, 2006.

[20] A. Razak, Industrial Gas Turbines: Performance and Operability, CRC Press, Boca Raton, 2007.

[21] D. Dimiduk, J. Perepezko, Mo-Si-B alloys: Developing a revolutionary turbine-engine material, in: MRS Bulletin, 2003, pp. 639–645.

[22] M. Heilmaier, H. Saage, M. Krüger, P. Jéhanno, M. Böning, H. Kestler, Current status of Mo-Si-B silicide alloys for ultra-high temperature applications, in: MRS Proceedings, volume 1128, 2008, pp. 1128–U07–07 (12 pages).

[23] J. Lemberg, R. Ritchie, Mo-Si-B alloys for ultrahigh-temperature structural applications, Adv. Mater. 24 (2012) 3445–3480.

[24] P. Jéhanno, H. Kestler, A. Venskutonis, M. Böning, M. Heilmaier, B. Bewlay, M. Jackson, Assessment of a powder metallurgical processing route for refractory metal silicide alloys, Metall. Mater. Trans.: A 36 (2005) 515–523.

[25] M. Heilmaier, M. Krüger, H. Saage, J. Rösler, D. Mukherji, U. Glatzel, R. Völkl, R. Hüttner, G. Eggeler, C. Somsen, T. Depka, H.-J. Christ, B. Gorr, S. Burk, Metallic materials for structural applications beyond nickel-based superalloys, JOM 61 (2009) 61–67.

[26] J. Davis, A. Committee, ASM Specialty Handbook: Heat-Resistant Materials, ASM specialty handbook, ASM International, 1997.

[27] J. Kruzic, J. Schneibel, R. Ritchie, Ambient- to elevated-temperature fracture and fatigue properties of Mo-Si-B alloys: Role of microstructure, Metall. Mater. Trans.: A 36 (2005) 2393–2402.

[28] M. Krüger, Pulvermetallurgische Herstellung und Charakterisierung von oxidationsbeständigen Molybdänbasislegierungen für Hochtemperaturanwendungen, Ph.D. thesis, Otto-von-Guericke-Universität Magdeburg, 2010.

[29] M. Mendiratta, T. Parthasarathy, D. Dimiduk, Oxidation behavior of α-Mo-Mo_3Si-Mo_5SiB_2 (T2) three phase system, Intermetallics 10 (2002) 225–232.

[30] F. Rioult, S. Imhoff, R. Sakidja, J. Perepezko, Transient oxidation of Mo-Si-B alloys: Effect of the microstructure size scale, Acta Mater. 57 (2009) 4600–4613.

[31] S. Majumdar, B. Gorr, H.-J. Christ, D. Schliephake, M. Heilmaier, Oxidation mechanisms of lanthanum-alloyed Mo-Si-B, Corros. Sci. 88 (2014) 360–371.

[32] S. Burk, B. Gorr, V. Trindade, H.-J. Christ, Effect of Zr addition on the high-temperature oxidation behaviour of Mo-Si-B alloys, Oxid. Met. 73 (2009) 163–181.

[33] I. Rosales, J. Schneibel, Stoichiometry and mechanical properties of Mo_3Si, Intermetallics 8 (2000) 885–889.

[34] I. Rosales, Synthesis and characterization of Mo_3Si single crystal, J. Cryst. Growth 310 (2008) 3833–3836.

[35] E. Ström, Mechanical properties of Mo_5Si_3 intermetallics as a function of composition, Mater. Charact. 55 (2005) 402–411.

[36] F. Chu, D. Thoma, K. McClellan, P. Peralta, Mo_5Si_3 single crystals: Physical properties and mechanical behavior, Mater. Sci. Eng.: A 261 (1999) 44–52.

[37] K. Ihara, K. Ito, K. Tanaka, M. Yamaguchi, Mechanical properties of Mo_5SiB_2 single crystals, Mater. Sci. Eng.: A 329–331 (2002) 222–227.

[38] M. Berczik, Method for enhancing the oxidation resistance of a molybdenum alloy, and a method of making a molybdenum alloy, 1997. United States Patent 5,595,616.

[39] M. Berczik, Oxidation resistant molybdenum alloys, 1997. United States Patent 5,693,156.

[40] J. Kruzic, J. Schneibel, R. Ritchie, Fracture and fatigue resistance of Mo-Si-B alloys for ultrahigh-temperature structural applications, Scripta Mater. 50 (2004) 459–464.

[41] M. Krüger, P. Jain, K. Kumar, M. Heilmaier, Correlation between microstructure and properties of fine grained Mo-Mo_3Si-Mo_5SiB_2 alloys, Intermetallics 48 (2014) 10–18.

[42] B. Li, G. Zhang, J. Feng, R. Shuai, L. Gang, S. Jun, Preparation of fine-grained Mo-12Si-8.5B alloys with improved mechanical properties via a mechanical alloying process, J. Alloys Compd. 609 (2014) 80–85.

[43] Z. Guo-jun, D. Qian, K. Hao, W. Rui-hong, L. Gang, S. Jun, Microstructure and mechanical properties of lanthanum oxide-doped Mo-12Si-8.5B(at.%) alloys, J. Alloys Compd. 577 (2013) S493–S498.

[44] J. Schneibel, M. Kramer, O. Ünal, R. Wright, Processing and mechanical properties of a molybdenum silicide with the composition Mo-12Si-8.5B (at.%), Intermetallics 9 (2001) 25–31.

[45] J. Lemberg, M. Middlemas, T. Weingärtner, B. Gludovatz, J. Cochran, R. Ritchie, On the fracture toughness of fine-grained Mo-3Si-1B (wt.%) alloys at ambient to elevated (1300 °C) temperatures, Intermetallics 20 (2012) 141–154.

[46] H. Choe, D. Chen, J. Schneibel, R. Ritchie, Ambient to high temperature fracture toughness and fatigue-crack propagation behavior in a Mo-12Si-8.5B (at.%) intermetallic, Intermetallics 9 (2001) 319–329.

[47] H. Choe, J. Schneibel, R. Ritchie, On the fracture and fatigue properties of Mo-Mo_3Si-Mo_5SiB_2 refractory intermetallic alloys at ambient to elevated temperatures (25 °C to 1300 °C), Metall. Mater. Trans.: A 34 (2003) 225–239.

[48] R. Mitra, A. Srivastava, N. Prasad, S. Kumari, Microstructure and mechanical behaviour of reaction hot pressed multiphase Mo-Si-B and Mo-Si-B-Al intermetallic alloys, Intermetallics 14 (2006) 1461–1471.

[49] R. Ritchie, Mechanisms of fatigue-crack propagation in ductile and brittle solids, Int. J. Fract. 100 (1999) 55–83.

[50] J. Rösler, H. Harders, M. Bäker, Mechanical Behaviour of Engineering Materials: Metals, Ceramics, Polymers, and Composites, Springer, Wiesbaden, 2006.

[51] C. Gupta, Extractive Metallurgy of Molybdenum, Taylor & Francis, 1992.

[52] T. Tietz, J. Wilson, Behavior and Properties of Refractory Metals, Stanford University Press, 1965.

[53] E. Passmore, Correlation of temperature and grain size effects in the ductile-brittle transition of molybdenum, Philos. Mag. 11 (1965) 441–450.

[54] J. Bechtold, B. Shaw, Fracture of Metals: An Advanced Treatise, Academic Press, New York, 1969.

[55] T. Watanabe, S. Tsurekawa, Toughening of brittle materials by grain boundary engineering, Mater. Sci. Eng.: A 387–389 (2004) 447–455.

[56] A. Van der Ven, G. Ceder, The thermodynamics of decohesion, Acta Mater. 52 (2004) 1223–1235.

[57] A. Kumar, B. Eyre, Grain boundary segregation and intergranular fracture in molybdenum, Proc. R. Soc. Lond. A 370 (1980) 431–458.

[58] M. Krüger, D. Schliephake, P. Jain, K. Kumar, G. Schumacher, M. Heilmaier, Effects of Zr additions on the microstructure and the mechanical behavior of PM Mo-Si-B alloys, JOM 65 (2013) 301–306.

[59] A. Koval, A. Vasilev, S. Firstov, Fracture toughness of molybdenum sheet under brittle-ductile transition, Int. J. Refract. Met. H. 15 (1997) 223–226.

[60] J. Schneibel, M. Brady, H. Meyer, J. Horton, J. Kruzic, R. Ritchie, Mo-Si-B alloy development, 2005.

[61] W. Martienssen, H. Warlimont, Springer Handbook of Condensed Matter and Materials Data, Springer, Berlin, 2005.

[62] M. Miller, E. Kenik, M. Mousa, K. Russell, A. Bryhan, Improvement in the ductility of molybdenum alloys due to grain boundary segregation, Scripta Mater. 46 (2002) 299–303.

[63] M. Miller, A. Bryhan, Effect of Zr, B and C additions on the ductility of molybdenum, Mater. Sci. Eng.: A 327 (2002) 80–83(4).

[64] Y. Hiraoka, H. Irie, M. Okada, Tensile properties of electron-beam-welded Mo-Nb, Mo-Zr and Mo-Re alloys, J. JPN Weld. Soc. 2 (1984) 154–159.

[65] B. Cockeram, E. Ohriner, T. Byun, M. Miller, L. Snead, Weldable ductile molybdenum alloy development, J. Nucl. Mater. 382 (2008) 229–241.

[66] M. Krüger, D. Schliephake, P. Jain, K. Kumar, G. Schumacher, M. Heilmaier, Effects of Zr additions on the microstructure and the mechanical behavior of PM Mo-Si-B alloys, JOM 65 (2013) 301–306.

[67] J. Becker, M. Krüger, Impact of phase distribution on the fracture toughness of high temperature resistant Mo-Si-B alloys, Pract. Metallogr. 52 (2015) 295–313.

[68] C. Hochmuth, D. Schliephake, R. Völkl, M. Heilmaier, U. Glatzel, Influence of zirconium content on microstructure and creep properties of Mo-9Si-8B alloys, Intermetallics 48 (2014) 3–9.

[69] I. Shabalin, Ultra-High Temperature Materials I: Carbon (Graphene/Graphite) and Refractory Metals, Springer, Heidelberg, 2014.

[70] Y. Hiraoka, M. Okada, H. Irie, Alloying to improve the properties of welded molybdenum, J. Nucl. Mater. 155 (1988) 381–385.

[71] R. Janisch, C. Elsässer, Segregated light elements at grain boundaries in niobium and molybdenum, Phys. Rev. B 67 (2003) 224101.

[72] D. Scheiber, R. Pippan, P. Puschnig, A. Ruban, L. Romaner, *Ab initio* search for cohesion-enhancing impurity elements at grain boundaries in molybdenum and tungsten, Modelling Simul. Mater. Sci. Eng. 24 (2016) 085009 (12pp).

[73] M. Gibson, C. Schuh, A compilation of ab-initio calculations of embrittling potencies in binary metallic alloys, Data in Brief 6 (2016) 143–148.

[74] R. Tran, Z. Xu, N. Zhou, B. Radhakrishnan, J. Luo, S. Ong, Computational study of metallic dopant segregation and embrittlement at molybdenum grain boundaries, Acta Mater. 117 (2016) 91–99.

[75] D. Scheiber, R. Pippan, P. Puschnig, A. Ruban, L. Romaner, Ab-initio search for cohesion-enhancing solute elements at grain boundaries in molybdenum and tungsten, Int. J. Refract. Met. H. 60 (2016) 75–81.

[76] J. Rice, J.-S. Wang, Embrittlement of interfaces by solute segregation, Mater. Sci. Eng.: A 107 (1989) 23–40.

[77] J. Beltrán, M. Muñoz, *Ab initio* study of decohesion properties in oxide/metal systems, Phys. Rev. B 78 (2008) 245417–1.

[78] J. Bartolomé, J. Beltrán, C. Gutiérrez-González, C. Pecharromán, M. Muñoz, J. Moya, Influence of ceramic-metal interface adhesion on crack growth resistance of ZrO_2-Nb ceramic matrix composites, Acta Mater. 56 (2008) 3358–3366.

[79] W. Zhang, J. Smith, X.-G. Wang, A. Evans, Influence of sulfur on the adhesion of the nickel/alumina interface, Phys. Rev. B 67 (2003) 245414–1.

[80] M. Mousa, N. Wanderka, M. Timpel, S. Singh, M. Krüger, M. Heilmaier, J. Banhart, Modification of Mo-Si alloy microstructure by small additions of Zr, Ultramicroscopy 111 (2011) 706–710.

[81] R. Martin, Electronic Structure: Basic Theory and Practical Methods, Cambridge University Press, Cambridge, 2004.

[82] J. Wills, O. Eriksson, P. Andersson, A. Delin, O. Grechnyev, M. Alouani, Full-potential electronic structure method, volume 167 of *Springer Series in Solid-State Science*, Springer, 2010.

[83] P. Hohenberg, W. Kohn, Inhomogeneous electron gas, Phys. Rev. 136 (1964) 864–871.

[84] V. Levitin, Interatomic Bonding in Solids: Fundamentals, Simulation, and Applications, Wiley, 2014.

[85] R. Jones, O. Gunnarsson, The density functional formalism, its applications and prospects, Rev. Mod. Phys. 61 (1989) 689–746.

[86] D. Ceperley, B. Alder, Ground state of the electron gas by a stochastic method, Phys. Rev. Lett. 45 (1980) 566–569.

[87] J. Perdew, J. Chevary, S. Vosko, K. Jackson, M. Pederson, D. Singh, C. Fiolhais, Atoms, molecules, solids, and surfaces: Applications of the generalized gradient approximation for exchange and correlation, Phys. Rev. B 46 (1992) 6671–6687.

[88] J. Perdew, K. Burke, M. Ernzerhof, Generalized gradient approximation made simple, Phys. Rev. Lett. 77 (1996) 3865–3868.

[89] H. Monkhorst, J. Pack, Special points for Brillouin-zone integrations, Phys. Rev. B 13 (1976) 5188–5192.

[90] P. Blöchl, Projector augmented-wave method, Phys. Rev. B 50 (1994) 17953–17979.

[91] R. Feynman, Forces in molecules, Phys. Rev. 56 (1939) 340–343.

[92] F. Murnaghan, The compressibility of media under extreme pressures, P. Natl. Acad. Sci. USA 30 (1944) 244–247.

[93] F. Murnaghan, Finite deformations of an elastic solid, Am. J. Math. 59 (1937) 235–260.

[94] F. Birch, Finite elastic strain of cubic crystals, Phys. Rev. B 71 (1947) 809–824.

[95] F. Featherston, J. Neighbours, Elastic constants of tantalum, tungsten, and molybdenum, Phys. Rev. 130 (1963) 1324–1333.

[96] D. Bolef, J. Klerk, Elastic constants of single-crystal Mo and W between 77° and 500° K, J. Appl. Phys. 33 (1962) 2311–2314.

[97] J. Che, C. Chan, W.-E. Jian, T. Leung, Surface atomic structures, surface energies, and equilibrium crystal shape of molybdenum, Phys. Rev. B 57 (1998) 1875–1880.

[98] J.-M. Zhang, D.-D. Wang, K.-W. Xu, Calculation of the surface energy of bcc transition metals by using the second nearest-neighbor modified embedded atom method, Appl. Surf. Sci. 252 (2006) 8217–8222.

[99] A. Tahir, R. Janisch, A. Hartmaier, Ab initio calculation of traction separation laws for a grain boundary in molybdenum with segregated C impurites, Model. Simul. Mater. Sc. 21 (2013) 075005–075020.

[100] K. Lipkowitz, R. Larter, T. Cundari, Reviews in Computational Chemistry, Bd. 21, Wiley, New Jersey, 2005.

[101] A. Yakoubi, O. Baraka, B. Bouhafs, Structural and electronic properties of the Laves phase based on rare earth type BaM_2 (M = Rh, Pd, Pt), Res. Phys. 2 (2012) 58–65.

[102] J. Gan, D. Keiser Jr., B. Miller, N. Eriksson, Y. Sohn, M. Kirk, Irradiation induced structural change in Mo_2Zr intermetallic phase, Scripta Mater. 121 (2016) 56–60.

[103] G. Rohrer, Structure and Bonding in Crystalline Materials, Cambridge University Press, Cambridge, 2004.

[104] A. Misra, J. Petrovic, T. Mitchell, Microstructures and mechanical properties of a Mo_3Si-Mo_5Si_3 composite, Scripta Mater. 40 (1998) 191–196.

[105] S. Aryal, M. Gao, L. Ouyang, P. Rulis, W. Ching, Ab initio studies of Mo-based alloys: Mechanical, elastic, and vibrational properties, Intermetallics 38 (2013) 116–125.

[106] L. Zhang, W. Du, M. Wang, Y. Hou, X. Ni, J. Lin, Intrinsic brittlement of Mo_3Si by first-principle calculations, Mater. Sci. Forum 747–748 (2013) 63–68.

[107] J. Xu, W. Hu, Y. Yan, X. Lu, P. Munroe, Z.-H. Xie, Microstructure and mechanical properties of a Mo-toughened Mo_3Si in situ nanocomposite, Vacuum 109 (2014) 112–119.

[108] M. Baskes, Atomistic potentials for the molybdenum-silicon system, Mater. Sci. Eng.: A 261 (1999) 165–168.

[109] H. J. Jansen, Electronic structure of cubic and tetragonal zirconia, Phys. Rev. B 43 (1991) 7267–7278.

[110] G. Teufer, The crystal structure of tetragonal ZrO_2, Acta Crystallogr. 15 (1962) 1187.

[111] P. Aldebert, J.-P. Traverse, Structure and ionic mobility of zirconia at high temperature, J. Am. Ceram. Soc. 68 (1985) 34–40.

[112] R. Terki, G. Bertrand, H. Aourag, C. Coddet, Structural and electronic properties of zirconia phases: A FP-LAPW investigations, Mat. Sci. Semicon. Proc. 9 (2006) 1006–1013.

[113] S. Fabris, A. Paxton, M. Finnis, Relative energetics and structural properties of zirconia using a self-consistent tight-binding model, Phys. Rev. B 61 (2000) 6617–6630.

[114] R. Cohen, M. Mehl, L. Boyer, Phase transitions and elasticity in zirconia, Physica B+C 150 (1988) 1–9.

[115] G. Stapper, M. Bernasconi, N. Nicoloso, M. Parrinello, *Ab initio* study of structural and electronic properties of yttria-stabilized cubic zirconia, Phys. Rev. B 59 (1999) 797–810.

[116] V. Milman, A. Perlov, K. Refson, S. Clark, J. Gavartin, B. Winkler, Structural, electronic and vibrational properties of tetragonal zirconia under pressure: A density functional theory study, J. Phys.: Condens. Matter 21 (2009) 485404–485415.

[117] J. Jaffe, R. Bachorz, M. Gutowski, Low-temperature polymorphs of ZrO_2 and HfO_2: A density-functional theory study, Phys. Rev. B 72 (2005) 144107–144115.

[118] Y. Natanzon, M. Boniecki, Z. Łodziana, Influence of elastic properties on superplasticity in doped yttria-stabilized zirconia, J. Phys. Chem. Solids 70 (2009) 15–19.

[119] J. Wachtman, W. Cannon, M. Matthewson, Mechanical Properties of Ceramics, 2nd ed., Wiley, Danvers, 2009.

[120] J. Nye, Physical Properties of Crystals: Their Representation by Tensors and Matrices, Clarendon Press, Oxford, 1957.

[121] E. Kisi, C. Howard, Elastic constants of tetragonal zirconia measured by a new powder diffraction technique, J. Am. Ceram. Soc. 81 (1998) 1682–1684.

[122] L. Sham, W. Kohn, One-particle properties of an inhomogeneous interacting electron gas, Phys. Rev. B 145 (1966) 561–567.

[123] G. Kresse, J. Furthmüller, Efficient iterative schemes for *ab initio* total-energy calculations using a plane-wave basis set, Phys. Rev. B 54 (1996) 11169–11186.

[124] G. Kresse, J. Furthmüller, Efficiency of *ab initio* total-energy calculations for metals and semiconductors using a plane-wave basis set, Comp. Mater. Sci. 6 (1996) 15–50.

[125] R. Bader, Atoms in Molecules: A Quantum Theory, International Ser. of Monogr. on Chem, Oxford University Press, Oxford, 1994.

[126] W. Tang, E. Sanville, G. Henkelman, A grid-based Bader analysis algorithm without lattice bias, J. Phys.: Condens. Matter 21 (2009) 084204.

[127] E. Sanville, S. Kenny, R. Smith, G. Henkelman, An improved grid-based algorithm for Bader charge allocation, J. Comp. Chem. 28 (2007) 899–908.

[128] G. Henkelman, A. Arnaldsson, , H. Jónsson, A fast and robust algorithm for Bader decomposition of charge density, Comput. Mater. Sci. 36 (2006) 254–360.

[129] N. Lang, W. Kohn, Theory of metal surfaces: Charge density and surface energy, Phys. Rev. B 1 (1970) 4555–4568.

[130] P. Sprunger, L. Petersen, E. Plummer, E. Lægsgaard, F. Besenbacher, Giant Friedel oscillations on the beryllium(0001) surface, Science 275 (1997) 1764–1767.

[131] J. Friedel, Metallic alloys, Nuovo Cimento 7 (1958) 287–311.

[132] J.-H. Cho, Ismail, Z. Zhang, E. Plummer, Oscillatory lattice relaxation at metal surfaces, Phys. Rev. B 59 (1999) 1677–1680.

[133] Y. Sun, A. Huan, Y. Feng, A. Wee, Reduction of amplitude and wavelength of Friedel oscillation on Na(111) surface, Phys. Rev. B 72 (2005) 153404–153407.

[134] J. Li, J. Wang, Q. Sun, Y. Jia, First-principles study of Friedel oscillations normal to the low index surfaces of Al, Physica B: Condens. Matter 406 (2011) 2767–2771.

[135] W. Pfeiler (Ed.), Alloy Physics: A Comprehensive Reference, Wiley-VCH, Weinheim, 2007.

[136] Y. Mishin, M. Sørensen, A. Voter, Calculation of point-defect entropy in metals, Phil. Mag. A 81 (2001) 2591–2612.

[137] R. Tilley, Understanding Solids: The Science of Materials, Wiley, New Delhi, 2004.

[138] V. Paidar, P. Lejček, Anisotropic behaviour of grain boundaries, Mater. Sci. Forum 482 (2005) 63–70.

[139] A. Lozovoi, A. Paxton, M. Finnis, Structural and chemical embrittlement of grain boundaries by impurities: A general theory and first-principles calculations for copper, Phys. Rev. B 74 (2006) 155416–155428.

[140] J. Howe, Interfaces in Materials: Atomic Structure, Thermodynamics and Kinetics of Solid-Vapor, Solid-Liquid and Solid-Solid Interfaces, Wiley, 1997.

[141] D. McLean, Grain Boundaries in Metals, Monographs on the physics and chemistry of materials, Clarendon, Oxford, 1957.

[142] R. Pond, V. Vitek, Periodic grain boundary structures in aluminium. I. A combined experimental and theoretical investigation of coincidence grain boundary structure in aluminium, Proc. Roy. Soc.: A (London) 357 (1977) 453–470.

[143] I. Kaur, Y. Mishin, W. Gust, Fundamentals of Grain and Interphase Boundary Diffusion, 3rd. rev. and enl. ed., Wiley, Chichester, 1995.

[144] A. Sutton, R. Balluffi, Interfaces in Crystalline Materials, volume 51 of *Oxford Science Publications*, Clarendon Press, Oxford, 1996.

[145] D. Wolf, S. Yip (Eds.), Materials Interfaces: Atomic-Level Structure and Properties, Chapman and Hall, London, 1992.

[146] M. Kronberg, F. Wilson, Secondary recrystallization in copper, Trans. AIME 185 (1949) 501–514.

[147] J. Sólyom, Fundamentals of the Physics of Solids. Volume 1: Structure and Dynamics, Springer, 2007.

[148] S. Ranganathan, On the geometry of coincidence-site lattices, Acta Cryst. 21 (1966) 197–199.

[149] J. Lalena, D. Cleary, M. Weiser, Principles of Inorganic Materials Design, Wiley, New Jersey, 2010.

[150] H. Kurishita, S. Kuba, H. Kubo, H. Yoshinaga, Misorientation dependence of grain boundary fracture in molybdenum bicrystals with various <110> twist boundaries, Trans. JPN Inst. Met. 26 (1985) 332–340.

[151] H. Kurishita, A. Ôishi, H. Kubo, H. Yoshinaga, Grain boundary fracture in molybdenum bicrystals with various <110> symmetric tilt boundaries, Trans. JPN Inst. Met. 26 (1985) 341–352.

[152] G. Palumbo, K. Aust, Structure-dependence of intergranular corrosion in high purity nickel, Acta Metall. 38 (1990) 2343–2352.

[153] A. King, S. Shekhar, What does it mean to be special? The significance and application of the Brandon criterion, J. Mater. Sci. 41 (2006) 7675–7682.

[154] D. Turnbull, R. Hoffman, The effect of relative crystal and boundary orientations on grain boundary diffusion rates, Acta Metall. 2 (1954) 419–426.

[155] J. Gibbs, The scientific papers of J. Willard Gibbs, volume 1. Thermodynamics, Dover Publications, Inc., New York, 1961.

[156] P. Wynblatt, D. Chatain, Anisotropy of segregation at grain boundaries and surfaces, Metall. Mater. Trans.: A 37 (2006) 2595–2620.

[157] H.-J. Butt, K. Graf, M. Kappl, Physics and Chemistry of Interfaces, Wiley-VCH, Weinheim, 2003.

[158] K. Reuter, M. Scheffler, Composition and structure of the $RuO_2(110)$ surface in an O_2 and CO environment: Implications for the catalytic formation of CO_2, Phys. Rev. B 68 (2003) 045407–045417.

[159] P. H. R.W. Cahn (Ed.), Physical Metallurgy: 2, 4th. ed., North-Holland, Amsterdam, 1996.

[160] R. Faulkner, Non-equilibrium grain-boundary segregation in austenitic alloys, J. Mater. Sci. 16 (1981) 373–383.

[161] E. Hondros, The influence of phosphorus in dilute solid solution on the absolute surface and grain boundary energies of iron, P. Roy. Soc.: A 286 (1965) 479–498.

[162] F. Erdogan, Fracture mechanics, Int. J. Solids Struct. 37 (2000) 171–183.

[163] W. Hosford, Mechanical Behavior of Materials, Cambridge, New York, 2005.

[164] R. Hertzberg, R. Vinci, J. Hertzberg, Deformation and Fracture Mechanics of Engineering Materials, 5th ed., Wiley, Danvers, 2013.

[165] E. Orowan, Fracture and strength of solids, Rep. Prog. Phys. 12 (1949) 185.

[166] M. Janssen, J. Zuidema, R. Wanhill, Fracture Mechanics, 2nd ed., Spon Press, Oxfordshire, 2004.

[167] E. Mittemeijer, Fundamentals of Materials Science, Springer, Stuttgart, 2011.

[168] D. Buckley, Surface Effects in Adhesion, Friction, Wear, and Lubrication, Elsevier, Amsterdam, 1981.

[169] B. Lawn, Fracture of Brittle Solids, 2nd ed., Cambridge University Press, Cambridge, 1993.

[170] E. Douglas, Introduction to Materials Science and Engineering: Guided Inquiry, 1st ed., Pearson, London, 2014.

[171] A. Griffith, The phenomena of rupture and flow in solids, Philos. Trans. Roy. Soc.: A 221 (1921) 163–198.

[172] C. Inglis, Stresses in a plate due to the presence of cracks and sharp corners, Proc. Inst. Naval Arch. 55 (1913) 219–230.

[173] M. Finnis, The theory of metal-ceramic interfaces, J. Phys.: Condens. Matter 8 (1996) 5811–5836.

[174] A. Dupré, Theorie Mecanique de La Chaleur, Gauthier-Villars, Paris, 1869.

[175] P. Lazar, Ab initio modelling of mechanical and elastic properties of solids, Ph.D. thesis, University of Vienna, 2006.

[176] J. Rose, J. Smith, J. Ferrante, Universal features of bonding in metals, Phys. Rev. B 28 (1983) 1835–1845.

[177] J. Ham, An introduction to arc-cast molybdenum and its alloys, ASME Trans. 73 (1951) 723–732.

[178] H. Okamoto, Mo-Zr (Molybdenum-Zirconium), J. Phase Equilib. Diff. 25 (2004) 485.

[179] E. Rudy, Ternary phase equilibria in transition metal-boron-carbon-silicon systems, Technical Report, Air Force Materials Laboratory, Metals And Ceramics Division, 1969.

[180] L. Brewer, Molybdenum: Physico-Chemical Properties of its Compounds and Alloys, volume 7 of *Special Issue Series*, International Atomic Energy Agency, 1980.

[181] A. Gokhale, G. Abbaschian, The Mo-Si (Molybdenum-Silicon) system, J. Phase Equilib. 12 (1991) 493–498.

[182] H. Okamoto, Mo-Si (Molybdenum-Silicon), J. Phase Equilib. Diff. 32 (2011) 176.

[183] W. Moffat, The Handbook of Binary Phase Diagrams, General Electric Co., Schenectady, N.Y., 1976.

[184] P. Tayler, D. V. Wagoner, C. Pitt, Solubility limits of selenium in copper, Metall. Trans. B 7 (1976) 103–106.

[185] A. Tsurekawa, T. Tanaka, H. Yoshinaga, Grain boundary structure, energy and strength in molybdenum, Mat. Sci. Eng.: A 176 (1994) 341–348.

[186] K. Ikeda, K. Morita, H. Nakashima, H. Abe, Misorientation dependence of grain boundary fracture strength and grain boundary energy for molybdenum <001> symmetric tilt boundaries, J. JPN Inst. Met. Mater. 63 (1999) 179–186.

[187] V. Sursaeva, V. Glebovsky, Y. Schulga, L. Schvindlerman, Strength of individual special tilt and twist boundaries in molybdenum bicrystals, Scripta Met. 19 (1985) 411–414.

[188] C. Kopetskii, A. Pashkovskii, Mechanical properties of molybdenum bicrystals, Sov. Phys. Dokl. 18 (1973) 340.

[189] S. Ratanaphan, D. Olmsted, V. Bulatov, E. Holm, A. Rollett, G. Rohrer, Grain boundary energies in body-centered cubic metals, Acta Mater. 88 (2015) 346–354.

[190] T. Ochs, C. Elsässer, M. Mrovec, V. Vitek, J. Belak, J. Moriarty, Symmetrical tilt grain boundaries in bcc transition metals: Comparison of semiempirical with ab-initio total-energy calculations, Phil. Mag. A 80 (2000) 2405–2423.

[191] T. Ochs, O. Beck, C. Elsässer, B. Meyer, Symmetrical tilt grain boundaries in body-centred cubic transition metals: An ab initio local-density-functional study, Phil. Mag. A 80 (2000) 351–372.

[192] A. Tahir, Development and validation of a scale-bridging method for simulation of intergranular fracture in body centered cubic metals, Ph.D. thesis, Ruhr-Universität Bochum, 2013.

[193] M. Methfessel, D. Hennig, M. Scheffler, Trends of the surface relaxations, surface energies, and work functions of the 4*d* transition metals, Phys. Rev. B 46 (1992) 4816–4829.

[194] T. Wang, X. Tian, Y. Yang, Y.-W. Li, J. Wang, M. Beller, H. Jiao, Structures of seven molybdenum surfaces and their coverage dependent hydrogen adsorption, Phys. Chem. Chem. Phys. 18 (2016).

[195] V. Vitek, G. Wang, Segregation and grain boundary structure, Surf. Sci. 144 (1984) 110–123.

[196] S. Srivastava, L. Seigle, Solubility and thermodynamic properties of oxygen in solid molybdenum, Metall. Trans. 5 (1974) 49–52.

[197] L. Brewer, R. Lamoreaux, The Mo-O system (Molybdenum-Oxygen), Bull. Alloy Phase Diagr. 1 (1980) 85–89.

[198] R. Yang, Y. Wang, H. Ye, C. Wang, First-principles study of the segregation effects on the cohesion of F.C.C. grain boundary, J. Phys.: Condens. Matter 13 (2001) 4485–4493.

[199] Y. Mishin, P. Sofronis, J. Bassani, Thermodynamic and kinetic aspects of interfacial decohesion, Acta Mater. 50 (2002) 3609–3622.

[200] I. Batirev, A. Alavi, M. Finnis, T. Deutsch, First-principles calculations of the ideal cleavage energy of bulk Niobium(111)/α-Alumina(0001) interfaces, Phys. Rev. Lett. 82 (1999) 1510–1513.

[201] W. Zhang, J. Smith, Stoichiometry and adhesion of Nb/Al_2O_3, Phys. Rev. B 61 (2000) 16883–16889.

[202] A. Christensen, E. Carter, First-principles characterization of a heteroceramic interface: ZrO_2(001) deposited on an α-Al_2O_3(1$\bar{1}$02) substrate, Phys. Rev. B 62 (2000) 16968–16983.

[203] A. Christensen, E. Carter, Adhesion of ultrathin ZrO_2(111) films on Ni(111) from first principles, J. Chem. Phys. 114 (2001) 5816–5831.

[204] R. French, S. Glass, F. Ohuchi, Y.-N. Xu, W. Ching, Experimental and theoretical determination of the electronic structure and optical properties of three phases of ZrO_2, Phys. Rev. B 49 (1994) 5133–5142.

[205] A. Christensen, E. Carter, First-principles study of the surfaces of zirconia, Phys. Rev. B 58 (1998) 8050–8064.

[206] A. Hofmann, S. Clark, M. Oppel, I. Hahndorf, Hydrogen adsorption on the tetragonal ZrO_2(101) surface: A theoretical study of an important catalytic reactant, Phys. Chem. Chem. Phys. 4 (2002) 3500–3508.

[207] I. Iskandarova, A. Knizhnik, E. Rykova, A. Bagatur'yants, B. Potapkin, A. Korkin, First-principle investigation of the hydroxylation of zirconia and hafnia surfaces, Microelectron. Eng. 69 (2003) 587–593.

[208] A. Eichler, G. Kresse, First-principles calculations for the surface termination of pure and yttria-doped zirconia surfaces, Phys. Rev. B 69 (2004) 045402–045418.

[209] M. Chase (Jr.), C. Davies, J. Downey (Jr.), D. Frurip, R. McDonald, A. Syverud, NIST-JANAF thermochemical tables, available at http://kinetics.nist.gov/janaf/, 2013.

[210] W. Zhang, J. Smith, X.-G. Wang, Thermodynamics from *ab initio* computations, Phys. Rev. B 70 (2004) 024103–024111.

[211] W. Zhang, J. Smith, A. Evans, The connection between *ab initio* calculations and interface adhesion measurements on metal/oxide systems: Ni/Al_2O_3 and Cu/Al_2O_3, Acta Mater. 50 (2002) 3803–3816.

[212] W. Pabst, G. Tichá, E. Gregorová, Effective elastic properties of alumina-zirconia composite ceramics - Part 3. Calculation of elastic moduli of polycrystalline alumina and zirconia from monocrystal data, Ceramics-Silikáty 48 (2004) 41–48.

[213] R. Farraro, R. Mclellan, Temperature dependence of the Young's modulus and shear modulus of pure nickel, platinum, and molybdenum, Metal. Trans.: A 8 (1977) 1563–1565.

[214] J. Rösler, M. Bäker, H. Harders, Mechanical Behaviour of Engineering Materials: Metals, Ceramics, Polymers, and Composites, Springer, Berlin, Heidelberg, 2007.

[215] J. K. J.H. Schneibel, M.P. Brady, R. Ritchie, On the improvement of the ductility of molybdenum by spinel ($MgAl_2O_4$) particles, Z. Metallkd. 96 (2005) 632–637.

[216] I. Gunter, J. Schneibel, J. Kruzic, Ductility and fracture toughness of molybdenum with $MgAl_2O_4$ additions, Mater. Sci. Eng.: A 458 (2007) 275–280.

[217] J. Lemberg, Fracture behavior of advanced structural materials, Ph.D. thesis, University of California, Berkeley, 2011.